ADDIS ABABA UNIVERSITY

COLLEGE OF NATURAL AND COMPUTATIONAL SCIENCES

SCHOOL OF EARTH SCIENCES

2D/3D analysis of magnetotelluric data in the Central Main Ethiopian Rift (CMER): Implications for Geothermal Resources

by

Aklilu Abossie

A Dissertation Submitted in Partial Fulfillment of the Requirements for the Degree of Doctor of Philosophy

in

Geophysics (Applied Geophysics)

Addis Ababa University

Addis Ababa

Ethiopia

Jan 2024

ADDIS ABABA UNIVERSITY

COLLEGE OF NATURAL AND COMPUTATIONAL SCIENCES

SCHOOL OF EARTH SCIENCES

This is to certify that the dissertation prepared by Aklilu Abossie, entitled: "2D/3D analysis of magnetotelluric data in the Central Main Ethiopian Rift (CMER): Implications for Geothermal Resources," and submitted in partial fulfillment of the requirements for the degree of Doctor of Philosophy in Applied Geophysics, complies with the regulations of the University and meets the accepted standards concerning originality and quality.

Signed by the examining committee:

	Signatures	Date
Examiner Dr. Friedmann Samrock (External examiner)	______________	______________
Examiner Prof. Tigistu Haile (Internal examiner)	______________	______________
Advisor Dr. Shimeles Fisseha (Principal advisor)	______________	______________
Advisor Prof. Bekele Abebe (Co-advisor)	______________	______________

Abstract

2D/3D analysis of magnetotelluric data in the Central Main Ethiopian Rift (CMER): Implications for Geothermal Resources

Aklilu Abossie

Addis Ababa University, 2024

Abstract

The Main Ethiopian Rift (MER) is a seismically and volcanically active portion of the East Africa Rift System (EARS). In the Central Main Ethiopian Rift (CMER), there are several active volcanoes and calderas that are known to be constantly changing, with periods of rising and sinking. Geothermal resources are often associated with these active volcanoes. This dissertation deals with the analysis of the 2D/3D crustal geoelectric models obtained through 2D joint (TE - transverse electric and TM - transverse magnetic modes) inversion of magnetotelluric (MT) data across CMER and a 3D inversion model from one of the hydrothermal occurrences in the CMER, Ashute geothermal field, which is found close to the western escarpment. This is aimed at investigating heat sources, heat flow paths, and geothermal resources to delineate and characterize the geothermal structures and comprehend the tectono-magmatic setting of the crust beneath the study area. Furthermore, the static shift correction data were used to obtain better and more accurate estimates of subsurface resistivities structure and thicknesses by using 1D joint inversion of TEM and MT data in the Ashute area. Based on the 3D inversion resistivity model, the subsurface beneath the Ashute geothermal site can be described by three main geoelectric layers. The top layer, which is relatively thin and highly resistant (> 100 Ωm) and extends down to 400 m depth, consists of unaltered volcanic rocks near the surface. Below this is a conductive layer (< 10 Ωm) with a maximum thickness of 1 Km, likely caused by the presence of clay layers (smectite, illite/chlorite zones) resulting from the alteration of volcanic rocks. In the third and deepest layer resistance of the subsurface gradually increases to an intermediate range (10–46 Ωm). This could be linked to the formation of high-temperature alteration minerals such as chlorite and epidote at depth, indicating the presence of a heat source. Similar to a typical geothermal system, the increase in electrical resistance below the conductive clay layer may suggest the existence of a geothermal reservoir Otherwise, no exceptional low resistivity (high conductivity) anomaly is detected at depth. The phase tensor analysis results across the CMER show a small beta value at low periods (nearly below 10 s), which indicates 1D or 2D structures, while at long periods (> 10 s), the data show 3D structures with a large value of $|\beta| > 3^0$. This asserts that the 2D inversion model can suitably describe the resistivity structures of the shallow crust. The dominant geo-electrical strike is estimated to be N15^0E using a Z-invariant and phase tensor azimuth. The results of 2D joint inversion of TE and TM modes seemingly identified partial melt within an upper crustal fracture zone (fault) with a resistivity of less than 5 Ωm at a depth of 12–22 km**.** This partial melt extends beneath the SDFZ with a width of approximately 10 kilometers horizontally. It could be related to the source of heat for the Ashute and Aluto geothermal fields.

Key Words: Magnetotelluric, TEM, Dimensional Analysis, Strike Analysis, Joint inversion, Static shift, Geothermal field, Resistivity, 2D inversion, 3D inversion, Ashute, CMER, Ethiopia.

Acknowledgments

First and foremost, I am grateful to my heavenly father for his ability to provide sustenance, which is my strength, throughout all of my dissertation work. Secondly, my deep gratitude goes to my advisors, Dr. Shimeles Fisseha and Prof. Bekele Abebe, for being an advisor in this research. They give me proper direction, encouragement, crucial comments, sound suggestions, and support through my research. I especially appreciate Dr. Shimeles Fisseha's willingness to provide the chance for fieldwork to develop my field experiences and to devote much of his time and energy to the entire stages of my work. I would like to express my gratitude to the Geological Survey of Ethiopia for supplying the original raw MT data and for loaning the MT instruments for data collection. I am appreciative of the support and assistance provided by the geophysicists at the Geological Survey of Ethiopia, including Kebede Mengesha, Asefa Yismaw, Tsegaye Wondefraw, Getachew Birusa, and Nantnaiel Mulugeta, during the fieldwork data collection. I would like to thank my friends, particularly Dr. Biruke Abera Cherkose, Yoseph Kebede, Dr. Adise Eshetu, Dr. Mebatseyon Shawel, Dr. Hailemichael Kebede, Dr. Yaya Ali, Dr. Jima, Dereje Mathewos, Dr. Barsisa Bekele, Dr. Bisrate Kebede, and Dr. Mingistu W. Tinsay, for their encouragement and support, as well as their provision of important materials. Additionally, I extend my thanks to the RiftVolc project for providing funding to supplement my research fieldwork. I am grateful to Dr. Dessie Nadew and Prof. Tigistu Haile, members of the supervisory committee, for their comments, follow-up, and encouragement. I would also like to thank the supervisory committee members, Dr. Dessie Nadew and Prof. Tigistu Haile, for their comments, follow-up, and encouragement.

I also want to express my gratitude to my mother, Abebech W. Georgis, my father, Abossie Anshebo, my family members, Mitiku Wachemo, Mathewos W. Georgis' entire family, and Etaferu Bishamo and her family for their patience and support. Lastly, I am deeply thankful to my family for their care and encouragement which has been instrumental in my academic journey. I would like to sincerely thank all the staff and colleagues at the School of Earth Sciences, especially Prof. Tilahun Mamo, Prof. Tigistu Haile, Dr. Bayisa Regassa, and Dr. Ameha Atnafu, for their support in the completion of my dissertation. I am also grateful to my colleagues at the School of Earth Sciences, AAU, for their contribution to my Ph.D. research work.

Table of contents

List of Figures

List of Abbreviations

1D, 2D and 3D	One, Two and Three Dimension
EARS	East African Rift System
SDFZ	Silti Debrezyte Fault Zone
WFB	Wonji Fault Belt
MT	Magnetotelluric
EM	Electromagnetic
MER	Main Ethiopian Rift
CMER	Central Main Ethiopian Rift
WZF	West Ziway fault
GSE	Geological Survey of Ethiopia
EAGLE	Ethiopia Afar Geoscientific Lithosphere Experiment
JICA	Japan International Cooperation Agency

Chapter 1 Introduction

1.1 Background

Geothermal energy is a superior option to renewable energy sources because it is both environmentally beneficial and sustainable. The attractive feature of geothermal energy is its independence from weather conditions, distinct from other renewable energy sources like wind, hydropower, and solar (Samrock et al., 2015). However, as Muñoz (2014) pointed out, unlike other renewable energy sources such as solar or wind energy, which have grown exponentially in recent years, geothermal energy has grown linearly (Bertani, 2010; Rybach, 2010)**.** Geothermal resources can be categorized based on their use for electricity production or other purposes. High-enthalpy resources, such as dry steam and hot fluids found in volcanic regions, and medium-enthalpy resources, utilized in contemporary binary cycle plants, are used for electricity production (Gupta, 2007). Meanwhile, resources with moderate to low-temperature ranges, like warm to hot seas, are ideal for direct heating and cooling purposes (Gupta, 2007). Geothermal resources vary based on their origin, with classifications including igneous intrusions, convective hydrothermal systems, and non-volcanic geothermal regimes Gupta (2007). Additionally, geothermal systems can be volcanic, non-volcanic, or a combination of both, each characterized by distinct heat transfer processes (Andersen & Wei, 2020; Hochstein, 2005). The characteristics of geothermal resources, such as temperature, depth, rock chemistry, groundwater quantity, and geological settings, vary significantly from region to region (Gupta, 2007). Geothermal resources are typically found in rifts, oceanic island hotspots, tectonically active regions, and along convergent plate edges. One well-known tectonically active region with significant geothermal potential is the East African Rift System (EAR), particularly in Ethiopia (Pürschel et al., 2013). The Main Ethiopian Rift (MER) is a seismically and volcanically active portion of the EAR, with the Central MER (CMER) extending from Lake Koka to Lake Awasa (Abossie et al., 2023a; Agostini et al., 2009; Gashawbeza et al., 2004; Keranen & Klemperer, 2008). Geothermal activity in the MER is primarily driven by the interaction of circulating water with a heat source, originating from the rift flanks and traveling through fault systems within the axial valley (e.g., Bretzler et al., 2011; Kebede, 2010; Pürschel et al., 2013). The Central MER (CMER) is a part of the MER that extends from Lake Koka to Lake Awasa and has boundary faults that typically run between N30°E and N35°E (Abossie et al., 2023a; Agostini et al., 2009; Keranen & Klemperer, 2008). In general, geothermal activity is mostly started in the majority of areas by the interaction of circulating water with a heat source. The water circulation of the geothermal activity in the MER originates from the rift flanks and travels via the dominant NS to NNE trending fault system within the axial valley (e.g., Bretzler et al., 2011; Kebede, 2010; Pürschel et al., 2013). The Ashute (around Butajira) geothermal field is found closer to the western rift escarpment in the CMER, where thermal manifestations like mud pools and hot springs are aligned NNE-SSW (Abossie et al., 2023a; Sinetebeb et al., 2020). The surface manifestation of the upper mantle-derived material (intrusion) was detected by using the map of residual anomalies in the rift floor, mostly associated with Quaternary peralkaline rhyolite centers of the MER floor (Mahatsente et al., 1999). According to Mahatsente et al. (1999), gravity data anomalies coincide with the inferred zone of intrusion, which is primarily concentrated in the north and central sectors of the rift floor.

Geophysical methods are used for the detection and monitoring of geothermal systems at several kilometers of depth in reservoirs during the exploration stage (Spichak, 2020). Spichak and colleagues (2013) proposed a novel theoretical framework for the Icelandic geothermal system, indicating that it is powered by an interlinked system of high-temperature magma channels positioned predominantly at depths ranging from 10 to 15 kilometers below the surface, with some extending beyond 20 kilometers. The rapid development of seismic techniques over the past ten years has made it possible to monitor reservoirs utilizing repetitive 3D surface seismic, surface-to-borehole vertical profiling of seismic, and borehole-to-borehole cross-well seismic (Muñoz, 2014). Meanwhile, Kim and team (2012), in their examination of background seismic disturbances, detected regions of reduced seismic wave velocity beneath the WFB, at the intersection of the NMER and CMER, and under the SDFZ on the western side of the CMER at depths within the mid-crustal range of 10–20 km. This result is in good agreement with the occurrence of high conductivity at SDFZ in the recent magnetotelluric studies across the rift, CMER (Abossie et al., 2023a; Hübert et al., 2018). Since electromagnetic techniques have been widely used to detect geothermal reservoirs, subsurface fluid circulation, and geoelectrical structures, resistivity has been shown to be incredibly sensitive to the presence of brine. The most effective EM technique for the characterization of a conductive reservoir covered by a larger and more conductive clay cap has been found to be magnetotelluric (Abossie et al., 2023a;

Spichak & Manzella, 2009). Accordingly, EM is now easily available, logistically practical, and supported by improved techniques and tools, and it has become quite popular. In the geothermal area, there are complicated geological structures due to hydrothermal circulation and alteration. Since the 3D inversion of the resistivity model is more appropriate than the 1D and 2D interpretations (Gupta, 2007). Árnason et al. (2010) found strong agreement between the 3D magnetotelluric (MT) model and the three-dimensional distribution of resistivity obtained through a joint 1D inversion of transient electromagnetic (TEM) and MT data. As a result, the crustal geoelectric structure of the eastern flank of the CMER and the major structural features like the Wonji Fault Belt are studied in sufficient detail by means of the MT method. On the other hand, despite being characterized by densely clustered volcanic vents (near the Butajira volcanic field), which is part of the SDFZ; a full description of the subsurface geoelectrical picture of the western portion of the CMER still requires additional data.

This thesis focuses on determining the 3D geoelectric structure by using data acquired from 30 MT stations in the Ashute geothermal field close to the SDFZ in order to detect hydrothermal alteration zones, explore and delineate geothermal resources for additional implementation and investigates a detailed 2D analysis of all the existing data from closely spaced twenty-one (21) broadband MT (BBMT) stations between Adami Tulu and the western margin of the CMER. As a result, the primary aim of this study is to develop a 3D resistivity model of the subsurface in order to map and characterize the geothermal structures in the Ashute geothermal field. Additionally, the 2D analysis of the MT data is instrumental in providing insight into the magmatic and thermal conditions, heat flow pathways, and understanding the tectono-magmatic environment of the crust beneath the western flank. This is by giving a special emphasis on the role of major tectonic features such as the SDFZ, Gademotta, west Ziway fault (WZF), etc. In addition, the study areas were analyzed to determine their geoelectrical dimensionality and directionality in the subsurface. Furthermore, we attempted to compare 3D MT data with and without static-shifted models and accomplished a joint 1D inversion of TEM and MT data.

1.2 Overview of the Study Area

1.2.1 Location of the study area

The study area is located in the CMER latitude $7.0^0\mathrm{N} - 8.5^0\mathrm{N}$ and longitude $38.5^0\mathrm{N} - 39.5^0\mathrm{N}$ as shown in Figure 1.1. The study particularly focuses on 3D MT data analysis of the Ashute Area shown in the left top corner of the Location map with a latitude of $7.94^0\mathrm{N} - 8.05^0\mathrm{N}$ and a longitude of $38.31^0\mathrm{E} - 38.47^0\mathrm{E}$. Furthermore, the 2D MT data analysis area extends from latitude $7.75^0\mathrm{N} - 8.10^0\mathrm{N}$ and a longitude of $38.31^0\mathrm{E} - 38.70^0\mathrm{E}$ which follows northwest to the southeast.

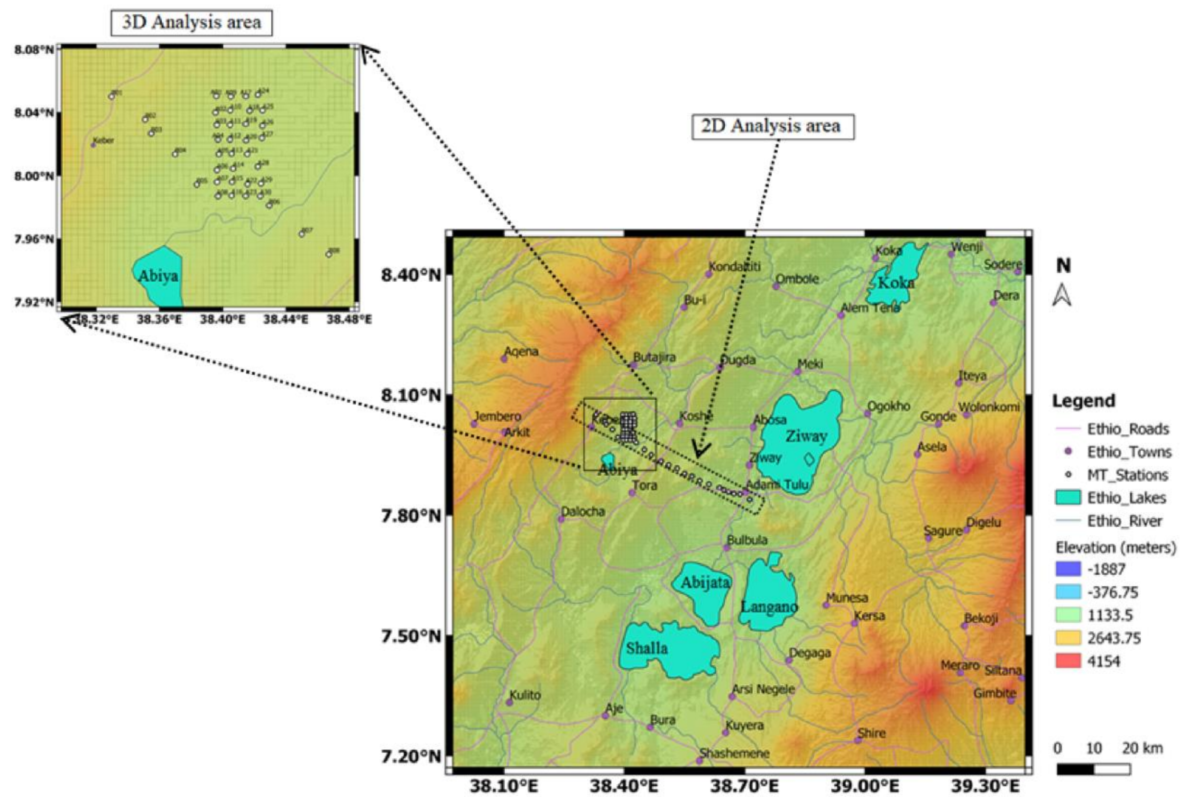

Figure .1.1 Location and topographic map of the study area

1.2.2 Tectonics and Geological settings

The Main Ethiopian Rift (MER) connects the Afar triple junction in the north with the Kenya Rift to the south of the East African Rift System (EARS) (Corti, 2009). The formation of the Ethiopian rift can be attributed to the influence of at least two mantle plumes, which are currently located beneath the Afar depression to the north of the MER and the Gregory Rift in Kenya, leading to the initiation of the rift. According to Yemane et al. (1999), the earlier Kenyan plume, which moved southward as the African plate shifted north, contributed to the Eocene-Oligocene magmatism of south Ethiopia. On the other hand, the Afar plume is supposed to be younger and is responsible for the majority of the magmatism in central Ethiopia and the Afar region (Morley et al., 1999). The MER, a roughly NE-oriented portion of the EARS, spans from the Afar to the Kenya Rift and comprises northern, central, and southern components (T. Abebe et al., 2010). As a magmatic rift, it has documented all stages of rift evolution, from its formation through the initiation of oceanic spreading. Consequently, it is an ideal location for studying various dynamics, including distributed energy, continental extension evolution, lithospheric plate rupture, and the progressive focus of continental deformation distributed at oceanic spreading centers (Corti, 2009).

The rift is situated within the Mozambique Belt, a wide Proterozoic mobile belt that stretches from Ethiopia southward through Kenya, Mozambique, and Tanzania (Keranen & Klemperer, 2008). The Quaternary-Recent axial segments in the central parts of the MER are laterally extended by approximately 10-15 km and are encompassed by a 60 km wide region distinct by NE-striking Miocene age of boundary faults that are anticipated to exploit similarly Proterozoic lithospheric fabric orientation (Bonini et al., 2005; Gashawbeza et al., 2004; Keranen & Klemperer, 2008). The volcanic chains of the Silti-Debre Zeit Fault Zone (SDFZ) are located near the western rift boundary. The Wonji Fault Belt (WFB) and SDFZ are two parallel bands of concentrated tectonic-magmatic activity inside this rift (Keir et al., 2015).

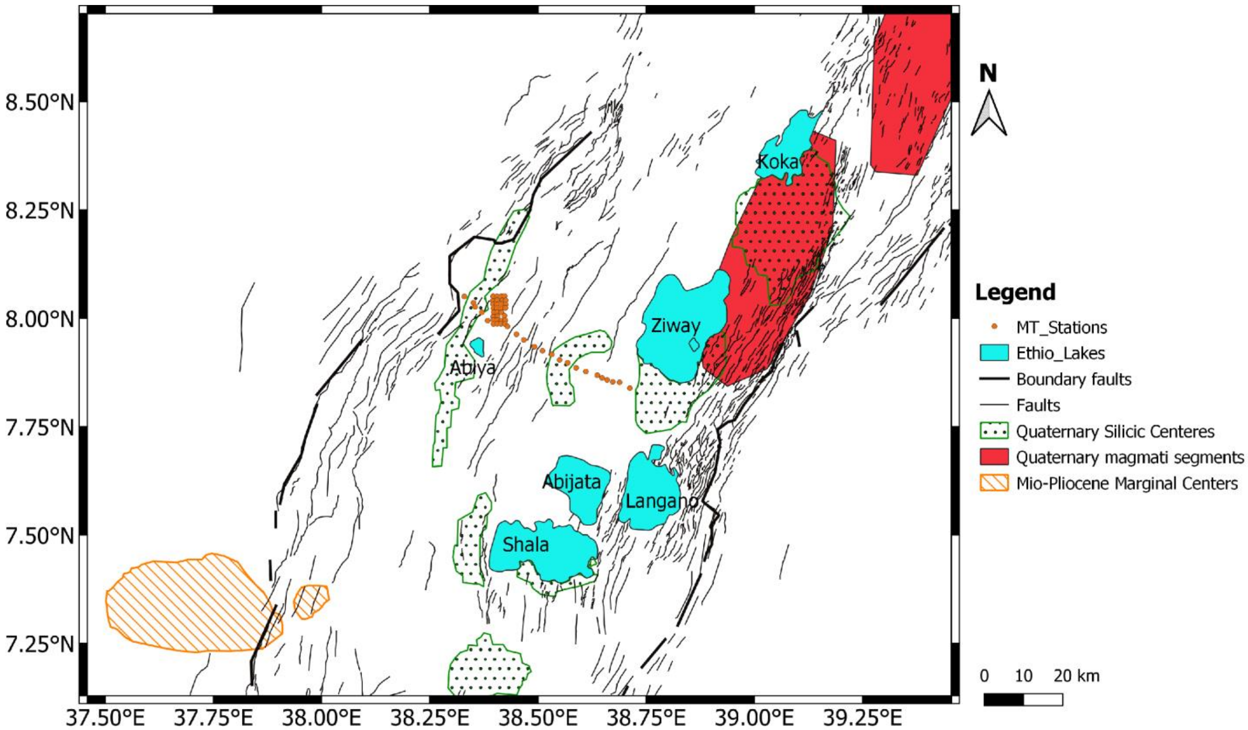

Figure 1.2 Tectonic setting in the Main Ethiopian Rift (MER) (Adapted and modified from Molin & Corti, 2015).

The majority of extensional deformation in the MER (> 50%) is thought to be accommodated by seismically-induced slip-on faults, which appear to have reduced in favor of the injection of magma through fractures associated with magmatic segments (Keir et al., 2006). The Ethiopia Afar Geoscientific Lithosphere Experiment (EAGLE) network of seismic stations collected comprehensive data regarding the seismic activity of the Northern and CMER between October 2001 and January 2003, revealing that seismic activity in these areas is often concentrated within Wonji segments, indicating a close link between the two (Keir et al., 2006). This revealed that seismic activity in these areas is often concentrated within segments called Wonji, suggesting a close connection between the two (Keir et al., 2006). A study using magnetotelluric techniques conducted by Whaler, K. A., & Hautot (2006) discovered areas of high electrical conductivity bodies, corresponding to the Boset-Kone magmatic segment and the northern end of the SDFZ, located at the upper and mid-crustal depths beneath the center and western flanks of the NMER. These findings align with images of seismic of the crustal structure in the MER (Kim et al., 2012). Furthermore, lower shear wave velocities are found at mid-crustal depths (10–20 km) beneath the SDFZ to the west and beneath the WFB in the transition zone between the CMER and the NMER. A 3D Magnetotelluric measurement of the electrical resistivity distribution in the Aluto-Langano geothermal area presented a conceptual model of high-enthalpy volcanic geothermal systems (Cherkose, B. A., & Mizunaga, 2018; Samrock et al., 2015). The 3D inversion analysis of the Aluto geothermal site has revealed several key resistivity structures, including a very low conductive layer at shallow depths, a conductive layer beneath it, and a high resistivity region at greater depths. The resistive propylitic up-flow zone underlays the conductive clay cap, as indicated by the data. The unrest at this site is possibly linked to variations in the hydrothermal system rather than changes within an active magmatic system. Moreover, the forward modeling of the tippers suggested that the presence of melt is mainly along an off-axis fault zone located 40 kilometers west of the CMER beneath the SDFZ (Samrock et al., 2015). This conductive body is consistent with a seismic low-velocity zone (Kim et al., 2012).

The floor of the rift, particularly the area surrounding Lake Langano, Ziway, and Awassa, is predominantly covered by lacustrine sediments of the Pleistocene-Holocene age. These sediments are intercalated with volcanic materials, particularly ashes, and tuffs, which are extensively developed in certain areas. Additionally, micro-organic deposits such as diatomite are associated with these lake sediments.

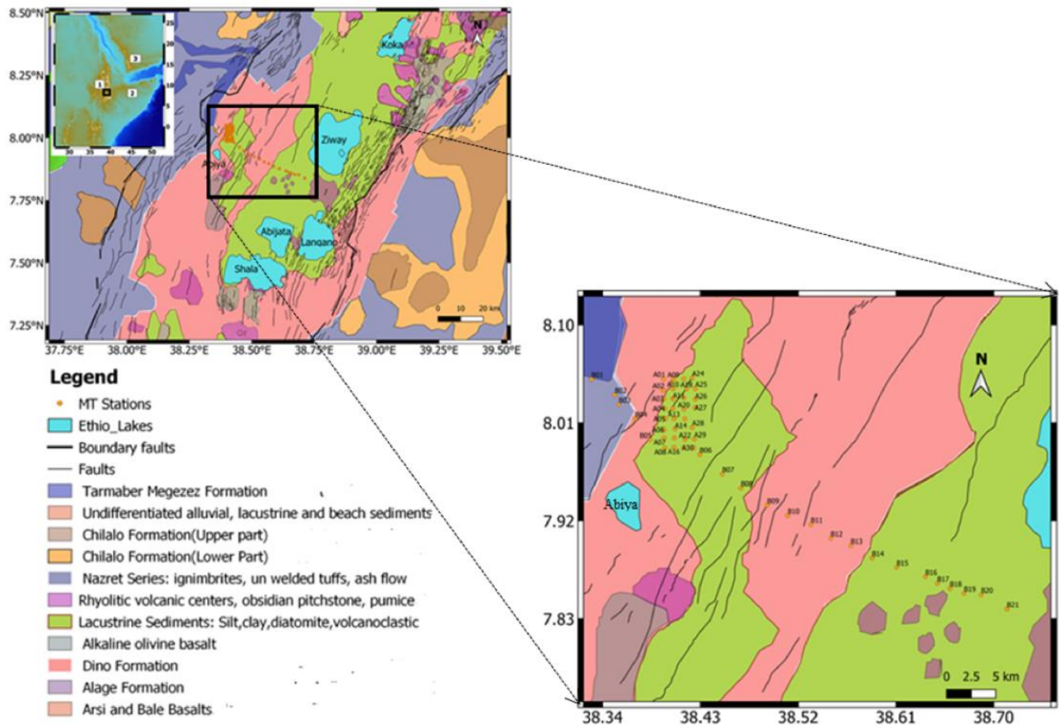

Figure 1.3 Geology and Fault Pattern of the CMER. Numbers 1, 2, and 3 represent the locations of the Nubian, Somalian, and Arabian tectonic plates respectively.

The strata of Pliocene-Pleistocene are generally observed at the scarps of these faults. Thick deposits of volcanic rocks are found at Gademotta and Mt. Aluto, but their distribution is obscured by overlying Holocene deposits (JICA & GSE, 2015). The western side of the CMER, particularly the SDFZ, is characterized by basaltic lava flows and Quaternary central volcanic, along with associated scoria cones and phreatomagmatic deposits (T. Abebe et al., 2010). The Bofa Basalt, the lowest geological unit, is only visible alongside the fault scarp situated to the east of Mt. Aluto. Geothermal borehole data indicates that the Bofa Basalt is covered by Gademotta Rhyolite. Similar rhyolite formations can be found to the east of Lake Ziway, suggesting the possible existence of rhyolitic volcanoes during that period. Additionally, Adami Tulu Basaltic Pyroclastics, Kulumusa highly welded tuff, and Ogolche Basalt are interspersed with lake sediments on top of the Gademotta Rhyolite. The area encompassing Lake Abijata-Langano-Shala and its surroundings lies on the basin floor of the CMER, which forms the flat floor of the Lake Ziway area. The basin floor is largely covered by Holocene lacustrine deposits, although the WFB (Wonji Fault Belt) intersects some of these sediments at specific points, resulting in a step-like topography. The positioning of Lake Langano and Lake Abijata is influenced by these faults. Lake Shalla is a caldera formed by a volcanic eruption, with the lowest geological unit in the area being rhyolitic tuff, visible at Munesa, located at the escarpment to the east of Lake Langano. This rhyolitic tuff is widespread in the surrounding area and is estimated to have formed between 3.17 and 3.48 million years ago, according to WoldeGabriel et al. (1990), indicating significant volcanic activity during that period(Le Turdu et al., 1999; WoldeGabriel et al., 1990). The strongly welded tuff of the Bilate River and its upper units are prominently displayed on the caldera wall of Lake Shala. Kuyera is a highly welded medium-tough rock, while poorly welded pumiceous pyroclastic rocks can be found from Lake Langano to Lake Abijata, extending to Shashamene Town. Volcanic activities during the Holocene period included rift floor basaltic activity southwest of Lake Shala, extending south towards the WFB, as well as simultaneous rhyolite volcanic activity northeast of Lake Shala.

Lake Awasa and its adjacent regions are situated within a caldera basin, which is encircled by a steep caldera wall. The volcanic rocks are visible along the wall from the Late Miocene to Pleistocene, while Holocene sediments are dispersed across the caldera floor (Le Turdu et al., 1999; Woldegabriel et al., 1990). The primary geological formation in the area is the Wendo Genet Rhyolite, which is prominently exposed at the base of the caldera wall and is believed to have originated from the Awasa caldera. In the western and southern sections of the caldera, the Wendo Genet rhyolite is covered by Abaye Ridge basaltic pyroclastics (Le Turdu et al., 1999; Woldegabriel et al., 1990). Welded tuffs, which are linked to the other two areas, are infrequently visible on the caldera wall. Notably, the Corbetti Volcano has played a significant role in Holocene volcanic activity, with its last eruption occurring approximately 20,000 years ago. Presently, fumaroles are present at the volcano's summit (Le Turdu et al., 1999; Woldegabriel et al., 1990). Therefore the geology of the CMER, particularly around Adami Tulu, Qoshe, Hiseno, Ashute, and Butajira, is characterized by a combination of volcanic, sedimentary, and tectonic features (Le Turdu et al., 1999). Volcanic rocks, including basalt, rhyolites, and ignimbrites, are abundant in the region, indicating past volcanic activity. These rocks are often found in layers, suggesting multiple volcanic events over time. The lacustrine sediments are exposed in the study area specifically around Adami Tulu and Ashute area. These sedimentary rocks provide valuable information about the past environmental conditions in the region.

Tectonically, the area is marked by active faulting, with faults and grabens being common features. This process, associated with the East African Rift System, involves the splitting of the African plate into Nubian and Somalian plates (Corti, 2009).

1.2.3 Previous Geothermal Exploration in the CMER

In the tectonically and volcanically active areas of the EARS, Ethiopia has a large potential for geothermal energy production (Pürschel et al., 2013). The MER is one section of the EARS system, which is a seismically and volcanically active portion that runs northeast through the Ethiopian plateau (Abossie et al., 2023a; Agostini et al., 2009; Gashawbeza et al., 2004; Keranen & Klemperer, 2008). The CMER is one portion of the MER where the geothermal resources are highly concentrated. The Tulu Moye, Aluto-Langano, Corbete, Ashute Shala, etc. are geothermal fields found in the CMER. As a result, Ethiopia is poised to emerge as a significant geothermal energy producer (Burnside et al., 2021). According to Burnside et al.(2021), the potential of geothermal energy in Ethiopia has an estimated value of >10,000 MW, compared with the country's current power generating capacity, which is estimated to be more than double (4,400 MW). Ongoing initiatives, including the expansion of the Aluto-Langano plant to 75 MW and plans for two additional 500 MW projects in Tulu Moye and Corbetti, underscore the nation's commitment to harnessing this valuable resource (Burnside et al., 2021; Tadesse et al., 2018). Therefore, different studies of geophysics have been conducted in order to explore the geothermal resource in the CMER, like magnetic, electrical, and magnetotelluric methods (Abossie et al., 2023b, 2023a; Cherkose, B. A., & Mizunaga, 2018; B. Kebede et al., 2023; Samrock et al., 2015). B. Kebede et al. (2023) used electrical resistivity, gravity, and magnetic surveys to describe the geothermal potential of the Corbetti Caldera in the CMER. The Aluto-Langano geothermal field was well studied by Cherkose, B. A., & Mizunaga (2018), and Samrock et al.(2015) using magnetotelluric data. The Tulu Moye geothermal field also has been studied with 3D inversion of magnetotelluric data (Samrock et al., 2018). However, this study focuses on investigating the geothermal system of the Ashute geothermal site by generating a 3D electrical resistivity model of the subsurface to delineate and characterize the geothermal structures. Additionally, the study aims to investigate the regional heat source and heat flow direction using magnetotelluric data.

1.3 Rationale and Objectives of the Study

1.3.1 Overview of Previous Studies

The MER is a seismically and volcanically active part of the EARS, connecting the Afar Depression to the Turkana Depression and the Kenya Rift to the south. Several volcanoes in the Central Rift Valley of Ethiopia exhibit periodic uplift and subsidence, with the Aluto volcanic complex hosting a productive geothermal field (Casey et al., 2006; Keranen & Klemperer, 2008). Several active volcanoes and caldera edifices are hosted in the CMER (Peccerillo et al., 2003). The observed surface deformation at Aluto has been attributed to either a shallow hydrothermal/non-volcanic system or a deeper volcanic system (Biggs et al.,2011). The prevailing tectono-volcanic setup beneath the Aluto geothermal plant is a central research theme for geoscientists due to its implications for productivity and volcanic hazards. While several investigations have indicated the presence of magma storage at 5 km depth, the recovered 3D conductivity models of the Aluto geothermal field do not provide evidence of an active magmatic system or partial melt under Aluto (Cherkose, B. A., & Mizunaga, 2018; Samrock et al., 2015). On the other hand, the new chronostratigraphic results of Hutchison et al.(2018) estimate that the youngest post-caldera eruptions at Aluto have taken place within the last 1,000 years, emphasizing the active nature of these volcanic complexes. This may lead to the optimistic idea that finding the heat source for the Aluto and other geothermal manifestations within the central MER is a plausible venture.

Electromagnetic (MT) studies have successfully identified conductivity anomalies associated with magma accumulation zones beneath active volcanoes (Árnason et al., 2010; Rosenkjaera et al., 2015). Samrock et al. (2015) and Cherkose, B. A., & Mizunaga (2018) conducted a broadband MT survey to examine the structure of electrical conductivity under the Aluto geothermal site. The resulting 3D subsurface conductivity model of the Aluto volcanic complex didn’t reveal high conductivity at a greater depth. Evidently, there was no indication of a deeper conductive anomaly that could signal the presence of interconnected magma storage at depth. However, the recovered 3D conductivity models of the Aluto geothermal field were interpreted in conjunction with the reservoir conceptual model of a high-enthalpy geothermal system and revealed that the top unaltered layer zone was defined by both subsurface geoelectrical models as a conductive clay cap zone overlying a resistive up-flow zone. However, neither provides evidence of an active magmatic system or partial melt under Aluto (Cherkose, B. A., &

Mizunaga, 2018; Samrock et al., 2015). This contrasts with findings from other investigations, such as InSAR, seismology, and CO2 degassing studies, which designate magma storage at a depth of 5 kilometers. However, simultaneous inversion of impedances and tippers revealed consistent behavior of eastward-pointing the real tippers over extended periods, which could not be explicated by any structure within the modeling region (Samrock et al., 2015). The only potential conductor that comes into consideration is the SDFZ, located approximately 40 kilometers west of Aluto, near the western rift border.

The work of Samrock et al. (2015) suggests the following:

1. The complex fluid flow and mixing of shallow and deep fluids in the reservoir may cause thermoelastic expansion and clay swelling, leading to cyclic surface deformations.
2. Magma and melt are mostly found at lower crustal depths along the western side of the main rift axis rather than along the seismically active faults along the central rift axis in the Lake District of the MER.
3. Conducting regional resistivity research in the rift valley and understanding the characteristics of the postulated deep conductor beneath the SDFZ is crucial for obtaining a comprehensive understanding of magmatic evolution and the thermal regime in the MER.

Hübert et al. (2018) also conducted the 2D inversion model, involving MT data from long-period and broadband measurements along a 110 km transect that crosses the Aluto active post-caldera stage volcano, revealing the electrical resistivity structure beneath the Central Main Ethiopian Rift (CMER). The outstanding feature in this model is a sub-vertical conductor (less than 10 Ωm resistivity), which spatially correlates with the SDFZ. Therefore, to gain a comprehensive understanding of magmatic evolution and the thermal regime in the MER, the first component of this study will undertake a detailed 2D analysis of all the existing data between Adami Tulu and the western Margine traverse, with a special emphasis on the role of major tectonic features such as the SDFZ, Gademotta, and the West Ziway Fault. The second major undertaking in this Ph.D. project will be the 3D magnetotelluric modeling of the gridded data from the Ashute geothermal manifestation south of Butajera town, to map the interrelationship between the silt-Aluto geothermal system, various thermal manifestations, and the litho-structural setup of the subsurface. This work will help identify the likely host and cap rocks in the study area and provide a clear picture of the magmatic evolution and thermal regime in the SDFZ-Aluto.

1.4 Research Objectives

1.4.1 General Objective

The general objective of this study is a 2D/3D analysis of magnetotelluric data in the Central Main Ethiopian Rift (CMER) to map geoelectrical structures, heat flow direction, and characterize the geothermal resource potential, with a focus on the western flank.

1.4.2 Specific Objective

The specific objectives of this study are:

1. Acquire process, and analysis of magnetotelluric data from the CMER region to obtain reliable information about the subsurface's electrical conductivity.
2. Determine a subsurface high conductive body beneath Adami Tulu to the western border of CMER (near Butajira) using a 2D inversion model of MT data. This will assist in finding the heat source of the Aluto and Ashute geothermal fields and determining the structural control of heat flow direction within the study area.
3. Create a 3D electrical resistivity model of the subsurface to identify and characterize hydrothermal alteration zones in the Ashute geothermal field. Additionally, pursue to compare the relationship between the 3D inversion model of the MT data with and without static shift correction, and ascertain the depth of the Caprock, which is associated with a high thermal anomaly in the study area.
4. Provide recommendations and insights for optimizing geothermal resource exploration and development strategies in the CMER. This will take into account identified reservoirs, their characteristics, and potential energy extraction capabilities.

1.5 Significance of the study

A comprehensive investigation was undertaken to resolve the geoelectrical structures of both the Ashute geothermal field and the Adami Tulu-Butajira profile within the CMER region. This extensive study delved into the analysis of 2D and 3D magnetotelluric data, aiming to delineate the geothermal resource, pinpoint melt and fluid pathways, and extract valuable insights into the subsurface geoelectrical structure of geothermal reservoirs. The examination of magnetotelluric data stands as a pivotal tool, indispensable for interpreting the intricate geological, geophysical, and tectonic processes associated with rift formation and evolution.

The knowledge garnered from this analysis assumes paramount importance, serving as a linchpin for resource exploration, hazard assessment, and scientific inquiry within the rift zone. The revelations derived from this study, strategically employed in hazard assessment, not only bear the potential for economic gain through power generation and investment but also contribute significantly to future geophysical research endeavors in the region. The acquired information thus plays a pivotal role in propelling geophysical research forward, fostering economic development through power generation, and deepening our comprehension of the dynamic processes within the rift zone.

1.6 The scope of a study

The scope of a study on the 2D/3D analysis of magnetotelluric data in the CMER typically includes the following key aspects:

1. Collection, Processing, and analysis of magnetotelluric (MT) data: This involves deploying MT stations in the CMER, recording natural variations of EM field in the Earth, and processing the collected data to create 2D/3D models of the subsurface electrical resistivity structure.
2. Conductivity Modeling: Researchers construct 2D or 3D models of subsurface conductivity using computational techniques and inversion algorithms to estimate the distribution of electrical properties in the CMER subsurface based on the processed magnetotelluric data.
3. Geoelectrical Structural and Tectonic Analysis: The derived 2D/3D models from the MT data are utilized to analyze the structural and tectonic features of the study area, identifying fault systems, magma chambers, and other geological structures that may influence the distribution and characteristics of geothermal resources.
4. Implications and Recommendations: The study provides valuable implications for geothermal resources in the region and may offer recommendations for further exploration or potential areas

for geothermal energy projects, considering the identified subsurface structures and their geothermal potential.

In summary, the study aims to evaluate the geothermal potential of the CMER by acquiring, analyzing, and interpreting MT data. Its goal is to provide a comprehensive understanding of the subsurface structure, identify potential geothermal resources, and guide geothermal exploration and development in the region.

1.7 Limitation of the Thesis Work

The research conducted on 2D/3D analysis of magnetotelluric data in CMER offers valuable insights into the implications of geothermal resources. However, there are some limitations to consider.

- There is limited data coverage, particularly in the southern part of the Ashute geothermal field, due to budget constraints.
- Insufficiently constraining geophysical data (like seismic, gravity, and borehole data) and geological models can help improve the understanding of the subsurface and reduce uncertainties in geothermal resource implications in the study region.
- Economic viability: this study does not directly address economic viability and the commercial potential of geothermal resources. Factors such as drilling costs, reservoir productivity, and energy market considerations also need to be evaluated to assess the economic feasibility of geothermal development in the CMER region.

1.8 Thesis structure

The eight chapters of this dissertation are organized around three publications that have been either published or submitted in manuscript-refereed scientific journals (Appendices 1.1 to 1.3). of the three pieces, two have been published and one has been submitted. The appendices provide the titles, abstracts, publication, and submission details for each manuscript (Appendices 1.1 to 1.3). Appendix 2.1 provides Joint inversion of TEM and MT Sounding Curves. It should be prominent that each chapter has original findings that complement one another. There might, however, be an unavoidable repetition of background material in each article or chapter. An outline of how the thesis is structured is provided below:

The first chapter provides a broad introduction, detailing the study's background, and a comprehensive overview of the study area, starting with a description of its location and geological setting, followed by an examination of the geological and structural features in the region under consideration, and concluding with an exploration of the geothermal activity in the area, and research objectives. The major and specific goals of the study are laid out in this part after establishing and documenting the basis for the investigation by evaluating related prior research. Chapter 2 initiates a comprehensive explanation of the theoretical principles behind magnetotelluric methods. It covers the fundamental equations (mathematical formulation) of magnetotelluric methods along with a detailed explanation of magnetotelluric data acquisition processing and inversions. Chapter 3 describes data acquisition, processing, and inversion. In this section, the MT and TEM data acquisition and processing methods are first presented. Secondly, the 1D, 2D, and 3D inversion methodologies are stated.. Chapter 4 discusses a 3D analysis of magnetotelluric (MT) data to examine the resistivity structure beneath the Ashute Geothermal Site in the Central Main Ethiopian Rift (CMER). Chapter 5 delves into the Crustal Resistivity Structures beneath the western flank across the Central Main Ethiopian Rift and their implications for partial melting and pathways. Chapter 6 describes the joint 1D inversion of MT and transient electromagnetic (TEM) data, as well as the 3D inversion of static-shifted magnetotelluric data. This chapter represents the third significant finding of the thesis work, comparing the 1D joint inversion of TEM and MT data and 3D with and without static-shifted corrected MT data in the region under consideration. The thesis concludes with general conclusions and recommendations in Chapter 7. Each chapter ends with concluding remarks in this section, and the references used for this thesis are listed alphabetically at the end.

Chapter 2 Electromagnetic Methods for Geothermal Field Study

Electromagnetic induction studies, which are based on the time-varying electric and magnetic field measurements at an observation site on the Earth's surface, can be used to assess the distribution of electric conductivity in the subsurface. By applying electric conductivity measurement, electromagnetic methods are the best geophysical methods used in geothermal sites to characterize the geothermal setting as a system of faults and/or fractures filled with conducting geothermal fluids and altered rocks (Muñoz, 2014). The Maxwell equations, which relate the electromagnetic field to the physical properties, are in a three-dimensional medium. The measurement of electric conductivity is an important characteristic for defining the geothermal setting. The method provides useful information by relating the geothermal system's resistivity structure to parameters such as permeability, temperature, salinity, porosity, and the degree of hydrothermal alteration of the host rock, all of which are commonly used to describe geothermal systems (Hersir & Bjornsson, 1991). Controlled sources of electromagnetic methods, such as TEM, and natural source electromagnetic methods, such as MT, are the most extensively utilized sources of electromagnetic methods for geothermal areas.

2.1. Magnetotelluric Method

2.1.1 Introduction

The magnetotelluric technique is a passive geophysical method built on measurements of the natural Earth's EM fields to explore the subsurface electrical resistivity distribution from depths of tens of meters to the upper mantle (Vozoff, 1991). EM induction studies, based on measurements of natural transient electric and magnetic fields at an observation point on the Earth's surface, provide a means of determining the subsurface distribution of electrical resistivity. The natural signal EM-induction studies are mainly carried out by means of two well-established techniques: the magnetotelluric (MT) and the geomagnetic depth sounding (GDS) method. As a technique in applied geophysics, the MT method was first recognized in the 1950s and was initially outlined by Tikhonov (1950), and later by Cagniard (1953). A broadband depth sounding ranging in frequency from > 0.0001 Hz to < 10,000 Hz can be employed for shallow and deep structural investigations. The natural MT fields of frequencies from 0.0001 to 1Hz are generally produced by geomagnetic micro pulsations. The skin depth is defined as the depth at which the field amplitude of a plane EM wave is attenuated by ≈ 0.37 of its surface value, which is a good measure of depths of penetration. The greater the depth of penetration, the longer the period T, and vice versa. The term "skin depth" or "penetration depth" (δ) is frequently used to define the relationship as

$$\delta(T,\rho) \approx 500\sqrt{T\rho} \quad (2.1)$$

where $T=2\pi/\omega$ is the period in (s), and ρ is the uniform half-space of the equivalent average resistivity in (Ωm).

For MT studies, the usual components measured at a single site are time variations of the three orthogonal magnetic fields and two electric fields simultaneously acquired on the Earth's surface. The basic concept is that subsurface information is sought at an observation point, and the horizontal components of EM fields measured that caused by natural sources. The ratio of the electrical field to the magnetic field intensities, the electromagnetic impedance, yields Earth resistivity as a function of frequency, subsequent in the form of depth sounding. Owing to the simplicity of the theory in the time domain, MT processing is preferably done in the frequency domain, in which impedances, Tippers, and the corresponding statistical errors are computed. These calculated parameters are interpreted based on the relationship between electrical resistivity, position, and depth. For the outcome, numerical models for one, two, and three-dimensional structures are employed. Moreover, the magnetic transfer functions are used in dimensional analysis, resulting in a complete description of conductivity structures in the subsurface. The electrical conductivity of the subsurface is recognized as an important parameter for characterizing geothermal settings. Due to the low resistivity of the magma in volcanic environments, the magnetotelluric (MT) approach can offer significant constraints on volcanism. The MT technique is a crucial tool for researching magma storage, partial melt, and routes in active rift zones and other tectonic regimes since the Earth's bulk electrical resistivity is intrinsically dependent on variables like fluid content and temperature. In geothermal systems, the fluids that come from the Earth's heat are found in areas with faults and fractures that can contain high concentrations of dissolved salts. This creates conducting electrolytes within the rock. The temperature affects the ability of both the fluid and the rock to conduct electricity, although the impact on the rock is minimal. Generally, geothermal systems have lower resistance to electricity than the surrounding rocks. The hydrothermal processes in these systems cause changes in clay minerals, which also affect resistance to electricity(Tuyen et al., 2014). The magnetotelluric (MT) method has long been recognized as the ideal technique for geothermal exploration, given its ability to investigate great depths and effectively map low-conductivity zones linked to high-temperature phenomena. (Zhdanov & Keller, 1994). Accordingly, MT measurements presented the best method for detecting the greater depth of the geothermal reservoir beneath a thick, highly conductive "clay cap" at the top of the reservoir. It delivers a significant contribution to geothermal exploration and exploitation through cautious data acquisition, processing, modeling, and interpretation in terms of mapping several kilometers needed for some geothermal targets (Tuyen et al., 2014). Its integration with other geological and geophysical data, in particular seismic data, will recover imaging of the geothermal systems of static and dynamic processes (Spichak & Manzella, 2009). As a result, the magnetotelluric (MT) method has long been recognized as the best approach for exploring geothermal areas due to its ability to investigate deep underground and identify areas with low electrical conductivity caused by high temperatures (Zhdanov & Keller, 1994). MT measurements are particularly effective at detecting the depth of the geothermal reservoir beneath a thick layer of highly conductive clay at the top of the reservoir. By carefully collecting, processing, modeling, and interpreting data, the MT method provides valuable insights for mapping geothermal targets over several kilometers. When combined with other geological and geophysical data, especially seismic data, it can produce images of both the static and dynamic processes within geothermal systems. (Spichak & Manzella, 2009)

In this paper, the researcher presented the results of 3D inverse modeling of a detailed MT survey of the geothermal system of the Ashute area near the SDFZ and a 2D inversion model on the Butajira-Adami Tulu traverse.

2.1.2 Sources of Magnetotelluric Signal

The MT method is a survey technique that measures the electric and magnetic field components on the surface of the Earth. These measurements are used to analyze the wide spectrum of EM field waves, known as the natural source field, which are generated by changes in the magnetic field of the Earth (Chave & Jones, 2012; Vozoff, 1991). These fields cause Earth's surface currents to be generated, and these currents can be monitored to reveal subsurface resistivity patterns. The sources of these fields are two i.e. lightning strokes of the natural MT fields of the higher frequency signal (greater than 1 Hertz) created by worldwide thunderstorms, usually near the equator (Figure 2.1b). The other source is the interaction of the solar wind with the magnetosphere) at frequencies below 1 Hz (Figure 2.1a) (Vozoff, 1991). The Earth's geomagnetic field interacts with the solar wind through a centered magnetic dipole that is 11° inclination to the planet's axis. In addition to Mercury, Jupiter, Saturn, and Neptune, the other planets in our solar system are magnetic bodies submerged in the solar activity-produced growing coronal atmosphere (Conde, 2018). As solar storms emit streams of ions, this energy disturbs the magnetic field of the Earth and causes low-frequency energy to penetrate the Earth's surface. The fields originated in outer space, mostly due to solar wind, which perturbs the terrestrial magnetic field. Such perturbations lead to the deformation of the magnetosphere, which is partly constituted of ionized plasma. When these waves reach the Earth, they act like plane waves, with only a small amount of energy propagating vertically downward into the Earth and most of the energy being reflected. The structure of electrical resistivity in the subsurface influences the phase, amplitude , and directional relationships between the electromagnetic fields on the surface (Vozoff, 1991).

As discussed by Yungul (1996) and Mohamed (2002) electrical storms or meteorological activities in the higher frequencies greater than 1 Hertz are the main source of fields in the lower atmosphere. It consists of fields from lightning and is associated with thunderstorms. The lighting signals from the release are known as "sferics," and their frequency ranges are between 5 Hz and 30 MHz. They attain their peaks in the early afternoon, local time. The low-amplitude signals in the shift between the meteorological and the solar-triggered at a frequency of about 1 Hz are mentioned as the MT "dead band" (Miensopust, 2010; Simpson & Bahr, 2005). Its wave-guide width is 60 km in the daytime and during nighttime time increases to 90 km. The complex interaction between the Earth's magnetic field and atmosphere and the solar wind (charged particles emanating from the sun) results in what is called "micro pulsations," which are the key source of fields in the frequency range of 0.00167 to 5Hz (Yungul, 1996). The equatorial regions of Brazil, central Africa, and Malaysia are home to three storm centers. Protons and electrons are produced by ionized particles as they come into contact with the Earth's magnetosphere while they are traveling away from the sun. Protons and electrons are deflected in opposite directions when they come into contact with the terrestrial magnetic field. As a result, current systems are created with their secondary magnetic field to counteract the Earth's field, which presents to alter at a level of a few gammas at the "magnetopause," or the outer edge of the magnetosphere (Mohamed, 2002).

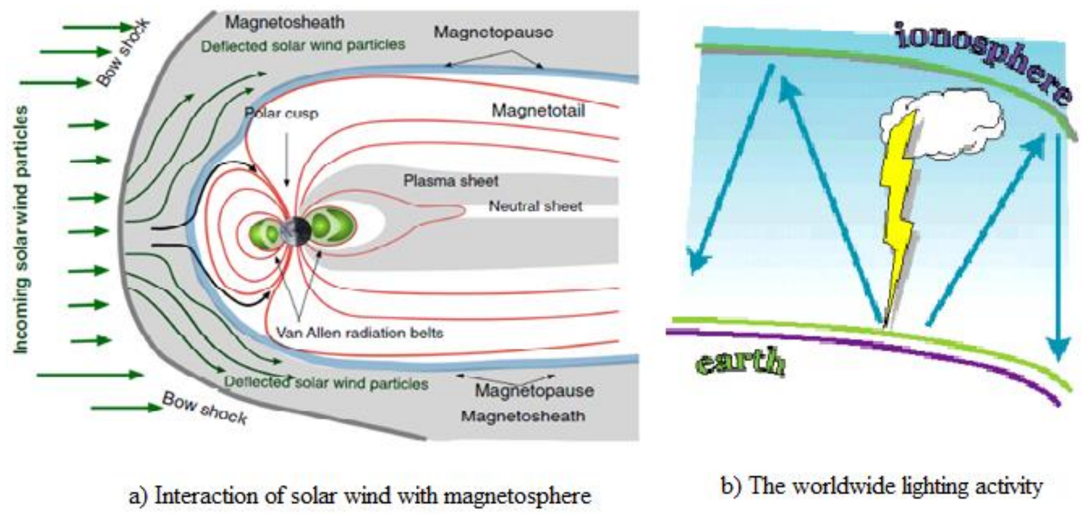

Figure 2.1 The source of the natural electromagnetic field (a) with frequencies < 1 Hz, the interaction of solar wind with the magnetosphere, and (b) >1 Hz, the worldwide lighting activity (Adapted from Christopherson (1998) and Conde (2018))

According to Conde (2018), the magnetosphere of the planets is a region of space where large-scale fluxes of charged particles and the solar wind are diverted around the planetary magnetic fields resulting from their interaction. The Earth's magnetosphere is shaped like a compressed area around 6–10 times the Earth's radius from the sun, where the magnetized solar wind creates a shock wave called the bow shock. This is represented by the thick grey line in Figure 2.1a. The magnetopause surface encloses the atmosphere, ionosphere, and Van Allen radiation belts. (the blue thick line in Figure 2.1a denotes the magnetosphere's outer boundary). The magnetotail spans 1000 times the radius of Earth on the night side, and the region of tail currents is surrounded by plasma known as the plasma sheath (Figure 2.1a), which depicts the night side's green zone. The area of space around 10 Earths is known as the magnetosheath.

The Van Allen radiation belts consist of protons and electrons trapped by the planet's magnetic field in torus-shaped regions around the equator, shown as green areas in Figure 2.1a. The inner belt, located at an altitude of 0.2–2 RE, contains trapped particles.

2.1.3 Electromagnetic properties of Earth materials

Grounded on observations of naturally occurring variations in the geomagnetic and geoelectric fields near the Earth’s surface, magnetotellurics (MT) is an EM geophysical technique for estimating the subsurface electrical conductivity of the planet. Electromagnetic research of the Earth's subsurface is conducted based on measurable differences in the electrical conductivity (σ), magnetic permeability (μ), and dielectric permittivity (ε) of various Earth materials when exposed to an electromagnetic field. The goal of electromagnetic methods is to determine the spatial distribution of these properties beneath the Earth's surface.

2.1.3.1 Electrical Properties of Rocks and Minerals

The electrical properties of rocks and minerals play a vital role in methods such as electrical resistivity and induced polarization, which are used to locate ore deposits and investigate the Earth's internal thermal and compositional structure (Yoshin, 2011). These properties are influenced by a combination of different electrical components within the rocks, including solids (such as silicates, oxides, and metals), pores filled with liquid or, air, and boundaries between liquids and solids. The resistivity of materials beneath the surface of the Earth is affected by the movement of charged ions in pore fluids and the conduction of secondary minerals.

Electrical permittivity and conductivity, often known as the reciprocal parameter resistivity, define a material's electrical properties. The electrical conductivity materials of Earth can vary greatly, up to ten orders of magnitude, as shown in Figure 2.2, which is extremely sensitive to even small variations in the minor variations in the composition of the rocks. The conductivity of a rock unit is influenced by the connectivity of insignificant (via fluid or partial melting) or the existence of highly conductive minerals like graphite, as the conductivity of most matrix materials is extremely low $\left(10^{-2}\,\frac{mS}{m}\right)$ (Vozoff, 1972).

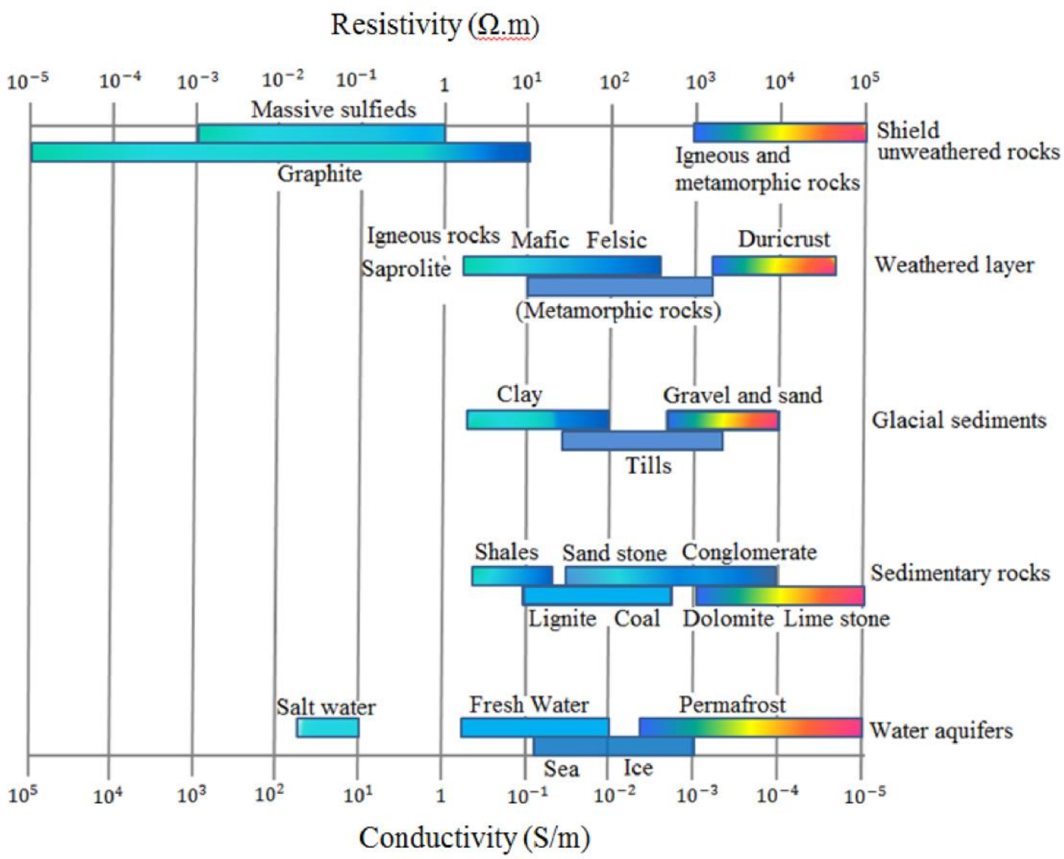

Figure 2.2 Electrical resistivity of Earth materials (Adapted and modified from Palacky, 1987).

The dielectric permittivity (ε) in a vacuum is $\varepsilon = \varepsilon_o = 8.85 \times 10^{-12}$ F/m. In the Earth, this value ranges from ε_o to 80 ε_o represent vacuum and air and water respectively. It can also differ reliant on the frequency of the EM fields (Keller, 1988).

The magnetic permeability (μ) in a vacuum is approximately 4 x 10^{-7} H/m. However, in extremely magnetized materials, this value can be large due to factors such as an increase in magnetic susceptibility when the temperature is below the Curie point (Hopkinson effect). The values of ε and μ can also vary with the frequency of the EM fields (Radhakrishnamurty & Likhite, 1970).

2.1.4 *High-enthalpy geothermal system* and its resistivity distribution.

High-enthalpy geothermal systems, characterized by high temperatures of volcanic origin have temperatures exceeding 150 ◦C and energy potential, are valuable sources of clean, renewable energy that can be harnessed for electricity generation and direct heating applications (Ussher et al., 2000; Lund, 2010; Muñoz, 2014; Pandeli et al., 2013). These systems typically occur in regions with significant tectonic activity, such as volcanic areas or geothermal fields, where reservoirs of hot water or steam are trapped beneath the Earth's surface, resulting in high enthalpy due to the high temperatures and pressures (Ussher et al., 2000; DiPippo, 2015). The high enthalpy of these reservoirs allows for the efficient conversion of geothermal energy into electricity through the use of turbines and generators (Samrock et al., 2015; DiPippo, 2015). This process of harnessing geothermal energy from high-enthalpy systems offers a sustainable alternative to traditional fossil fuel-based energy sources. Understanding the geological and hydrological characteristics of high-enthalpy geothermal systems is essential for effective exploration and development (Tester et al., 2006). Ongoing research and advancements in the field of geothermal energy continue to enhance our understanding of these systems, leading to increased utilization of this abundant and environmentally friendly energy source. A conceptual model of a high-enthalpy geothermal system includes various components that influence the generation and circulation of geothermal fluids. The heat source in such systems is often associated with magmatic activity or deep-seated heat sources (Ussher et al., 2000). Reservoir rocks, typically porous and permeable formations like volcanic rocks or hydrothermal breccias, act as the host for geothermal fluids (Muñoz, 2014). Fluid pathways, including fractures, faults, and permeable zones, facilitate fluid movement within the system (Samrock et al., 2015). The cap rock, an impermeable seal above the reservoir, helps maintain the pressure and containment of geothermal fluids. Surface manifestations such as hot springs and fumaroles provide visible indications of subsurface geothermal activity. Geophysical properties like resistivity, seismic velocity, and gravity anomalies are crucial for characterizing the subsurface structure and fluid distribution within geothermal systems. This integrated conceptual model aids in resource assessment, exploration, and sustainable utilization of high-enthalpy geothermal resources.

A conceptual model for high-enthalpy systems, as described by Johnston et al. (1992) and Cumming & Mackie (2007), illustrates the temperature distribution, alteration zones, and resistivity patterns as shown in Figure 2.3. The electrical resistance of rocks is influenced by factors such as porosity, temperature, changes in composition, and the salinity of fluids within the rock's pores (Ussher et al., 2000). In high-temperature geothermal systems, the distribution of electrical resistance is primarily impacted by changes in the rock caused by the heat from underground water sources. In shallower areas where temperatures are below 70°C, unaltered rocks exhibit high electrical resistance values exceeding 100 $\Omega.m$ and are typically not the primary focus of geothermal reservoir exploration. Beneath the resistive unaltered layer, the presence of clay minerals, particularly smectite, leads to high conductivity in the region where temperatures range from 70°C to 200°C with a resistivity of 10 $\Omega.m$. Smectite and illite are the predominant alteration products in this zone. Once temperatures exceed 200°C, the permeable up-flow zone below the conductive clay zone is identified as the geothermal reservoir in such systems, exhibiting high resistivity (10-60 $\Omega.m$) due to the development of secondary minerals like chlorite and epidote (Ussher et al., 2000). In this area, hot geothermal fluid ascends along fractures and fault systems driven by buoyancy forces (Cherkose, B. A., & Mizunaga, 2018; Muñoz, 2014; Samrock et al., 2015).

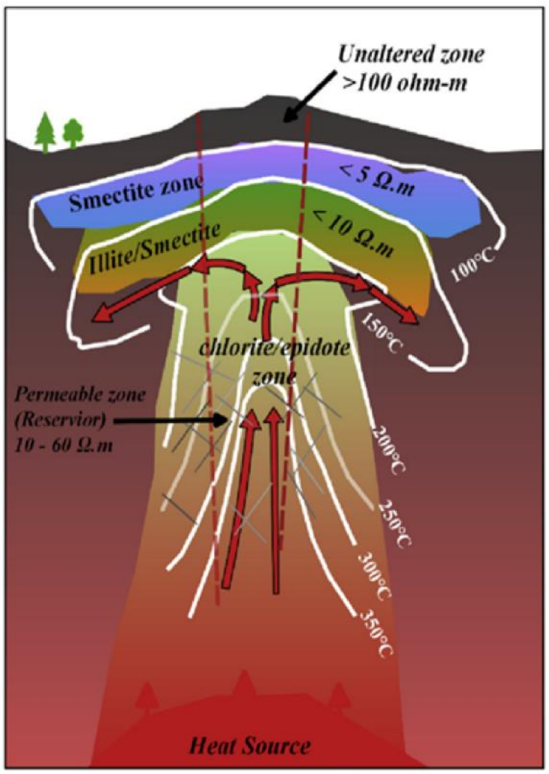

Figure 2.3 Conceptual model of High-enthalpy geothermal systems Johnston et al.(1992) and Cumming & Mackie(2007) (Adopted from Cherkose, B. A., & Mizunaga, 2018)

2.1.4 Assumptions of the MT method

Regarding EM induction in the Earth for the MT situation, a variety of simplifying assumptions are used. The main hypotheses for the Earth's electromagnetic induction include the following

(Simpson & Bahr, 2005), and they have been contested in several publications (Cagniard, 1953; Simpson & Bahr, 2005; Vozoff, 1991) :

i. The general Maxwell's electromagnetic equations are obeyed
ii. The Earth doesn't generate EM energy; it only dissipates or absorbs it.
iii. Away from the sources, all electromagnetic fields are preserved as conservative and analytic.
iv. The electromagnetic source field can be considered as a plane wave with almost vertical incidence everywhere except the equatorial and polar regions.
v. The 1D layers of the Earth are not anticipated to support any accumulation of free charges. In a 2D /3D Earth, non-inductive effects of static shift can be caused by charges due to gathered and dissipated along conductivity discontinuities.
vi. Earth functions as an Ohmic conductor, meaning that the charge must be conserved. It follows the formula

$$J = \sigma E \tag{2.2}$$

where j is the total electric current density (in Am^{-2}), σ is the sounding medium conductivity(in Sm^{-1}), and E is the electric field (in Vm^{-1}).
vii. For MT-sounding periods, the electric displacement field is essentially quasi-static. Because time-varying conduction currents are very large compared to time-varying displacement currents (caused by polarisation effects), electromagnetic induction in the Earth is best thought of as a simple diffusion process.
viii. It is considered that any variations in the magnetic permeability and of electrical permittivity rocks are insignificant in comparison to changes in the bulk conductivities of rocks.

2.1.5 Basic EM Theory and Maxwell's Equations

The distribution of an EM field in a geologic medium depends on several factors, particularly the physical properties of the rocks that fill this medium. Apart from these physical parameters, an additional factor occurs in the mathematical description of the electromagnetic field, i.e., the time dependence.

Within a given region five field vectors are needed to determine the electric and magnetic fields. These are the four vectors B, H, E, and D, which describe the electromagnetic field; and the electric current density, J, which describes the motion of free charge. Maxwell's equations, which define the behavior of EM fields and their interaction, are the fundamental formulas of electromagnetic theory. Thus, these four equations serve as the basis for the physical principles of the MT method at any frequency:

I. According to Faraday's Law, any change in the temporal magnetic field induces a corresponding change in the spatial variation of the electric field. In other words, the electric field circulating in a closed loop with its axis aligned with the inducing field undergoes equivalent changes due to temporal variations in the magnetic field.

$$\nabla \times \mathbf{E} = -\frac{\partial \mathbf{B}}{\partial t} \qquad \text{Faraday's law} \tag{2.3}$$

II. Ampère-Maxwell's Law: The Spatial variation of the magnetic field along the edges of a surface is equal to the temporal variations of the current displacement through the surface and the sum of the electric currents. The magnetic field depends on the temporal variation of the electric displacement and the electrical current density of free charges.

$$\nabla \times \mathbf{H} = \mathbf{J} + \frac{\partial \mathbf{D}}{\partial t} = \qquad \text{Ampere's law} \tag{2.4}$$

III. Gauss' Law for Electrostatics

$$\nabla \cdot \mathbf{D} = \rho \qquad \text{Gauss's law} \tag{2.5}$$

IV. According to Gauss' Law, there is no source in the magnetic field. Magnetic monopoles are nonexistent because there are no free magnetic charges.

$$\nabla \cdot \mathbf{B} = 0 \qquad \text{Gauss's law for magnetism} \tag{2.6}$$

where **E** is the electric field intensity in (V/m, **B** is the magnetic induction in (T) **H** is the magnetic field intensity (A/m), ρ and **J** are the free charges and the conduction current densities, respectively, σ is the tensor electric conductivity (S/m), ε is the electric permittivity (F/m), μ is the tensor magnetic permeability (H/m) and **D** is the electric displacement density (C/m^2). For isotropic media, the above three quantities $\sigma, \varepsilon, and\ \mu$, can be treated as scalars that vary with spatial position, as assumed throughout the entire thesis.

Using the continuity equation which gives current flow as the rate of flow of indestructible charge

$$\nabla \cdot \mathbf{J} = -\frac{\partial \rho}{\partial t} \tag{2.7}$$

Where $\nabla \cdot \mathbf{D} = \rho$; substituting this in the above equation instead of ρ, we have the following

$$\nabla \cdot \mathbf{J} = -\frac{\partial}{\partial t}(\nabla \cdot \mathbf{D}) \tag{2.8}$$

Again

$$-\frac{\partial \rho}{\partial t} + \frac{\partial}{\partial t}(\nabla \cdot \mathbf{D}) = 0 \tag{2.9}$$

Or

$$\frac{\partial(\nabla \cdot \mathbf{D} - \rho)}{\partial t} = 0 \tag{2.10}$$

Following that fact D and J must be time-invariant for a trivial solution of Equation (2.10), but we require they be time-dependent, the above equation gives

$$(\nabla \cdot \mathbf{D} - \rho) = 0 \ \text{ or } \ \nabla \cdot \mathbf{D} = \rho \tag{2.11}$$

This equation is general and it is possible to show that in any medium of non-vanishing conductivity, the charge density will reach its equilibrium value, i.e. steady state, in an extremely short time.

This means no free charges can accumulate within a layered Earth during the flow of current (from an assumption of the MT method (v)), and hence

$$\nabla \cdot \mathbf{J} = 0 \tag{2.12}$$

and from Equation (2.7).i.e.

$$\nabla \cdot \mathbf{J} + \frac{\partial}{\partial t}(\nabla \cdot \mathbf{D}) = 0 \tag{2.13}$$

$$(\nabla \cdot \boldsymbol{D}) = 0 \tag{2.14}$$

Using the vector identity $\nabla \cdot (\nabla \times A) = 0,$ which states that the divergence of the curl of any vector field A equals zero and assuming that the Earth is a uniform conductor we get from Equations (2.4) and (2.12):

$$\nabla \cdot (\nabla \times \boldsymbol{E}) = 0 = \nabla \cdot \boldsymbol{J} + \frac{\partial}{\partial t}(\nabla \cdot \boldsymbol{D}) \quad \Longrightarrow \quad \nabla \cdot \boldsymbol{D} = 0 \tag{2.15}$$

For isotropic and linear media, the vector fields in Maxwell´s equations can be related through constitutive relationships as :

$$\mathbf{D} = \varepsilon\mathbf{E} \tag{2.16}$$

$$\mathbf{B} = \mu\mathbf{H} \tag{2.17}$$

$$\mathbf{J} = \sigma\mathbf{E} \tag{2.18}$$

where $\mu = \mu_o\mu_r$ and $\varepsilon = \varepsilon_o\varepsilon_r$ denote the magnetic permeability and dielectric permittivity, respectively with $\mu_o = 4\pi \times 10^{-7}\frac{H}{m}$ is the magnetic permeability of free space and $\varepsilon_o = 8.85 \times 10^{-12}\frac{F}{m}$ is the dielectric permittivity of free space. Variation of μ_r *and* ε_r are assumed negligible compared to the bulk conductivity σ of the rock.

In a homogeneous medium, electromagnetic waves travel according to the Maxwell Equations (2.3) to (3.6). The behavior of the fields at the interfaces between media with varied electrical characteristics can be inferred from them. Let us examine a border that separates two media, 1 and 2, which have the physical properties $\sigma_{1;}\mu_{1;}\varepsilon_1$ and $\sigma_{2;}\ \mu_{2;}\ \varepsilon_2$ respectively. The tangent, t, is parallel to the boundary, and the normal, n, is positive across the boundary between mediums 1 and 2.

Therefore, at the border dividing the two media, medium 1 and medium 2, the boundary conditions (Miensopust, 2010; Stratton, 1941) are as follows:

i) The electric field tangent to this interface must be continuous

$$\hbar \times E_1 = \hbar \times E_2 \quad \text{or} \quad \hbar \times E_1 - \hbar \times E_2 = 0$$

ii) The current density normal to the interface must be continuous

$$\hbar \cdot (\sigma_1 E_1) = \hbar \cdot (\sigma_2 E_2) \qquad \text{or} \quad \hbar \cdot (\sigma_1 E_1) - \hbar \cdot (\sigma_2 E_2) = 0$$

iii)The magnetic field tangential to the interface must be continuous

$$\hbar \times H_1 = \hbar \times H_2 \quad \text{or} \quad \hbar \times H_1 - \hbar \times H_2 = 0$$

iv) The flux density normal to the interface must be continuous

$$\hbar \cdot (\mu_1 H_1) = \hbar \cdot (\mu_2 H_2) \quad \text{or} \quad \hbar \cdot (\mu_1 H_1) - \hbar \cdot (\mu_2 H_2) = 0$$

For complex media, e.g. anisotropic, the constitutive parameters are better expressed by tensors, and time dependence may be observed.

When the current density "**J**" points in the same direction as the electrical field vector, **E**, and the resistivity of the medium is a scalar function of the observation point, the medium is said to be electrically isotropic. In anisotropic material, **J** has a directional property, often not aligning with **E**. This leads to adjustments in Ohm's law.

$$\mathbf{J}_x = \sigma_{xx}\mathbf{E}_{x+}\sigma_{xy}\mathbf{E}_y + \sigma_{xz}\mathbf{E}_z \quad (2.19)$$

$$\mathbf{J}_y = \sigma_{yx}\mathbf{E}_{x+}\sigma_{yy}\mathbf{E}_y + \sigma_{yz}\mathbf{E}_z \quad (2.20)$$

$$\mathbf{J}_z = \sigma_{zx}\mathbf{E}_{x+}\sigma_{zy}\mathbf{E}_y + \sigma_{zz}\mathbf{E}_z \quad (2.21)$$

However, recalling that the following set of assumptions is generally considered to be valid for EM induction studies on Earth.

1) The Earth is a continuous isotropic medium, ε and μ are time independent constants, with no magnetic material present such that $\mu = \mu_0$,

2) **E** and **B** vary harmonically with time, in such a manner that the explicit dependence is generally expressed as $exp^{(i\omega t)}$,

Using assumption 2 for **E** and **H**, the time dependence of the form

$$\mathbf{E}_{(r,t)} = \mathbf{E}_{o(r,\omega)}e^{i\omega t}\,,\ \mathbf{H}_{(r,t)} = \mathbf{H}_{o(r,\omega)}e^{i\omega t} \quad (2.22)$$

where ω is the angular frequency of the field (i.e., $\omega\ = 2\pi f$),

Using the harmonic expressions of the EM fields (Equation (2.22) and Applying constitutive relationships (Equations (2.3) to (2.6)), Maxwell's equations can be rewritten in the form:

$$\nabla \times \mathbf{E} = -i\omega\mu\mathbf{H} \quad (2.23)$$

$$\nabla \times \mathbf{H} = (\sigma + i\omega\varepsilon)\mathbf{E} \quad (2.24)$$

$$\nabla \cdot \mathbf{E} = 0 \quad (2.25)$$

$$\nabla \cdot \mathbf{H} = 0 \quad (2.26$$

Taking the curl of Equations (2.23) and (2.24) and substituting one into the other. Then by making use of the vector identity;

$$\nabla \times (\nabla \times \mathbf{A}) = \nabla(\nabla \cdot \mathbf{A}) - \nabla \cdot \nabla\mathbf{A} = \nabla(\nabla \cdot \mathbf{A}) - \nabla^2\mathbf{A} \quad (2.27)$$

Using Equations (2.25) and (2.26) by applying the curl to Equations (2.23) and (2.24) respectively we arrive at the following equations:

$$\nabla \times (\nabla \times \mathbf{E}) = \nabla(\nabla \cdot \mathbf{E}) - \nabla \cdot \nabla\mathbf{E} = -\nabla^2\mathbf{E} = i\omega\mu(\nabla \times \mathbf{H}) \quad (2.28)$$

$$\nabla \times (\nabla \times \mathbf{H}) = \nabla(\nabla \cdot \mathbf{H}) - \nabla \cdot \nabla\mathbf{H} = -\nabla^2\mathbf{H} = \sigma + i\omega\mu(\nabla \times \mathbf{E}) \quad (2.29)$$

Substituting Equations (2.23) and (2.24) in the above equations and rearranging them we have:

$$\nabla^2\mathbf{E} = (i\sigma\omega\mu - \omega^2\mu\varepsilon)\mathbf{E} \tag{2.30}$$

$$\nabla^2\mathbf{H} = (i\sigma\omega\mu - \omega^2\mu\varepsilon)\mathbf{H} \tag{2.31}$$

The above equations are the wave equations in the frequency domain, more commonly known as the Helmholtz equations in **E** and **H**.

where, ∇^2 is the Laplacian operator acting on the rectangular components of a given vector and $i\sigma\omega\mu - \omega^2\mu\varepsilon = K^2$ is known as the square of the wave number.

It's reasonable to neglect the non-diffusive part of the EM wave in Equations (2.30) and (2.31), $\mu\varepsilon\omega^2 \ll \mu\sigma\omega$ for Earth materials at frequencies below 10^5 Hz, i.e., displacement currents are significantly smaller than conduction currents. This reduction lowers the wave propagation constant $K^2 = i\sigma\omega\mu$, known as the quasi-static approximation. In this approximation, Equations (2.30) and (2.31) are simplified to:

$$\nabla^2\mathbf{E} - i\sigma\omega\mu\mathbf{E} = 0 \tag{2.32}$$

$$\nabla^2\mathbf{H} - i\sigma\omega\mu\mathbf{H} = 0 \tag{2.33}$$

Under this circumstance, the wave number is given by

$$K = (i\sigma\omega\mu\}^{\frac{1}{2}} \tag{2.34}$$

Equations (2.32) and (2.33) represent diffusion equations. Maxwell's equation for natural source fields can be expressed as

$$\nabla \times \mathbf{E} = i\sigma\omega\mu\mathbf{H} \tag{2.35}$$

$$\nabla \times \mathbf{H} = \sigma\mathbf{E} \tag{2.36}$$

Hence, the natural source (MT) fields are quasi-static fields that diffuse throughout the Earth in the same manner as thermal diffusion processes.

For a geographic Cartesian coordinate system $\{x.y,z\}$, which x, y, and z directing north, east, and pointing vertically downwards respectively, so Equations (2.35) and (2.36) do not only depend on the conductivity σ and angular frequency ω but are also dependent on depth $H = H(z)$. Therefore, the solutions of diffusion equations have the following:

$$\mathbf{H} = \mathbf{H}_1 e^{-ikz} + \mathbf{H}_2 e^{-ikz} \quad (2.37)$$

$$\mathbf{E} = \mathbf{E}_1 e^{-ikz} + E_2 e^{-ikz} \quad (2.38)$$

With $K^2 = i\omega\sigma\mu$

$$K = \sqrt{i\omega\sigma\mu} = \sqrt{i}\sqrt{\omega\sigma\mu} = \sqrt{\omega\sigma\mu e^{-i\frac{\pi}{4}}} = (1+i)\sqrt{\frac{\omega\sigma\mu}{2}} = (1+i)\upsilon \quad (2.39)$$

The depth at which the amplitude of a plane EM wave will be attenuated to $\frac{1}{e} \approx 0.37$ of its surface amplitude and the inverse of the real part of K $\left(\frac{1}{\upsilon}\right)$ is also known as the skin depth or penetration depth δ.

$$\delta = \frac{1}{\upsilon} = \sqrt{\frac{2}{\sigma\omega\mu}} \quad (2.40)$$

where υ is the Amplitude Factor of the wave.

Since the magnetic permeability μ does not vary substantially on the Earth. Therefore the skin depth in (m) can be approximated as: $\delta(T,\rho) \approx 500\sqrt{T\rho}$

Where ρ_a is the apparent resistivity or the equivalent average resistivity of the uniform half space in (Ωm) and $T = \frac{2\pi}{\omega}$ is the period in(s).

From the different electric and magnetic field components of Faraday's law (Equations (2.3) and (2.23) respectively), we obtain relationships of K:

$$-\frac{\partial \mathbf{E}_y}{\partial z} = -\mu \frac{\partial \mathbf{H}_x}{\partial t} \quad \Longrightarrow \quad K\mathbf{E}_y = i\omega\mu\mathbf{H}_x \quad (2.41)$$

$$\frac{\partial \mathbf{E}_x}{\partial z} = -\mu \frac{\partial \mathbf{H}_y}{\partial t} \quad \Longrightarrow \quad K\mathbf{E}_x = -i\omega\mu\mathbf{H}_y \quad (2.42)$$

According to Schmucker (1970, 1973), and Weidelt (1972), the inverse of the Schmucker-weidelt transfer function is referred to as K. The Schmucker-Weidelt transfer function also can be expressed as a link between the components of the electric and magnetic field as follows:

$$C = \frac{1}{K} = \frac{\mathbf{E}_x}{i\omega\mu\mathbf{H}_y} = -\frac{\mathbf{E}_y}{i\omega\mu\mathbf{H}_x} \tag{2.43}$$

Combining Equation (2.43) with the definition of K (Equation (2.39)) yields,

$$\rho = \frac{1}{\sigma} = \frac{1}{|K|^2}\mu\omega = |C|^2\mu\omega \tag{2.44}$$

where ρ is the resistivity and σ is the conductivity of the homogeneous half-space.

Since C is complex, a phase φ can also be derived and written as

$$\varphi = \tan^{-1}\frac{(\mathrm{Im}\ C)}{(\mathrm{Re}\ C)} \tag{2.45}$$

2.1.6 The Magnetotelluric Transfer functions

Magnetotelluric transfer functions, often known as the "responses of MT," are functions that link the observed components of the EM fields at different frequencies. Provided that the source fields can be described as "plane waves," these functions depend on the characteristics of electrical material and frequency, not on the EM sources. There are a number of different transfer functions in use in addition to the Schmucker-Weidelt one listed above. The impedance tensor (also called the MT tensor) and the geomagnetic transfer function (sometimes called the tipper vector or the vertical magnetic transfer function) are the two most widely used representations of MT transfer functions. The two transfer functions that are most frequently utilized for MT data are the impedance tensor and the geomagnetic transfer function (tipper vector).

3.1.6.1 The impedance tensor

The impedance tensor Z is a complex second-rank, frequency-dependent matrix and it describes the relationship between the orthogonal fields of electric $(\mathbf{E}_x, \mathbf{E}_y)$ and magnetic components ($\mathbf{H}_x, \mathbf{H}_y$ or $\frac{\mathbf{B}_x}{\mu}, \frac{\mathbf{B}_y}{\mu}$ respectively) at a given frequency.

$$\mathbf{E} = Z\mathbf{H} \quad \text{or} \quad \begin{pmatrix}\mathbf{E}_x\\ \mathbf{E}_y\end{pmatrix} = \begin{pmatrix}Z_{xx} & Z_{xy}\\ Z_{yx} & Z_{yy}\end{pmatrix}\begin{pmatrix}\mathbf{H}_x\\ \mathbf{H}_y\end{pmatrix} \tag{2.46}$$

or the linearly related electric and magnetic field spectra are :

$$\mathbf{E}_x(\omega) = Z_{xx}(\omega)\mathbf{H}_x(\omega) + Z_{xy}(\omega)\mathbf{H}_y(\omega) \tag{2.47}$$

$$\mathbf{E}_y(\omega) = Z_{yx}(\omega)\mathbf{H}_x(\omega) + Z_{yy}(\omega)\mathbf{H}_y(\omega) \tag{2.48}$$

where Z_{xx} and Z_{xy} are the supplementary ones (contributions from parallel components of the electric and magnetic field) while Z_{xy} and Z_{yx} are called the principal impedances. $\hat{Y}$ is the admittance which is the inverse of the impedance tensor $\hat{Z}\left(\hat{Y} = \hat{Z}^{-1}\right) \Rightarrow \mathbf{H} = \hat{Z}^{-1}\mathbf{E}$ or $\mathbf{H} = \hat{Y}\,\mathbf{E}$

The term MT tensor (M), is a similar narrative of the transfer function, except that it uses the B instead of the H field by Weaver et al. (2000).

$$\mathbf{E} = M\mathbf{B} \quad \text{or} \quad \begin{pmatrix} \mathbf{E}_x \\ \mathbf{E}_y \end{pmatrix} = \begin{pmatrix} M_{xx} & M_{xy} \\ M_{yx} & M_{yy} \end{pmatrix} \begin{pmatrix} \mathbf{B}_x \\ \mathbf{B}_y \end{pmatrix} \tag{2.49}$$

Since both tensors (Z and M) are complex, every element of the matrix is a complex number with real and imaginary components, meaning that every element has a phase in addition to a magnitude.

3.1.6.2 The geomagnetic transfer function

The geomagnetic transfer function also recognized as the tipper vector, $\mathcal{T}$ is a complex dimensionless vector that displays the relationship between the horizontal and the vertical magnetic field component as, i.e.

$$\mathbf{H}_z = \begin{pmatrix} \mathcal{T}_{zx} & \mathcal{T}_{zy} \end{pmatrix} \begin{pmatrix} \mathbf{H}_x \\ \mathbf{H}_y \end{pmatrix} \tag{2.50}$$

$$\mathbf{H}_z = \mathcal{T}_{zx}\mathbf{H}_x + \mathcal{T}_{zy}\mathbf{H}_y \tag{2.51}$$

The induced vertical magnetic field H_z for a homogeneous or 1D Earth does not exist, and the transfer functions $(\mathcal{T}_{zx}, \ \mathcal{T}_{zy})$ are zero but, in the 3D case, they are different from zero. In contrast, there is an induced H_z field near the structures of a vertical boundary between low and high conductivity (for instance, between the ocean and land boundary). The induction arrow, which was first proposed by Parkinson (1959) and Wiese (1962), is a widely used representation of the tipper vector. It is represented by two real dimensionless vectors on the XY plane, consisting of real and imaginary parts.

$$\mathcal{T}_{\Re} = \left(\Re\mathcal{T}_{zx}, \Re\mathcal{T}_{zy}\right) \tag{2.52}$$

and

$$T_{\Im} = \left(\Im\mathcal{T}_{zx}, \Im\mathcal{T}_{zy}\right) \tag{2.53}$$

where $\Re$ and $\Im$ are the real and imaginary parts of the tipper, respectively.

The occurrence o or absence of changes in conductivity in the horizontal direction is inferred using induction arrows, as the vertical magnetic fields are produced by the gradients of lateral conductivity. (Jones & Foster, 1986; Jones & Price, 1970; Simpson & Bahr, 2005). The induction arrows are may plotted using the Parkinson and Wiese conventions. The vectors in the Wiese convention are oriented laterally away from increases in electrical conductivity (Wiese, 1962). The Parkinson convention, on the other hand, has vectors pointing toward excessive current concentration (Parkinson, 1959; Parkinson et al., 1962). Both conventions are cited in papers and publications, with the Parkinson convention being the more popular (Jones & Price, 1970; Jones & Foster, 1986; Miensopust, 2010).

The arrows' orientation, which is positive for clockwise from the x-direction (typically geomagnetic north), is also governed by:

$$\alpha_{\Re} = \tan^{-1}\left(\frac{\Re\mathcal{T}_{zy}}{\Re\mathcal{T}_{zx}}\right) \tag{2.54}$$

$$\alpha_{\Im} = \tan^{-1}\left(\frac{\Im\mathcal{T}_{zy}}{\Im\mathcal{T}_{zx}}\right) \tag{2.55}$$

where α_R and $\alpha_{\Im}$ are positive for clockwise angles from the x-axis (geomagnetic north). On a map, Parkinson's arrows should point toward the region of high conductivity and away from resistant blocks.

2.1.7 Dimensionality of MT transfer functions

2.1.7.1 Electromagnetic Induction in One-Dimensional Earth

1D in MT assumes a layered Earth structure for which the conductivity varies only with depth, i.e., $\sigma = \sigma(z)$. As a convention, the geomagnetic reference coordinate system adopts the common Cartesian coordinates represented by the axes X (north), Y (east), and Z pointing downwards. Assume further that there is no variation of electric and magnetic fields with respect to the horizontal directions but it is a function of only the z-coordinate and the resistivity distribution i.e. $\frac{\partial}{\partial x} = 0$ and $\frac{\partial}{\partial y} = 0$ and the vertical electric field is $\mathbf{E}_z = 0$. Such an electromagnetic field can be caused by a horizontal current sheet located above the free surface of the Earth, z < 0. The current in the source plane wave generates a uniform magnetic field H_y that is directed perpendicularly to the current (J_x). As the primary magnetic field varies with time, the primary vortex electric field arises. The differential forms of Equations (2.35) and (2.36) assuming quasi-static approximation are:

$$\frac{\partial \mathbf{E}_x}{\partial z} = i\omega\mu\mathbf{H}_y \tag{2.56}$$

$$\frac{\partial \mathbf{H}_y}{\partial z} = -\sigma\mathbf{E}_x \tag{2.57}$$

Differentiating Equations (2.56) and (2.57) with respect to z, yields the diffusion equation in a one-dimensional problem that can be written as:

$$\frac{\partial^2 \mathbf{E}_X}{\partial z^2} = -i\omega\mu\sigma\mathbf{E}_x = K^2\mathbf{E}_x \tag{2.58}$$

$$\frac{\partial^2 \mathbf{H}_y}{\partial z^2} = i\omega\mu\sigma\mathbf{H}_y = K^2\mathbf{H}_y \tag{2.59}$$

which, the general solution of Equation (2.58) is of the form:

$$\mathbf{E}_x(z) = E_1 e^{-kz} + E_2 e^{kz} \tag{2.60}$$

2.1.7.1.1 A homogenous half-space

Considering a uniform half-space as the simplest 1D case, one can see that the field intensity should decrease with increasing z values due to the transformation of EM energy to heat. This leads to nullifying the coefficient of a positive exponent of e, i.e. $E_2 = 0$. Moreover, the MT field is known to be quasi-periodic in the frequency range employed, and thus for a harmonically time-varying field, we have a more general solution given by:

$$\mathbf{E}_x(z) = \left(\mathbf{E}_1 e^{-kz}\right) \cdot e^{i\omega t} = \mathbf{E}_1 e^{i\omega t - kz} \tag{2.61}$$

where k is the wave number and is related to the skin depth as:

$$K = (i\omega\sigma\mu)^{\frac{1}{2}} = \frac{1+i}{\sqrt{2}}\sqrt{i\omega\sigma\mu} = \sqrt{\frac{\omega\sigma\mu}{2}} + i\sqrt{\frac{\omega\sigma\mu}{2}} \tag{2.62}$$

The inverse of the real part k in Equation (2.62) is the EM skin depth or penetration depth δ, of a half-space of conductivity (σ), at an angular frequency (ω). Moreover, the inverse of k is known as the Schumcker-Weidelt transfer function C and invokes a frequency-dependent linear system with an input and predictable output.

Maxwell's equation, for this particular problem, Equation (2.58), $\frac{\partial \mathbf{E}_x}{\partial z} = i\omega\mu\mathbf{H}_y$

Using the expression in Equation (2.61) for the electric field intensity, the above equation yields:

$$i\omega\mu\mathbf{H}_y(z) = K\mathbf{E}_x \qquad (2.63)$$

Thus, the Schumcker-Weidelt transfer function C can be calculated from the measured field components as:

$$C = \frac{1}{K} = \frac{\mathbf{E}_x}{i\omega\mu\mathbf{H}_y} = -\frac{\mathbf{E}_y}{i\omega\mu\mathbf{H}_x} \Longrightarrow \quad C = \frac{Z_{xy}}{i\omega\mu} = -\frac{Z_{yx}}{i\omega\mu} \qquad (2.64)$$

where Z is the Tikhonov-Cagniard wave impedance, it is the ratio of orthogonal components of the EM fields and represents a characteristic measure of the EM properties of the subsurface, i.e. $Z = \frac{\mathbf{E}}{\mathbf{H}} \quad \Longrightarrow \quad Z_{xy} = \frac{\mathbf{E}_x}{\mathbf{H}_y}$ and $Z_{yx} = \frac{\mathbf{E}_y}{\mathbf{H}_x}$, Hence in one dimension $Z_{xy} = -Z_{yx}$, and $Z_{xx} = Z_{yy} = 0$

For a homogenous half-space, the real and imaginary parts of C, have the same magnitudes and establish a linear relationship between the physical properties that are measured in the fields. From Equation (2.58), we get:

$$K = (i\omega\sigma\mu)^{\frac{1}{2}} \Longrightarrow \rho = \frac{1}{\sigma} = \frac{1}{|K|^2}\mu\omega = |C|^2\mu\omega(\Omega m) = \frac{1}{\mu\omega}|Z|^2(\Omega m) \qquad (2.65)$$

Once, C is known from the measured field values, the resistivity of the homogenous half-space can be obtained as shown above.

2.1.7.1.2 Transfer function of N-layered half-space

For an n-layered homogenous half-space, the diffusion Equation (2.58) will yield a solution of the form:

$$E_{xn}(K_n, \omega) = E_{1n}e^{i\omega - k_n z} + E_{2n}e^{i\omega + k_n z} = a_n(k_n, \omega)e^{-k_n z} + b_n(k_n, \omega)e^{k_n z} \qquad (2.66)$$

Where k_n is being defined as before but, in this case, for a particular conductivity of σ_n of the n^{th} layer.

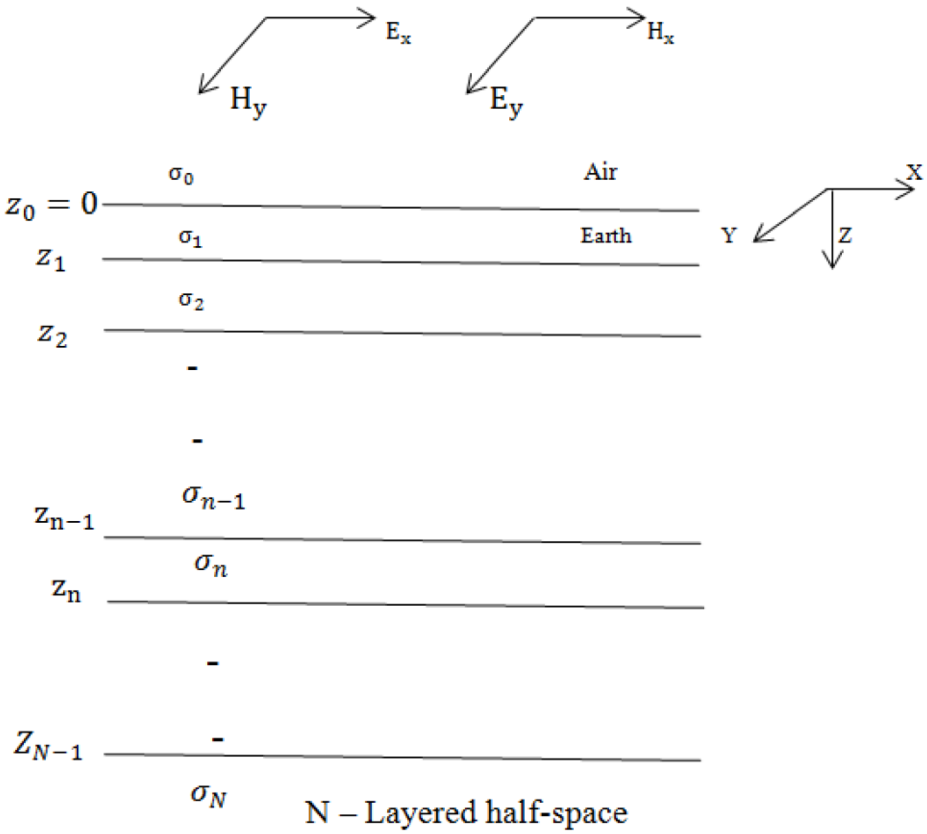

Figure 2.4 N-Layered half-space (Adopted and modified from Simpson & Bahr, 2005).

Similarly, the magnetic field in the n^{th} layer:

$$\boldsymbol{B}_{yn}(K_n, \omega) = \frac{k_n}{i\omega}[a_n(k_n, \omega)e^{-k_n z} + b_n(k_n, \omega)e^{k_n z}] \tag{2.67}$$

A typical MT sounding, penetrating the n^{th} layer would measure the above two components and allow us to calculate

$$C_n(z) = \frac{E_n(z)}{i\omega B_n(z)} \quad and \quad K_n(z) = \sqrt{i\omega\sigma_n\mu} \tag{2.68}$$

Using Equations (2.66) and (2.67) to evaluate Equation (2.68) gives:

At the top of the n^{th} layer:

$$C_n(z_{n-1}) = \frac{a_n e^{-k_n z_{n-1}} + b_n e^{q_n z_{n-1}}}{K_n(a_n e^{-k_n z_{n-1}} - b_n e^{q_n z_{n-1}})} \tag{2.69}$$

At the bottom of the n^{th} layer:

$$C_n(z_n) = \frac{a_n e^{-k_n z_n} + b_n e^{q_n z_n})}{K_n(a_n e^{-k_n z_n} - b_n e^{q_n z_n})} \tag{2.70}$$

Rearranging Equation (2.66) to get the ration $\frac{a_n}{b_n}$ and substituting in (2.65):

$$C_n(z_{n-1}) = \frac{1}{k_n}\frac{k_n C_n(z_n) + \tanh[k_n(z_n - z_{n-1})]}{1 + k_n C_n(z_n) + \tanh[k_n(z_n - z_{n-1})]} \tag{2.71}$$

The field components are continuous across the layer boundaries and so does the transfer function, C.

$$C_n(z_n) = \lim_{z \to z_n - 0} C_n(z) = \lim_{z \to z_n + 0} C_{n+1}(z) = C_{n+1}(z_n) \tag{2.72}$$

Introducing the continuity conditions and replacing $l_n = z_n - z_{n-1}$ in Equation (2.67) yields:

$$C_n(z_{n-1}) = \frac{1}{k_n}\frac{k_n C_{n+1}(z_n) + \tanh[k_n\, l_n]}{1 + k_n C_{n+1}(z_n) + \tanh[k_n l_n]} \tag{2.73}$$

Equation (2.62) is known as Waits recursive formula and is used to calculate C at the top of the nth layer, if C, at the top of (n+1) th layer is known. Hence, we start to iterate from the top of the bottommost (N th) layer, which satisfies the condition of a homogeneous half-space such that:

$$C_n = \frac{1}{K_n} \tag{2.74}$$

Then we apply Equation (2.79) N-1 times until we have C at the top of the layered half-space.

3.1.7.1.3. Apparent resistivity (ρ_a), and Impedance phase (φ)

The Earth response functions in MT survey are commonly expressed in terms of apparent resistivity (ρ_a), and phase (φ). The resistivity, given by Equation (2.65), in the case of a layered earth model, is termed apparent resistivity and is defined as the average resistivity of an equivalent uniform half-space

$$\rho_{xy}(\omega) = \left|C_{xy}(\omega)\right|^2 \mu\omega(\Omega\text{m}) \tag{2.75}$$

The response function C, being complex also has a phase lag known as an impedance phase, and in the case of 1D layered half-space:

$$\varphi_{xy} = Arg\left(C_{xy}\right) = tan^{-1}\left(\frac{E_x}{B_y}\right) \tag{2.76}$$

Both the apparent resistivity (ρ_a), and impedance phase (φ) are commonly plotted as the function of period, $T = \frac{2\pi}{\omega}$, and they are interdependent relationships described by Kramers–Kroenig (Weidelt, 1972): is shown by:

$$\varphi(\omega) = \frac{\pi}{4} - \int_0^\infty \log\frac{\rho_a(x)}{\rho_0}\frac{dx}{x^2 - \omega^2} \tag{2.77}$$

I.e., if ρ_a is plotted on a log-log scale, its phase (φ) is proportional to the slope of the curve, but from a baseline at 45 degrees. ρ_o is the high-frequency asymptotic value of $\rho_a(\omega)$. As a crude approximation, it can be re-written as:

$$\varphi(f) \approx \frac{\pi}{4}\left[1 + \frac{\partial \log \rho_a(f)}{\partial \log f}\right] \qquad (2.78)$$

The two idealized two-layer models in order to estimate the effect of conductive or resistive layers on the impedance phase described by Simpson & Bahr (2005) are as follows:
In both Models, the skin depth can be larger than the thickness of the top layers.

$$|k_1 l_1| \ll 1 \; and, hence, tanh(k_1 l_1) = k_1 l_1 \qquad (2.79)$$

Under such conditions, Equation (2.70) reduces o:

$$C_1(z_n = 0) = \frac{C_2 + l_1}{1 + k_1 C_2 k_1 l_1} \qquad (2.80)$$

In model - I, the ratio $\frac{\sigma_1}{\sigma_2} \ll 1 \Rightarrow |q_1 C_2| \ll 1$, therefore:

$$C_1 = C_2 + l_1 = C_2 + h \qquad (2.81)$$

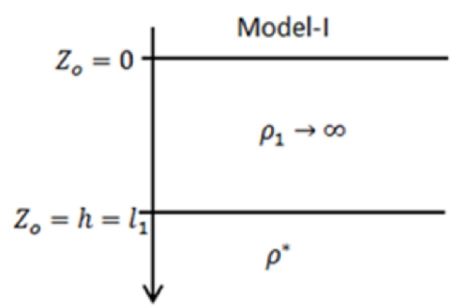

Equation (2.81) shows that the real and imaginary part of the transfer function, C_1 , in the top layer, will be scaled up by a factor 'h' from that of C_2 and hence $\varphi > 45^o$. Therefore, $\varphi > 45^o$ is indicative of a substratum with resistivity decreasing with depth.

In model –II, the wave number,

$${C_1}^2 = i\omega\mu\sigma_1 \;,\; l_1 \ll |C_2| \; and \; l_1\sigma_1 = \tau, \; resulting \; in:$$

$$C_1 = \frac{C_2}{1 + i\omega\mu\tau C_2} \qquad (2.82)$$

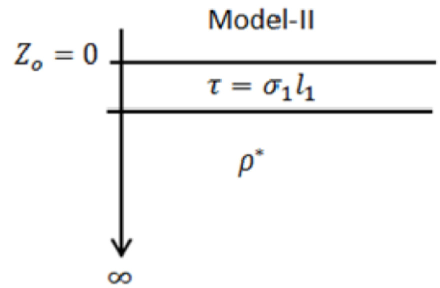

From Equation. (2.63), we have seen that the real and imaginary parts of the transfer function, C_2, of a homogenous half-space, are equal suggesting that $\varphi = 45^o$. The real and imaginary parts of the transfer function C1, are reduced in the conducting top layer following the attenuation of the EM amplitude implying that $\varphi < 45^o$. Therefore, $\varphi < 45^o$ is indicative of a substratum with resistivity increasing with depth.

The major conclusions drawn from Equation (2.74) where $T = \frac{2\pi}{\omega}$ are:

(i) $\varphi = 45^o$ for a homogeneous halfspace where $\frac{d \log \rho_a(T)}{d \log T} = 0$. This already follows from Equation (2.59), if phases are shifted into the upper right quadrant of the complex plane.

(ii) $\varphi < 45^o$,if the apparent resistivity *decreases* with period $\frac{d \log \rho_a(T)}{d \log T} < 0$

(iii) $\varphi > 45^o$,if the apparent resistivity *increases* with period $\frac{d \log \rho_a(T)}{d \log T} > 0$

(iv) The absolute values of $\rho_a(\omega)$ have no influence on the shape of $\varphi(\omega)$. Sets of ρ_a curves with equal $\frac{d \log \rho_a(T)}{d \log T}$have an identical _-curve and are unaffected by the choice of ρ_o in Equation (2.73)

ρ* - Z* transformation

A convenient presentation and a first-hand approximation of a 1D model of the measured MT data can be attained by a *ρ* - Z* transformation*.

Z* is defined by the real part of the transfer function, Re (C), while

$$\rho^* = 2\rho_a cos^2\varphi \;\; for\ \varphi > 45^o\ and,$$

$$\rho^* = \frac{\rho_a}{(sin^2\varphi)}\ for\ \varphi < 45^o \tag{2.83}$$

For $\varphi = 45^0$, both the above equations yield $\rho^* = \rho_a$, i.e., a homogeneous half-space.

2.1.7.2 Electromagnetic Induction in Two-Dimensional Earth

In a 2D subsurface structure, the conductivity remains constant in one horizontal direction but varies in vertical and the other horizontal directions. The direction where the conductivity remains constant is referred to as the geoelectrical or electromagnetic strike. Geological structures such as dykes, rift valleys, faults, contact zones, etc., are generally categorized in a 2D classification. In a 2D structure, the assumption is that the strike length is significantly longer than the strike depth. While the strike length is smaller than the strike depth, i.e., either the body is very small or a 2D interpretation will not be effective, a 3D interpretation becomes essential.

The fields do not differ in thestrike direction (defined as the x-direction), i.e., $\frac{\partial}{\partial x} = 0.$ for a body with an infinite along-strike direction (or significantly longer than the penetration depth) and a constant conductivity along it. Therefore Equations (2.35) and (2.36) become

$$\begin{pmatrix} \frac{\partial}{\partial x} \\ \frac{\partial}{\partial y} \\ \frac{\partial}{\partial z} \end{pmatrix} \times \begin{pmatrix} \mathbf{E}_x \\ \mathbf{E}_y \\ \mathbf{E}_z \end{pmatrix} = \begin{pmatrix} \frac{\partial \mathbf{E}_z}{\partial y} - \frac{\partial \mathbf{E}_y}{\partial z} \\ \frac{\partial \mathbf{E}_x}{\partial z} - 0 \\ 0 - \frac{\partial \mathbf{E}_x}{\partial y} \end{pmatrix} = -i\omega\mu \begin{pmatrix} \mathbf{H}_x \\ \mathbf{H}_y \\ \mathbf{H}_z \end{pmatrix} \tag{2.84}$$

and

$$\begin{pmatrix} \frac{\partial}{\partial x} \\ \frac{\partial}{\partial y} \\ \frac{\partial}{\partial z} \end{pmatrix} \times \begin{pmatrix} \mathbf{H}_x \\ \mathbf{H}_y \\ \mathbf{H}_z \end{pmatrix} = \begin{pmatrix} \frac{\partial \mathbf{H}_z}{\partial y} - \frac{\partial \mathbf{H}_y}{\partial z} \\ \frac{\partial \mathbf{H}_x}{\partial z} - 0 \\ 0 - \frac{\partial \mathbf{H}_x}{\partial y} \end{pmatrix} = \sigma \begin{pmatrix} \mathbf{E}_x \\ \mathbf{E}_y \\ \mathbf{E}_z \end{pmatrix} \tag{2.85}$$

When a magnetic field is aligned with the direction of the strike, it induces electric fields exclusively in the vertical plane that is perpendicular to the strike $(\mathbf{E}_{y,}\ \mathbf{E}_z)$, which is referred to as B polarization or transverse magnetic (TM) mode. Conversely, when an electric field $(\mathbf{E}_x)$ aligns with the strike, it produces magnetic fields solely in the vertical plane that is perpendicular to the strike $(\mathbf{H}_y\ ,\ \mathbf{H}_z)$, known as E-polarization or transverse electric (TE) mode. In this ideal 2D scenario, the electromagnetic fields are perfectly perpendicular to each other.

The resulting sets of Equations (2.84) and (2.85) decouple into B-polarization and E-polarization, two distinct modes. The terms "transverse electric" (TE) and "transverse magnetic"

(TM) are also used to describe these two polarization modes. In TE mode, the electric current is flowing along a parallel axis (x), which is often related to the direction of the strike.TE mode has the electric current flowing along the independent axis (x) normally associated with the strike direction. It is given by the set of equations expressed by the combinations $[\mathbf{E}_x(y, z), \mathbf{H}_y \text{ and } \mathbf{H}_z]$. In the case of B - polarization we have a set of equations in terms of $[\mathbf{H}_x(y, z), \mathbf{H}_y \text{ and } \mathbf{E}_z]$ and are known as the TM mode.

The E-polarization describes currents flowing parallel to strike, is known as the transverse electric (TE), and is composed of in terms of the electromagnetic field components $\boldsymbol{E}_x$, $\boldsymbol{H}_y$ *and* $\boldsymbol{H}_z$:

$$\frac{\partial \boldsymbol{H}_y}{\partial z} - \frac{\partial \boldsymbol{H}_z}{\partial y} = \sigma \boldsymbol{E}_x$$

$$\frac{\partial \boldsymbol{E}_x}{\partial z} = -i\omega\mu \boldsymbol{H}_y \qquad T_E\ mode/\ E - polarization \qquad (2.86)$$

$$\frac{\partial \boldsymbol{E}_x}{\partial y} = i\omega\mu \boldsymbol{H}_z$$

The alternative mode, called the transverse magnetic (TM) mode or B-polarization, illustrates currents that flow at right angles to the strike direction.

of $\mathbf{H}_x$, $\mathbf{E}_y$ and $\mathbf{E}_z$:

$$\frac{\partial \boldsymbol{E}_z}{\partial y} - \frac{\partial \boldsymbol{E}_y}{\partial z} = -i\omega\mu \boldsymbol{H}_x$$

$$\frac{\partial \boldsymbol{H}_x}{\partial z} = \sigma \boldsymbol{E}_y \qquad T_M\ mode/\ P - polarization \qquad (2.87$$

$$-\frac{\partial \boldsymbol{H}_x}{\partial y} = \sigma \boldsymbol{H}_z$$

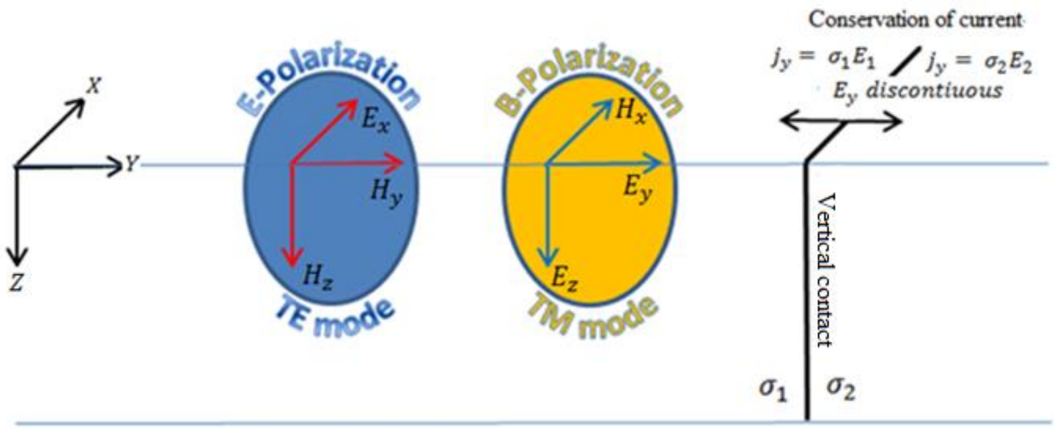

Figure 2.5 depicts a simple 2D resistivity model with a lateral contact striking along the x-axis and two-quarter spaces of different conductivities; the y-component of the electrical field Ey is discontinuous across the contact due to the conservation of current across the vertical discontinuity. The EM fields can be split into two distinct TE and TM modes for the ideal 2D case. Redrawn and modified from Simpson & Bahr (2005).

In the 2D scenario, if the x or y axis aligns with the geoelectric strike direction, then the diagonal elements of Z ($Z_{xx} = Z_{yy} = 0$, become zero, and the off-diagonal elements become unequal ($Z_{xy} \neq -Z_{yx}$).. Where Z_{xy} *and* Z_{yx} are the off-diagonal elements and are sometimes known as transverse electric and transverse magnetic modes respectively. If neither axis aligns with the strike in the measured data, it is often difficult to find a direction where the condition $Z_{xx} = Z_{yy} \neq 0$ holds. For a nearly 2D structure and noise-free data, it is feasible to rotate to the strike by minimizing the diagonal elements of the impedance tensor.

$$Z = \begin{bmatrix} Z_{xx} & Z_{xy} \\ Z_{yx} & Z_{yy} \end{bmatrix} = \begin{bmatrix} 0 & Z_{xy} \\ Z_{yx} & 0 \end{bmatrix} \tag{2.88}$$

The impedance tensor, denoted as Z(Z_{ij}), is a complex quantity consisting of both real and imaginary parts. Therefore, each component, Z_{ij} of Z has both magnitude and phase, as given by (Equations (2.89)): having magnitude and phase given by:

$$\rho_{aij}(\omega) = \frac{1}{\mu_0 \omega} \left|Z_{ij}(\omega)\right|^2 \quad and \quad \varphi_{ij}(\omega) = \tan^{-1}\left(\frac{Im\{Z_{ij}(\omega)\}}{Re\{Z_{ij}(\omega)\}}\right) \tag{2.89}$$

where, $\rho_{a_{ij}(\omega)}$ is the apparent resistivity in the i and j components and $Z_{ij}(\omega) = \frac{\boldsymbol{E_i}}{\boldsymbol{H_J}}$.

2.1.7.3 Electromagnetic Induction in Three-Dimensional Earth

The 3D conductivity of Earth models represents the comprehensive geoelectric structure, with conductivity changing in all directions (σ=σ(x,y,z)). In this scenario, it is not possible to rotate the impedance tensor to make the on-diagonal components of Z become zero or to make any component of the tipper vector vanish. Therefore, in the 3D-Earth, resistivity variations occur in all three directions. As a result, the impedance tensor is:

$$Z = \begin{bmatrix} Z_{xx} & Z_{xy} \\ Z_{yx} & Z_{yy} \end{bmatrix} \qquad (2.90)$$

where $Z_{xx} \neq Z_{yy} \neq 0 \; and Z_{xy} \neq Z_{yx}$

The rotational dependent tensor elements (Zxy and Zyx), provide the apparent resistivity and phase as:

$$\rho_{axy}(\omega) = \frac{1}{\mu\omega}\left|Z_{xy}(\omega)\right|^2 and \; \rho_{ayx}(\omega) = \frac{1}{\mu\omega}\left|Z_{yx}(\omega)\right|^2 \qquad (2.91)$$

and

$$\varphi_{xy}(\omega) = tan^{-1}\left(\frac{\Im\{Z_{xy}(\omega)\}}{\Re\{Z_{xy}(\omega)\}}\right) \; and \; \varphi_{yx}(\omega) = tan^{-1}\left(\frac{\Im\{Z_{yx}(\omega)\}}{\Re\{Z_{yx}(\omega)\}}\right) \qquad (2.92)$$

The rotationally independent determinant: $Z_{det} = \sqrt{Z_{xx}Z_{yy} - Z_{xy}Z_{yx}}$, gives

$$\rho_{det}(\omega) = \frac{1}{\mu\omega}|Z_{det}(\omega)|^2 \; and \; \varphi_{det}(\omega) = tan^{-1}\left(\frac{\Im\{Z_{det}(\omega)\}}{\Re\{Z_{det}(\omega)\}}\right) \qquad (2.93)$$

The off-diagonal impedance tensor components of the Earth properties and the Schmucker - Weidelt transfer function C relationship are noted below, in order to elude confusion with the equation in this chapter:

$$\left|Z_{xy1D}\right| = \left|Z_{yx1D}\right| = i\omega\mu C \qquad (2.94)$$

In a 3D earth model (see Figure 4.11), conductivity varies in all three directions (x, y, z). The general form of the impedance tensor in a 3D earth model (Equation (2.95))is

$$Z_{3D} = \begin{pmatrix} Z_{xx} & Z_{xy} \\ Z_{yx} & Z_{yy} \end{pmatrix} \qquad (2.95)$$

where $Z_{xx} \neq Z_{yy} \neq 0 \; and \; Z_{xy} \neq Z_{yx}$. There is no mechanism to rotate the impedance tensor such that on-diagonal elements on Z become zero.

The interpretation must take into account each component of the tensor. The diagonal element the impedance tensor and any part of the tipper vector are all non-zero elements and do not vanish in any direction. For the 3D earth, the full impedance tensor with four complex elements for each frequency can be used to calculate different forms of apparent resistivity. It consists of conversely, identifiable modes in TE and TM modes that may result from a perturbing near-surface 3D structure when the vertical magnetic transfer function is applied on a dense and substantial grid (Becken et al., 2008; Miensopust, 2010).

An anisotropic body or layer's resistivity may only be described by a full 3 x 3 tensor, as shown below

$$\rho(x, y, z) = \begin{pmatrix} \rho_{xx} & \rho_{xy} & \rho_{xz} \\ \rho_{yx} & \rho_{yy} & \rho_{yz} \\ \rho_{zx} & \rho_{zy} & \rho_{zz} \end{pmatrix} \qquad (2.96)$$

Apparent resistivity (ρ), and phase (φ) of the Earth response functions in MT surveys are often used. An equivalent uniform half-space average resistivity is used to calculate the apparent resistivity of a layered earth model.

$$\rho_{ij}(\omega) = \left|C_{ij}(\omega)\right|^2 \mu\omega(\Omega m) \qquad (2.97)$$

The response functions $C = \frac{1}{K} = \frac{E_x}{i\omega\mu H_y} = \frac{-E_y}{i\omega\mu H_x}$, is complex and has a phase lag known as an impedance phase, and in the case of 1- D layered half-space:

$$\varphi_{ij(\omega)} = Arg\left(C_{ij}(\omega)\right) \qquad (2.98)$$

2.1.8 Rotation of Impedance Tensors

The location of a geoelectric strike is rarely known, even in the ideal two-dimensional Earth. The coordinate system axes in the field layout do not coincide with the strike direction as a result. Using the rotation matrix R and its transpose, RT, the impedance tensor can be rotated by an angle to any other coordinate system. From the x-axis, the angle of rotation is in a clockwise orientation. In Figure 2.5, the rotation operator is displayed.

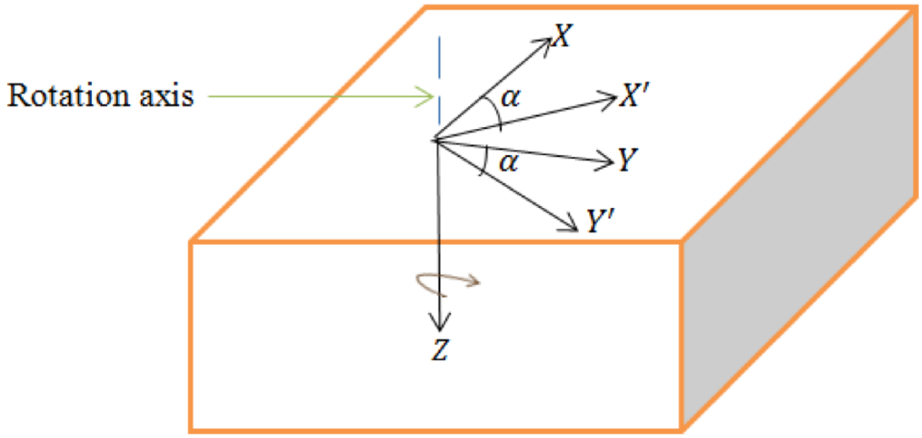

Figure 2.6 Rotation of coordinates of impedance tensor by angle α.

$$Z' = R_\alpha Z R_\alpha{}^T \tag{2.99}$$

where $R_\alpha = \begin{pmatrix} \cos\alpha & \sin\alpha \\ -\sin\alpha & \cos\alpha \end{pmatrix}$ is a rotation matrix and $R_\alpha{}^T$ is the transpose of the rotation matrix, $\boldsymbol{Z}obs$ is the measured impedance in the original coordinate.

$$R_\alpha{}^T = \begin{pmatrix} \cos\alpha & -\sin\alpha \\ \sin\alpha & \cos\alpha \end{pmatrix} \tag{2.100}$$

Thus, the rotational impedance tensor can be rewritten as:

$$\begin{bmatrix} Z'_{xx} & Z'_{xy} \\ Z'_{yx} & Z'_{yy} \end{bmatrix} = \begin{bmatrix} \cos\alpha & \sin\alpha \\ -\sin\alpha & \cos\alpha \end{bmatrix} \begin{bmatrix} Z_{xx} & Z_{xy} \\ Z_{yx} & Z_{yy} \end{bmatrix} \begin{bmatrix} \cos\alpha & -\sin\alpha \\ \sin\alpha & \cos\alpha \end{bmatrix} \tag{2.101}$$

In the new coordinate system, the elements of the impedance tensor Z' can be written in terms of elements of the original impedance tensor as

$$\mathrm{Z'_{xx}} = \mathrm{Z_{xx}}\cos^2(\alpha) + \cos(\alpha)\sin(\alpha)\left(\mathrm{Z_{xy}} + \mathrm{Z_{yx}}\right) + \sin^2(\alpha)\,\mathrm{Z_{yy}}$$

$$\mathrm{Z'_{xy}} = \mathrm{Z_{xy}}\cos^2(\alpha) + \cos(\alpha)\sin(\alpha)\left(\mathrm{Z_{yy}} - \mathrm{Z_{xx}}\right) - \sin^2(\alpha)\,\mathrm{Z_{yx}} \tag{2.102}$$

$$\mathrm{Z'_{yx}} = \mathrm{Z_{yx}}\cos^2(\alpha) + \cos(\alpha)\sin(\alpha)\left(\mathrm{Z_{yy}} - \mathrm{Z_{xx}}\right) - \sin^2(\alpha)\,\mathrm{Z_{xy}}$$

$$\mathrm{Z'_{yy}} = \mathrm{Z_{yy}}\cos^2(\alpha) - \cos(\alpha)\sin(\alpha)\left(\mathrm{Z_{xy}} + \mathrm{Z_{yx}}\right) + \sin^2(\alpha)\,\mathrm{Z_{xx}}$$

Or, more elegantly

$$Z'_{xx} = S_1 + S_2 \sin\alpha\cos\alpha$$

$$Z'_{xy} = D_2 + S_1 \sin\alpha\cos\alpha \quad (2.103)$$

$$Z'_{yx} = D_2 - D_1 \sin\alpha\cos\alpha$$

$$Z'_{yy} = -D_1 - D_2 \sin\alpha\cos\alpha$$

where S_1, S_2, D_1 and D_2 are the modified impedances (Vozoff, 1972):

$$S_1 = Z_{xx} + Z_{yy} \qquad S_2 = Z_{xy} + Z_{yx} \qquad D_1 = Z_{xx} - Z_{yy} \qquad D_2 = Z_{xy} - Z_{yx} \quad (2.104)$$

The rotated modified impedances are simply

$$S_1{}' = Z'_{xx} + Z'_{yy} = Z_{xx} + Z_{yy} = S_1 \quad D'_1 = Z'_{xx} - Z'_{yy} \quad 2.105)$$

$$D'_1 = (\cos\alpha^2 - \sin\alpha^2)(Z_{xx} - Z_{yy})2\cos\alpha\sin\alpha\left(Z_{xy} + Z_{yx}\right) = \cos\alpha^2 D_2 + \sin\alpha^2 S_1 \quad (2.106)$$

and, similarly,

$$S'_2 \cos\alpha^2 S_1 - \sin\alpha^2 D_2 \qquad \text{and} \qquad D'_2 = D_2 \quad (2.107)$$

Hence, S_1 and D_2 are rotationally invariant.

The impedance tensor of the 1D isotropic model (Cagniard, 1953), the diagonal elements $Z_{xx} = Z_{yy} = 0$ and the off-diagonal elements, $Z_{xy} = -Z_{yx}$. Therefore, the above expression reduces to: $Z'_{xx} = Z'_{yy}$, $Z'_{xy} = Z_{xy}$ *and* $Z'_{yx} = Z_{yx}$. This implies that the impedance tensor is independent of the measurement axis.

Szarka & Menvielle(1997) developed several independent real-valued rotational invariants based on three complex magnitudes commonly used in magnetotelluric impedance tensors:

i) The trace: $S_1 = Z_{XX} + Z_{YY}$

ii) The determinant: $detZ = Z_{xx}Z_{yy} - Z_{xy}Z_{yx}$ (2.108)

iii) The difference between the off-diagonal elements: $D_2 = Z_{xy} - Z_{yx}$

The principle direction is defined as the direction when the off-diagonal components of $Z(\alpha)$ are maximized after rotation. Maximizing $\left(\left|Z_{xy}(\alpha)\right|^2 + \left|Z_{yx}(\alpha)\right|^2\right)$ gives:

$$\alpha = \frac{1}{4}\arctan\frac{(Z_{xx} - Z_{yy})(Z_{xy} + Z_{yx})^* + (Z_{xx} + Z_{yy})^*(Z_{xy} - Z_{yx})}{\left|Z_{xx} - Z_{yy}\right|^2 - \left|Z_{xy} + Z_{yx}\right|^2} \tag{2.109}$$

Where α is the resulting strike angle, also known as Swift angle (Swift, 1967), and * means the complex conjugate.

2.1.9 Distortion of MT impedance tensors

The electromagnetic signal distortion is a result of local and near-surface conductive inhomogeneities of the subsurface, which are much smaller than the targets of interest, and skin depths and topography differences (Jiracek, 1990; Sternberg et al., 1988). In magnetotelluric data, the response of regional structures can be masked by the distortion produced by small-scale, near-surface conductivity inhomogeneities (Alan D. Chave and J. Torquil Smith, 1994; Karsten Bahr, 1991; Berdichevsky & Dimitriev, 1976; Jiracek, 1990; A. G. Jones, 1988; Kaufman, 1988)

Distortion of MT-sounding curves can be inductive or galvanic, which arises mainly from the telluric field, as discussed by Berdichevskiy and Dmitriev (1976 a, b). inductive distortions are caused by current distributions with lower magnitudes that decay over time. Eddy currents create secondary fields that combine with the primary magnetic field within areas of abnormal conductivity. When the condition σ >> ωε (quasi-static approximation) is met, the displacement can be disregarded (Berdichevskiy and Dmitriev, 1976; Jiracek, 1990)), resulting in an electric field that induces a secondary electric field within and around the conductivity anomaly. Galvanic distortion occurs due to charge distributions building up on shallow body surfaces, or it happens when the secondary electric field develops as a result of electric charge buildup on boundaries with varying conductivities, which results in an aberrant electromagnetic field. In the context of magnetotelluric studies, the abnormal electric field is comparable in magnitude to the regional electric field and remains constant across all frequencies, while the abnormal magnetic field is minimal (Bahr, 1988; Jiracek, 1990). In the presence of a conductive inclusion, the boundary charges give rise to a secondary electric field that opposes the primary field along the sides and above the negatively charged body. This phenomenon, known as galvanic distortion, impacts both electromagnetic fields, resulting in galvanic electric and galvanic magnetic distortion. These effects on the electromagnetic fields are interconnected (e.g., Alan D. Chave and J. Torquil Smith, 1994; Chave and Jones., 1997; Garcia & Jones, 2002; J Torquil Smith, 1997). The boundary charges create a secondary electric field that opposes the primary field above and along the sides of the negatively charged material when a conductive inclusion is present. As a result, the total field throughout the body decreases, while the field increases near the ends and sides of the body. Conversely, positive charges accumulate on the side of a resistive abnormal body that faces the primary electric field. This causes a secondary electric field to form inside and around the abnormal conductivity zone. As shown in Figure 2.6 (Jiracek, 1990). the secondary field inside the resistive body aligns with the primary field, causing an enhancement of the total field throughout the body, a decrease along its sides, and a reduction at the end of the body.

In conductive inhomogeneities and around resistive inhomogeneities, this phenomenon efficiently guides the current (Smith, 1997). Thus, across a conductive patch (current channeling), the apparent resistivities in the observed magnetotelluric (MT) soundings are pushed downward, while they are shifted higher immediately above a surficial resistant mass (current deflection). Topography or near-surface inhomogeneities are the causes of the static shift effect, a well-known example of galvanic distortion (Árnason, 2015; Sternberg et al., 1988). In volcanic situations, where resistivity fluctuations are frequently high near the surface, static shifts can present serious issues. The easiest way to characterize the influence on the magnetotelluric data is as a relative upward or downward shift in the magnetotelluric transfer function's resistivity amplitude from one station to the next. These corresponding shifts in the curve of apparent resistivity can guide substantial inversion errors in the data. In the context of magnetotelluric studies, the 1D Earth case involves galvanic distortion causing a consistent change in apparent resistivity across all frequencies, termed a "static shift," which does not impact the phase (Pellerin and Hahmann, 1990). The key difference between static shift and current channeling lies in the fact that the static shift does not alter the phase of the MT impedance tensor, whereas current channeling does ((A. G. Jones, 1988; Simpson & Bahr, 2005). This static shift phenomenon also occurs in a 2D Earth. While there is no widely applicable analytical or numerical method to model the origin of the static shift, it is suitable when MT and Transient Electromagnetic (TEM) data are jointly inverted. In a 2D Earth, this static shift phenomenon also occurs. The static shift's origin can be modeled, but it is only suitable when MT and transient electromagnetic (TEM) data are concurrently inverted; otherwise, there is no universally applicable analytical or numerical solution.

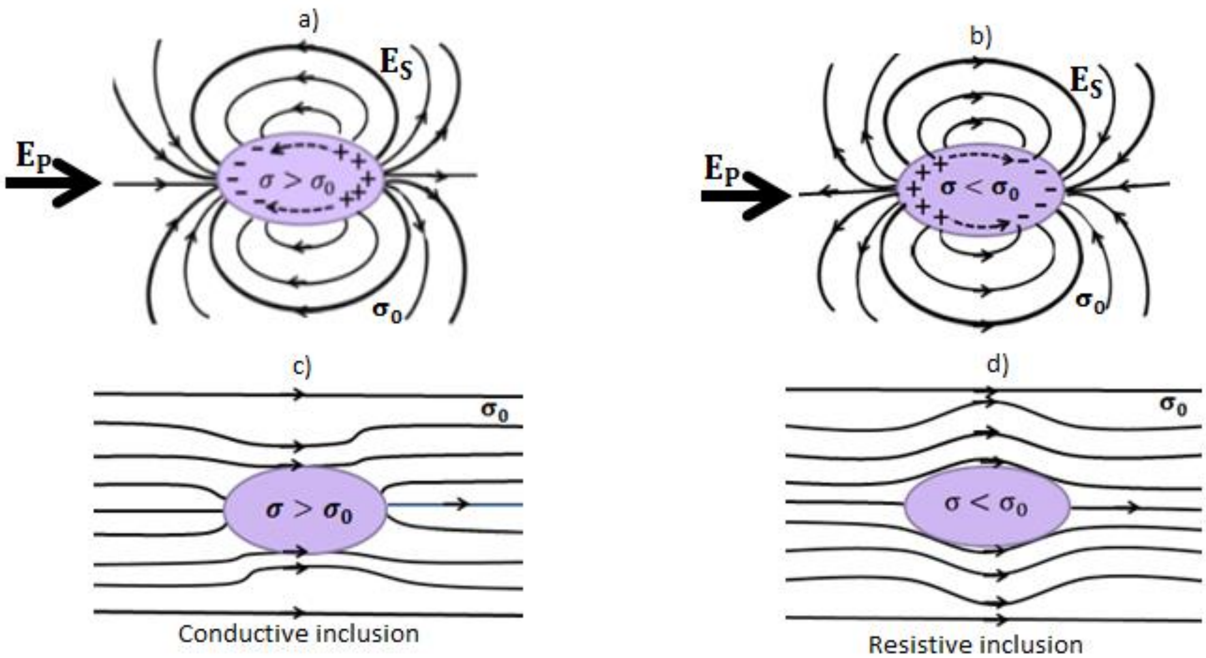

Figure 2.7 Galvanic effects for a conductive (left) and a resistive inclusion (right). Boundary charges build up on the surface bodies generating a secondary electric field E_S which adds vectorially to the primary field E_P (bottom) resulting in current channeling (bottom, left) and current deflection (bottom, right) as shown in the lower part of the figure. The figure was redrawn from Jiracek (1990).

Topographic features can also lead to galvanic effects, alongside resistive or conductive inclusions (Jiracek, 1990). Current flow is influenced by the hills and valleys, affecting the current density. The topographic galvanic effect happens when the primary electric field is at a right angle to the topographic direction, especially when it comes to the TM mode, which is linked to these effects. The most significant charge concentration is found where the topography is most pronounced. As a result of the overall electric field, current flows tangentially to the subsurface topography. Electric fields are heightened in valleys and reduced at the peaks of hills, leading to higher apparent resistivity values in valleys and lower values at the topographic crests. These topographic galvanic effects do not rely on the presence of conductivity heterogeneity, making them distinct galvanic distortion effects. The primary electric field induces the accumulation of charges on the surface of abnormal structures, with negative charges accumulating on the opposite sides of the primary field's direction and positive charges appearing on the lee side. The total electric field on hills is reduced due to the generation of secondary electric fields in the hills, which oppose the primary field. At the bottom of valleys, the primary and secondary electric fields align in the same direction, increasing the electric field there.

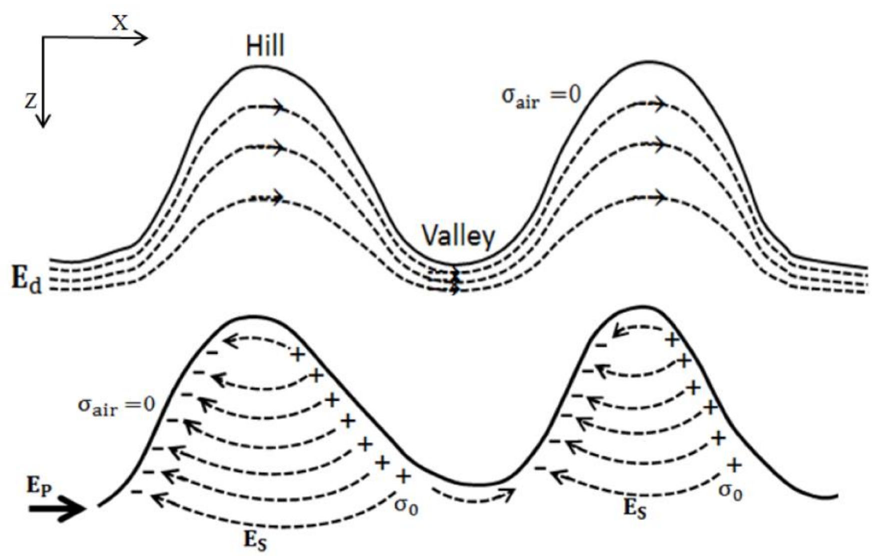

Figure 2.8 displays the total current and induced secondary electric field due to the galvanic effect of topography. Total electric field lines E_d are shown on the top of the hill valley. Due to the topography-related lateral conductivity contrast between conductive Earth charge accumulates beneath the surface and non-conductive air generating the secondary electric field E_S illustrated in the lower part of the figure, which is added vertically to E_P. The figure was adopted and redrawn from Jirucek (1990).

The induction-induced distortion effects are contingent upon subsurface shape, electrical characteristics, and frequency. In comparison to the primary magnetic field, the secondary magnetic field phase for the inductive case differs between 0 (the resistive limit) and $\frac{\pi}{2}$ (the inductive limit). On the other hand, the galvanic effect is produced when the secondary electric field and the primary electric field are in phase. The primary distinction between these two categories of distortion effects is that, as frequency rises, induction grows and saturates in relation to the magnetic field (Jiracek, 1990).

For the quasi-static approximation, which is one of the assumptions in MT, inductive distortion can be insignificant (Berdichevsky and Dmitriev, 1976a).

The mathematical description of galvanic distortion is described by Chave and Smith (1994) and Smith (1997). The measured electric field E_{obs} is proportional to the regional, 2D electric field E_{2D}

$$\mathrm{E_{obs}} = \mathrm{CE_{2D}} \tag{2.110}$$

where C represents the matrix of electric galvanic distortion. The currents can be expressed as follows since the magnetic field of the galvanic distorted $\mathrm{B_{dist}}$) is proportionate to and in phase with them, just as the currents are with the regional electric field.

$$\mathrm{B_{dist}} = \mathrm{DE_{2D}} \tag{2.111}$$

where D represents the matrix of magnetic galvanic distortion. The frequency-independent of both matrices of EM distortion are real. They could be expressed as

$$\mathrm{C} = \begin{pmatrix} \mathrm{C_{11}} & \mathrm{C_{12}} \\ \mathrm{C_{21}} & \mathrm{C_{22}} \end{pmatrix} \text{ and } \mathrm{D} = \begin{pmatrix} \mathrm{D_{11}} & \mathrm{D_{12}} \\ \mathrm{D_{21}} & \mathrm{D_{22}} \end{pmatrix} \tag{2.112}$$

The observed magnetic field $\mathrm{B_{obs}}$ itself is the sum of the galvanic distorted magnetic field $\mathrm{B_{dist}}$, and the regional magnetic field $\mathrm{B_{2D}}$ i.e.,

$$\mathrm{B_{obs}} = \mathrm{B_{2D}} + \mathrm{B_{dist}} = \mathrm{B_{2D}} + \mathrm{DE_{2D}} \tag{2.113}$$

The observed electric $\mathrm{E_{obs}}$ is related to the magnetic fields $\mathrm{B_{obs}}$, and measured impedance $\mathrm{Z_{obs}}$:

$$\mathrm{E_{obs}} = \mathrm{Z_{obs}B_{obs}} \tag{2.114}$$

By analogy, the regional impedance $\mathrm{Z_{2D}}$ is given by

$$\mathrm{E_{2D}} = \mathrm{Z_{2D}B_{2D}} \tag{2.115}$$

In Equation (2.114), replacing Eobs, Bobs, and E2D with Equations (2.110), (2.113), and (2.115) yields

$$\mathrm{CZ_{2D}B_{2D}} = \mathrm{Z_{obs}B_{2D}} + \mathrm{Z_{obs}DZ_{2D}B_{2D}} \tag{2.116}$$

This holds for all polarizations of the regional magnetic field B_{2D}, therefore

$$CZ_{obs} = Z_{obs} + Z_{obs}DZ_{2D} = Z_{obs}(I + DZ_{2D}) \qquad \Rightarrow Z_{obs} = CZ_{obs}(I + DZ_{2D})^{-1} \qquad (2.117)$$

where the identity matrix is represented by I. If the observation coordinate system differs from the strike or 2D regional reference frame, then an angle rotation (as in Equation (2.99)) must be used, i.e.

$$Z_{obs}(\theta) = R(\theta)CZ_{obs}(I + DZ_{2D})^{-1}R^{T}(\theta) \qquad (2.118)$$

The frequency-dependent (Z_{2D}) product of DZ_{2D} and disappears for low frequencies (long periods) giving the galvanic magnetic distortion.

Consequently, in the MT scenario, the magnetic galvanic distortion is typically disregarded (Garcia & Jones, 2002) and in Equation (2.118), becomes

$$Z_{obs}(\theta) = R(\theta)CZ_{obs}R^{T}(\theta) \qquad (2.119)$$

Chave and Smith (1994)showed using two distinct cases that the negligible assumption of magnetic galvanic distortion is not always true. The first one uses information from a location in central Ontario, Canada called Carty Lake, which has magnetometers on the lake's coastline and electrodes at the bottom. In this instance, the distortion of the MT response could not be adequately described by the electric galvanic distortion decomposition at higher frequencies (shorter periods). In this instance, they were able to sufficiently characterize the distortion on the response by accounting for both the electric and magnetic galvanic distortion effects. The second example demonstrates the significant seabed MT data of magnetic field galvanic distortion, possibly as a result of the highly resistive rocks directly beneath the oceanic crust that cause a significant concentration of electric current and channeling within the strongly conductive ocean (Chave and Smith, 1994). The scenario of seafloor differs from the land case in that the magnetic field measurement location is below the sheet of distorting current, which results in significant modifications of the fields even when there is no distortion relative to the surface (background) values. The magnitude of this attenuation is diminished by galvanic distortion.

A number of distortion correction strategies have been developed to deal with or are: theoretically, statistically, or physically based ways have been employed to eradicate the undesirable galvanic distortion caused by near-surface inhomogeneities and terrain (e.g., Groom

& Bahr, 1992; Jiracek, 1990). A 1D joint inversion of MT and TEM is one of these methods for solving the static shift difficulties; this will be covered in more detail in Section 3.5.2. Additionally, the 3D sample displays the same distortion effects. Moreover, several additional galvanic distortion effects emerge due to field curvature, which can be categorized into two types: concentration (where the current concentrates in a conductive structure) and where the current travels around resistive structures (flow-around) (Berdichevsky and Dmitriev, 1976b). However, it is possible to reduce the distortion effects of the 3D subsurface model of MT data by inverting both the full phase and impedance tensors (Grayver, 2015; Samrock et al., 2018) and by jointly inverting MT impedance tensor data and a frequency-independent full distortion matrix (Avdeeva et al., 2015).

2.1.10 Correction of Static Shift

The apparent resistivity vs. period curve in the MT log-log display is effectively altered, either upwards or downwards, due to the static shift, leading to a modification in the apparent resistivity curve. A static shift in the data is suggested if the two polarizations of the apparent resistivity curves shift in tandem. However, the absence of a parallel shift between two curves of apparent resistivity does not always indicate the presence of a static shift, as both curves may change by the same amount (Simpson & Bahr, 2005). According to Árnason et al. (2010)), there are two primary causes of static shifts: voltage distortion, which occurs when the electric field is dependent on the resistivity at the voltage measurement site, and current distortion, which is caused by current channeling (Árnason et al., 2010). If the transverse electric and transverse magnetic apparent resistivity sounding curves are not parallel and the phases are not identical, this indicates an inductive response from 2D or 3D structures (Wannamaker et al.,1984).

Several methods have been proposed to correct static shifts. One approach involves using TEM data alongside MT data from the same site to address static shift issues (Pellerin and Hohmann, 1990; Simpson & Bahr, 2005; Sternberg et al., 1988). Other static shift correction methods may include statistical averaging techniques and long-period corrections based on assumed deep structure, such as at the mid-mantle transition zones a resistivity drop, or long-period magnetic transfer functions (refer DeGroot-Hedlin, C., and Constable, 1990; Ogawa & Uchida, 1996). It is anticipated that in static shift correction, the shifts primarily arise from electric field distortion. Scaled apparent resistivity curves with upward or downward shifts derived from MT data are in agreement with TEM curves or are jointly inverted with TEM data (Sternberg et al., 1988). This is due to the TEM is not influenced by the static shift problem because the decaying magnetic field at the surface is significantly less affected by local inhomogeneities than the electric field associated with the MT. To adjust for the telluric shift in the MT in this work, the MT and TEM-sounding data that were gathered at the same site were jointly inverted. The transient electromagnetic technique, or TEM, is the most effective and widely utilized treatment for a static shift. The declining magnetic field at the surface of the TEM is far less impacted by local inhomogeneities than the electric field associated with the MT, which is why the static shift issue does not exist. The telluric shift correction in the MT is thus applied in this study by concurrently inverting the MT and TEM-sounding data that were acquired at the same place.

2.2 The TEM method

2.2.1 Basic Principles of TEM

The transient electromagnetic (TEM) method, which is also known as time-domain electromagnetic (TDEM) or pulse electromagnetic (PEM), is a geophysical technique used for obtaining information about subsurface resistivity or conductivity. This method is relatively new compared to other electromagnetic (EM) methods and was first developed in the early 1950s, with further advancements made primarily in the 1970s. The instruments and interpretation methods for TEM soundings were highly developed and widely used (Spies and Frischknecht, 1991). In this method, as described by Spies and Frischknecht (1991), a constant current is applied to a loop to generate a steady magnetic field of known intensity. When the current is suddenly switched off, the magnetic field diminishes, leading to the induction of electrical currents in the ground. These induced currents, in turn, produce a secondary magnetic field that also diminishes over time. To achieve this, a transmitter is used to generate a time-varying current in an ungrounded surface wire loop. The rate at which the secondary magnetic field diminishes is measured by the voltage induced in a small receiver loop or coil placed at the center of the transmitting loop. These secondary electromagnetic fields are detected at the surface using a receiver loop or magnetic antenna and are recorded as the energy spreads into the Earth. The transient electromagnetic (TEM) method can be utilized in different configurations and can investigate depths from tens of meters to over 1000 meters. The depth of investigation largely relies on the size of the transmitter loop, the transmitted power, and the amount of background noise.

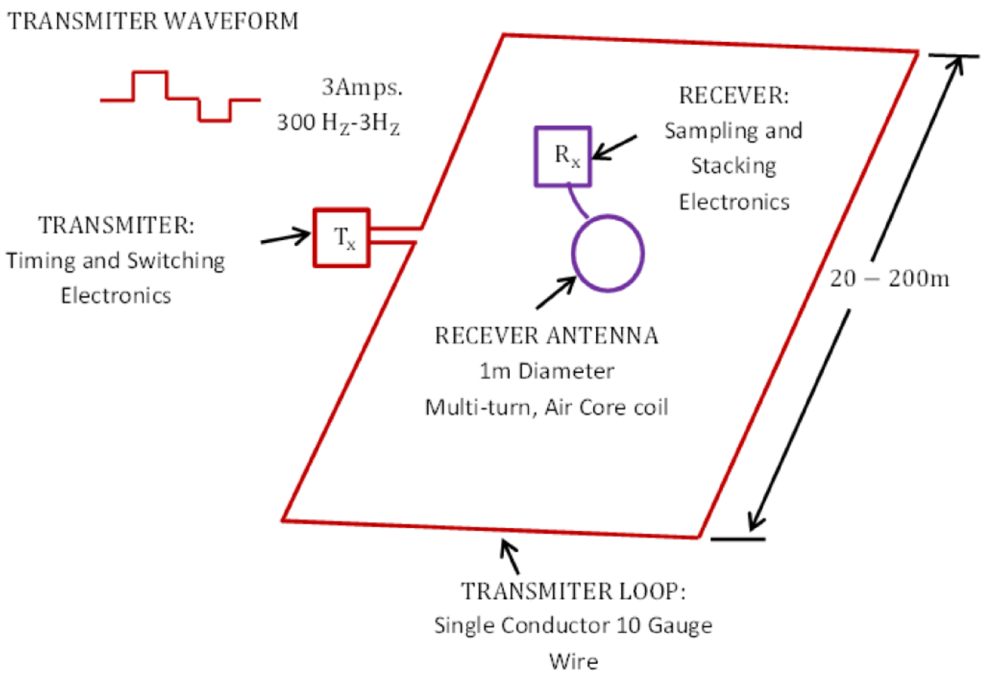

Figure 2.9 The set-up TEM sounding, the receiver coil is at the center of the transmitter loop (redrawn from Rowland, 2002).

According to Faraday's law of induction (Equation (2.3)), a magnetic field that changes over time generates an electric field, which leads to the formation of an electric current. As a result, when the magnetic field changes rapidly, it causes eddy currents to flow in nearby conductors, resulting in the creation of small secondary magnetic fields. These secondary magnetic fields gradually decrease in strength over time. The terms "transient" and "time domain" are used to explain this method, as shown in Figure 2.9.

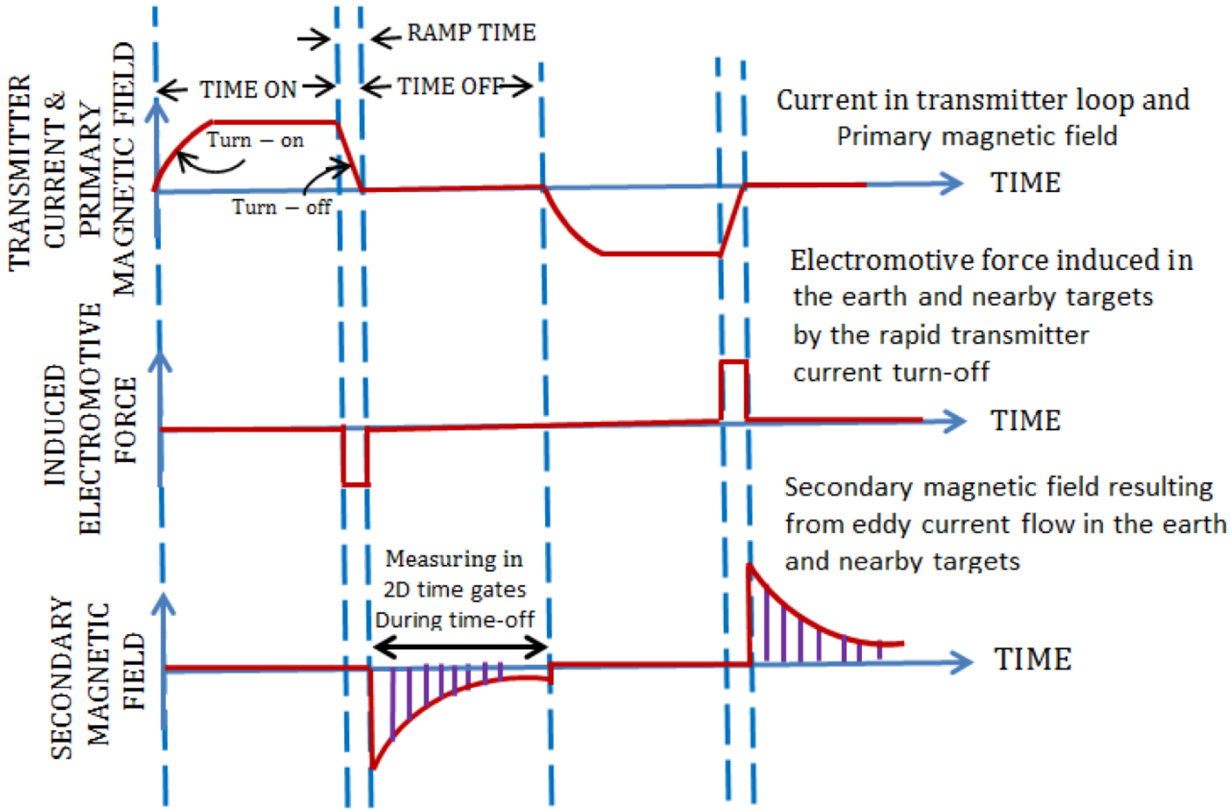

Figure 2.10 Basic principles of the TEM method: at the top the current in the transmitter loop; at the middle and the bottom the induced electromotive force in the ground; the the receiver coil measured secondary magnetic field (redrawn and minor modified from Christiansen et al., 2006).

Due to ohmic dissipation, the EM eddy currents decay into Earth, whereby the induction process continues and induced magnetic fields decrease. The time interval between the current turn-off and the Earth's conductivity determines how deep eddy currents can travel before reaching the planet (Nabighian & Macnae, 1991). The diffusion depth (time domain equivalent of skin depth) of the central loop TEM method is as follows, per Sternberg et al. (1988

$$\delta_{TEM}(t) = 1.28\sqrt{\frac{t}{\sigma\mu}}[m] \quad (2.120)$$

The Earth's resistivity structure determines both the secondary magnetic field decay rate and the current distribution; on a more conductive Earth, the decay is more gradual. According to Árnason (1989), the voltage induced in the receiving coil on a homogeneous half-space of conductivity, σ, is as follows at what are known as late times:

$$V_{(t,r)} \approx I_0 \frac{C(\mu_0 \sigma r^2)^{\frac{3}{2}}}{10\pi^{\frac{1}{2}} t^{\frac{5}{2}}} \quad (2.121)$$

where $C = A_r n_r A_s n_s \frac{\mu_0}{2\pi r^3}$

and Ar = Area of the receiver coil [m^2];

A_s = Area of the transmitting loop [m^2]

n_r = Number of turns on the receiver coil;

n_s = Number of turns in the transmitting loop;

t = Time elapsed after the current in the transmitter is turned off [s];

μ_0= Magnetic permeability [Henry/m];

I_0 = Current in the transmitting loop [A];

$V(r,t)$ = Transient voltage [V];

R = Radius of the transmitter loop [m].

This indicates that the transient voltage, occurring after the transmitter current is abruptly switched off, is proportional to $\sigma^{\frac{3}{2}}$ and diminishes over time as $t^{\frac{-5}{2}}$. By solving for resistivity in Equation (2.121), the apparent resistivity for TEM can be determined using Equation (2.122).

$$\rho_a(r,t) = \frac{\mu_0}{4\pi}\left(\frac{2\mu_0 A_r n_r n_s I_0}{5t^{\frac{5}{2}} V(t,r)}\right)^{\frac{2}{3}} \quad (2.122)$$

Chapter 3 Data acquisition, processing, analysis, and inversion

3.1 Data Acquisition

3.1.1 MT Data Acquisition in Study Area

The natural time variations of the electrical and magnetic fields of the broadband MT data for the entire 30 MT stations in the Ashute area near the SDFZ were gathered within two months. The distance between stations varies, but it is roughly 1 kilometer on average. For the MT data utilizing (MTU-5A/MTU-5/V5) a V5 System 2000 MTU Phoenix Geophysics at local and remote stations. It was carried out in 2017 under the supervision of GSE geophysical personnel. Whereas the Adami Tulu to the western border of CMER the MT data were collected in spring 2019 from 21 stations along a 52 km long profile. The time series data were acquired during > 24 h of installations, with station separation of 2.5 km on average. A five-component MT unit typically consists of five non-polarized electrodes, four of which measure two perpendicular electric field components (E_x, E_y) in the horizontal directions, i.e., along with the N-S and E-W directions, while the fifth electrode serves to ground the MTU data logger in the center. These electrodes are usually comprised of a porous pot that contains metal interacting with a solution, which connects to the ground via porous materials, commonly SO_4 or $PbCl_2$. Three induction coils were used for measuring the magnetic field, two of which measured the horizontal orthogonal components (H_x, H_y) and the rest measured the vertical component (Hz), as illustrated in Figure 4.3. Magnetic sensors (induction coils) measure the horizontal and vertical magnetic field components on the Earth's surface. In order to minimize noise and the effect of everyday temperature variations, the two magnetic coils were buried. The magnetic field in the vertical direction, Hz, was measured by burying the induction coil as much as possible vertically, 90 degrees into the ground.

The data logger serves as the MT measuring system's central controller unit. It manages the acquisition process and signals of amplifier sensors before sending them to an AD converter for conversion to digital format. As a stable power source, a standard 12 V car battery was used. The field setup displayed in Figure 4.3 is as

The GPS time signals were used to obtain timing at each MT station. To remove electromagnetic noise (cultural noise) induced by artificial electrical sources, vibrations, and electromagnetic signals from other sources at each measuring station, a remote reference located 15 km NW of the Ashute Geothermal field was chosen. The coils and wires were buried in the ground to reduce wind noise, with the added benefit of lowering heat impacts on the induction coils. At most of the sites, the devices were deployed and running for more than 24 hours.

3.1.2 TEM survey instrumentations

The TEM survey was conducted in 2019 within the Ashute area near SDFZ and along the traverse SDFZ-Adami Tulu by the Authors, Institute of Geophysics Space Sciences and Astronomy (IGSSA), and Geological Survey of Ethiopia (GSE) it was funded by the UK Natural Environment Research Council through the RiftVolc consortium. A total of 51 TEM soundings were employed in this project, as they were gathered near the same locations as the MT soundings, enabling the joint inversion to rectify the MT data static shift. The time domain electromagnetic data were gathered using Geonics Ltd., Canada's PROTEM-67 devices. They include a digital receiver with an integrated data logger, a receiver coil with an effective area of $100\, m^2$, a square receiving loop with an effective, area of $5613\, m^2$, a motor generator, a current transmitter connected to an external power module, and a current transmitting loop (wires) as shown in Figure 2.8.

To track the transient decay of the secondary magnetic field, the digital receiver measures the voltage created in the receiving coil, which is located in the middle of the current transmitting loop. The timing of the current transmitter and the digital receiver is regulated by synchronized precision crystal clocks. The receiver always measures the voltage produced in the receiver coil whenever the transmission current is cut off. The TEM instrument may be operated at different frequencies, including 1, 8, and 16 Hz, and transmit half-duty square wave current.

3.2 MT data processing and data analysis

3.2.1 Time series processing

The processing of MT data involves converting the raw, time-varying orthogonal components of electromagnetic fields into Earth response functions, providing insights into the distribution of the conductivity structure. In this research, MT transfer functions were obtained from the collected MT data using the SSMT2000 software created by Phoenix Geophysics in Canada (Phoenix Geophysics, 2005) and MT Editor. The software takes raw time series files, site parameter files, and calibration files as input. Each measured field component is calibrated based on the sensitivity of the specific instrument, employing frequency-dependent or frequency-independent functions. The parameter file was adjusted to match the data acquisition setup, and the resulting time series data were converted into the frequency domain using a cascade decimation method. A robust processing method was used to calculate Fourier transform band-averaged cross- and auto-powers. The Fourier transformation extracts the frequency components of each segment. Subsequent editing was carried out visually using the graphical user interface software, MT-Editor. This program takes MT Plot files as input, displaying resistivity and phase curves, along with individual cross-powers used to calculate each point on the curves. Time series processing steps were employed, and the cross-powers were graphically edited to eliminate noisy data points, ensuring "smooth" curves for both phase and apparent resistivity. The resulting auto- and cross-powers, in addition to all pertinent MT parameters including impedances, phase coherences, strike directions, and apparent resistivity, were stored in a standard file format (EDI files).

3.2.1.1 Data setup and preconditioning,

Each of the M segments that make up the obtained time series data has N data points. Whereas the N target frequencies are uniformly separated on a logarithmic scale, the value of N represents frequencies in the raw spectral window that are evenly distributed on a linear scale. The form of the spectral window is a trade-off between data resolution and degrees of freedom. To facilitate additional statistical estimation of the transfer functions, each time window needs to be segmented into a sufficient number of segments. After the segments are defined, they are analyzed manually or automatically with the use of the MT Editor application to find and remove noise effects (spikes) and trends.

3.2.1.2 Time to frequency domain conversion

The time series channels $E_i(i = x, y)$ and $H_j(j = x, y, z)$ are converted into the frequency domain using methods such as the Discrete Fourier Transform (Brigham, 1988) or Cascade Decimation (Wight & Bostick, 1980), both of which rely on the Fast Fourier Transform (FFT), or by utilizing the wavelet transform (Zhang and Paulson, 1997; Trad & Travassos, 2000) for each segment. This process yields a raw spectrum with N/2 frequencies. Following this, evaluation frequencies, evenly distributed on a logarithmic scale, typically 6–10 per period per decade, are chosen. The resulting spectra are then smoothed by averaging neighboring frequencies using a window function.

It is essential to calibrate each field component based on the instrument sensitivity at a specific frequency. The products of the field components and their respective complex conjugates generate auto and cross spectra of a segment k, computed from the original time series segments for each frequency, represented as:

$E_{kj}(\omega)\cdot E_{kj}{}^{*}(\omega), H_{kj}(\omega)\cdot H_{kj}{}^{*}(\omega), E_{kj}(\omega)\cdot H_{kj}{}^{*}(\omega)$ and $H_{kj}(\omega)\cdot E_{kj}{}^{*}(\omega)$. These are stored in the spectral matrix, containing contributions from all the segments at a specific frequency.

An estimated average Auto-spectra density or spectrum of one channel A, in the frequency band $(f_{j-m,}f_{j+m})$ around the central frequency, fj is calculated by (ref Vozoff 1991) which will generally be complex. The square root is called the cross-spectral density and is also complex.

$$\langle A(f_j)\rangle = \sqrt{\frac{1}{2m+1}\sum_{k=j-m}^{j+m} A_k A_k{}^{*}} = \langle A_j A_j{}^{*}\rangle^{\frac{1}{2}} \tag{3.1}$$

where A is the Fourier transform elements of **E** or **H** they consist of five field components $(E_x, E_y, H_x, H_y \text{ and } H_z)$. The square of this is the auto power spectra density, or auto power, at f_j. In the same way, we can calculate the cross-power density at f_j of two channels, say A and B, is given by

$$\langle A(f_j), B(f_j)\rangle = \frac{1}{2m+1}\sum_{k=j-m}^{j+m} A_j B_j{}^{*} = \langle A_j B_j{}^{*}\rangle \quad , \tag{3.2}$$

The coherence or coherency of the two channels at frequency fj is defined as the ratio of the cross-spectral density to the square root of the product of the auto-spectra densities.

$$coh(A_j, B_j) = \frac{1}{2m+1}\sum_{k=j-m}^{j+m} \frac{A_k B_k{}^{*}}{\sqrt{(A_k A_k{}^{*})(B_k B_k{}^{*})}} = coh(A, B)_j \tag{3.3}$$

Which is complex with a modulus between 0 and 1. It will have a phase given by arc tan $\left[\frac{\Im(coh)}{\Re(coh)}\right]$. Coherency and cross-power are very powerful tools in the extraction of information from the

3.2.1.3 Estimation of the MT transfer functions

In order to evaluate the MT transfer functions from Equations (2.48), (2.49) and (2.52), spectra over a number of closely spaced frequencies must be averaged. It is also necessary to make at least two independent measurements of the electric and magnetic field components in the frequency domain.

$$E_x(\omega) = Z_{xx}(\omega)H_x(\omega) + Z_{xy}(\omega)H_y(\omega) \tag{3.4}$$

$$E_y(\omega) = Z_{yx}(\omega)H_x(\omega) + Z_{yy}(\omega)H_y(\omega) \tag{3.5}$$

$$H_z(\omega) = \mathcal{T}_{zx}H_x(\omega) + \mathcal{T}_{zy}H_y(\omega) \tag{3.6}$$

The plane wave source field approximation creates uncertainty in the impedance tensor and is the cause of measurement noise in the measured electric and magnetic field Equations (3.4) to (3.6). In terms of statistics, recording multiple sets is better because it makes averaging easier and lowers noise.

The conventional method of solving the aforementioned equations makes the assumption that is constant over an averaging band (window), which is reasonable from a physical standpoint if the bands are sufficiently narrow (Vozoff, 1991),

In every frequency range, the cross power for each equation is generated in the frequency domain by multiplying the impedances in Equations (3.4) and (3.5) by the complex conjugates of the magnetic spectra, H_x^* and H_y^* successively, resulting in six distinct equations as detailed below:

$$\begin{aligned}
\langle E_x(\omega)H_x^*(\omega)\rangle &= Z_{xx}(\omega)\langle H_x(\omega)H_x^*(\omega)\rangle + Z_{xy}(\omega)\\
\langle E_x(\omega)H_y^*(\omega)\rangle &= Z_{xx}(\omega)\langle H_x(\omega)H_y^*(\omega)\rangle + Z_{xy}(\omega)\langle H_y(\omega)H_y^*(\omega)\rangle\\
\langle E_y(\omega)H_x^*(\omega)\rangle &= Z_{yx}(\omega)\langle H_x(\omega)H_x^*(\omega)\rangle + Z_{yy}(\omega)\langle H_y(\omega)H_x^*(\omega)\rangle\\
\langle E_y(\omega)H_y^*(\omega)\rangle &= Z_{yx}(\omega)\langle H_x(\omega)H_y^*(\omega)\rangle + Z_{yy}(\omega)\langle H_y(\omega)H_y^*(\omega)\rangle
\end{aligned} \tag{3.7}$$

In the same way, the tipper cross power of Equation (3.6) multiplied by the complex conjugates of the magnetic spectra, Hx* and Hy*in turns, gives the following pairs of equations :

$$\begin{aligned}
\langle H_z(\omega)H_x^*(\omega)\rangle &= \mathcal{T}_{zx}(\omega)\langle H_x(\omega)H_x^*(\omega)\rangle + \mathcal{T}_{zy}(\omega)\langle H_y(\omega)H_x^*(\omega)\rangle\\
\langle H_z(\omega)H_y^*(\omega)\rangle &= \mathcal{T}_{zx}(\omega)\langle H_x(\omega)H_y^*(\omega)\rangle + \mathcal{T}_{zy}(\omega)\langle H_y(\omega)H_y^*(\omega)\rangle
\end{aligned} \tag{3.8}$$

The six equations below are derived from solving Equations (3.7) and (3.8) for the cross- and auto-powers of the EM fields:

$$Z_{xx} = \frac{\langle E_x H_x^* \rangle \langle H_y H_y^* \rangle - \langle E_x H_y^* \rangle \langle H_y H_x^* \rangle}{\langle H_x H_x^* \rangle \langle H_y H_y^* \rangle - \langle H_x H_y^* \rangle \langle H_y H_x^* \rangle} \tag{3.9a}$$

$$Z_{xy} = \frac{\langle E_x H_x^* \rangle \langle H_x H_y^* \rangle - \langle E_x H_y^* \rangle \langle H_x H_x^* \rangle}{\langle H_y H_x^* \rangle \langle H_x H_y^* \rangle - \langle H_y H_y^* \rangle \langle H_x H_x^* \rangle} \tag{3.9b}$$

$$Z_{yx} = \frac{\langle E_y H_x^* \rangle \langle H_y H_y^* \rangle - \langle E_y H_y^* \rangle \langle H_y H_x^* \rangle}{\langle H_x H_x^* \rangle \langle H_y H_y^* \rangle - \langle H_x H_y^* \rangle \langle H_y H_x^* \rangle} \tag{3.9c}$$

$$Z_{yy} = \frac{\langle E_y H_x^* \rangle \langle H_x H_y^* \rangle - \langle E_y H_y^* \rangle \langle H_x H_x^* \rangle}{\langle H_y H_x^* \rangle \langle H_x H_y^* \rangle - \langle H_y H_y^* \rangle \langle H_x H_x^* \rangle} \tag{3.9d}$$

$$\mathcal{T}_{zx} = \frac{\langle H_z H_x^* \rangle \langle H_y H_y^* \rangle - \langle H_y H_x^* \rangle \langle H_z H_y^* \rangle}{\langle H_x H_x^* \rangle \langle H_y H_y^* \rangle - \langle H_y H_x^* \rangle \langle H_x H_y^* \rangle} \tag{3.9e}$$

$$\mathcal{T}_{zy} = \frac{\langle H_z H_y^* \rangle \langle H_x H_x^* \rangle - \langle H_z H_x^* \rangle \langle H_x H_y^* \rangle}{\langle H_x H_x^* \rangle \langle H_y H_y^* \rangle - \langle H_y H_x^* \rangle \langle H_x H_y^* \rangle} \tag{3.9f}$$

3.2.1.4 Remote-reference estimates

Hence, bias effects that arise from the existence of uncorrelated noise at both local and remote sites can be removed from measurements of designated electromagnetic components. To minimize wind noise, the coils and cables were buried in the ground, giving the additional advantage of reducing thermal effects on the induction coils. In the robust processing stage, auto-powers were calculated and averaged over the Fourier transform band, and a regression scheme was used over the EM cross-spectra for combined single and remote reference stations in the robust processing method. The presence of consistent background noise in the data at a single location can lead to a biased estimate of impedance, denoted as Z_{ij}. To address this issue, the remote reference technique is employed. This method involves placing additional MT sensors at a quiet site, away from cultural noise and the survey area, in order to counteract environmental noise (Clarke et al., 1983; Gamble et al., 1979; Goubau et al., 1978).

To eliminate any bias resulting from uncorrelated noise between the sites, specific electromagnetic components are measured at both the local and remote locations. Typically, the separation between the remote and local sites is between 10 and 100 km, a significant distance that ensures the noise sources are independent. In this investigation, the distance between the remote reference (RR) and the measurement area was approximately 15 km. Therefore, it is feasible to remove noise-induced uncorrelated bias effects by measuring certain EM components at both the local and remote sites.

However, this method is ineffective when correlated noise exists at both the local and remote sites.

The auto-powers of the magnetic field are involved in the Equations in (3.7) that are discussed below. The problem with the previously described process is that the impedance estimate is biased due to continuous noise at a particular site. Robust processing techniques are available to improve the estimated magnetotelluric transfer function's accuracy (Gamble et al., 1979). In magnetotelluric surveys, the remote reference method is commonly used to provide noise spectrum estimates in each channel. By simultaneously measuring the horizontal magnetic field (BR) at a remote station, this approach makes use of the plane wave assumption. Therefore, the noise at the local magnetotelluric station can be removed when there is uncorrelated magnetic noise between the local and remote stations by replacing the remotely recorded magnetic field.

At both the local and remote sites, the spectrums of the magnetic and electric fields are linearly related. Multiplying Equations (3.4), (3.5) & (3.6) by spectra $R_x^*(\omega)$ *and* $R_y^*(\omega)$ instead of complex conjugates of the magnetic spectra, H_x^* *and* H_y^* and averaging over frequency intervals, we get six independent equations as follows:

$$Z_{xx} = \frac{\langle E_x R_x^* \rangle \langle H_y R_y^* \rangle - \langle E_x R_y^* \rangle \langle H_y R_x^* \rangle}{\langle H_x R_x^* \rangle \langle H_y R_y^* \rangle - \langle H_x R_y^* \rangle \langle H_y R_x^* \rangle} \tag{3.10a}$$

$$Z_{xy} = \frac{\langle E_x R_x^* \rangle \langle H_x R_y^* \rangle - \langle E_x R_y^* \rangle \langle H_x R_x^* \rangle}{\langle H_y R_x^* \rangle \langle H_x R_y^* \rangle - \langle H_y R_y^* \rangle \langle H_x R_x^* \rangle} \tag{3.10b}$$

$$Z_{yx} = \frac{\langle E_y R_x^* \rangle \langle H_y R_y^* \rangle - \langle E_y R_y^* \rangle \langle H_y R_x^* \rangle}{\langle H_x R_x^* \rangle \langle H_y R_y^* \rangle - \langle H_x R_y^* \rangle \langle H_y R_x^* \rangle} \tag{3.10c}$$

$$Z_{yy} = \frac{\langle E_y R_x^* \rangle \langle H_x R_y^* \rangle - \langle E_y R_y^* \rangle \langle H_x R_x^* \rangle}{\langle H_y R_x^* \rangle \langle H_x R_y^* \rangle - \langle H_y R_y^* \rangle \langle H_x R_x^* \rangle} \tag{3.10d}$$

and the tipper elements are given by

$$\mathcal{T}_{zx} = \frac{\langle H_z R_x^* \rangle \langle H_y R_y^* \rangle - \langle H_y R_x^* \rangle \langle H_z R_y^* \rangle}{\langle H_x R_x^* \rangle \langle H_y R_y^* \rangle - \langle H_y R_x^* \rangle \langle H_x R_y^* \rangle} \tag{3.10e}$$

$$\mathcal{T}_{zy} = \frac{\langle H_z R_y^* \rangle \langle H_x R_x^* \rangle - \langle H_z R_x^* \rangle \langle H_x R_y^* \rangle}{\langle H_x R_x^* \rangle \langle H_y R_y^* \rangle - \langle H_y R_x^* \rangle \langle H_x R_y^* \rangle} \tag{3.10f}$$

The magnetic components H_x and H_y of the remote reference stations are denoted by the letters R_x and R_y in the equations above, respectively. It is also possible to use the remote reference's electric field components Ex and Ey. However, the horizontal magnetic field is often used instead of the electric field because it is less susceptible to polarization and noise contamination. Sims et al. (1971) also, describe methods of Similar least squares estimates of the impedance tensor.

However, in many scenarios with severe noise effects, the resulting cross-powers may not be as smooth as intended. To achieve more realistic results and smoother curves, the MT-Editor program is utilized to manually change the stacking apparent resistivity values for every frequency. The auto-powers and Fourier transform band averaged cross for the topic under discussion were produced using a robust processing technique. The MT-Editor software was utilized to assess coherences for both phase and apparent resistivity by graphically editing the cross-powers by masking the noisy data points. Because of this, MT-Editor also has the ability to exclude particular cross powers from calculations, allowing for the editing of low-quality data.

3.3 TEM data processing

The internal memory of the receiver's raw Transient Electromagnetic (TEM) data was downloaded. Special programs TEMX and TEMTD were developed by Iceland GeoSurvey (ÍSOR) for processing this data. TEMX can average data collected at the same frequency and calculate the apparent resistivity of late time as a function of time after the turn-off. Prior to using the data for interpretation, it helps to remove outliers and suspect data points. 1D inversion of TEM data was accomplished using the Linux-based TEMTD tool created at ISOR (Árnason, 2006).

The forward algorithm calculates the transient voltage induced in the receiver by summing the responses from successive current turn-on and turn-off timings. Both the induced voltage and the late-time apparent resistivity as a function of time are utilized to calculate the transient response. As per (Árnason, 1989), the inversion algorithm utilized in the program is a non-linear least-squares inversion based on the Levenberg-Marquardt approach.

The data and a conservative initial model estimate serve as the foundation for the inversion. Through an iterative procedure, the inversion method refines the model. It makes iterations to the model based on the discrepancy between the observed data and the model's response until a mutually agreeable conclusion is obtained. Estimates of the model parameters are determined and the statistically optimal solution is generated by the inversion. According to Flóvenz et al.

(2012), it can identify parameters that are well-determined or poorly determined as well as potential relationships between the estimates(Flóvenz et al., 2012).

The difference between the estimated and measured values, weighted by the standard deviation of the measured values, is the root-mean-square (chi2, χ2), which is the misfit function. The user can decide if the application matches the measured (Árnason, 2006a)

The actual function that is minimized is not just the weighted root-mean-square (chi^2) but the potential (pot).

$$Pot = chi^2 + \alpha DS1 + \beta DS2 + \gamma DD1 + \delta DD2 \quad (3.11)$$

where, DD1 and DD2 represent the first and second derivatives of the logarithms of layer depth ratios, while DS1 and DS2 represent the first and second derivatives of log-conductivities in the layered model. The coefficients α, β, η, and δ represent the respective contributions of the various damping factors.

The same technique can also be used to perform minimum structure (Occam) inversion, where the output file from TEMX for TEM is used as the input file for TEMTD. In this case, the conductivity distribution is smoothed by adjusting α and β, while maintaining constant and equally spaced layer thicknesses on the logarithmic scale (Equation (4.7)).

3.4 MT Data Analysis

MT data analyses are commonly used prior to modeling and inversion. These include dimensionality analysis, strike angle calculation (Caldwell et al., 2004; Kirkby & Duan, 2019), and distortion removal (Caldwell et al., 2004). The parameters and approaches used for MT data analysis and results of the Ashute area were discussed in more detail as follows.

3.4.1 A Dimensionality Analysis

The dimensionality analysis of MT data is an approach to determine whether the site's impedance tensors and tippers are compatible with structures of 1D or 2D or show more complex 3D structures. Many methodologies have been developed to investigate the dimensionality of MT data at various times. The most widely utilized techniques are the phase tensor (Caldwell et al., 2004), rotational invariants, and WAL (Weaver et al., 2000; Martí et al., 2010), Groom and Bailey decomposition (Groom & Bailey, 1989), Bahr's phase-sensitive skew (Bahr, 1988, 1991), ellipticity (Word et al., 1970), and the skew parameter of Swift (Swift, 1967). The Ashuite MT data was subjected to dimensionality analysis using the Phase tensor (Caldwell et al., 2004), the

Swift-skew (Swift, 1967), and Bahr's phase-sensitive skew (Bahr, 1988), The Ashute geothermal field's dimensionality analysis shows that there are 3D structures at deeper depths and 1D and 2D structures at shallower depths.

The following sections provide a more thorough explanation of the parameters and methods utilized for the dimensionality analysis of the Ashuite MT data and results.

3.4.1.1 Swift-Skew

The tensors of impedance Swift's skew (κ) is a rotationally invariant characteristic that is defined as the ratio of two rotationally invariant modified impedances (Swift, 1967), as shown below:

$$Skew(k) = \frac{|Z_{xx}+Z_{yy}|}{|Z_{xy}-Z_{yx}|} \qquad (3.12)$$

For noise-free data, the Swift-skew is zero for the structure of the 1D and 2D cases, and the existence of 3D structures shows a high value (Vozoff, 1991). In the 1D structures, $Z_{xx}\ and\ Z_{yy}$ are zero but $Z_{xy}\ and\ Z_{yx}$ are not zero and unequal; so, k=0. The subsurface structure is considered as 1D when k< 0.1 and the impedance are equal in the two orthogonal directions. The skew is minimal in the 2D assumption, and the apparent resistivities are not equal. When the skew value is considerable, greater than 0.2–0.3, it is believed to be 3D effects are significant (Vozoff, 1991). The difficulty of dimensionality indicators such as Swift-skew is very sensitive to noise (Chave & Jones, 2012).

For the Ashuite field data, the threshold value of a Swift-skew was taken as 0.2. Values below the threshold would indicate 1D and 2D structures. Most stations of the Ashute MT data at shallow depth indicate 1D and 2D structures and the values of Swift-skew are below the threshold values at periods less than 10 s. Above 10 s, the Swift-skew indicates three-dimensional structures that correspond to deeper depths (see Figure 3.1). The Swift-skew has been schemed for selected MT stations (A05, A17, A23, and A30) in Figure 3.1, and Swift-skew is drawn for all MT stations as shown in Figure 3.2.

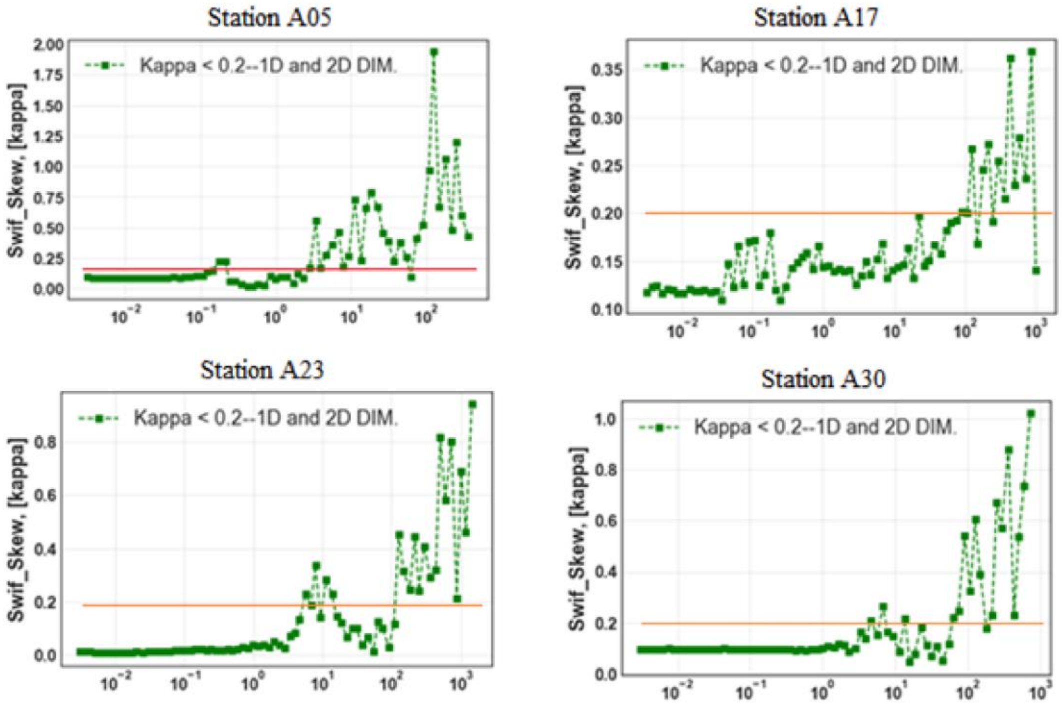

Figure 3.1 Swift-skew at MT stations A05, A17, A23, and A30.

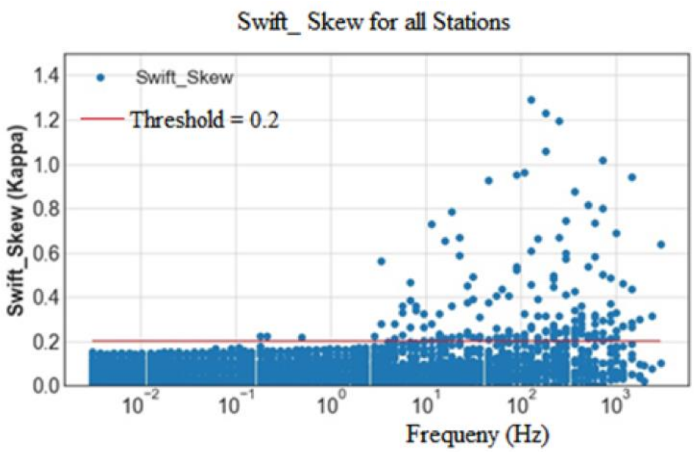

Figure 3.2 Swift-skew drew for all MT station

3.4.1.2 Bahr's phase-sensitive skew, η

Bahr (1988) suggested phase-sensitive skew, a rotationally invariant parameter, as the first modern dimensionality tool. It measures the skew of the impedance tensor's phases and is provided by:

$$\eta = \frac{|[D_1, S_2] - [S_1, D_2]|^{\frac{1}{2}}}{|D_2|} \tag{3.13}$$

where the D (difference) and S (sum) impedances are recognized as modified impedances (Bahr, 1988) given by

$$D_1 = Z_{xx} - Z_{yy}, D_2 = Z_{xy} - Z_{yx} \quad (3.14)$$

$$S_1 = Z_{xx} + Z_{yy}, S_2 = Z_{xy} + Z_{yx} \quad (3.15)$$

According to the criteria of Bahr (1988, 1991), for interpreting η based on its value of distorted 2D (3D /2D), or 1D, 2D examples are indicated by the skews value of phase-sensitive smaller than 0.1 while 3D data is represented by the skew parameters of 'phase sensitive', with values of η greater than 0.3. A modified dataset of 3D/2D with values between 0.1 and 0.3 ($0.1 < \eta < 0.3$) is regarded to be suggestive (Chave & Jones, 2012).

Figures 3.4 to 3.5 show Bahr's phase-sensitive skew for the Ashuite MT data for selected MT stations. As demonstrated in Figure 3.5, Bahr's phase-sensitive skew was presented for the entire MT stations in the Ashute geothermal region.

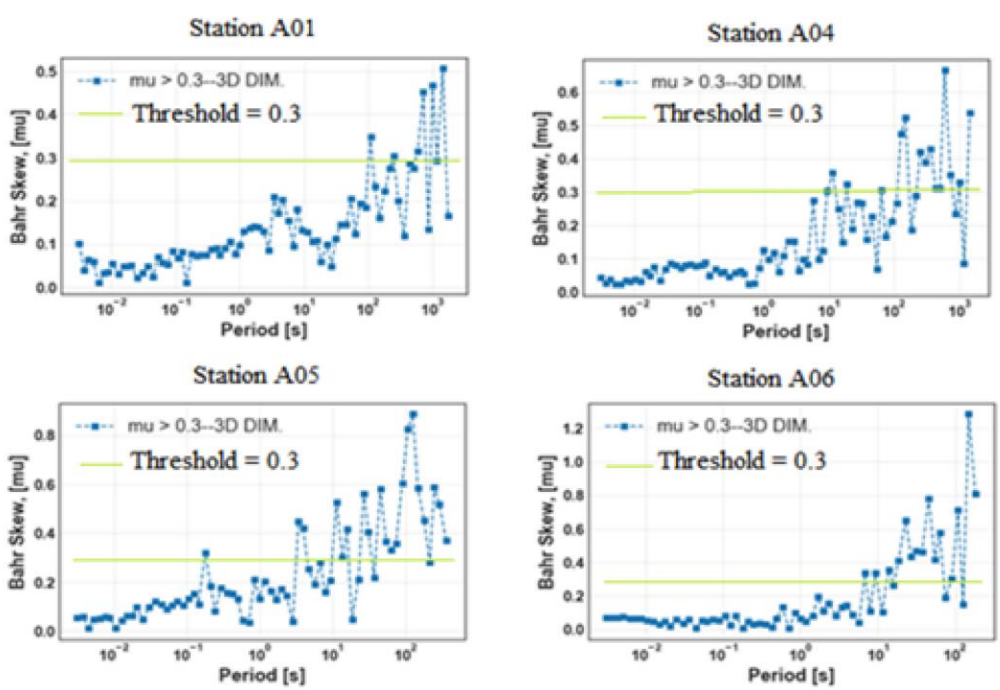

Figure 3.3 The Bahr's phase-sensitive skew plot for stations A01, A04, A05, and A06

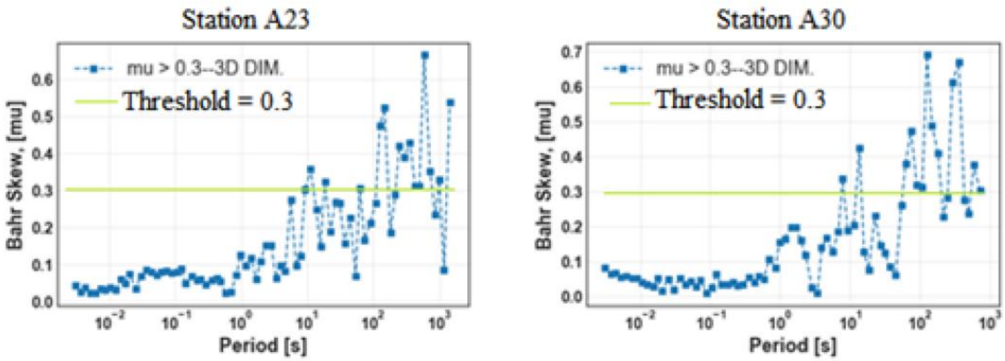

Figure 3.4 The Bahr's phase-sensitive skew plot for stations A23 and A30

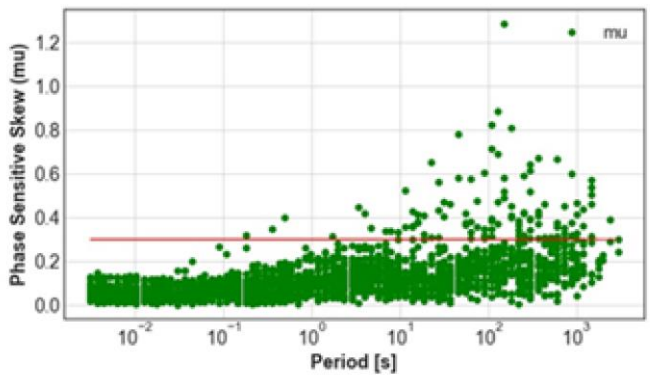

Figure 3.5 The Bahr's phase-sensitive skew plot of the Ashute geothermal field for all stations

The value of η is comparable to a swift, with low values near zero (below 0.3) for short periods (< 10 s), suggesting a 1D or 2D nature at shallow depths. Conversely, high values above the threshold for longer periods (> 10 s) indicate 3D characteristics at greater depths. The expected value estimator for η in the 1D, 2D, and 3D/2D cases is skewed. As the noise level rises, the η value also increases, while it decreases for low noise levels. The η value is influenced by the noise level. (Chave & Jones, 2012).

3.4.1.3 Phase Tensor Analysis

The phase tensor analysis method, created by Caldwell et al. in 2004, serves as a tool for obtaining information about the regional dimensionality structure in cases where the phase tensors are not affected by galvanic distortion, It can be graphically represented as ellipses (Booker, 2014). The ratio of the real (X) to the imaginary (Y) sections of the complex tensor of impedance, Z, is called the phase tensor (Φ).

$$\varphi = X^{-1}Y \quad (3.16)$$

$$Z = X + iY \quad (3.17)$$

The observed impedance $Z = CZ_R$, if galvanic distortion is present, where C is the distortion tensor, and $Z_R = X_R + iY_R$ is the regional impedance. As a result, the distorted real part $X = CX_R$, and the distorted imaginary part as $Y = CY_R$ can be written. The regional and observed phase tensors are the same and free of galvanic distortion, according to the following correlations:

$$\varphi = {X_R}^{-1}Y = (CX_R)^{-1}(CY_R) = {X_R}^{-1}C^{-1}CY_R = {X_R}^{-1}Y_R = \varphi_R \tag{3.18}$$

In the case of phase tensor, which is a 2nd rank tensor can be described as

$$\varphi = \begin{pmatrix} \varphi_{xx} & \varphi_{xy} \\ \varphi_{yx} & \varphi_{yy} \end{pmatrix} \tag{3.19}$$

The phase tensor elements can be given by

$$\begin{pmatrix} \varphi_{xx} & \varphi_{xy} \\ \varphi_{yx} & \varphi_{yy} \end{pmatrix} = \frac{1}{\det(X)} \begin{pmatrix} X_{yy}Y_{xx} - X_{xy}Y_{yx} & X_{yy}Y_{xy} - X_{xy}Y_{yy} \\ X_{xx}Y_{yx} - X_{yx}Y_{xx} & X_{xx}Y_{yy} - X_{yx}Y_{xy} \end{pmatrix} \tag{3.20}$$

where $\det(X) = X_{xx}X_{yy} - X_{xy}X_{yx}$is the determinant of X.

Caldwell et al. (2004) defined three tensor invariants, namely the trace, determinant, and skew, using the matrix of phase tensors in Equations (3.21), 3.22), and (3.23).

$$\varphi_1 = \frac{\varphi_{xx} + \varphi_{yy}}{2} \quad \text{Trace} \tag{3.21}$$

$$\varphi_2 = \varphi_{xx}\varphi_{yy} - \varphi_{xy}\varphi_{yx} \quad \text{Determinant} \tag{3.22}$$

$$\varphi_3 = \frac{\varphi_{xy} - \varphi_{yx}}{2} \quad \text{Skew} \tag{3.23}$$

The coordinate invariants defined by Caldwell et al. (2004) comprise the skew angle (β), the maximum (φ_{max}) and the minimum (φ_{min}) principal phase, (Figure 2.6) and the azimuthal angle (α) . Thus, the four invariants of an ellipse are given by

$$\varphi_{min} = ({\varphi_1}^2 + {\varphi_3}^2)^{1/2} - ({\varphi_1}^2 + {\varphi_3}^2 - {\varphi_2}^2)^{1/2} \tag{3.24}$$

$$\varphi_{max} = ({\varphi_1}^2 + {\varphi_3}^2)^{1/2} + ({\varphi_1}^2 + {\varphi_3}^2 - {\varphi_2}^2)^{1/2} \tag{3.25}$$

$$\beta = \frac{1}{2}\tan^{-1}\left(\frac{\varphi_3}{\varphi_1}\right) = \frac{1}{2}\tan^{-1}\left(\frac{\varphi_{xy} - \varphi_{yx}}{\varphi_{xx} + \varphi_{yy}}\right) \tag{3.26}$$

$$\alpha = \frac{1}{2}\tan^{-1}\left(\frac{\varphi_{xy} + \varphi_{yx}}{\varphi_{xx} - \varphi_{yy}}\right) \quad (3.27)$$

where α is the angle formed between the coordinate axes and the reference axes.

The principal or singular values of, φ, α, and β, which describe the phase tensor, can be represented as expressed by $\varphi_{max}$and φ_{min} are given by:

$$\varphi = R^{T}(\alpha - \beta)\begin{bmatrix}\varphi_{max} & 0 \\ 0 & \varphi_{min}\end{bmatrix}R(\alpha + \beta), \quad (3.28)$$

Here R^T represents the transposed or inverse of the rotation matrix, while $R(\alpha + \beta)$ represents the rotation matrix.

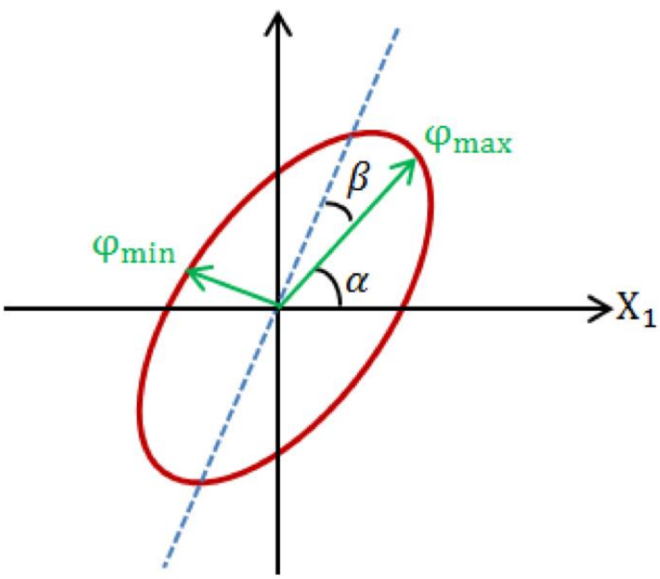

Figure 3.6 An elliptical illustration of the MT phase tensor graphically. The lengths of the semi-major and semi-minor axes of the ellipse are proportional to the principal values φ_max andφ_min. The skew angle is a third coordinate invariant used to characterize a non-symmetric tensor. The observer's reference frame (X_1, X_2) is used to calculate the tensor's relationship. The angle (α), determines the direction of the ellipse's principal axis. (Redrawn from Caldwell et al., 2004)

Bibby et al. (2005) defined ellipticity (λ) as a dimensionality metric as follows:

$$\lambda = \frac{\left[(\varphi_{xx} - \varphi_{yy})^2 + (\varphi_{xy} + \varphi_{yx})^2\right]^{1/2}}{\left[(\varphi_{xx} + \varphi_{yy})^2 + (\varphi_{xy} - \varphi_{yx})^2\right]^{1/2}} \quad (3.29)$$

The principal values of the phase tensor are identical to its eigenvalues if the phase tensor is symmetric (β=0), implying that the regional conductivity distribution is mirror-symmetric (Caldwell et al., 2004). This occurs for 1D or 2D regional distribution. The phase tensor of the 1D structure has a circular shape ($\varphi_{max} = \varphi_{min}$) with the values $\beta = 0$ and $\lambda = 0$. The phase tensor is depicted as an ellipse that is lower to extremely small, approaches zero (β = ± 3 degrees), and the principal values of a 2D regional structure of resistivity are usually unique ($i.e\ \varphi_{max} \neq \varphi_{min}$) with value 0. The phase tensor ellipse, on the other hand, has a part of its principal axes in the direction of the strike. Whereas the non-symmetric phase tensor has a considerable skew angle (β). An alternative sign of a 3D structure is a quick lateral variation in the major axis when a 3D structure is present. As a result, all of the invariants, namely $\beta \neq 0, \lambda \neq 0, \varphi_{max} \neq 0\ and\ \varphi_{min} \neq 0$, are non-zero when assuming a 3D structure.

Figures (3.8), (3.9), and (3.10) depict phase tensor maps at various frequencies in the Ashute geothermal field that indicate the dimensionality of MT data. The 1D symbol occurs at 320, 50, and 9.4 Hz, and has a small skew angle (-3 3) the phase tensor is circular in shape, as illustrated in Figure 3.7. Figure 3.8 shows that 2D structures viewed near and less than 0.215 Hz have a small skew angle and an elliptical phase tensor. The phase tensor analysis result, as shown in Figure 3.9, reveals 3D. At 0.0088, 0.00275, and 0.0011 Hz are indicated as the deeper structures with large skew angles. Consequently, the phase tensor analysis at shallow depths shows dimensionality of 1D and 2D, and high skew angles at deeper depths described 3D effects below 0.011 Hz.

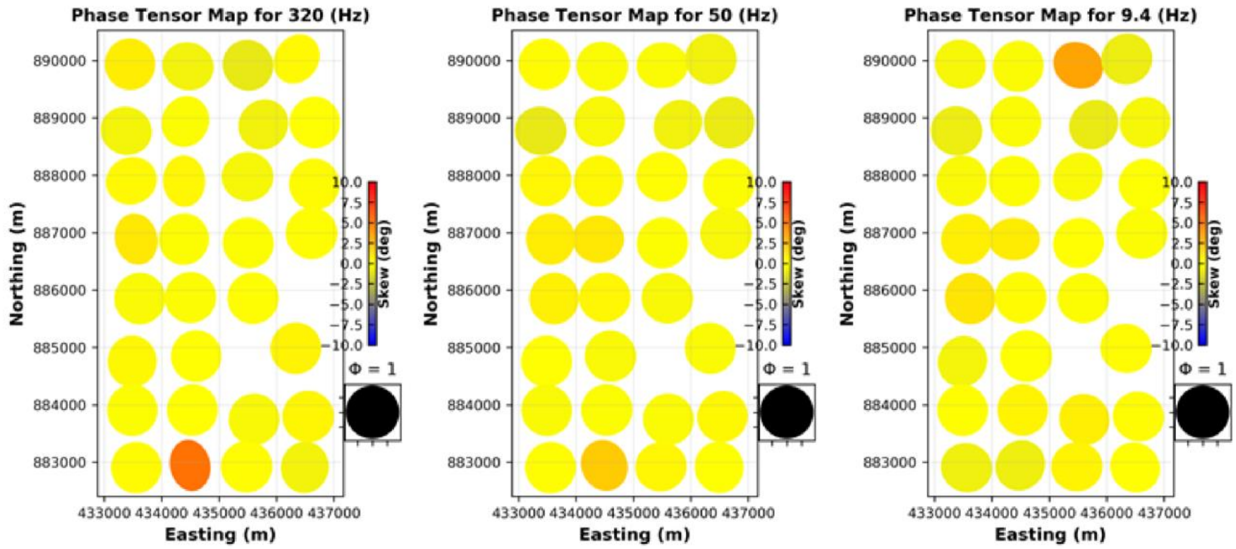

Figure 3.7 The maps of Phase tensors at 320, 50, and 9.4 Hz respectively.

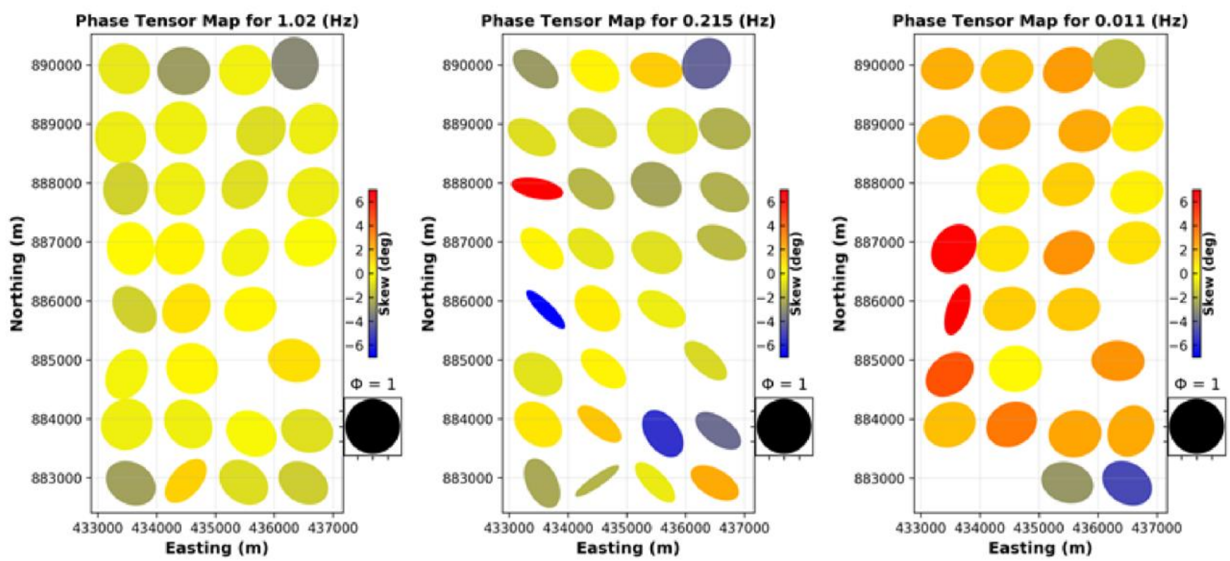

Figure 3.8 The maps of the Phase tensor at 1.02, 0.215, and 0.011Hz respectively.

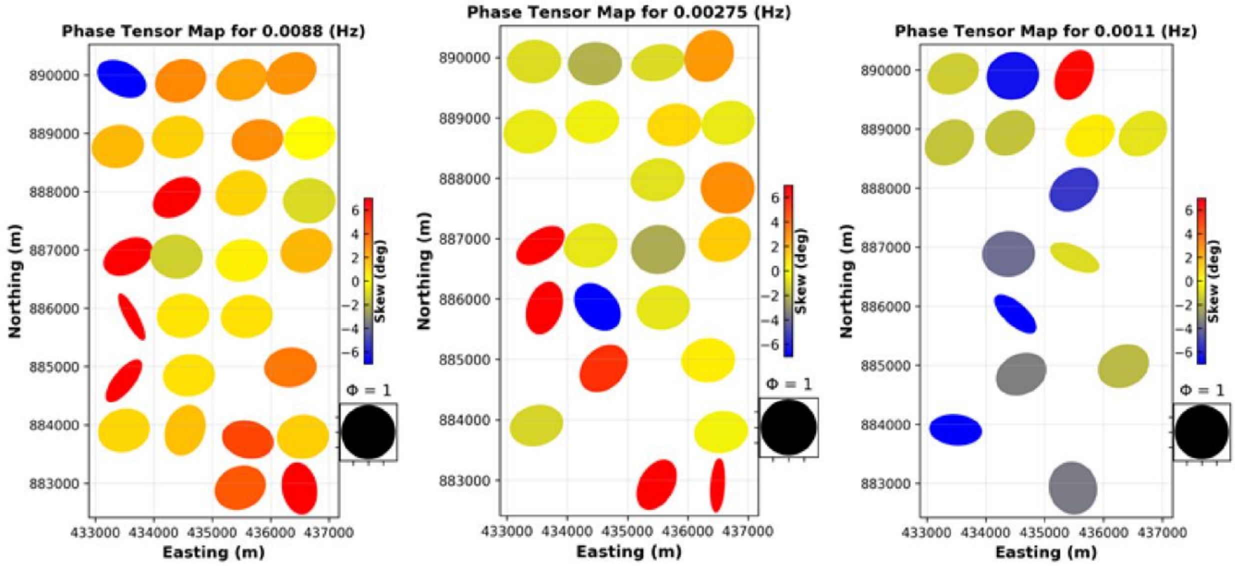

Figure 3.9 The maps of the Phase tensor at 0.0088, 0.00275, and 0.0011 Hz respectively.

3.4.2 Strike Angle estimation

In the 2D Earth condition, resistivity varies in one horizontal direction with depth, while it remains constant in another horizontal direction. The direction in which the resistivity remains constant is mentioned as a geoelectric strike. In the case of MT data with a 2D or 3D/2D structure, the direction of geoelectric strike calculation is established correctly. Despite the noise and local distortion, the analysis of geoelectric strike for MT data estimates the strike of the 2D major geo-electrical structure. The striking angle is usually the most unstable parameter that can be inferred from MT data (Groom et al., 1993; Jones & Groom, 1993).

The most frequent formulation for geoelectric strike estimate is to minimize the diagonal elements and maximize the squares off-diagonal elements of the MT tensor, using these elements of the sum of the square modulus (Swift, 1967; Vozoff, 1972; Simpson & Bahr, 2005). This leads to the Swift angle (Swift, 1967), which is known as strike angle α and it is expressed as:

$$\tan(\alpha) = \frac{(Z_{xx} - Z_{yy})(Z_{xy} + Z_{yx}) + (Z_{xx} + Z_{yy})(Z_{xy} - Z_{yx})}{(Z_{xx} - Z_{yy})^2 - (Z_{xy} + Z_{yx})^2} \qquad (3.30)$$

Bahr (1988) proposed a phase-based strike angle estimator. A phase-sensitive strike is a rotating 2D regional structure of the response tensor into the strike direction produced using the Bahr model and provided by

$$\tan(2\theta_B) = \frac{[S_1, S_2] - [D_1, D_2]}{[S_1, D_1] + [S_2, D_2]} \qquad (3.31)$$

where $S_1, S_2, D_1 and\ D_2$ are given by Equation (4.31) and known as modified impedances. The function [x, y] is taken to mean $[x, y] = \Re_x\Im_y - \Im_x\Re_y$ (Simpson & Bahr, 2005).

The strike estimation proposed by Groom and Bailey (1989) is the more stable and most widely used technique. The Groom and Bailey strike estimator is unbiased even in the presence of noise associated with other estimators Chave & Jones, 2012). McNeice and Jones (2001) developed STRIKE, a program based on the Groom and Bailey decomposition, which provides a more stable estimate of the strike.

For the Ashute data, the phase tensor (Caldwell et al., 2004)and rotational invariant (Weaver et al., 2000) approaches were utilized to estimate the strike angle using an open-source Python program (MTpy) for all data (Krieger & Peacock, 2014). The phase tensor method is resistant to galvanic distortions and is the preferred method for strike estimation. In the case of the Ashuite data, strike angle estimation was conducted using rotational invariants and WAL invariants (Weaver et al., 2000) as shown in Figure 3.10. TThe estimates of the strike angle are widely dispersed for shorter periods (<1s), suggesting an influence from the local shallow structure. However, for longer periods (1 – 10s), there is a consistent strike direction of 125 degrees within the dataset. This estimate of 125 degrees is not entirely consistent with the main NNE-SSW fault system in the Ashute field, and it may be influenced by the pre-existing NW-SE basement structures within the period of 1s to 10s. A negative gravimetric anomaly throughout the MER floor between 7^0N and 8^0N latitudes revealed a pre-existing NW-SE striking subsurface graben packed with low-density sediments (Korme et al., 2004). Before performing the two-dimensional inversion, the impedance components are rotated N125W.

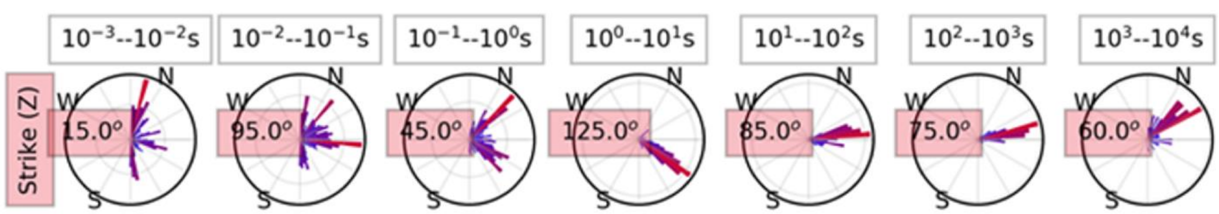

Figure 3.10 The strike estimates for the Ashuite geothermal field using rose diagrams.

In the case of a 2D geoelectrical structure, the phase tenser's principal axes are aligned with the strike of the regional conductivity structure (Caldwell et al., 2004). The phase tenser principal axes are oriented along the direction of the geoelectric structure in the Ashute geothermal field, as illustrated in Figure 3.11 at a period of 10-100 sec, according to the analysis of MT data.

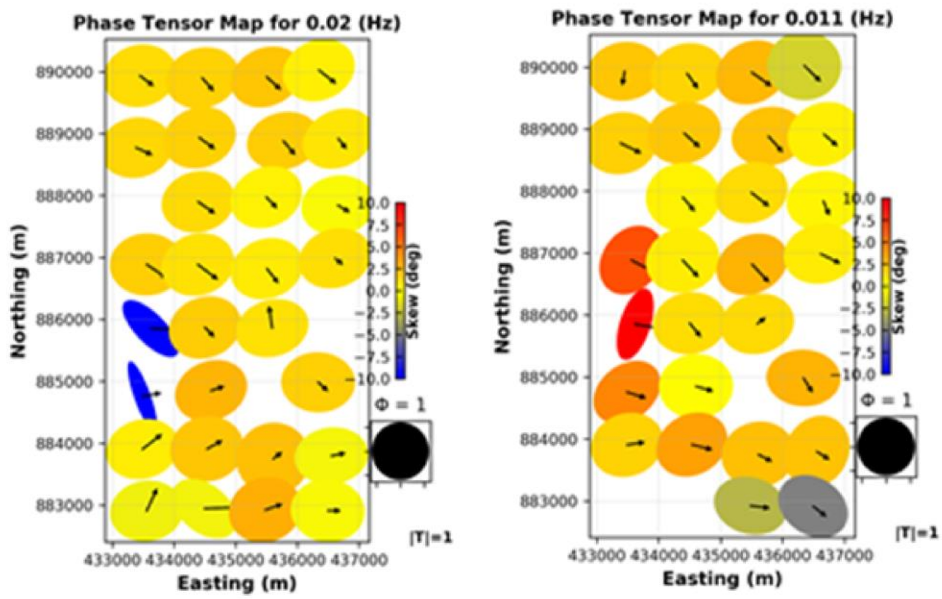

Figure 3.11 The map depicts all stations at the 50s (0.02HZ) and 90.9s (0.011HZ) periods of tipper vectors, and phase tensor ellipses (plotted according to Parkinson convention). The strike direction of S55E is supported by the orientation of the phase tensor ellipse

The phase tensor's principal axes reveal the horizontal directions of the strongest and weakest induction currents, which imply lateral differences in the underlying regional conductivity (Caldwell et al., 2004). The regional conductivity structure's geoelectric strike axis is aligned with the phase tensor's principal axes, representing the existence of a 2D regional structure. The alignment of the principal axes, like the induction arrows related to the deep conductor, indicates the optimal inductive current flow direction. The tippers that developed as described by a forward model were seen and placed restrictions on the possibility of melting within MER (Samrock et al., 2015). It's worth noting that the tippers suggest an elongated NW-SE highly conductive structure that can be found about 5-10 kilometers east of the Ashute geothermal zone.

3.5 Overview of inversion

Geophysical inverse problems frequently involve retrieving information about subsurface physical parameters (magnetic susceptibility, density, electrical conductivity, and so on) from observable geophysical data (Menke, 1984, 1989, 2018; Oldenburg, 2005; Zhdanov, 2002). In order to accomplish this, it discretizes the Earth into a vast number of discrete elements, then uses regularization and the governing partial differential equations to create a model that both fits the data and complies with a priori restrictions. In MT inversion, subsurface resistivity patterns are calculated from the surface-measured natural electric and magnetic field variations (Zhdanov, 2002). Inversion solutions often assume a beginning model, compute the theoretical geophysical response from the starting model, and compare the results with the data (Guillen et al., 2010). This iterative inversion approach seeks to discover one or more resistivity models whose predicted response best matches the observed data. Based on the type of inversion algorithm used in geophysics, a damping factor or regularization parameter is applied to minimize the error vector and stabilize the inversion process, as outlined by Xiang et al. in 2017. An objective function that describes the data misfit is minimized by a suitable optimization procedure (Godio & Santilano, 2017; Oldenburg, 2005). The final iteration of the estimated model is recognized as the solution of the inversion and signifies the geological structure. Forward modeling is the central importance of any inversion method and hence must be fast, accurate, and reliable

The geological model can be characterized by a finite number of discrete parameters, as indicated by Lei et al., 2017 and Menke 1989. It is important to note that model parameters described by a continuous function are not excluded, as continuous parameter distributions can be resolved by a finite number of parameters through the use of an appropriate discretization scheme, as demonstrated by Menke in 1984, 1989, and 2018.

The inverse models of the Earth assume that discretized into a series of constant blocks as the column vector of M number of model parameters (Menke, 1984, 1989), $m = [m_1, m_2, \dots m_M]^T$. There are N observed data with a column vector of N elements $d = [d_1, d_2, \dots d_N]^T$, having the corresponding uncertainties $e = [e_1, e_2, \dots e_N]^T$. The inverse problem can be formulated by using the observed data d with the theoretical model responses $F(m)$ can be expressed as

$$d = F(m) + e \qquad (3.32)$$

where d is a vector that contains the conductivity, phase, apparent resistivity, and other data space components such as the magnetotelluric transfer function. The model space m reflects the Earth's real resistivity values, while F is a forward function forecasting the theoretical values of the data for a hypothetical (model) representation of the Earth. In the theoretical case e = 0, the solution to Equation (3.32) becomes $m = F^{-1}(d)$, hence the term inverse problem.

$$\hat{m} = G(d) \qquad (3.33)$$

Here G is a meaningful substitute for F^{-1}.

The geophysical inverse theory relies on the least-squares estimation (Chave & Jones, 2012; Menke, 1984, 1989, 2018). Finding the minimal solution of a fitting function and determining the degree of goodness of fit between the model and the observed data is known as a least-squared solution.

This data misfit of a penalty function can be expressed by

$$\Phi_d(\mathbf{m}) = \left(\mathbf{d} - \mathbf{F}(\mathbf{m})\right)^{\mathrm{T}} \mathbf{W}\left(\mathbf{d} - \mathbf{F}(\mathbf{m})\right) \qquad (3.34)$$

where W is the weight matrix is the inverse of the covariance matrix of the data $\left(W = {C_d}^{-1}\right)$ (Egbert & Kelbert, 2012; Menke, 1984, 2018; Siripunvaraporn & Sarakorn, 2011), and the residual vector is r = d −F (m). Minimizing $\Phi_d(m)$ is done by starting from some initial model and iteratively solving the inverse problem until a predefined data misfit is reached. According to Menke (1989, 2018) a least square objective function Equation (3.34) of a linearised inverse problem, can be minimized by taking its derivative with respect to m_j and setting the result to zero. However, the MT forward operator F is non-linear due to the nature of the product relation between the EM fields and conductivity in Maxwell's equations (Equations (2.30) and (2.31)) defining it, i.e., $F(am_1 + bm_2) = aF(m_1) + bF(m_2)$ cannot be satisfied for arbitrary real numbers a and b (Chave and Jones, 2012; Beka, 2016). **F** can be linearised through Taylor expansion about some trial model m_k, gives the following approximation (F) is made using the first two terms:

$$\acute{\mathrm{F}}_{(\mathrm{m})} = \mathrm{F}_{(\mathrm{m_k})} + \frac{\partial \mathrm{F}(\mathrm{m_k})}{\partial \mathrm{m_k}}(\mathrm{m} - \mathrm{m_k}) = \mathrm{F}(\mathrm{m_k}) + \mathrm{J}\delta\mathrm{m} \qquad (3.35)$$

In Equation (3.35), $\delta\mathrm{m} = \mathrm{m} - \mathrm{m_k}$ are small perturbations in the model, J is the Jacobian or the sensitivity matrix of N x M partial derivatives $\frac{\partial \mathrm{F(m)}}{\partial \mathrm{m_J}}$, where i= 1,2….N & j =1,2,…,M. The Jacobian describes the sensitivity of the predicted data due to the small perturbation in the model. The following solution of Equation (3.36) is obtained from the linearised form of F (Equation (3.35)) and minimizing Equation (3.34) (e.g., Beka, 2016; Chave & Jones, 2012; Menke, 1989, 2018; Meqbel, 2009):

$$\delta\mathbf{m} = (\mathbf{J}^{\mathrm{T}}\mathbf{J})^{-1}\mathbf{J}^{\mathrm{T}}\mathrm{r}, \qquad (3.36)$$

where r =. Equation (3.36) is obtained using the Taylor approximated F (Equation (3.35)). It is the Gauss-Newton solution of the unconstrained least square problem. Iterative methods can optimize the solution. But in most MT data inversion schemes, Equation (3.36) doesn't have a unique solution (Chave & Jones, 2012), especially in least squares for finite-dimensional inverse problems where the number of model parameters (N) is much larger than the data parameters

(M). To address the ill-posed nature, a constraint can be imposed on the objective function to find a stable and regularized solution ("Solutions of Ill-Posed Problems," 1977): The optimization process minimizes the following objective function:

$$\Phi_{\mathrm{m}} = \Phi_{\mathrm{d}}(\mathrm{m}) + \lambda\Omega(\mathrm{m}) \tag{3.37}$$

where λ is the trade-off parameter (also known as the regularization parameter) that "regularizes" or balances the impacts of the two terms, $\Omega(\mathrm{m})$ represents the model roughness, and $\Phi_{\mathrm{d}}(\mathrm{m})$ is a measure of data misfit. For large values of λ emphasis on model smoothness and the data, misfit is less important, whereas for a small λ puts more weight on fitting the data. Thus an optimal λ should be chosen to maintain adequate data fit without compromising model roughness. This kind of objective function is often also called Tikhonov regularized penalty function.

The stabilizing function described by (Chave & Jones, 2012; Leeuwen, 2016) is defined as

$$\Omega(\mathbf{m}) = (\mathbf{m} - \mathbf{m}_0)^{\mathrm{T}}\mathrm{K}(\mathbf{m} - \mathbf{m}_0) \tag{3.38}$$

where m_0 denotes the beginning or starting model, and $\left(\mathrm{K} = \mathrm{C_m}^{-1}\right)$. represents the penalty K's structure, which can be understood as an inverted a priori model covariance matrix.

Equation (3.37) is the damped least-squares functional, and the regularized objective function is obtained by inserting Equations (3.34) and (3.38) into it.

$$\Phi(\mathrm{m}) = \left(\mathbf{d} - \mathbf{F}(\mathbf{m})\right)^{\mathrm{T}}\mathbf{C}_{\mathrm{d}}{}^{-1}\left(\mathbf{d} - \mathbf{F}(\mathbf{m})\right) + \lambda(\mathbf{m} - \mathbf{m}_0)^{\mathrm{T}}\mathbf{C}_{\mathrm{m}}{}^{-1}(\mathbf{m} - \mathbf{m}_0) \tag{3.39}$$

The majority of the electromagnetic inversion algorithms try to minimize the damped least squares functional of Equation (3.39) efficiently by utilizing different approaches (Leeuwen, 2016).

3.5.1 Occam approach for a linearized problem

The minimizing of regularized objective function $\Phi(\mathrm{m})$ in the vicinity of $\mathrm{m_k}$ for small perturbations $\Delta\mathrm{m}$ leads to M x M system of normal equations

$$\left(\mathbf{J}^{\mathrm{T}}\mathrm{C_d}^{-1}\mathbf{J} + \lambda\mathrm{C_m}^{-1}\right)\Delta\mathbf{m} = \mathbf{J}^{\mathrm{T}}\mathrm{C_d}^{-1}\left(\mathbf{d} - \mathbf{F}(\mathbf{m}_{\mathrm{k}})\right) - \lambda\mathrm{C_m}^{-1}(\mathbf{m}_{\mathrm{k}} - \mathbf{m}_0) \tag{3.40}$$

Equation (3.40) can be solved for Δm as a trial solution $m_{k+1} = m_k + \Delta m$. The linearized scheme generally requires a damped least square problem for stability (e.g. a Levenberg–Marquardt approach; (e.g. a Levenberg–Marquardt approach; Beka, 2016; Egbert & Kelbert, 2012; Marquardt, 1963; Rodi & Mackie, 2001) which can be improved iteratively. Several techniques are used to solve Equation (3.40) for magnetotelluric data with different λ to minimize the data misfit until reaches the desired station level (Parker, 1994).

In the Occam approach (Constable et al., 1987), an iterative sequence of approximate solutions for Equation (3.40) is expressed through:

$$\mathbf{m}_{k+1}(\lambda) = \mathbf{m}_k + \Delta\mathbf{m} = \left(\mathbf{J}^{T}\mathbf{C}_d{}^{-1}\mathbf{J} + \lambda\mathbf{C}_m{}^{-1}\right)^{-1}\mathbf{J}^{T}\mathbf{C}_d{}^{-1}\mathbf{d}_k + m_0 \tag{3.41}$$

where $d_k = d - F(m_k) + J(m_k - m_0)$. As discussed in Parker (1994), the Occam procedure indeed involves a two-step process: first, reducing the misfit to the desired level, and then, while maintaining the misfit at that level, achieving a small model norm by varying the trade-off parameter λ. In each iteration, the trade-off parameter serves to control step length and act as a smoothing parameter.

3.5.2 One-dimensional MT inversion

Numerous methods have been used to solve the 1D inversion of magnetotelluric data (Constable et al., 1987; Fischer & Le Quang, 1982; Parker, 1980). While the Earth is believed to be made up of a stack of homogeneous layers in some inversion methods, resistivity changes continuously with depth in other approaches. The inversions use a variety of algorithms, depending on the kind of model. Using Marquardt-Levenberg and Occam's inversion techniques, 1D inversion of MT data in the central main Ethiopian rift was performed in this work. The smoothest model that fits the measured data set within predefined boundaries is found using Occam's inversion approach (Constable et al., 1987). For parameter fitting, the Marquardt-Levenberg method, often known as ridge regression, is dependable and effective. It has been extensively used to interpret geoelectrical data (e.g., Inman, 1975; Petrick et al, 1977).

3.5.2.1.1 MT 1D Inversion using Marquardt-Levenberg method

The Marquardt-Levenberg inversion method was first presented by Levenberg (1944), however, Marquardt provided a more thorough description of it in 1963. Ridge regression and damped least squares regression are other names for this technique. Model parameters have been estimated and geophysical issues have been solved using the Marquardt-Levenberg approach (Inman, 1975; Petrick et al, 1977). The ridge regression estimator is more stable than the generalized linear inverse estimator, and it produces a better estimate of the unknown parameters than the least squares approach (Inman, 1975; Marquardt, 1963). Nonlinear least-squares methods (e.g., Marquardt-Levenberg) work well for inverting geophysical model responses since many of them are nonlinear functions of the model parameters (Lines & Treitel, 1984). The Marquardt-Levenberg approach is a powerful method for interpreting resistivity soundings over planar multilayered structures that is based on the minimization of the following cost function, S (m) (Levenberg, 1944; Marquardt, 1963):

$$S(\Delta\mathbf{m},\lambda) = [\mathbf{D} - \mathbf{F}(\mathbf{m})]^{\mathrm{T}}[\mathbf{D} - \mathbf{F}(\mathbf{m})] + \lambda, \quad (3.42)$$

In the given equations, D and F(m) represent the model responses and the observations, respectively, while Δm represents the model update. The data misfit is depicted by the first term on the right side of the equation, with λ denoting the damping factor (Lagrange multiplier). Equation (3.42) provides the solution for model update minimization

$$\Delta\mathbf{m} = (\mathbf{J}^{\mathrm{T}}\mathbf{J} + \lambda\mathbf{I})^{-1}\mathbf{J}^{\mathrm{T}}\mathrm{g}, \quad (3.43)$$

where I is the identity matrix, J represents the Jacobian, and g is the discrepancy vector, indicating the difference between the initial model response and the observed data.

For the 1D MT inversion in the central main Ethiopian rift, the Marquardt-Levenberg algorithm was utilized to invert the collected MT data. In the inversion process, an initial model (m_0) of the subsurface is assumed, and the program conducts forward modeling to compute the model response based on the starting model parameters. The Marquardt-Levenberg algorithm is used to iteratively minimize the error between the observed and model responses in the least squares sense until a suitable fit for the observation within the convergence criteria is achieved.

The effective apparent resistivity, a rotationally invariant calculated from the impedance tensor elements (Ranganayaki, 1984; Vozoff, 1991) is determined in this study through 1D inversion of MT data in the form of the determinant mode of the apparent resistivity (ρ_d) using the following formula.

$$\rho_{\mathrm{d}} = \frac{1}{\mu_0\omega}\left(Z_{xx}Z_{yy} - Z_{xy}Z_{yx}\right) \quad (3.44)$$

A Python program is used to create the necessary input file, which contains the MT observation and initial model for inversion. The initial model utilized for 1D inversion is a four-layer model applied to all stations. This initial model assumption was based on drilling data from the research area and the observed trend of the apparent resistivity curves. It is designed with a damping factor, λ, set to a value of 10. Although the program's maximum iteration is set to 100, all inversions cease before reaching the maximum. The RMS misfit and fitting of observed and estimated models were examined during the inversion phase before the 1D models were accepted. The Marquardt-Levenberg technique minimizes the error between observed and model responses iteratively in the least squares sense until the observation fits within the convergence requirements.

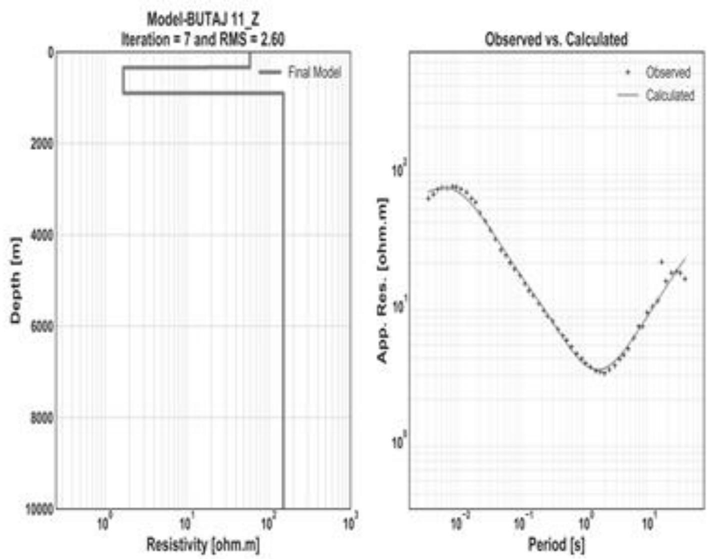

Figure 3.12 1D model and misfit curves at station B11 using Marqaurdt-Levenberg.

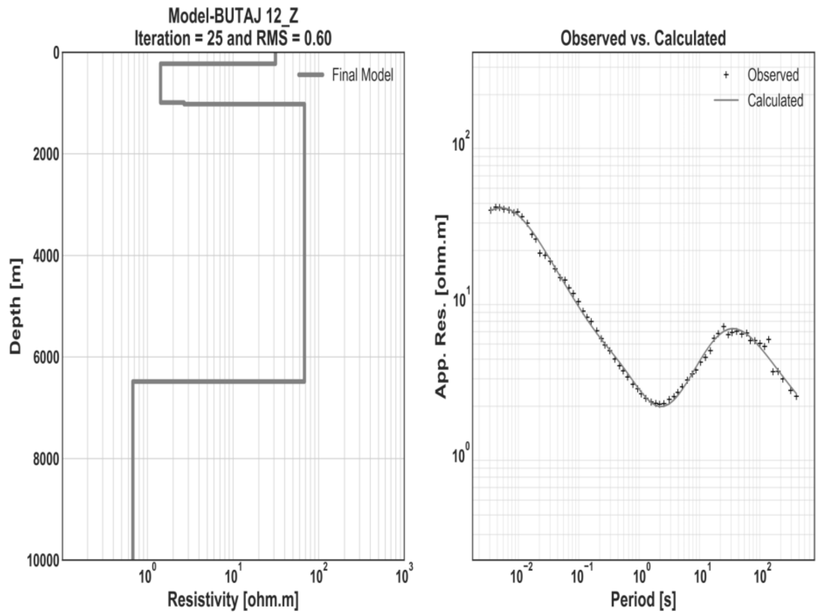

Figure 3.13 1D model and misfit curves at station B12 using Marqaurdt-Levenberg.

The Marquardt inversion was used to create 1D models of the Adamitul-Western margin of the rift (near Butajira) for 21 stations and Ashute geothermal 30 stations inverted using the Marquardt-Levenberge algorithm. Figures 3.12 and 3.13 show the 1D inversion models and misfit observed vs calculated) for some selected stations in the Ashute geothermal field.

This ridge regression estimator is more stable than the generalized linear inverse estimator that was advocated in a previous paper (Inman, 1975).

3.5.2.2 MT 1D Inversion using OCCAM

Finding a conductivity model that fits a given data set is the inverse problem, and solutions to this problem are well-defined in the literature on electromagnetic (EM) geophysics (Zhdanov, 2002). Because a particular data collection is finite and imperfect, an endless number of solutions to the inverse problem exist. To uncover features that emerge in the model, the smoothing model that fits the magnetotelluric (MT) data is obtained using Occam inversion (Constable et al., 1987). The model investigations here employ Occam's inversion approach (Constable et al., 1987), which finds the smoothest model that fits the data in order to solve the regularized problem. The value of this method is that the model that corresponds to features that are well constrained by the data commonly produces smooth peaks, whereas features not constrained by the data will be smoothed over or absent in the model. The optimal minimize the functional regularized inverse problem (Constable et al., 1987)

$$U = \|\partial \mathbf{m}\|^2 + \|\mathbf{P}(\mathbf{m} - \mathbf{m}_*)^2\| + \mu^{-1}\{\mathbf{W}\|\mathbf{d} - \mathbf{F}(\mathbf{m})\|^2 - X_*{}^2\}, \tag{3.45}$$

where **P** is a diagonal matrix, **m** is the model, $\mathbf{m}_*$ is the prior model, μ is Lagrange multiplier, **W** is the data covariance weighting function, **d** is the observed data, **F**(**m**) is the forward operator, X is the desired misfit.

Applying a differencing operator ∂ to the elements of the model vector m yields the first term in the equation, which reflects the norm of the model roughness. The model update is represented by the second term. Scaling factors that establish the relative weighting of preference and model roughness are contained in the diagonal matrix P. The trade-off between the model's roughness and preference and the data fit is balanced by the Lagrange multiplier μ^{-1} .

The relative contribution of each datum to the misfit is weighted according to its uncertainty by the data covariance weighting function, W. As a result, large error data are scaled to reduce their impact, but small mistake data will increase the misfit budget (Key, 2009).

The targeted misfit is expressed as an expression X^2, and the presence of it shows that finding a smooth model that falls within the designated target misfit rather than the best-fitting model is what is meant to be found while minimizing U.

By taking the derivative with respect to m and setting it to zero, one can typically minimize U. Since F(m) has a nonlinear derivative in electromagnetics, the equation that results must be solved repeatedly by building a series of models, each of which progressively improves the fit to the data. Once a first model has been linearized, the formula for the subsequent model in the series m_{k+1}

$$\mathbf{m}_{k+1} = [\mu(\partial^T \partial + \mathbf{PP}) + (\mathbf{W}J_k)^T\mathbf{W}\mathbf{J}_k]^{-1}[(\mathbf{W}\mathbf{J}_k)^T\mathbf{W}\mathbf{d} + \mu\mathbf{P}\mathbf{m}_*], \tag{3.46}$$

Where m_{k+1} is the iteration k is the iteration number, p is the diagonal matrix, m_* is the prior model, μ is Lagrange multiple, W is the data covariance weighting function, d is data, and J is the Jacobian.

The target misfit is usually chosen so that the root mean square (RMS) misfit (x_{rms}) is equal to unity:

$$X_{rms} = \sqrt{\frac{X^2}{n}} = \sqrt{\frac{1}{n}\sum_{i=1}^{n}\left(\frac{d_i - F_i(m)}{s_i}\right)^2} \qquad (3.47)$$

The number of data points is represented by n, and si denotes the standard error of the ith data point. More detailed explanations of Occam can be found in (Constable et al., 1987; DeGroot-Hedlin, C., and Constable, 1990; Key, 2009).

The program OCCAM1DCSEM, developed at the Scripps Institution of Oceanography, University of California, San Diego (Key, 2011), was used for 1D inversion in the Ashute geothermal field and from Adami Tulu to the Western margin of the rift. OCCAM1DCSEM is a free Fortran program created to produce smooth 1D models from CSEM and MT data. This program is particularly useful for geophysical research and exploration in the specified areas.

3.5.3 Joint 1D inversion of TEM and MT soundings

The joint inversion of the EM data to correct for static shifts in the MT data is an important step in addressing the potential challenges arising from large near-surface resistivity contrasts. In this process, a model is obtained by performing one-dimensional joint inversion simultaneously for both TEM and MT data, with the aim of resolving static shift issues by fitting both data sets. The TEMTD program was used to invert TEM and MT data jointly and separately for one dimension. The program responsible for this was developed by Kntur Árnason of ÍSOR *(Árnason, 2006)*and it effectively achieves this through the use of an algorithm that determines the appropriate shift factor to constrain the MT data to fit the TEM response. This approach is valuable for mitigating the impact of static shifts and improving the overall accuracy of the inversion results. Inversions of minimum structure (Occam) can also be performed with the program (Constable et al., 1987). For the rotationally invariant determinant apparent resistivity and phase of the Ashute area and the traverse along SDFZ-Aluto, a joint 1D Occam inversion was performed over all of the MT soundings and TEM soundings at the same sites applied for 1D data. It is one-of-a-ki, and it's unaffected by strike direction (Árnason, 2015). Determinant data is chosen because it is rotationally invariant and averages out all of the data's "dimensionality".

3.5.4 Two-dimensional Inversion

The widely used two-dimensional MT theory and inversion algorithms are well-developed (DeGroot-Hedlin, C., and Constable, 1990; Jupp & Vozoff, 1977; Ogawa, 2002; Ogawa &

Uchida, 1996b; Rodi & Mackie, 2001; Siripunvaraporn & Egbert, 2000). The main algorithms used for 2D inversion are Occam inversion, the Gauss–Newton method, and the nonlinear conjugate gradient method.

The 2D inversion-modeling Occam's 2D inversion code program used in this study was developed by the Scripps Institution of Oceanography based on the work of DeGroot-Hedlin, C., and Constable (1990). Occam's 2D inversion is founded on the minimization of an unconstrained functional.

$$U = \left\|\partial_y \mathbf{m}\right\|^2 + \|\partial_z \mathbf{m}\|^2 + \mu^{-1}\left\{\left\|\mathbf{W}\left(\mathbf{d} - \mathbf{F}(\mathbf{m})\right)\right\|^2 - x_*{}^2\right\}, \qquad 3.48$$

where $\left\|\partial \mathbf{m}_y\right\|^2 + \|\partial \mathbf{m}_z\|^2$ is the norm of model roughness, $\mu{-1}$ is the Lagrange multiplier, $x_*{}^2$ is the data misfit, $\mathbf{d}$ is the observation vector, $\mathbf{W}$ is the $M \times M$ diagonal weighting matrix, and $\mathbf{F}(\mathbf{m})$ is the model response.

The 2D inversion along the Adami Tulu-western margin of the CMER traverses each station approximately 2.5 km apart in a nearly E-W direction, with 21 MT stations (**Figure 1.3**). In this profile, a joint 2D inversion was carried out that takes into account both TE and TM modes. To provide a comprehensive view of the subsurface conductivity structure in the SDFZ-Adamitulu field, a joint inversion of the TE and TM mode data was carried out. For 2D inversion, 76 frequencies from 0.011 to 320 Hz were used in total. The data are rotated to the proper geoelectric striking direction prior to inversion The preferred geo-electric strike (i.e., N15^{0}E) is consistent with the direction of the major fault (NNE-SSW) in the Ashute geothermal field. The main structural setting in the Ashute geothermal field is NNE-SSW.

3.5.5 Three-dimensional MT Inversion

Many 3D inversion algorithms have been developed and are available for use (Avdeev & Avdeeva, 2009; Cumming & Mackie, 2007; Egbert & Kelbert, 2012; Gribenko & Zhdanov, 2007; Kelbert et al., 2014; Newman & Alumbaugh, 2000; Sasaki & Meju, 2006; Siripunvaraporn & Egbert, 2009; Siripunvaraporn & Sarakorn, 2011; Smith & Booker, 1991). For academic purposes, the ModEM and WSINV3DMT Inversion codes are available for free. In this study, the ModEM inversion tool (Egbert & Kelbert, 2012; Kelbert et al., 2014; Meqbel, 2009) was employed to conduct 3D MT inverse modeling using a full impedance tensor as input data elements. The ModEM program (Egbert & Kelbert, 2012; Kelbert et al., 2014; Meqbel, 2009), developed at Oregon State University by Naser Meqbel, Gary Egbert, and Anna Kelbert, was utilized for electromagnetic data inversions. This program, written in Fortran 90, employs the Non-Linear Conjugate Gradients (NLCG) for the inversion process and the finite difference method (FDM) to solve the 3D forward problem.

The 3D inversion algorithm was preferred to 1D and 2D models due to their ambiguity and inability to map complex geological structures. The ModEM3DMT algorithm seeks the optimal model to minimize the objective function (see Equation (3.49)), which comprises model regularization and a data regularization term in the 3D magnetotelluric inversion process (Kelbert et al., 2014).

$$\phi(\mathrm{m},\mathrm{d}) = \left(\mathrm{d}-\mathrm{f}(\mathrm{m})\right)^{\mathrm{T}} \mathrm{C_d}^{-1}\left(\mathrm{d}-\mathrm{f}(\mathrm{m})\right) + \lambda\left(\mathrm{m}-\mathrm{m_{prior}}\right)^{\mathrm{T}} \mathrm{C_m}^{-1}\left(\mathrm{m}-\mathrm{m_{prior}}\right) \qquad 3.49$$

where d represents the observed data, $\mathrm{f(m)}$ represents the forward response, m represents the conductivity model, $\mathrm{C_d}$ represents the covariance of data, $\mathrm{C_m}$ represents the covariance of the model, $\mathrm{m_{prior}}$ ($\mathrm{m_0}$) represents the prior model, and a trade-off parameter (λ).

The Siripunvaraporn & Egbert (2000) approach is similar to the 3D smoothing and scaling operator used by the model covariance (C_m). C_m is applied to the difference between the current model m and the a priori model m_{prior}; in other words, as part of the model update search, ModEM3DMT penalizes smoothed departures from a previous model.

The recovered 3D inversion of the resistivity model of the Ashute geothermal site was interpreted to correlate with the conceptual model of a high-enthalpy geothermal system. For the 3D inversion, 30 sites of MT data covering a total of 80 frequencies over a period ranging from 0.001 to 1000 s were utilized for the inversion process. 3D inversion, the initial model used consists of 54 x 34 x 45 cells in the x, y, and z directions, respectively. The total number of cells is 82, 620 as shown in Figure 4.9. Poor-quality (large error bars) data with wide scatter were recognized and removed manually from the input data, and the data was carefully selected. The data includes the full impedance tensor. It enhances the recovery of the actual resistivity structure and makes the previous model less reliant (Tietze et al., 2015). The inner grid in the model's central component (core) has a grid cell size of 200 x 200 m in the x and y directions, respectively, with 7 padding cells rising by a factor of 1.3 in each direction. There are a total of 45 layers in the vertical direction, with the first layer thickness of 15 meters increasing by a factor of 1.1 for the successive layers (Figure 4.9).

Chapter 4 3D analysis of the MT data for resistivity structure beneath the Ashute geothermal site, Central Main Ethiopian Rift (CMER).

4.1 Introduction

The Main Ethiopian Rift (MER) is one of the East Africa Rift Systems (EARS), which is a seismically and volcanically active portion that runs northeast through the Ethiopian plateau (Agostini et al., 2009; Gashawbeza et al., 2004; Keranen & Klemperer, 2008). The Central MER (CMER) is a component of the MER that spans from Lake Koka to Lake Awasa and has boundary faults that run roughly N30°E–N35°E on average (Agostini et al., 2009; Keranen & Klemperer, 2008). Several active volcanoes and caldera edifices are hosted in the CMER (Peccerillo et al., 2003). Geothermal resources are often associated with these active volcanoes (Glassley, 2010; Nowacki et al., 2018). The Ashute (around Butajira) geothermal field is found closer to the western rift escarpment in the CMER, where thermal manifestations like mud pools and hot springs are aligned NNE-SSW (Sinetebeb et al., 2020).

EM instruments are widely used in the geothermal industry to examine geothermal systems, including the characterization of altered rocks and faults and the detection of geothermal fluids filled with cracks (Muñoz, 2014). According to (Árnason et al., 2010), these instruments are also utilized to detect accumulated magma zones beneath active volcanoes, which are associated with high conductivity anomalies. (Muñoz, 2014)asserts that subsurface electrical conductivity is a critical feature for characterizing and identifying geothermal environments. Geothermal systems with fault zones and conductive fluids containing fractures that may contain significant amounts of dissolved salts serve as sources of conducting electrolytes. (Spichak & Manzella, 2009). Temperature, Water content, porosity, fractures, permeability, and the concentration of dissolved solids are the key factors that affect resistivity values and rock matrix (to a minor level), and the host rocks have less conductivity than the geothermal system (Mohamed Abdelzaher, Jun Nishijima, Hakim Saibi, Gad El-Qady, Usama Massoud, Mamdouh Soliman, Abdellatif Younis, 2012; Tuyen et al., 2014). Clay mineral alteration has a high conductivity signature produced by hydrothermal processes in geothermal systems (Tuyen et al., 2014). The MT method has been recognized for a long time as the best method for geothermal exploration due to its numerous advantages in delineating high resistivity zones associated with high-temperature effects and its deeper depth of investigation (Grandis et al., 2006). Many MT studies have been conducted in recent years in the major tectono-volcanic regimes of the Ethiopian rift to explore, delineate, and characterize the 3D electrical resistivity model of the geothermal systems (Cherkose, B. A., & Mizunaga, 2018; Cherkose & Saibi, 2021; Keto & Saibi, 2016; Samrock et al., 2015). The previous geophysical study in the CMER revealed that the high conductivity region was obtained using magnetotelluric data beneath the SDFZ (Samrock et al., 2015; Whaler, K. A., & Hautot, 2006). This region is consistent with the low seismic velocity region (Kim et al., 2012). However, the Ashute geothermal site is located within the CMER near the SDFZ, has not previously been studied in sufficient detail, and requires additional data. Accordingly, MT measurements proved the most effective method for detecting the highly conductive "clay cap" and the deep geothermal reservoir. Therefore, cautious data gathering, processing, modeling, and interpretation in terms of mapping large kilometers required for some geothermal fields make a valuable contribution to geothermal exploration and exploitation (Tuyen et al., 2014).

In this study, the main focus was on using 3D MT inverse modeling and data analysis to examine the geothermal field in the Ashute area near the SDFZ. The 3D inversion model was created using ModEM inversion codes (Egbert & Kelbert, 2012; Kelbert et al., 2014; Meqbel, 2009) and an open-source Python program (MTpy) for a specific dataset (Krieger & Peacock, 2014). This approach aimed to provide information about the underground geoelectrical structures to identify hydrothermal alteration zones, map and explore geothermal resources for future use, and determine the 3D distribution of resistivity in the study area. Additionally, the Ashute MT data were analyzed to determine its geoelectrical properties in the subsurface. Therefore, the main goal of this research was to create a 3D electrical resistivity model of the subsurface to map and characterize the geothermal structures in the Ashute geothermal field.

4.2 Tectonics and geologic setting

The EARS is a typical location for studying the evolution of continental extension, lithospheric plate rupture, and the dynamics through which distributed continental deformation is progressively concentrated at oceanic spreading centers (Corti, 2009). The Main Ethiopian Rift (MER) is the portion of the EARS that connects the Afar triple junction to the north and the Kenya Rift to the south (Bonini et al., 2005). The opening of the Ethiopian rift has been established by the unrest of at least two mantle plumes, currently found beneath the Afar depression to the north of MER and the Gregory Rift in Kenya. The Southern Ethiopia Eocene-Oligocene magmatism arose from the earlier Kenyan plume, which drifted southward when the African plate moved northward (Furman et al., 2004). The Afar plume is supposed to be younger, and it is considered to be the source of the majority of central Ethiopia and the Afar region magmatism (Morley, C.K., Ngenoh, D.K., Ego, 1999; Shinjo et al., 2011). Uplift of mantle plume activity produces uplift of rift shoulders and dome development in the escarpments of both rifts, resulting in the current relief of Ethiopia (Chorowicz, 2005; Ring, 2014; Sinetebeb et al., 2020). The main scarp between the northern flanking and plateaus of southern Ethiopia and the rift floor is built by dextrally stepped northeast striking normal border faults, with height differences reaching up to 2000 meters (Corti, 2009; Gebregzabher, 1986; Samrock et al., 2015). The occurrence of high enthalpy geothermal prospects and active magmatism in the MER is due to plume interaction (Demissie, 2010; Sinetebeb et al., 2020). The tectonic-magmatic activity throughout the Cenozoic era was significant in the formation of the Ethiopian rift valley that is active today.

The most notable volcano-tectonic event in the CMER is the copious flows of ignimbrites that formed due to the collapse of the Early Pliocene's extremely large calderas (Di Paola, 1972; Woldegabriel et al., 1990; Habteweld, 2014). From the Early Pleistocene until the present, the Silti Debre Zeit Fault Zone (SDFZ) to the west and the Wonji Fault Belt (WFB) to the east have been the epicenters of tectonic and volcanic activity (Di Paola, 1972; Keir et al., 2015; Maccaferri et al., 2014; Mohr P. A., 1962; T. Rooney et al., 2007).

The rift valley is noticeable by long rift escarpments on both the eastern and western borders. The boundary faults have an N30°E average trend (Figure 4.1). The ESE-dipping and N25°E–N35°E-trending Guraghe and Fonko faults form the western boundary, while the WNW-dipping and N30°E-trending Asela–Langano fault system forms the eastern boundary (Figure 4.1). On the western boundary of the CMER, bands of a few off-axis Quaternary volcanism can be detected, for example, in the SDFZ, which contains the Bishoftu and Butajira volcanic chains on the west side of Aluto. The SDFZ was initially estimated to be 100 km long and 2–5 km wide, but its exact size is still under debate (Samrock et al., 2015; Woldegabriel et al., 1990).

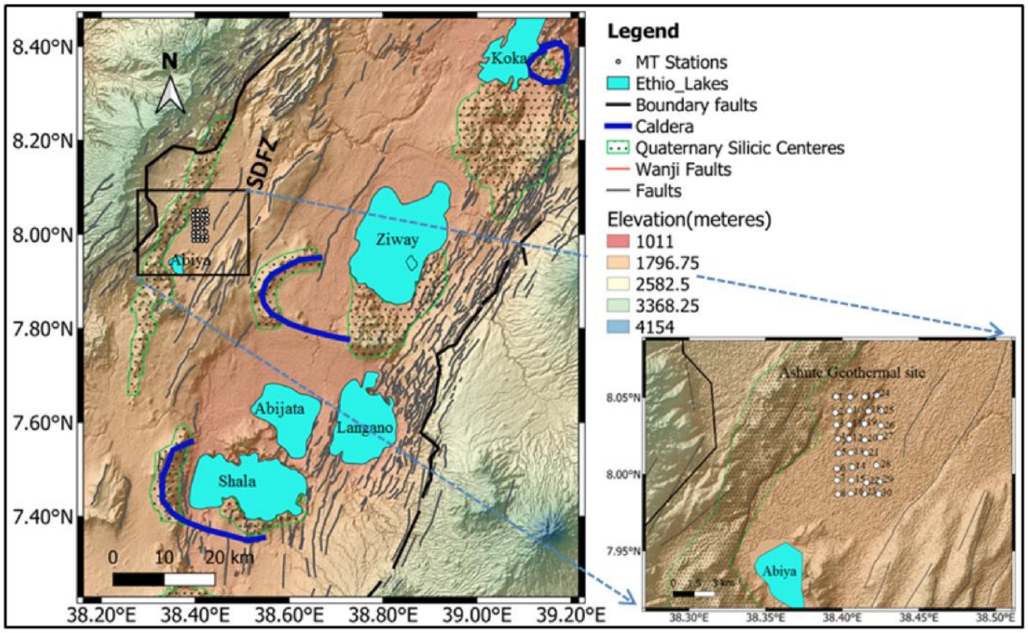

Figure 4.1 The map illustrates the tectonic setting and location of the Ashute geothermal field in the CMER. The ERS includes a zone of tectonically active regions between two expanding African plates, the Somalian and Nubian(modified from Molin & Corti, 2015).

Modest transversal structures and locally complicated geometries are common characteristics of segmented and articulated border fault systems. The NE–SW-trending border faults near the Lake Langano curve acquire a local NW–SE trend, and the main S or Z-shaped pattern of the Langano Rhomboidal fault system is formed by the interaction between these two intersecting trends (Agostini et al., 2009; Boccaletti et al., 1998; Le Turdu et al., 1999; Mohr, 1987). Fault-slip measurements on the two rift borders in the CMER reveal a stress field characterized by an ESE–WNW extension trend, with slight changes between NW–SE and E–W (Acocella et al., 2003; Agostini et al., 2009; Boccaletti et al., 1998; Bonini et al., 2005; Korme et al., 1997; Pizzi et al., 2006).

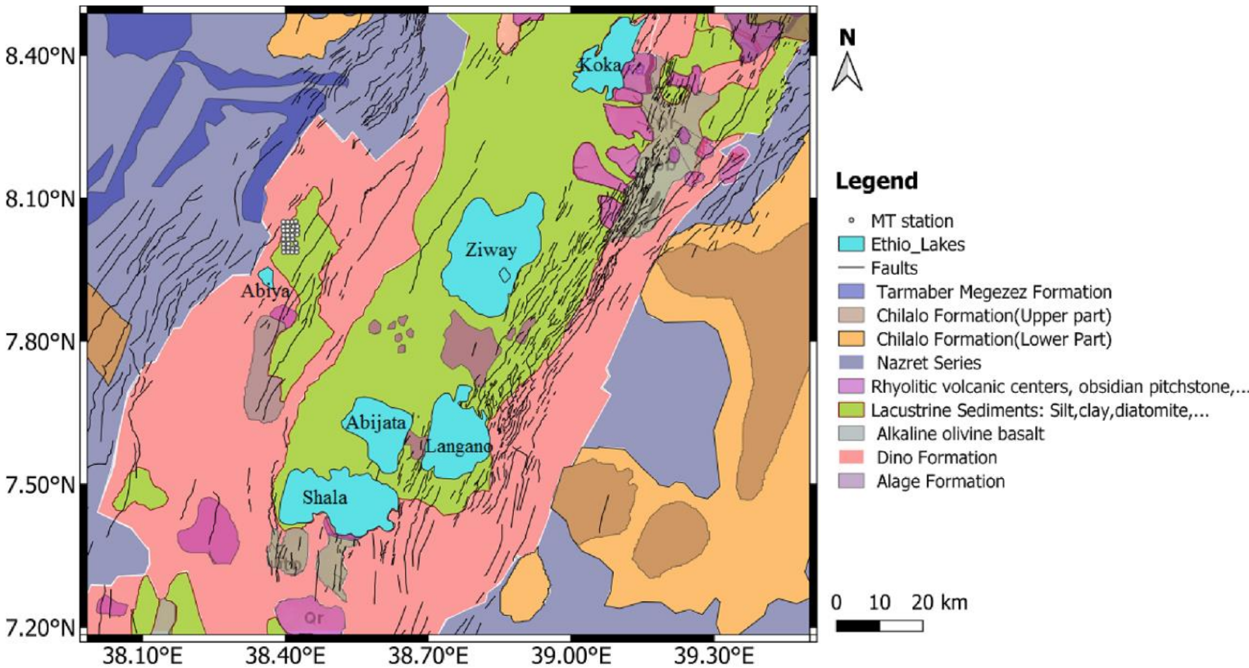

Figure 4.2 The map depicts the geology of CMER (Adopted and modified from the Geological Survey of Ethiopia, 1996).

In the central part of MER, the Lakes region is located on the basin floor and is covered by Holocene lacustrine deposits. These lake sediments are accompanied by micro-organic deposits (diatomite). However, WFB, on the other hand, cuts those sediments in some places and creates step-like terrain. The placement of Lake Abijata and Lake Langano is controlled by the influence of such faults, whereas Lake Shalla is a caldera-created lake through a volcanic eruption (JICA & GSE, 2015). on the western side of the CMER, the SDFZ is dominated by Quaternary core volcanoes, and basaltic lava flows, as well as associated scoria cones, and lava flows with phreatomagmatic deposits (T. Abebe et al., 2010). Several intermittent amalgamating nested scoria cones have been positioned parallel to the Guraghe escarpment near the SDFZ (Woldegabriel et al., 1990). Around the study area, scoria, highly vesicular basalt, rhyolite, layered pumice, crystalline ignimbrite, and deposits of pyroclastic flow with extreme differences in textural features are highly weathered and covered with 0.5-meter thick soil. The study area (Ashute), is typically covered by lacustrine sediment deposits (see Figure 4.2).

4.3 Magnetotelluric Method

The Magnetotelluric method (MT) is a part of studies of Electromagnetic (EM) induction, built on measurements of natural electromagnetic fields at an observation point on the surface of the Earth, providing the subsurface distribution of electrical resistivity. Natural signal EM-induction studies are mainly carried out through two well-established techniques, the MT method and the Geomagnetic Depth Sounding (GDS). A technique in applied Geophysics, the MT method was initially recognized and outlined by Tikhonov (1950) and then by (Cagniard (1953). A broadband depth sounding ranging in frequency from > 0.0001 Hz to < 10,000 Hz can be employed for shallow and deep structural investigations. The natural MT fields of frequencies from 0.0001 to 1Hz are generally produced by geomagnetic micro pulsations. At frequencies from 1 to 10,000 Hz, most of the signal is due to the current system of worldwide lightning activity.

For MT study, the usual components measured at a single site are time variations of the three orthogonal magnetic fields $\left(H_x, H_y, H_z\right)$ and two electric fields simultaneously measured on the surface of the Earth in MT surveying (Cagniard, 1953; Chave & Jones, 2012; Tikhonov, 1950).

Magnetotelluric transfer functions, often known as the responses of MT, are functions that connect the observed components of the electromagnetic fields at different frequencies. Provided that the source fields can be as consented to as plane waves, these functions depend on the material's electrical characteristics and frequency, not on the EM sources. As a result, according to the observed frequency, this characterizes the materials underlying the resistivity distribution. The most commonly used transfer functions of MT data are the impedance tensor and geomagnetic transfer function (tipper vector). The impedance tensor, Z, is the typical MT transfer function, and it signifies the direct relationship between the variations of electromagnetic fields in the horizontal direction at a particular location. It is a frequency-dependent, complex second-rank matrix (Equation (4.1)) that defines the interaction between orthogonal components of electric $\left(E_x, E_y\right)$ and magnetic fields $\left(H_x, H_y \text{ or } \frac{B_x}{\mu}, \frac{B_y}{\mu}\right)$ respectively at a specified frequency.

$$E = ZH \text{ or } \begin{pmatrix} E_x \\ E_y \end{pmatrix} = \begin{pmatrix} Z_{xx} & Z_{xy} \\ Z_{yx} & Z_{yy} \end{pmatrix} \begin{pmatrix} H_x \\ H_y \end{pmatrix} \tag{4.1}$$

or the EM field spectra are linearly related by way of:

$$E_x(\omega) = Z_{xx}(\omega)H_x(\omega) + Z_{xy}(\omega)H_y(\omega) \tag{4.2}$$

$$E_y(\omega) = Z_{yx}(\omega)H_x(\omega) + Z_{yy}(\omega)H_y(\omega) \tag{4.3}$$

where Z_{xy} and Z_{yx} are called the principal impedances while Z_{xx} and Z_{yy} are the supplementary as shown in Equations (4.2), and (4.3).

The MT tensor (M) was first coined by Weaver et al. (2000), which is a similar portrayal of the transfer function but uses the B field as an alternative to the H field (e.g., Equation (4.4)):

$$E = MB \text{ or } \begin{pmatrix} E_x \\ E_y \end{pmatrix} = \begin{pmatrix} M_{xx} & M_{xy} \\ M_{yx} & M_{yy} \end{pmatrix} \begin{pmatrix} B_x \\ B_y \end{pmatrix} \quad (4.4)$$

Every matrix member has both real and imaginary parts, signifying that each component has both a magnitude and a phase because both tensors (Z and M) are complex integers.

In a 3D earth model (see Figure 4.11), conductivity varies in all three directions (x, y, z). The general form of the impedance tensor in a 3D earth model (Equation (4.5)) is

$$Z_{3D} = \begin{pmatrix} Z_{xx} & Z_{xy} \\ Z_{yx} & Z_{yy} \end{pmatrix} \quad (4.5)$$

where $Z_{xx} \neq Z_{yy} \neq 0$ and $Z_{xy} \neq Z_{yx}$. There is no mechanism to rotate the impedance tensor such that on-diagonal elements on Z become zero.

The interpretation must take into account each component of the tensor. The diagonal elements of the impedance tensor and any part of the tipper vector are all non-zero elements and do not vanish in any direction. For the 3D Earth, the full impedance tensor with four complex elements for each frequency can be used to calculate different forms of apparent resistivity.

Apparent resistivity (ρ), and phase (φ) (see Equations (4.6), and (4.7), respectively) of the Earth response functions in MT surveys are often used. An equivalent uniform half-space average resistivity is used to calculate the apparent resistivity of a layered earth model.

$$\rho_{ij}(\omega) = \frac{1}{\mu\omega}\left|z_{ij}\right|^2 = \left|C_{ij}\,(\omega)\right|^2 \mu\omega(\Omega m) \quad (4.6)$$

The response functions $C = \frac{1}{K} = \frac{E_x}{i\omega\mu H_y} = \frac{-E_y}{i\omega\mu H_x}$, is complex and has a phase lag known as an impedance phase, and in the case of 1- D layered half-space:

$$\varphi_{ij} = \mathrm{Arg}(C_{ij}) = \tan^{-1}\left(\frac{E_i}{B_j}\right) \quad (4.7)$$

The tippers that developed as described by a forward model were seen and placed restrictions on the possibility of melting within MER (Samrock et al., 2015). The MT method has been widely used in geothermal exploration because of its ability to investigate deep into the earth and effectively identify low conductivity zones related to high-temperature effects, such as alteration

(Zhdanov & Keller, 1994). The mineralogy of hydrothermal alteration and the presence of reservoir fluids in fractured rocks are important factors in determining the distribution of electrical resistivities in geothermal systems, particularly in high-temperature fields(Cherkose & Saibi, 2021; Muñoz, 2014; Ussher et al., 2000).

4.3.1 Data acquisition and processing

The natural time variations of the electrical and magnetic fields of 30 MT sites were measured in a period range of 0.00313–2941.17 s, over a 32 km^2 rectangular grid with an interstation spacing of 1 km on average, and gathered within two months, utilizing (MTU-5A/MTU-5/V5) a V5 System 2000 MTU Phoenix Geophysics at local and remote stations. It was carried out in 2017 under the supervision of GSE geophysical personnel. The distance between stations varies, but it is roughly 1 kilometer on average. A five-component MT unit typically consists of five non-polarized electrodes, four of which measure two perpendicular electric field components $\left(E_x, E_y\right)$ in the horizontal directions, i.e., along with the N–S and E–W directions, while the fifth electrode serves to ground the MTU data logger in the center. These electrodes are usually comprised of a porous pot that contains metal interacting with a solution, which connects to the ground via porous materials, commonly $CUSO_4$ or $PbCl_2$. Three induction coils were used for measuring the magnetic field, two of which measured the horizontal orthogonal components (H_x, H_y) and the rest measured the vertical component (Hz), as illustrated in Figure 4.3. Magnetic sensors (induction coils) measure the horizontal and vertical magnetic field components on the Earth's surface. In order to minimize noise and the effect of everyday temperature variations, the two magnetic coils were buried. The magnetic field in the vertical direction, Hz, was measured by burying the induction coil as much as possible vertically, 90 degrees into the ground.

The data logger serves as the MT measuring system's central controller unit. It manages the acquisition process and signals from amplifier sensors before sending them to an AD converter for conversion to digital format. As a stable power source, a standard 12-volt car battery was used. The field configuration shown in Figure 4.3 is as follows:

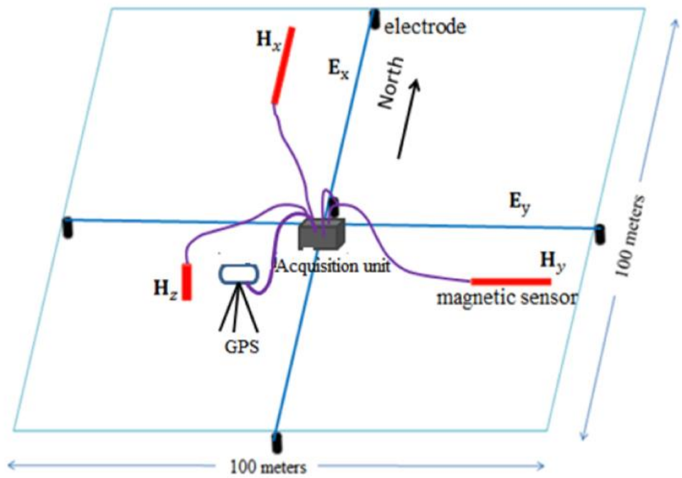

Figure 4.3 Schematic diagram showing the field setup for MT data acquisition.

The GPS time signals were used to obtain timing at each MT station. To suppress electromagnetic noise (cultural noise) induced by artificial electrical sources, vibrations, and electromagnetic signals from other sources at each measuring station, a remote reference was located 15 km NW of the Ashute Geothermal field for the entire duration. The coils and wires were buried in the ground to reduce wind noise, with the added benefit of lowering heat impacts on the induction coils. At most of the sites, the devices were deployed and running for more than 24 hours.

During the data processing stage, the time series data were utilized to estimate both the impedance tensor and tipper after the data were acquired. Prior to data analysis and inversion, we used the processed data (spectral data) in this investigation.

4.3.2 A Dimensionality Analysis

Many methodologies have been developed to investigate the dimensionality of MT data at various times.

The most widely used techniques are the phase tensor (Caldwell et al., 2004), rotational invariants, WAL (Martí et al., 2004, 2010), the skew parameter of Swift (Swift, 1967), ellipticity (Word et al., 1970), Groom and Bailey decomposition (Groom & Bailey, 1989), and Bohr's phase-sensitive skew (Bahr, 1988). The phase tensor (Caldwell et al., 2004) and Bahr’s phase-sensitive skew (Bahr, 1988, 1991) were used to analyze the dimensionality of the Ashuite MT data. The Ashute geothermal field's dimensionality analysis shows that there are 3D structures at deeper depths and 1D and 2D structures at shallower depths.

The parameters and approaches used for dimensionality analysis of the Ashuite MT data and results are explained in further depth in the following sections.

4.3.2.1 Bahr's phase-sensitive skew, η

Bahr (1991) suggested phase-sensitive skew, a rotationally invariant parameter, as the first modern dimensionality tool (see Equation (4.8)). It measures the skew of the impedance tensor's phases and is provided by:

$$\eta = \frac{|[D_1, S_2] - [S_1, D_2]|^{\frac{1}{2}}}{|D_2|} \tag{4.8}$$

where the D (difference) and S (sum) impedances (Equations (4.9), and (4.10), respectively) are recognized as modified impedances (Bahr, 1988) given by

$$D_1 = Z_{xx} - Z_{yy},\ D_2 = Z_{xy} - Z_{yx} \tag{4.9}$$

$$S_1 = Z_{xx} + Z_{yy}, S_2 = Z_{xy} + Z_{yx} \tag{4.10}$$

According to the criteria of Bahr (1988, 1991), for interpreting η based on its value of distorted 2D (3D /2D), or 1D, 2D examples are indicated by the skews value of phase-sensitive smaller than 0.1 while 3D data is represented by the skew parameters of 'phase sensitive', with values of η greater than 0.3. A modified dataset of 3D/2D with values between 0.1 and 0.3 ($0.1 < \eta < 0.3$) is regarded to be suggestive (Chave & Jones, 2012).

As demonstrated in Figure 4.4, Bahr's phase-sensitive skew was presented for the entire MT stations in the Ashute geothermal region.

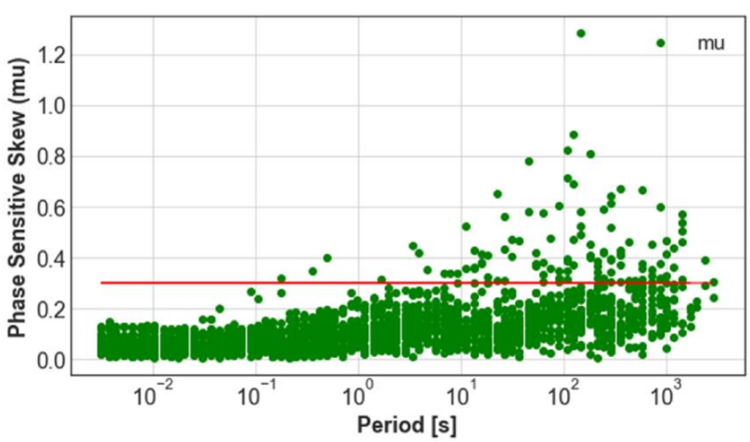

Figure 4.4 The Bahr's phase-sensitive skew plot of the Ashute geothermal field for all stations

The result of η indicates low values close to zero below 0.3 at periods (< 50 s), implying 1D, a 2D character at shallow depths for the majority of MT stations. The high values above the threshold for longer periods (> 50 s) indicate 3D dimensionality at deeper depths. The expectation value η estimator for the 1D, 2D, and 3D/2D cases is biased. η value increases as the noise level increases and decreases for low noise levels. η value is dependent on the noise level (Chave & Jones, 2012).

4.3.2.2 Phase Tensor Analysis

The phase tensor analysis method was created by (Caldwell et al., 2004) as a tool for getting information on the regional dimensionality structure which is not affected by galvanic distortion. The phase tensor can be graphically represented as ellipses (Booker, 2014). The phase tensor (φ) is defined as the ratio of the real (X) to imaginary (Y) sections of the complex tensor of impedance, Z, and is expressed as follows in Equations (4.11) and (4.12):

$$\varphi = X^{-1}Y \tag{4.11}$$

$$Z = X + iY \tag{4.12}$$

The observed impedance $Z = CZ_R$, if galvanic distortion is present, where C is the distortion tensor, and $Z_R = X_R + iY_R$ is the regional impedance. As a result, the distorted real part $X = CX_{R,}$ and the distorted imaginary part as $Y = CY_R$ can be written. The regional and observed phase tensors are the same (Equation (4.13)) and free of galvanic distortion, according to the following correlations:

$$\varphi = X_R{}^{-1}Y = (CX_R)^{-1}(CY_R) = X_R{}^{-1}C^{-1}CY_R = X_R{}^{-1}Y_R = \varphi_R \tag{4.13}$$

The principal or singular values of, φ, α, and β, which describe the phase tensor, can be represented as expressed by φ_{max} and φ_{min} are given by:

$$\varphi = R^T(\alpha - \beta)\begin{bmatrix} \varphi_{max} & 0 \\ 0 & \varphi_{min} \end{bmatrix} R(\alpha + \beta) \tag{4.14}$$

Here R^T represents the transposed or inverse of the rotation matrix, while $R(\alpha + \beta)$ represents the rotation matrix.

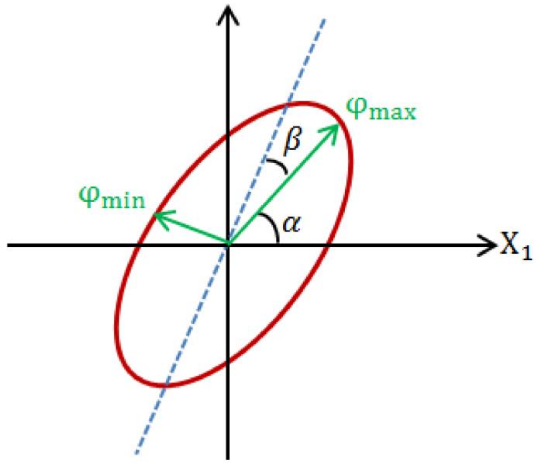

Figure 4.5 An elliptical illustration of the MT phase tensor graphically. The lengths of the semi-major and semi-minor axes of the ellipse are proportional to the principal values $\varphi_{max}, and\ \varphi_{min}$. The skew angle is a third coordinate invariant used to characterize a non-symmetric tensor. The observer's reference frame (X_1, X_2) is used to calculate the tensor's relationship. The angle $(\alpha - \beta)$, determines the direction of the ellipse's principal axis. (Caldwell et al., 2004)

Bibby et al. (2005) defined ellipticity (**λ**) expressed in Equation (4.15) as a dimensionality metric as follows:

$$\lambda = \frac{\left[\left(\varphi_{xx} - \varphi_{yy}\right)^2 + \left(\varphi_{xy} + \varphi_{yx}\right)^2\right]^{1/2}}{\left[\left(\varphi_{xx} + \varphi_{yy}\right)^2 + \left(\varphi_{xy} - \varphi_{yx}\right)^2\right]^{1/2}} \tag{4.15}$$

The principal values of the phase tensor are identical to its eigenvalues if the phase tensor is symmetric (β=0), implying that the regional conductivity distribution is mirror-symmetric (Caldwell et al., 2004). This occurs for 1D or 2D regional distribution. The phase tensor of the 1D structure has a circular shape $(\varphi_{max} = \varphi_{min})$ with the values $\beta = 0$, and $\lambda = 0$. The phase tensor is represented as an ellipse with a minor axis that is significantly small, approaching zero (β = ± 3 degrees), and the principal values of a 2D regional resistivity structure are typically distinct $(\mathrm{i.e}\ \varphi_{max} \neq \varphi_{min})$. The phase tensor ellipse, on the other hand, has part of its principal axes in the direction of the strike. Whereas the non-symmetric phase tensor has a considerable skew angle (β). An alternative sign of a 3D structure is a quick lateral variation in the major axis when a 3D structure is present. As a result, all of the invariants, namely, $\beta \neq 0, \lambda \neq 0, \varphi_{max} \neq 0$ and $\varphi_{min} \neq 0$, are non-zero when assuming a 3D structure.

Figures 4.6, 4.7, and 4.8 depict phase tensor maps at various frequencies in the Ashute geothermal field that indicate the dimensionality of MT data. The 1D symbol occurs at 320, 50, and 9.4 Hz, and has a small skew angle (-3, 3) the phase tensor is circular, as illustrated in Figure 4.6. Figure 4.7 shows that 2D structures viewed near or less than 0.02 Hz have a small skew angle and an elliptical phase tensor. The phase tensor analysis result, as shown in Figure 4.8, reveals 3D. At 0.0088, 0.00275, and 0.0011 Hz are indicated as the deeper structures with large skew angles. Consequently, the phase tensor analysis at shallow depths shows dimensionality of 1D and 2D, and high skew angles at deeper depths described 3D effects below 0.011 Hz.

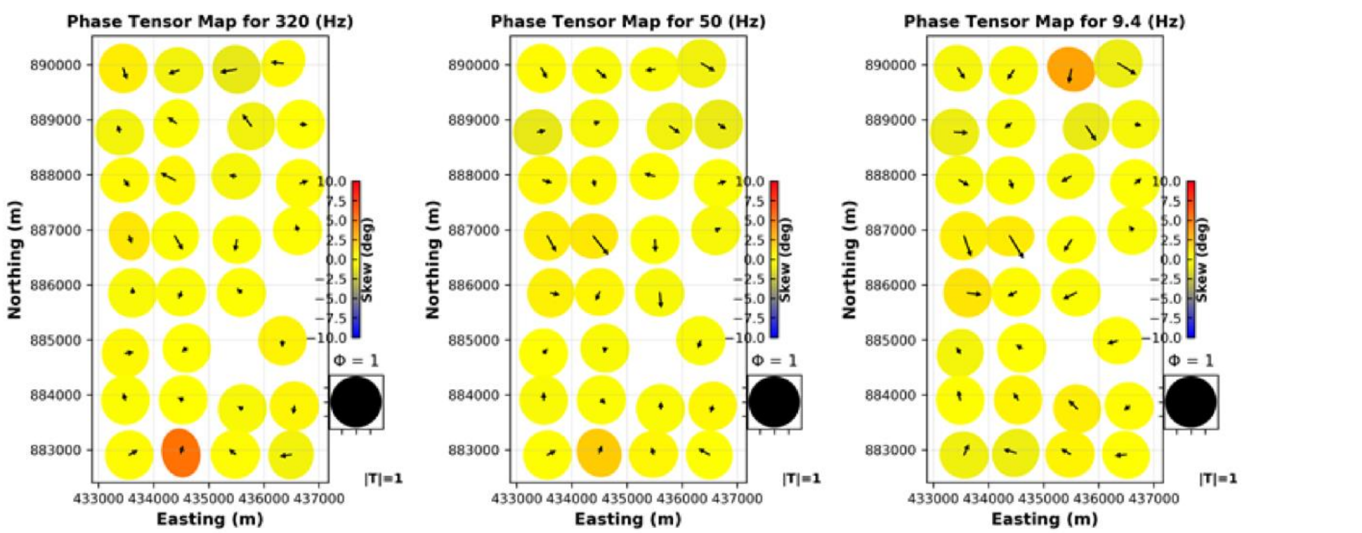

Figure 4.6 The maps depict the phase tensors of all stations at 320, 50, and 9.4 Hz frequencies from left to right, respectively, and tipper vectors and phase tensor ellipses (plotted according to the Parkinson convention).

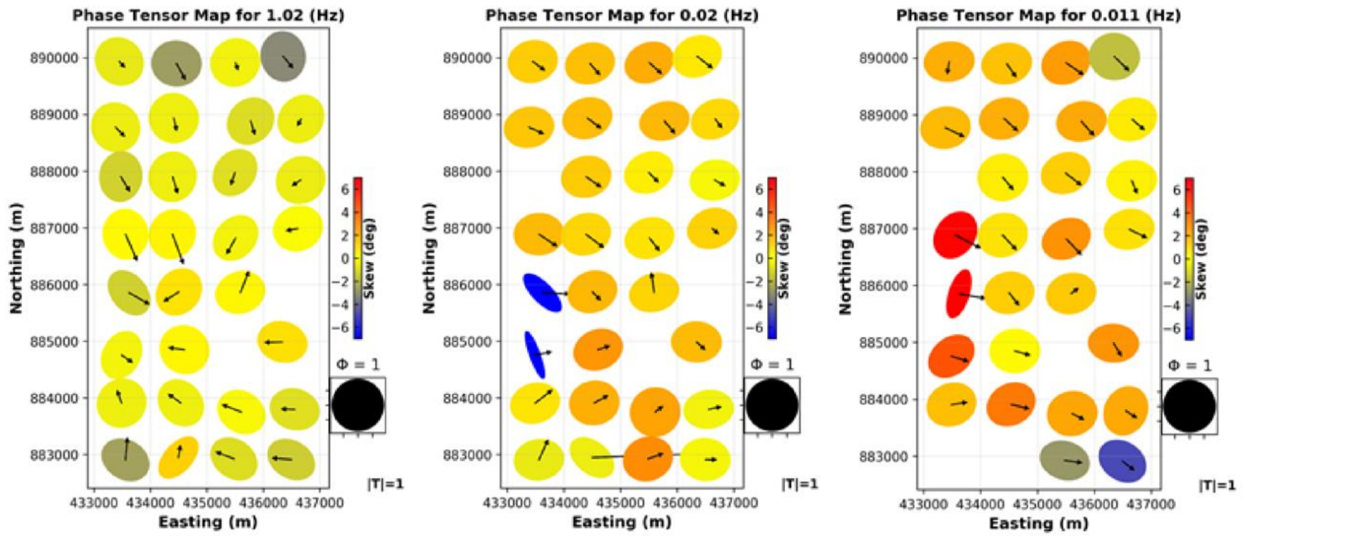

Figure 4.7 The maps depict the phase tensor of all stations at 1.02, 0.2, and 0.011 Hz frequencies from left to right, respectively, and tipper vectors and phase tensor ellipses (plotted according to the Parkinson convention).

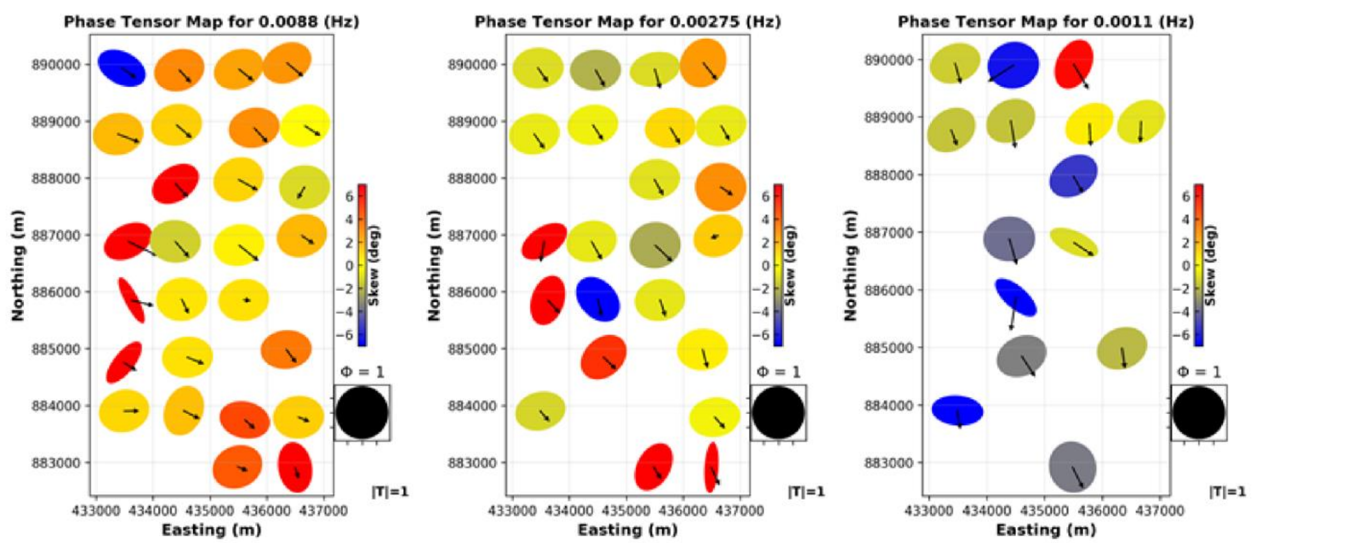

Figure 4.8 The maps depict the phase tensor of all stations at 0.0088, 0.00275, and 0.0011 Hz frequencies from left to right, respectively, and tipper vectors and phase tensor ellipses (plotted according to the Parkinson convention).

4.4 Three-Dimensional MT Inversion

There are many 3D inversion algorithms developed and available for use (Avdeev & Avdeeva, 2009; Cumming & Mackie, 2007; Egbert & Kelbert, 2012; Gribenko & Zhdanov, 2007; Kelbert et al., 2014; Newman & Alumbaugh, 2000; Sasaki & Meju, 2006; Siripunvaraporn & Egbert, 2009; Siripunvaraporn & Sarakorn, 2011; Smith & Booker, 1991). For academic purposes, the

ModEM and WSINV3DMT Inversion codes are available for free. In this study, the ModEM inversion tool (Egbert & Kelbert, 2012; Kelbert et al., 2014; Meqbel, 2009) was used to conduct 3D MT inverse modeling using a full impedance tensor as input data elements. The ModEM program (Kelbert et al., 2014) for electromagnetic data inversions was developed at Oregon State University by Naser Meqbel, Gary Egbert, and Anna Kelbert, and it was written in Fortran 90. The inversion process is established on Non-Linear Conjugate Gradients (NLCG), and the finite difference method (FDM) was utilized to solve the 3D forward problem. This approach requires extremely little memory since it keeps away from storing the Jacobian matrix and instead directly computes it. The line search strategy iteratively updates the original model, m_0. The ModEM3DMT algorithm seeks the optimal model to minimize the objective function (see Equation (4.16), which comprises model regularization and a data regularization term in the 3D magnetotelluric inversion process (Kelbert et al., 2014):

$$\Phi(m, d) = \left(d - f(m)\right)^T {C_d}^{-1}\left(d - f(m)\right) + \lambda(m - m_0)^T {C_m}^{-1}(m - m_0) \tag{4.16}$$

where d represents the observed data, f(m) represents the forward response, m represents the conductivity model, C_d represents the covariance of data, C_m represents the covariance of the model, m_{prior} (m_0) represents the prior model, and a trade-off parameter (λ).

For 3D inversion, the initial model used consists of 54 x 34 x 45 cells in the x, y, and z directions, respectively. The total number of cells is 82, 620 as shown in Figure 4.9. Poor-quality (large error bars) data with wide scatter were recognized and removed manually from the input data, and the data was carefully selected. The data includes the full impedance tensor. It enhances the recovery of the actual resistivity structure and makes the previous model less reliant (Tietze et al., 2015). The inner grid in the model's central component (core) has a grid cell size of 200 x 200 m in the x and y directions, respectively, with 7 padding cells rising by a factor of 1.3 in each direction. There are a total of 45 layers in the vertical direction, with the first layer thickness of 15 meters increasing by a factor of 1.1 for the successive layers (Figure 4.9).

For each iteration, the root mean square misfit (RMS) as expressed in Equation (4.17) and residuals r_i distribution (Equation (4.18)) were analyzed to assess the final recovery model's quality. The overall RMS is presented in ModEM, which is calculated as follows:

$$RMS = \sqrt{\frac{1}{N}\sum_{i=1}^{N}\frac{\left({d_i}^{obs} - {d_i}^{pred}\right)^2}{{e_i}^2}} \tag{4.17}$$

where d_i^{obs} and d_i^{pred} are represent the observed and predicted responses, respectively, and e_i is observed response errors, and N is the number of responses at all sites and times evaluated. The residuals are calculated as follows:

$$r_i = \frac{d_i^{obs} - d_i^{pre}}{d_i^{obs}} \qquad (4.18)$$

The recovered models are deemed suitable if the residuals have a mean value of zero and little variation, or are at least equally distributed. In this investigation, the initial RMS for the 3D inversion model was 40.6 at the start of the inversion and decreased to 1.69 after 94 iterations. The background resistivity of the initial model was set to 100 Ω m. In general, the resulting model's data misfit is reasonable, with only a few under or over-fitted data portions (Figure 4.10).

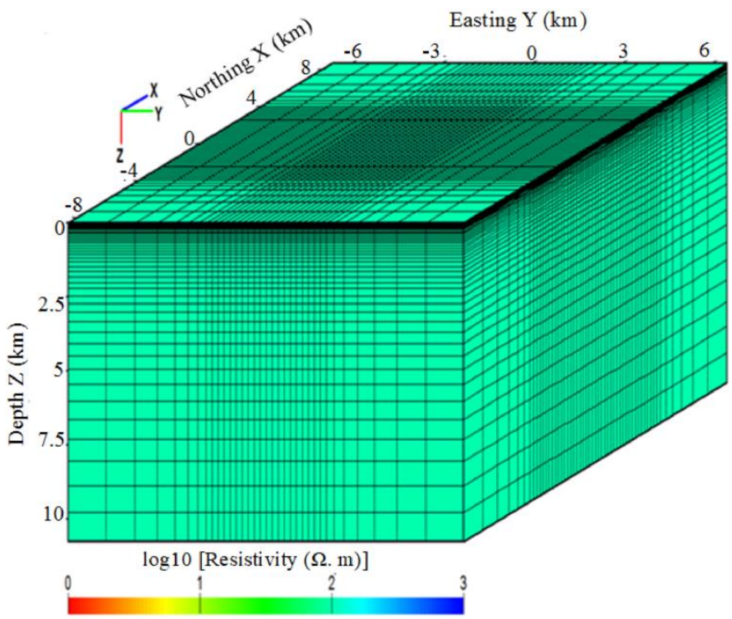

Figure 4.9 The map illustrates the model grid that was used for the 3D inversion of the Ashuite geothermal field data.

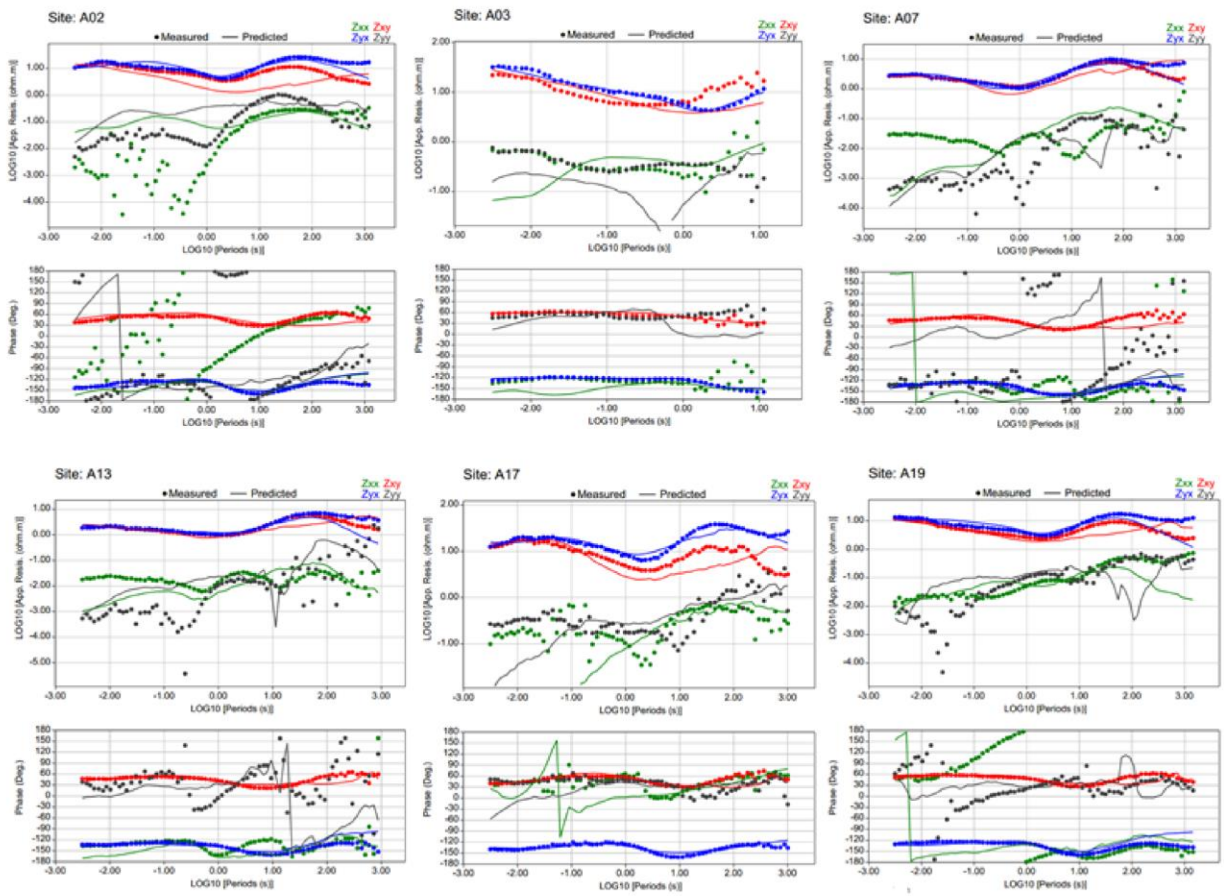

Figure 4.10 The results of a 3D inversion of measured and computed curve fitness of apparent resistivity and phase for a few selected stations. In the figure, red represents TE mode (Z_{xy}), blue represents TM mode (Z_{yx}), green and grey represents the diagonal elements of the impedance tensor $Z_{xx}, and\ Z_{yy}\ respectively$. The dotted lines represent the measured data, while the solid lines represent the computed response.

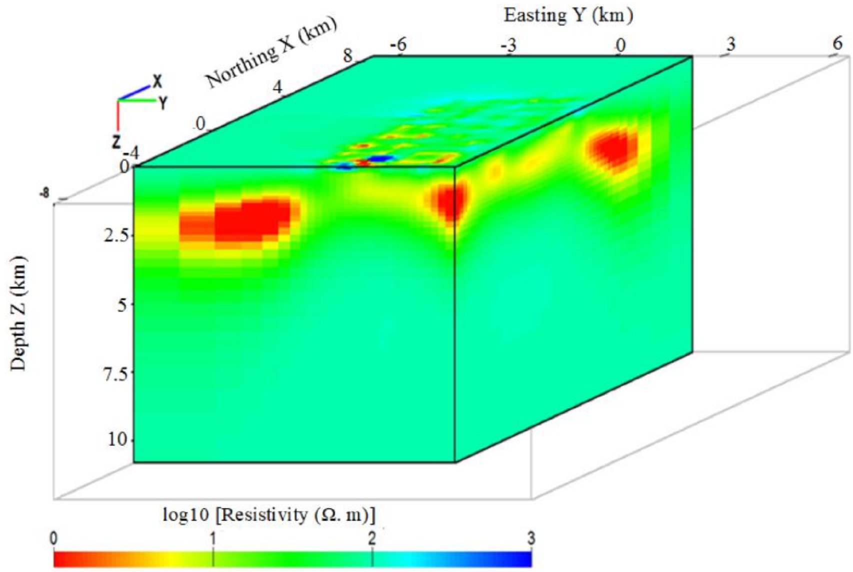

Figure 4.11 The recovered 3D inversion of resistivity model of the Ashute geothermal area

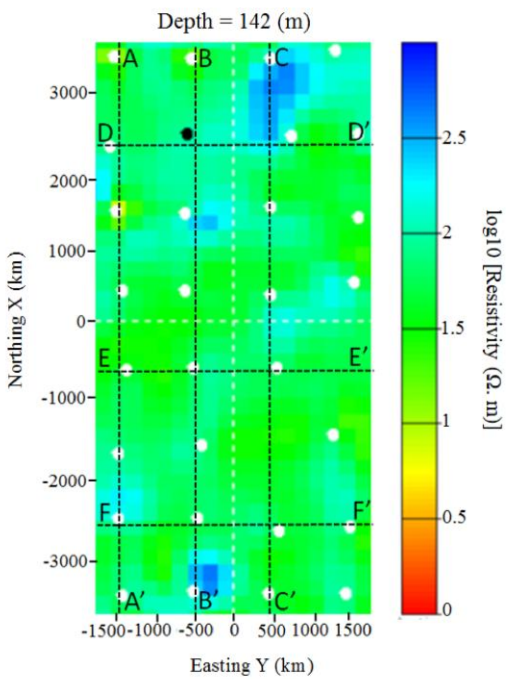

Figure 4.12 A Horizontal slice was obtained from the ground with Z =142 m. A white dot indicates an MT station. The initial subsurface layer without topography corresponds to the horizontal slice's depth. Figures 4.13 and 4.14 show resistivity cross-sections taken in N–S and E–W directions along with Lines AA', BB', CC' DD', EE', and FF'.

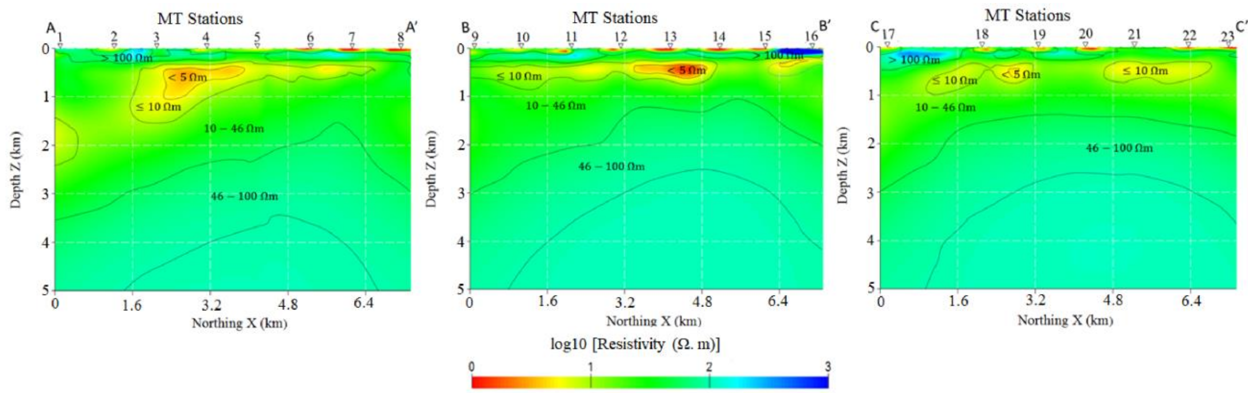

Figure 4.13 The vertical cross-sections drawn from the 3D inversion resistivity model of the Ashute geothermal site on the profiles AA', BB', and CC' in the direction of N–S, as shown in Figure 4.12.

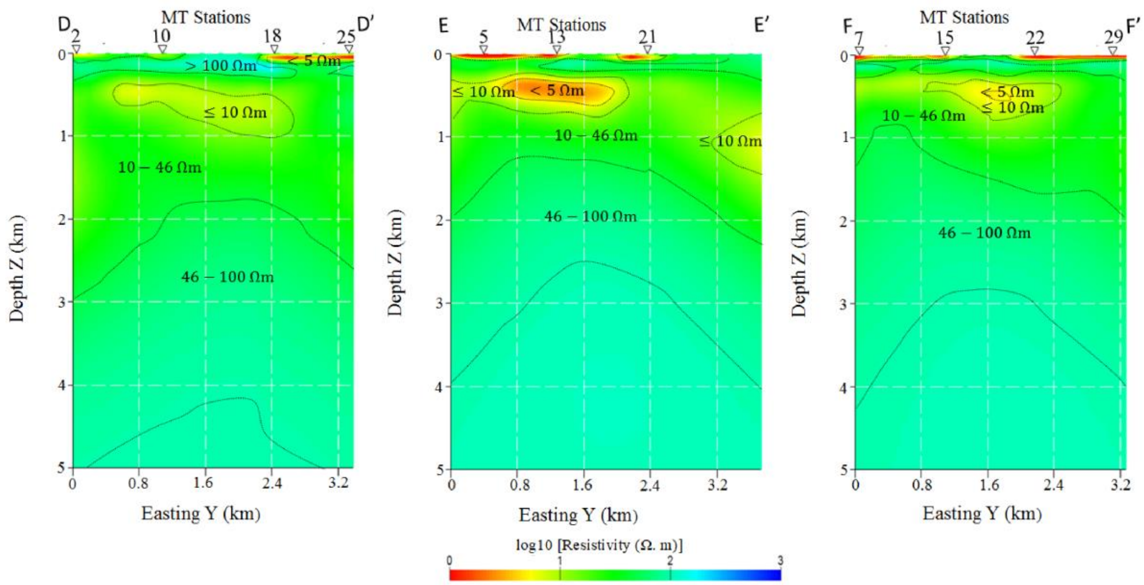

Figure 4.14 The vertical cross-sections drawn from the 3D inversion resistivity model of the Ashute geothermal site on the profiles DD', EE', and FF' in the direction of E–W, as shown in Figure 4.12.

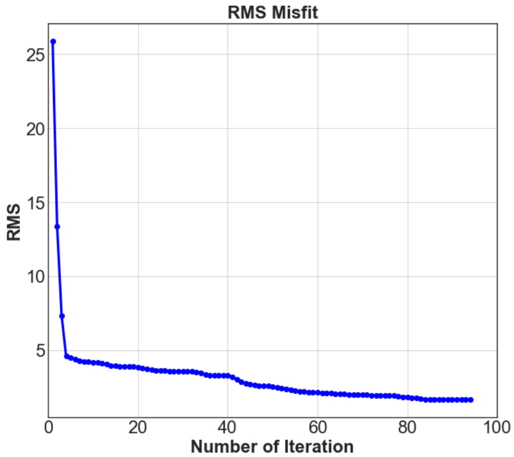

Figure 4.15 RMS misfit, calculated for the preferred model at each iteration number.

4.5 Result and Discussion

The dimensionality analysis results obtained from the phase-based tools of the Ashute MT data are consistent, and the MT dataset revealed that, at higher periodicity, the geoelectric subsurface structure is 3D in nature, implying the need for a 3D model. The identified notable structures of the 3D distribution of resistivity cross-section of the Ashute geothermal field were very high resistivity (> 100Ω.m) mixed with the low resistivity body, followed by a conductive layer below 10Ω.m overlay of the moderately resistive layer with resistivity values (10–46 Ωm), at deeper depths as shown in Figure 4.11. In the Ashute geothermal field at shallow depths, the geoelectrical structure is complex because of the non-uniform horizontal resistivity distribution of unconsolidated sediments and unaltered volcanic products exposed in the Ashuite site. At these depths, the layer has a high resistivity value with a thickness of roughly 300 m, whereas conductive layers have a thickness that extends up to 1500 m. In most of the study area, low resistivity appears at around 300 m, while at some spots in the area, it begins at the surface and discontinues. Resistivity gradually increases with depth below the conductive zone. Figures 4.13 and 4.14 show the cross-sections of resistivity in the directions of N–S, and E–W for the recovered 3D MT model. These sections of resistivity described the main characteristics of the Ashute subsurface formations. A 3D inversion model of the Ashute area indicates there are no substantial conductive features at deeper depths since the vertical slices are depicted up to a maximum depth of 5 km for simplicity and to obtain a much more zoomed-in map. However, we tried to make a 3D inversion model up to 10.8 km depth. The vertical Slice of the 3D model only along sections with good site coverage denoted as AA′, BB′, CC′, DD′, EE′, and FF′ were used in order to avoid misinterpretations as shown in Figures 4.13 and 4.14. The vertical slice along the

N–S is represented by profiles AA′, BB′, and CC′ which are shown in Figure 4.13. Due to the effect of altered lacustrine sediment, the vertical slice along AA′ indicates a low resistive zone (ρ < 5 Ωm) and (ρ < 10 Ωm) observed on the top layer at a depth down to 50 m. The presence of conductive clay minerals in the central region of the profile (1.6 < x < 6.4 km) at a depth between 30 m to 1500 m, the high resistivity (ρ ≥ 100 Ωm) of the upper few hundred meters of the shallow layers extend down to 200 m, whereas for profiles BB′ and CC′ have similar resistivity distribution as AA′, but the thickness of conductive clay minerals underlay the top high resistivity of them are smaller than AA′. At greater depths, resistivity increases step by step from a resistivity value of 10–46 Ωm to maximum values of ρ > 100 Ωm. The upper few hundred meters of shallow resistive layers is a resistive (ρ ≥ 100 Ωm) that is exposed on the surface at (6.4 km < x < 8 km) on the profile BB′.

The vertical slice along the E–W is represented by profiles DD′, EE′, and FF′ which are shown in Figure 4.14. The E–W slice along DD' in the north of the Ashuite reveals a shallow, thin high resistive zone (ρ ≥ 100 Ωm) started from the surface observed in the central region between 1–2.4 km in the east, which is only about the thickness of 300 m, whereas underlay this high resistivity body the low resistivity (ρ < 10 Ωm) also extends down between 400m to 800m in the central region between 0.6–2.4 km in the east. At greater depths, resistivity gradually increases from a resistivity value of 10–46 Ωm to maximum values of ρ > 100 Ωm. The E–W slice along with EE′, and FF′ in the central and south of the Ashute is shown in Figure 4.12. The high resistivity of the central and south of the Ashute overlays the low resistivity with almost the same thickness as DD' on the top layer for each slice exposed with low and high resistivity body interpreted as altered lacustrine sediment and unaltered volcanic material. For both vertical slices N–S and E–W, the zone of high resistivity (ρ ≥ 100 Ωm) extends a depth down to 400m and almost below 3 km, with a conductivity zone overlying a moderately resistive core (reservoir). At depths either below or above 10.8 kilometers, the recovered model shows no significant high conductive structure. The result of the resistivity pattern in this study is very similar to the previous magnetotelluric study at Aluto Langano geothermal field in CMER (Cherkose, B. A., & Mizunaga, 2018; Samrock et al., 2015). However, the only known structure coming into question as a potential conductor is the SDFZ, located 40 km west of Aluto at the western rift margin (Samrock et al., 2015).

In the western side of the study area, the Geological Survey of Ethiopia (GSE) collected and analyzed water samples from five sites from hot springs, mud pools, and a Crater Lake in 2017 (see. Figure 4.16). The thermal manifestations around the study area show a better permeable zone and high CO2 flux (Hunt et al., 2017; Sinetebeb et al., 2020). Hot springs were taken into account because of their high flow rates and high discharge temperatures. The standard method was used to analyze the water samples' chemical composition. The results of water samples in the Ashuite area (Figure 4.16) with codes of 0.01, 0.02, and 0.04 have a low ratio of Na/K and a high ratio of Na/Mg. These results revealed that the materials within the water samples had originated from the source of a deep reservoir. Water sample sites with codes 0.01, 0.03, and 0.05 have similar Cl/SO4 ratios, which suggests that the materials have the same geological context and originated from the same source (Gebrewold, 2017). The heat source of Ashute (Butajira) geothermal fluids is derived mainly from the crust because the expected value of the helium isotope ratio 3He/4He is smaller than that of mantle plumes. Because of interactions with crustal minerals, the helium isotope ratio can drop to as low as 2.3Ra (Sinetebeb et al., 2020).

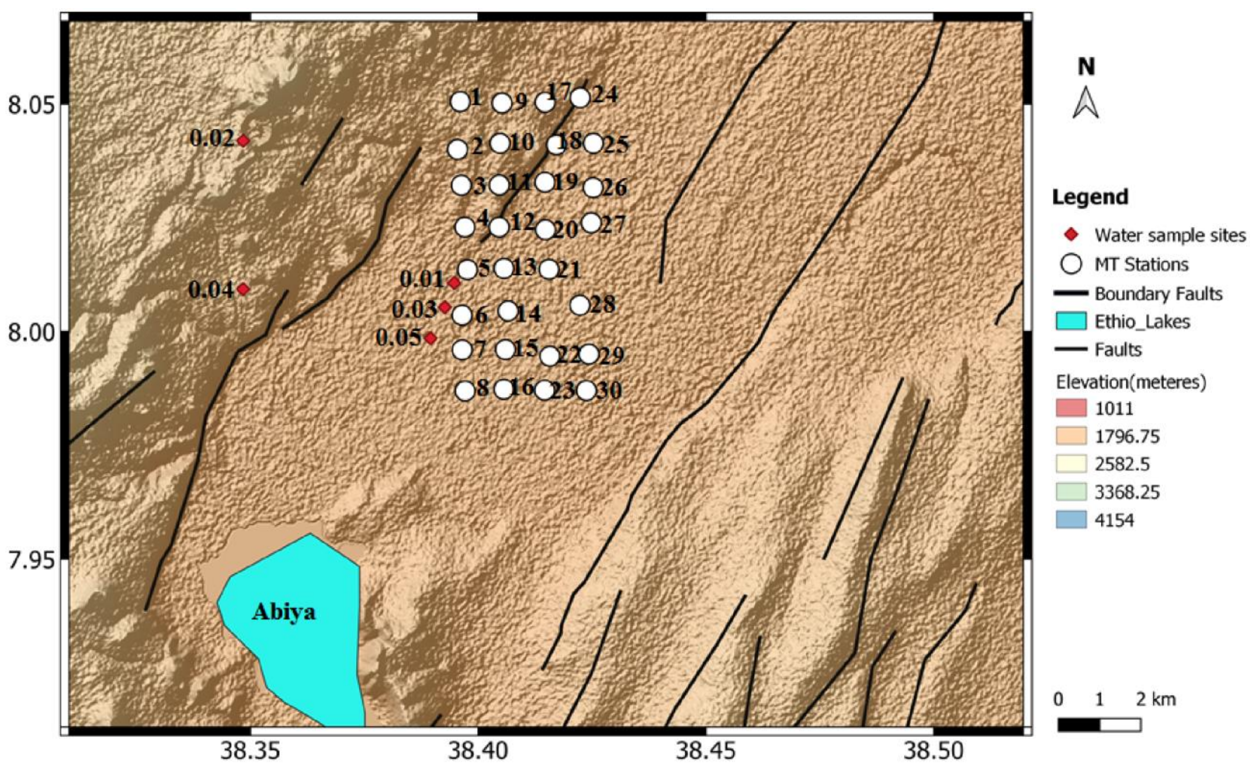

Figure 4.16 The elevation of the Ashute geothermal field, and the locations of the MT stations and water sample sites, are depicted on a map.

According to the silica geothermometers, sample code 0.03, which has a subsurface temperature of about 158.86 ℃, is the hottest spring in the Ashute area, followed by sample code 0.01, which has a subsurface temperature of about 151.8 ℃. The Na-K and K-Ca ratios for codes 0.01, 0.02, and 0.03 are 208 ℃, 754 ℃, 206 ℃, and 287.9 ℃, 374.5 ℃, 311.5 ℃, respectively. However, the values of the silica geothermometer are less than those of the Na-K and K-Ca geothermometers. These results are inconsistent with those obtained using Na-K geothermometers, which showed that the Haro Shetan water samples (with sample code 0.02) were the hottest. The difference in these geothermometers' results could indicate an effect of meteoric waters, which comprise dissolved constituents that differ from those found in the geological environment (shallow conditions mixing with groundwater). According to Gebrewold (2017), the discharge temperature of the hot springs in the study region (Ashute hot springs) ranges from 77.5 ℃ and 91.06 ℃, with pH values ranging from 7.0 to 8.92, indicating that they are closer to neutrality and some extent alkaline in nature.

The enthalpy, which is used to express the heat content of the fluids and acts as the carrier transferring heat from deep heated rocks to the surface, is often used to classify geothermal resources. The Ashute geothermal potential region, which uses a hinge on silica and the molecular ratio of geothermometers, is obtained from intermediate to high enthalpy resources (Gebrewold, 2017). According to a consequence of the geothermometer results, mud pools and some manifested hot springs have substantial heat-generating capabilities, indicating that more research is needed to determine their appropriateness for energy generation.

The recovered 3D inversion model of the resistivity of the Ashute area was interpreted to correlate with the conceptual model of a high-enthalpy geothermal system as explained by Johnston et al. (1992), Samrock et al. (2015), and Cherkose, B. A., & Mizunaga (2018). The alteration mineralogy is primarily responsible for the high-temperature subsurface resistivity distribution (Cherkose, B. A., & Mizunaga, 2018; Cumming & Mackie, 2007; Muñoz, 2014; Ussher et al., 2000). In the Ashute area, the resistivity cross-section of the model indicates three distinct anomalies: the very resistive top layer of approximately 300 m maximum thickness from the surface in the limited area; and the low resistive zone, which starts in the south of the survey area as a result of the unconsolidated sediment in the swampy area, followed by the altered zones of low resistivity. The presence of smectite, which has a low resistivity (< 5 Ωm) and a thickness of 750 m, distinguishes the upper smectite zone (alteration zone). The illite/chlorite zone, the second alteration zone, has a resistivity of < 10 Ωm, and a thickness of 250 m. The creation of alteration minerals has high temperatures and is mainly comprised of minerals like chlorite and epidote with resistivity (10–46 Ωm), which has resulted in the establishment of the last moderately resistant core (reservoir) zone underneath the conductive region as a source of heat. The up-flow zone is a region of the reservoir where the flow of fluid is mainly in the vertical direction and the distribution of temperature with depth has a low vertical gradient. Chlorite, epidote, smectite, calcite, and quartz are the most common alteration minerals in the major stages. We didn't obtain a low resistivity structure in a deep, active magmatic system under Ashute. However, a forward model was developed to explain the tippers indicating the possibility of melting located about 5–10 kilometers southeast of the Ashute geothermal zone. Samrock et al.(2015) used MT data analysis of forward modeling tipper results for the Aluto geothermal area along the SDFZ to predict the high-conductive region. This high conductive zone corresponds to the previous study of the low seismic velocity region (Kim et al., 2012) and the high conductive anomaly from the MT study (Hübert et al., 2018; Whaler, K. A., & Hautot, 2006). Therefore, the presence of a strong conductor under the SDFZ is approximately 5–10 km SE of Ashute Geothermal Field or 40 km NW of Aluto at lower crustal depths.

4.6 Conclusions

The magnetotelluric method, which determines the subsurface electrical resistivity distribution, is a frequently used technique for geothermal exploration. The dimensionality analysis of the Ashute MT data at shallow depths indicates 1D and 2D structures, and deeper depths show 3D structures, suggesting the requirement for 3D inversion to image the complicated structure of the subsurface. The inversion program used for the recovered 3D resistivity model was ModEM. For the 3D inversion, 30 sites of MT data covering a total of 80 frequencies over a period range of 0.001–1000 s were utilized for the inversion process. The recovered 3D inversion of the resistivity model of the Ashute geothermal site was interpreted to correlate with the conceptual model of a high-enthalpy geothermal system. It is immensely reliant on subsurface alteration mineralogy. The identified notable structures of the 3D distribution of resistivity cross-section of the Ashute geothermal field, were very high resistivity (> 100 Ωm) mixed with the low resistivity body at the top layer, followed by a conductive layer below 10 Ωm overlays of the moderately resistive layer with values of resistivity (10–46 Ωm), at deeper depths. The low resistivity zones are categorized into two parts with a resistivity value of less than 5 Ωm and less than 10 Ωm. The low resistivity begins to appear at 500 meters, becoming dominant in the area and, in some areas, extending from the surface to 1500 meters. As you go deeper below the conductive zone, the resistance gradually increases. The recovered 3D inversion model did not disclose an extremely low deep resistivity structure under the Ashute site. Thus, based on these findings, we conclude that the existence of a hot extended magma reservoir beneath the Ashute geothermal field is doubtful. The results of tipper forward modeling show a conducting region found about 5 km SE of Ashute along the SDFZ. A regional extremely conductive zone was identified 40 km west of Aluto, beneath the SDFZ, in a previous study (Hübert et al., 2018; Samrock et al., 2015). However, below the Ashute geothermal field, the deep, extensive, highly conductive body cannot exist because it is located about 45–50 km from the Aluto geothermal field.

Chapter 5 Crustal resistivity structures beneath the western flank across the Central Main Ethiopian Rift (CMER): Its implications for Partial Melt and Pathways

5.1 Introduction

The Aluto-Langano, Gedemotta, Shala, Corbetii, Debre Zeit, and Butajira volcanic fields are situated in the Central Main Ethiopian Rift (CMER) (B. Abebe et al., 2007). In this region, the crustal structure is influenced by Quaternary rifting (B. Abebe et al., 2007), where volcanism and dike intrusion occur as magmatic segments within the Main Ethiopian Rift (MER) (Dugda et al., 2005). The surface manifestation of the upper mantle-derived material (intrusion) was detected by using the map of residual anomalies of the gravity field in the rift floor, mostly associated with Quaternary peralkaline rhyolite centers of the rift floor (Mahatsente et al., 1999). Mahatsente et al. (1999) have shown that gravity data anomalies coincide with the inferred zone of intrusion predominantly concentrated in the north and central sectors of the rift floor. The seismic velocities of the upper crustal layers are 5–10 % higher than those outside the rift beneath the rift axis as a result of mafic intrusions linked with magmatic centers found in the Main Ethiopian rift valley (Mackenzie et al., 2005). Geochemical studies also indicate that the magmatic products in the Silti Debre Zeit Fault Zone (SDFZ) originated from sub-lithospheric depths (T. O. Rooney et al., 2005).

In a volcanic environment, the magnetotelluric (MT) method can provide important constraints on volcanism as a result of magma that indicates low resistivity (Hill et al., 2009; Johnson et al., 2016; Muñoz et al., 2018; Wannamaker et al., 2017; Whaler K.A. and Hautut S., 2006). Due to the intrinsic dependence of the bulk electrical resistivity of Earth material on factors such as fluid content and temperature, the MT method serves as an important tool for studying magma storage, partial melt, and pathways in active rift zones and other tectonic regimes (Beka et al., 2015; Cherevatova et al., 2014; Hill et al., 2009; Johnson et al., 2016; Muñoz et al., 2018; Segovia et al., 2021; Wannamaker et al., 2017). There have been many applications of the MT in the study of major tectono-volcanic regimes in different parts of the world, including the MER (Desissa et al., 2013; Muñoz et al., 2018; Patro & Sarma, 2007; Samrock et al., 2021; Wagner et al., 2017; Whaler K.A. and Hautut S., 2006). There also have been various MT studies in the CMER. However, only Hübert et al. (2018) and (Dambly et al., 2023) present the regional electrical resistivity structure of the crust using MT data along an end-to-end transect, crossing the entire rift from west to east. Otherwise, all other previous MT surveys conducted in the CMER were populated in the region east of the rift axis, especially areas of known geothermal potential such as the Aluto-Langano geothermal field, e.g. (Cherkose, B. A., & Mizunaga, 2018; Samrock et al., 2015, 2021). As a result, the crustal geoelectric structure of the eastern flank of the CMER and the major structural features like the Wonji Fault Belt (WFB) are studied in sufficient detail by means of the MT method. On the other hand, despite being characterized by densely clustered volcanic vents (near the Butajira volcanic field), which is part of the SDFZ, a full description of the subsurface geoelectrical picture of the western portion of the CMER still requires additional data.

The focus of this paper is to determine the subsurface electrical resistivity structure derived from closely spaced twenty-one (21) stations laid west of the rift axis, from Adami Tulu (the rift axis) to the western border of the CMER, traversing the major rift structures such as the SDFZ (see Figure 5.1). Previous research (Cherkose, B. A., & Mizunaga, 2018; Hübert et al., 2018; Samrock et al., 2015) found no significant low resistive body and structures on the eastern side of this profile. Aiming to contribute towards the understanding of the tectono-magmatic setting of the crust beneath the western flank and passways, the paper discusses the 2D analysis of MT data. The paper also scrutinizes the similarity and peculiarity of the crustal resistivity model to those obtained from previous MT studies in the eastern half of the CMER, especially from areas of known geothermal potential.

5.2 Geological setting

The study area is situated in the Central Main Ethiopian Rift (CMER), whose boundary faults span N30^{0}E–N35^{0}E (Bonini et al., 2005). The CMER formed 5–6 Ma after the occurrence of the northern Main Ethiopian Rift Valley (T. Abebe et al., 2010). The Quaternary activity of the boundary faults and subordinate axial faulting is the major geological activity of CMER (Agostini et al., 2011; Corti et al., 2020). The Quaternary volcano-tectonic setting in MER (Figure 5.1) is controlled by the arrangement of en-echelon faults in the WFB near the eastern margin (B. Abebe et al., 2007; Mohr P. A., 1962). Whereas on the western margin, Quaternary volcano-tectonic activity is represented by off-axis volcanism in the Butajira and Debre Zeit volcanic fields (B. Abebe et al., 2007). The WFB and the SDFZ are two linear belts in the CMER where recent magmatic and tectonic activities have been concentrated during the

Quaternary (Bonini et al., 2005; Casey et al., 2006; Chiasera et al., 2018; Ebinger & Casey, 2001; Morton, 1979; T. O. Rooney et al., 2014; Woldegabriel et al., 1990).

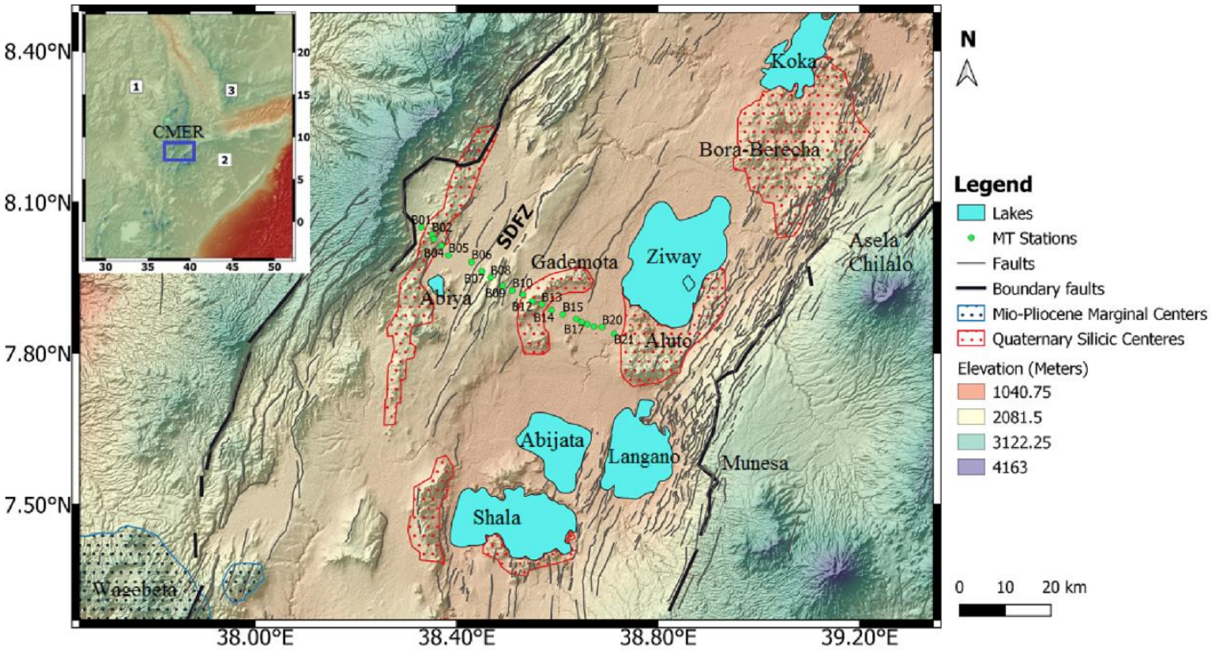

Figure 5.1 The geological setting map of the CMER with MT stations from Adami Tulu to the western border of the CMER and Quaternary Silicic centers in the study area. The measuring line is approximately 52 km long. The stations utilized in the 2D inversion are shown with green circles. There are faults in the east (Wonji Fault Belt) and the west (Silti Debre Zeit Fault Zone) (Adopted and modified from B. Abebe et al., 2007).

An en-echelon arrangement of the fault and magmatic centers of Quaternary magmatic segments (Figure 5.2) began at 1.6 Ma within the volcanism of the central rift valley and its flows originated from small cinder cones or fissures (Boccaletti et al., 1998; Keranen et al., 2004; Woldegabriel et al., 1990). The main characteristics of Quaternary magmatism in the MER are silicic centers and ignimbrites (2–1 Ma), with basaltic flows and scoria cones in the last 650 Ka (B. Abebe et al., 2007). In the CMER, magmatism subordinately affects the rift floor, but it is confined in proximity to the rift margins (Corti et al., 2020). Throughout MER, Plio-Pleistocene silicic volcanoes, calderas, and their eruptive products are present (B. Abebe et al., 2007; Woldegabriel et al., 1990). The SDFZ near the Western rift border is distinguished by a straight-line arrangement of basaltic flows associated with silicic centers, scoria cones, and nested calderas that run subparallel to the rift axis (Chiasera et al., 2018; Gasparon et al., 1993; T. Rooney et al., 2007; T. O. Rooney et al., 2011; Woldegabriel et al., 1990).

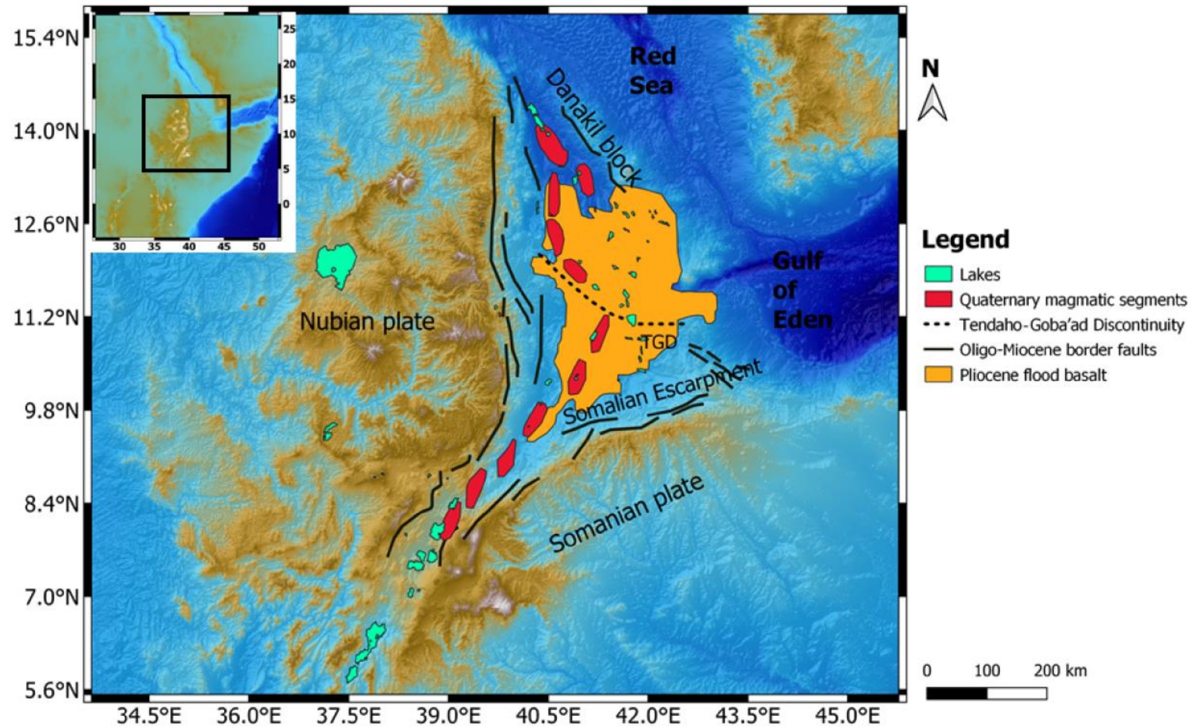

Figure 5.2 The map depicts the magmatic segments in the southern Red Sea, the westernmost part of the Gulf of Aden, and the MER systems (Beutel et al., 2010). The dashed lines represent the Tendaho Goba'ad Discontinuity (TGD), which extends the south Red Sea Rift zone and separates the N106 extending MER from the N41E (adapted and modified from Beutel et al., 2010).

5.3 Magnetotelluric Method

The magnetotelluric (MT) method uses natural electromagnetic field signals originating from the Earth's ionosphere (due to the interactions between the solar wind and the magnetosphere) and the Earth's atmosphere related to thunderstorm activity (Vozoff, 1991). The usual components of MT data from a single site comprise simultaneous records of the time variations of the two electric field components (E_X, E_y) and the three orthogonal magnetic field components (H_x, H_y, H_z), measured on the Earth's surface (Cagniard, 1953; Chave & Jones, 2012; N., Tikhonov, 1950; Simpson & Bahr, 2005). The depth variation is dependent on the measurement frequency range and the electrical resistivity in the subsurface, obeying the skin-depth rule of the propagation of EM signals. The broadband MT sounds with a period range from 0.001 s to 1000 s are usually suitable to probe from near the surface down to tens of kilometers beneath the measurement station (Simpson & Bahr, 2005).

The MT transfer functions, representing the frequency-dependent relation between the orthogonal pairs of electric and magnetic field components in the horizontal direction, are denoted by the complex impedance tensor **Z** (Simpson & Bahr, 2005; Vozoff, 1991), are given as:

$$\begin{pmatrix} E_x \\ E_y \end{pmatrix} = \begin{pmatrix} Z_{xx} & Z_{xy} \\ Z_{yx} & Z_{yy} \end{pmatrix} \begin{pmatrix} H_x \\ H_y \end{pmatrix} \tag{5.1}$$

where Z_{xx} , Z_{xy} , Z_{yx} and Z_{yy} are the impedance tensor elements of **Z**.

The components of the transfer function are then employed to obtain information on the subsurface resistivity distribution. At a given frequency, the mathematical equations that govern the relationship between the measured impedance (Z_{ij}), the apparent resistivity ($\rho_{a_{ij}}$) and phase (φ_{ij}) of the subsurface (Simpson & Bahr, 2005; Vozoff, 1991) are given as:

$$\rho_{a_{ij}}(r,\omega) = \frac{1}{\mu_0 \omega} \left| Z_{ij}(r,\omega) \right|^2 \tag{5.2}$$

$$\varphi_{ij}(r,\omega) = \arctan\left(\frac{\mathrm{Im}\left(Z_{ij}(r,\omega)\right)}{\mathrm{Re}\left(Z_{ij}(r,\omega)\right)} \right) \tag{5.3}$$

where, $\mathrm{Im}\left(Z_{ij}(r,\omega)\right)$ is the imaginary part of the electrical impedance, $\mathrm{Re}\left(Z_{ij}(r,\omega)\right)$ is the real part of the electric impedance, ω is the angular frequency and μ_0 denotes the magnetic permeability of free space.

The tipper vector (geomagnetic transfer function) T can be expressed as the complex dimensionless vector that relates the horizontal and vertical magnetic field components as:

$$H_z = T_{zx}H_x + T_{zy}H_y \tag{5.4}$$

where $T = (T_x, T_y)$ is known as the tipper.

Tippers can help to identify locations of high conductive zones, which are visualized as induction arrows and a 2D condition used to assist in defining the strike direction (Chave & Jones, 2012; Samrock et al., 2015). In accordance with the findings of Caldwell et al. (2004), the magnetotelluric phase tensor analysis of MT data have been employed to study the dimensionality information. The galvanic distortion that results from near-surface inhomogeneity does not affect a phase, which is a complex number represented as its ratio of real and imaginary parts.

The Earth's resistivity varies in a direction along with one of the horizontal directions and with depth in the 2D resistivity structure. The strike direction must be identified in order to decompose the impendence tensor in the TE (transfer electric) and TM (transfer magnetic) modes. The estimation of geoelectric strike direction was done by maximization of the off-diagonal elements and minimization of the diagonal elements of MT data by rotating the coordinate system (Simpson & Bahr, 2005; Swift, 1967; Vozoff, 1972). The 2D Occam inversion algorithm is used to recover the 2D electrical resistivity distribution on the profile along the Adami Tulu to the western border of CMER (near Butajira) which elucidates transfer function data and permits geological interpretations.

5.4 Data acquisition and processing

The MT data were collected in spring 2019 along a 52 km long profile spanning the CMER's western half, from Butajira (near the western border) to Adami Tulu (near the rift axis), as shown in Figure 5.1. The time series data were collected during > 24 h of installations, with an average station separation of 2.5 km. The MT recording system used at the local and remote stations was (MTU-5A) from Phoenix V5 system 2000, Canada (Phoenix Geophysics, 2009). A remote reference site was set at a sufficiently distant (about 20 km) and quiet place 5 channels were recorded as a time series of the electromagnetic fields simultaneously with all the measurement sites in the profile. These time series were transferred into the frequency domain in order to estimate the impedance tensor.

Remote referencing and robust processing were used to account for the presence of unidentified sources of noise (Clarke et al., 1983; Gamble et al., 1979; Goubau et al., 1978). The MT-Editor is also used for the removal of distinct cross-powers from the calculations and edits out noisy data to finally obtain a good-quality estimated transfer function and subsequently, the apparent resistivity and phase curves for the MT data (Ambunya, 2017).

5.5 Data analysis and 2D modeling

5.5.1 Dimensionality and Geoelectrical strike

Phase tensor analysis has been used to get dimensionality information on the regional structure and determine the regional strike of the study area (Caldwell et al., 2004). This is a very important step, prior to the inversion of MT data, in order to avoid model distortion. This means the model obtained after performing the analysis of phase tensor overcomes the problem of the model deviating from the true model (acceptable model). This also has the benefit of recovering the regional relationship of phase by removing the distortions due to the heterogeneity of the near-surface structure. The phase tensor is an efficient method for learning more about the dimensionality of the regional structure (Abossie et al., 2023a; Caldwell et al., 2004; Cherkose, B. A., & Mizunaga, 2018; Saibi et al., 2021). The advantage of using the phase tensor is in situations where the regional structure is three-dimensional. The phase tensor is beneficial in such cases because it does not rely on assumptions about the dimensionality of the underlying conductivity distributions. This means that it can effectively analyze and interpret data in complex geological settings where the conductivity distribution may not conform to simple, two-dimensional models (Saibi et al., 2021).

The phase tensor is graphically represented as an ellipse, with maximum ($\varphi_{\max}$), minimum ($\varphi_{\min}$), and skew angle, which is represented by the colour in ellipses, representing the major and minor axes, respectively (see Figures 5.3 and 5.4). The value of the skew angle (β), which can be utilized for dimensionality analysis, is frequently shown as coloured ellipses in phase tensor maps.

If the resistivity distribution of the region is 1D or 2D when the phase tensor is symmetric and skew angle is zero. In the 1D case, the values are equal, and β = 0, while in the 2D case, the regional resistivity structure has a different value, and for error-free data, β becomes small to zero. Therefore, the major axis of the phase ellipse is oriented by $\alpha - \beta$ (the alignment of one of the principal axes, which is parallel to the strike) (Caldwell et al., 2004; Heise et al., 2006). If the skew angle is different from zero (i.e $|\beta| > 3^0$) and the phase tensor is not symmetric, this implies the 3D regional resistivity distribution. For low skew values ($|\beta| < 3^0$), the geoelectric structure can still be called 2D. The phase tensor ellipse, on the other hand, has part of its principal axes in the direction of the strike. Whereas the non-symmetric phase tensor has a considerable skew angle (β). 3D resistivity structures are also implied by a rapid change in the phase tensor's principal axis laterally (Caldwell et al., 2004). As a result, all of the invariants, namely, $\beta \neq 0, \lambda \neq 0, \varphi_{\max} \neq 0,$ *and* $\varphi_{\min} \neq 0$, are non-zero when assuming a 3D structure)

In the present study, the MTpy open-source Python tool (Krieger & Peacock, 2014) was used to estimate the regional geoelectric structure and phase tensor pseudosection plots. The dimensionality of the subsurface formations beneath each station is shown by the phase tensor ellipses pseudo section, colour-coded by skew angle values, along the western margin (near Butajira) to the Adami Tulu transect shown in Figure 5.3. Accordingly, over the period range below 10 s, the phase tensor plot exhibits a dominantly circular and elliptical shape with a small skew angle ($|\beta| < 3^0$) indicating the subsurface resistivity structure as 1D and 2D, respectively. Over a long period, the phase tensor shows a few large values of skew angle ($|\beta| > 3^0$) which indicates the presence of a 3D resistivity structure.

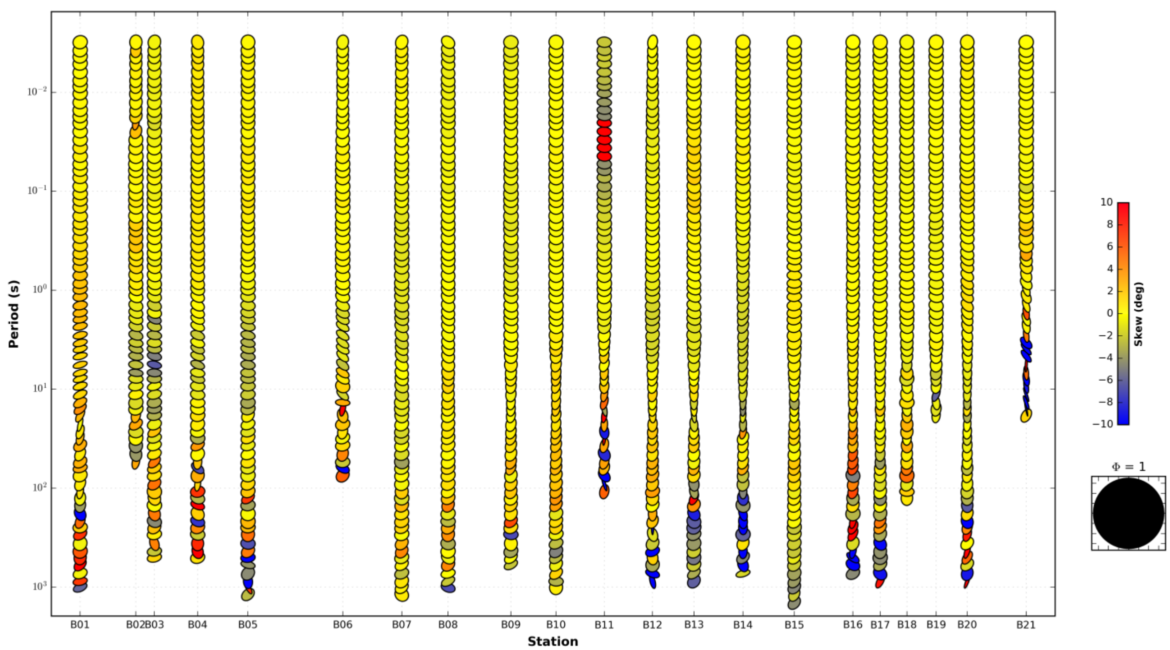

Figure 5.3 Map of the phase tensor pseudosection of MT data along the profile across the CMER for all recorded periods. The fill colors describe the value of the skew angle. The majority of stations and period ranges have low skew values ($|\beta| < 3^0$), indicating that a 2D inversion model is appropriate (Caldwell et al., 2004).

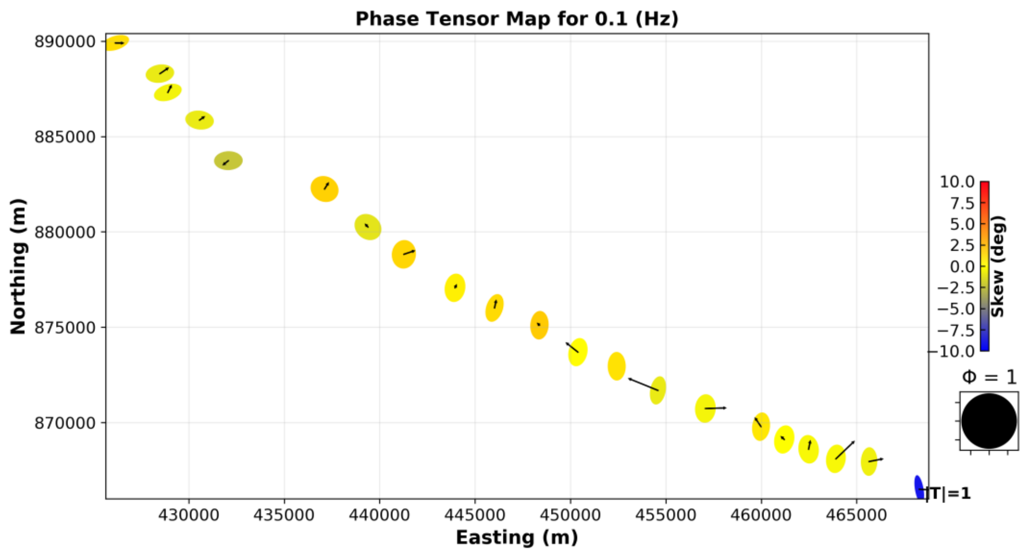

Figure 5.4 Map depicts the phase tensor of all stations from the western margin (near Butajira) to Adami Tulu at 0.1Hz frequency, and phase tensor ellipses and tipper vectors (plotted according to the Parkinson convention).

The geoelectric strike analysis along the transect was done using phase tensor azimuth and strike estimates by Z invariants and the result is shown in the rose diagram in Figure 5.5.

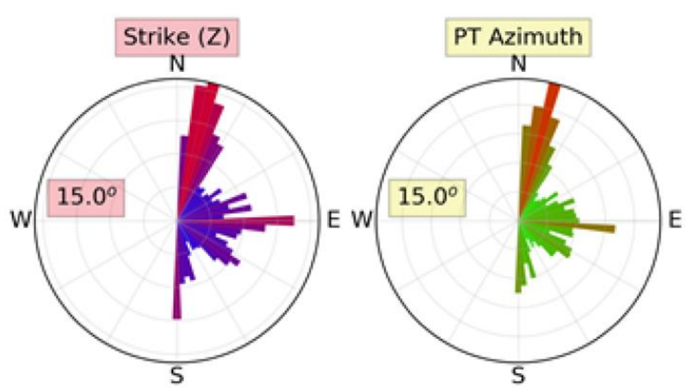

Figure 5.5 Rose diagram of phase tensor azimuth and strike estimates by Z-invariants of the study area along the western border to the Adami Tulu transect. The strike analysis is carried out across the entire frequency range.

Phase tensor azimuth and **Z** strike analysis were utilized to examine the geoelectrical strike direction of all 21 sites in the study area along the profile. The prevailing geoelectric strike direction for both methods of estimation is N15^{0}E (Figure 5.5). The Z-invariants and phase tensor strikes of geoelectric strike estimates (i.e., N15^{0}E), as shown in Figure 5.5, correspond well with NNE-SSW, the major fault system in the CMER, and are consistent with the regional strike direction (Corti et al., 2020; Korme et al., 2004; Pizzi et al., 2006; Samrock et al., 2021). The realization of the geoelectric strike direction and dimensionality situation is important to avoid model distortion before the inversion of the impedance data. Hence, the 2D inversion model of MT data were executed after rotating the components of the impedance tensor at N15^{0}E.

5.5.2 Two-dimensional Inversion

The widely used two-dimensional MT theory and inversion algorithms are well-developed (DeGroot-Hedlin, C., and Constable, 1990; Jupp & Vozoff, 1977; Ogawa & Uchida, 1996; Rodi & Mackie, 2001; Siripunvaraporn & Egbert, 2000). Occam's inversion, the Gauss-Newton method, and the nonlinear conjugate gradient method are the three most commonly used 2D inversion algorithms.

Based on DeGroot-Hedlin and Constable (1990), the Scripps Institution of Oceanography developed the 2D inversion modeling code for Occam's 2D inversion, which was employed in this study.

The minimization of an unconstrained functional is used to implement Occam's 2D inversion as follows:

$$\mathrm{U} = \left\|\partial_{\mathrm{y}}\mathbf{m}\right\|^2 + \|\partial_{\mathrm{z}}\mathbf{m}\|^2 + \mu^{-1}\left\{\left\|\mathbf{W}\big(\mathbf{d} - \mathbf{F}(\mathbf{m})\big)\right\|^2 - \mathrm{x}_*{}^2\right\} \tag{5.5}$$

where $\left\|\partial_{\mathrm{y}}\mathbf{m}\right\|^2 + \|\partial_{\mathrm{z}}\mathbf{m}\|^2$ is the norm of model roughness, μ^{-1} is the Lagrange multiplier, $\mathrm{x}_*{}^2$ is the data misfit, **d** is the observation vector, **W** is the $\mathrm{M} \times \mathrm{M}$ diagonal weighting matrix, and $\mathbf{F}(\mathbf{m})$ is the model response.

The 2D inversion of magnetotelluric data along the Butajira to Adami Tulu traverse in the CMER contains 21 MT stations, each about 2.5 km apart on average (Figure 5.1). Aimed at the inversion, 67 frequencies in the range (0.0014 Hz – 320 Hz) were used. In comparison to inverting the individual modes separately, the model obtained through a joint inversion of TE and TM modes was found to be smoother and more reliable in revealing the conductivity structure of the subsurface. The 2D inversion model was performed after rotating the MT data in the proper direction of the geoelectric strike at $\mathrm{N15^0E}$ (see Figure 5.5). The ideal geoelectric strike of the study area ($\mathrm{i.e., N15^0E}$) is consistent with the direction of the major fault (NNE-SSW) in the CMER.

During the inversion procedure, error floors for apparent resistivity greater than a phase were used to suppress a static shift effect in the MT data induced by local near-surface inhomogeneity (Ogawa, 2002; Saibi et al., 2021; Wu et al., 1993). To establish a suitable fit between the observation and the model response, different parameters like roughness type, mesh size, and error floor inversion were tested in order to obtain a good fit between the observation and model response. For the 2D transverse electric (TE), transverse magnetic (TM), and joint inversion of TE and TM modes, the error floors for apparent resistivity of 20% and phase of 7% (equivalent to 2.03^0) were used to suppress the parallel shift problem of the apparent resistivity curves caused by local near-surface inhomogeneity or topography, while the phase curves are basically consistent (Caldwell et al., 2004; Didana et al., 2014; Saibi et al., 2021; Tietze et al., 2015). A fine mesh was generated with a homogeneous half-space of 100 Ωm which was used as the starting initial model for the model presented here. Figure 5.6 shows pseudosection plots of the observed data and model response, while site-by-site plots of the model response give supporting information for Figure 5.7. The desired 2D resistivity model of the joint inversion of TE and TM modes data achieved a minimum misfit with an RMS misfit of 1.11 (Figure 5.7). The pseudosection reveals that the resistivity and phase of the TE and TM modes are different at periods > 10 s, which is consistent with the multidimensionality of the MT data revealed by the phase tensors.

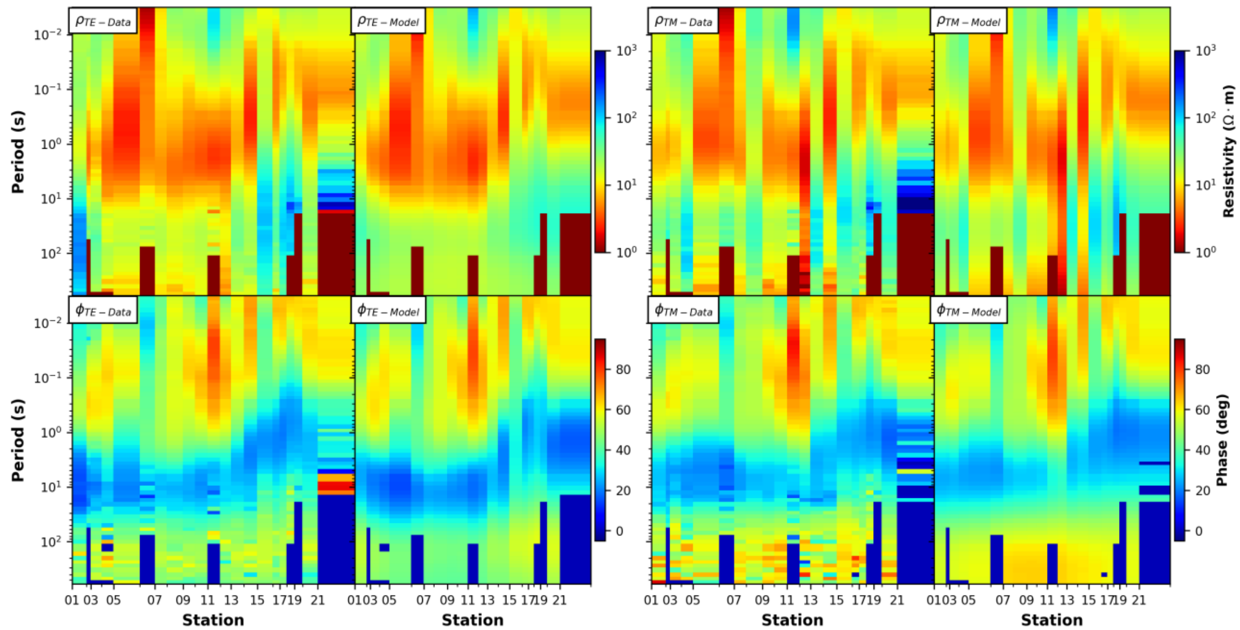

Figure 5.6 Pseudosections plots of the observed and calculated response of apparent resistivity and phase along the profile from the western margin of the rift (near Butajira) to Adami Tulu (near the rift axis). for TE mode (left) and TM mode (right). The psedosection indicates that the TE and TM mode resistivity and phase at periods > 10 s are different, which is consistent with the multidimensional nature of the MT data identified by the phase tensors. Apparent resistivity (top row); phase (bottom row).

The long-period phase response of the TM mode is indeed recognized for its enhanced sensitivity to deeper structures compared to the TE mode for the same period (Didana et al., 2014), Additionally, the inversion model for the TM mode displays a resistivity structure similar to that of the joint inversion, as shown in Figure 5.7 of the supporting information. The studies also indicate that the TM mode is more sensitive to near-surface structures and more robust against the effects of 3D structures when a conductive 3D structure is interpreted by a 2D approximation. On the other hand, the TE mode is described as inductive in nature and more sensitive to deeper structures. (Chao & Osella, 2003; Berdichevsky, 1998; Malleswari et al., 2019).

Thus, the gaps left by one mode can be filled by another mode. If so, the most comprehensive and reliable information on the conductivity of the Earth's interior can be obtained using both modes, i.e. the transverse and longitudinal MT curves (Chao & Osella, 2003; Berdichevsky, 1998; Malleswari et al., 2019). However, the joint inversion of TE and TM has been recommended in order to obtain complimentary information on the subsurface resistivity distribution in the case of the 2D model (Chao & Osella, 2003; Berdichevsky, 1998). For a lower resistivity (high conductivity) at a greater depth, the 2D model has a shortcoming in the poor model fit and in the dimensionality assumption rather than the 3D case (Wannamaker et al., 2017). We suppose this is the case because the lateral resolving contribution from the xy component of the impedance (TE mode) is absent in 2D. So in order to obtain a good fit, dimensionality, and a clear picture or extension of magma storage, a 3D analysis is needed by adding more than two profile parallels to this study area.

To evaluate the quality of the final recovery model, the root mean square misfit (RMS) and roughness distributions were examined for each iteration. The root-mean-square (RMS) data misfit (Xiang et al., 2017) is presented in Occam's inversion, which is calculated as follows:

$$\mathrm{RMS} = \sqrt{\frac{1}{N}\sum_{i=1}^{N}\left(\frac{d_i^{obs}-d_i^{cal}}{e_i}\right)^2} \qquad (5.6)$$

where d_i^{obs} and d_i^{cal} are represent the observed and predicted responses, respectively, and e_i is observed response errors, and N is the number of responses at all sites and times evaluated.

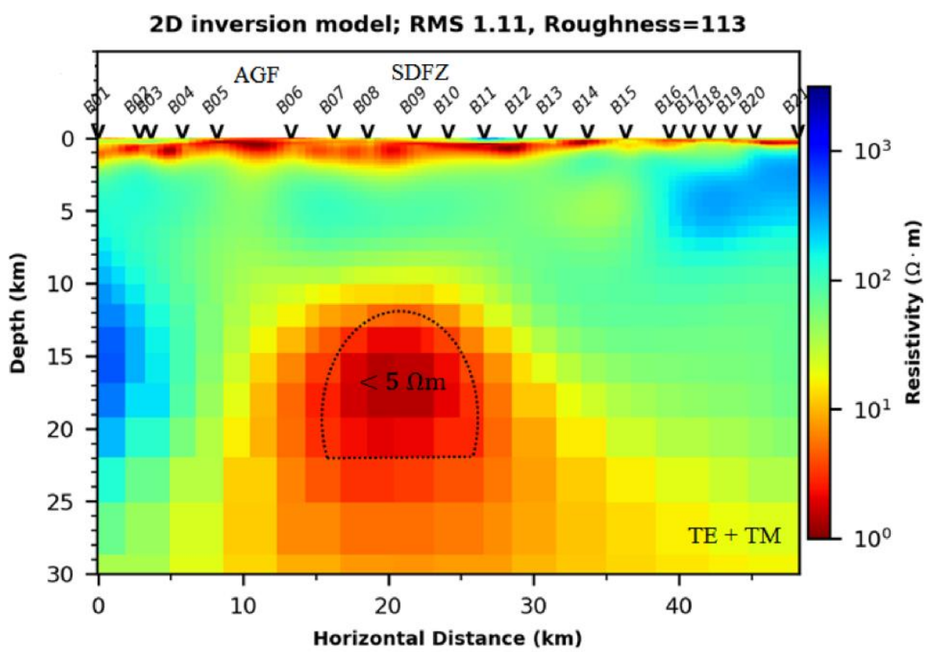

Figure 5.7 The subsurface electrical resistivity model resulted from the joint 2D inversion (TE & TM) of the MT transfer functions (apparent resistivity and phase) along the western margin of the rift (near Butajira) to Adami Tulu (near the rift axis) that crosses SDFZ and Ashute geothermal field (AGF) in the CMER.

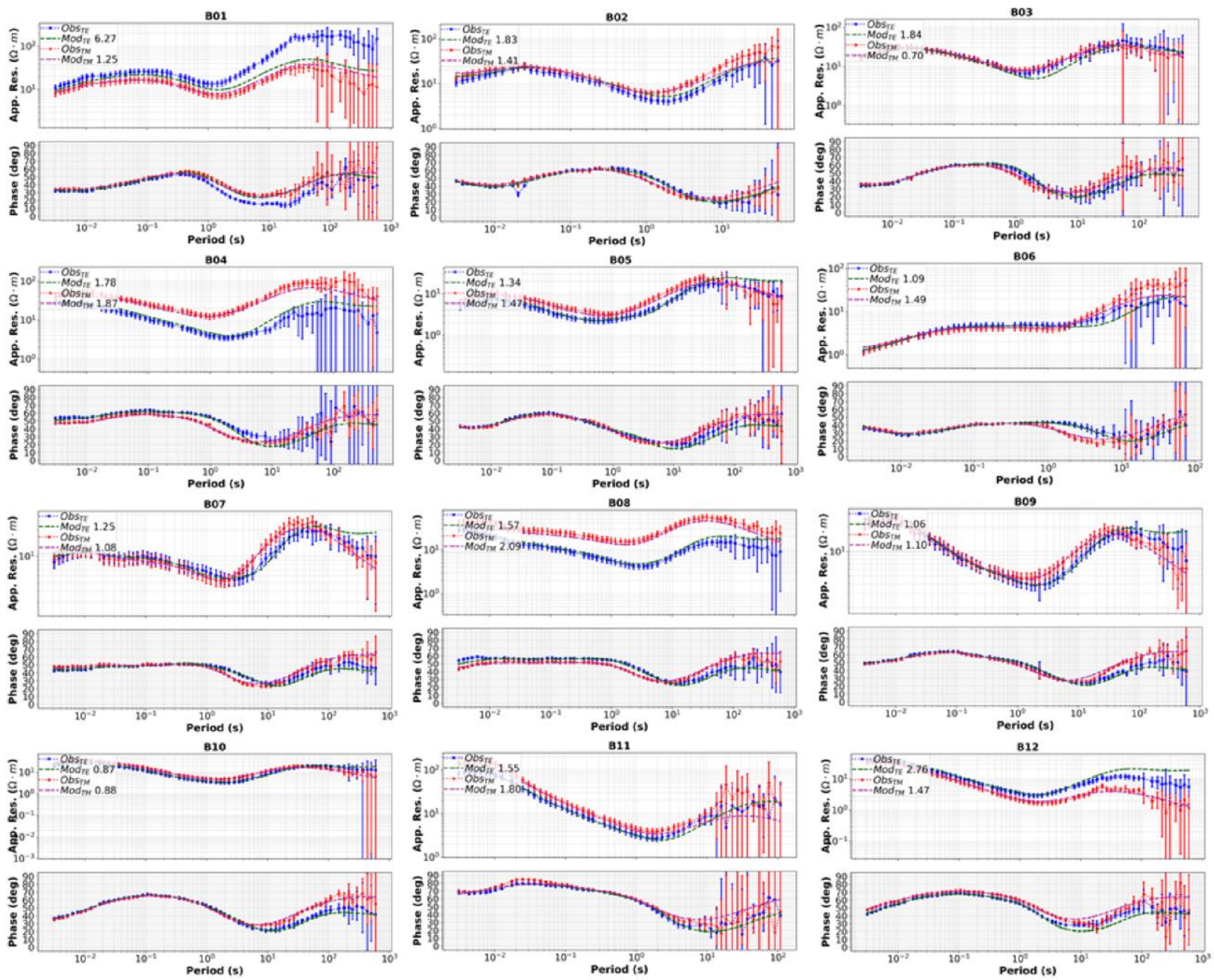

Figure 5.8 2D inversion data fits the observed data and calculated responses for twelve stations from B01 to B12 of the study area. The blue squares represent the TE observed response, the red dot represents the TM observed response, the green dash line represents the TE modeled (calculated) response, and the pink dash line represents the TM modeled (calculated) response.

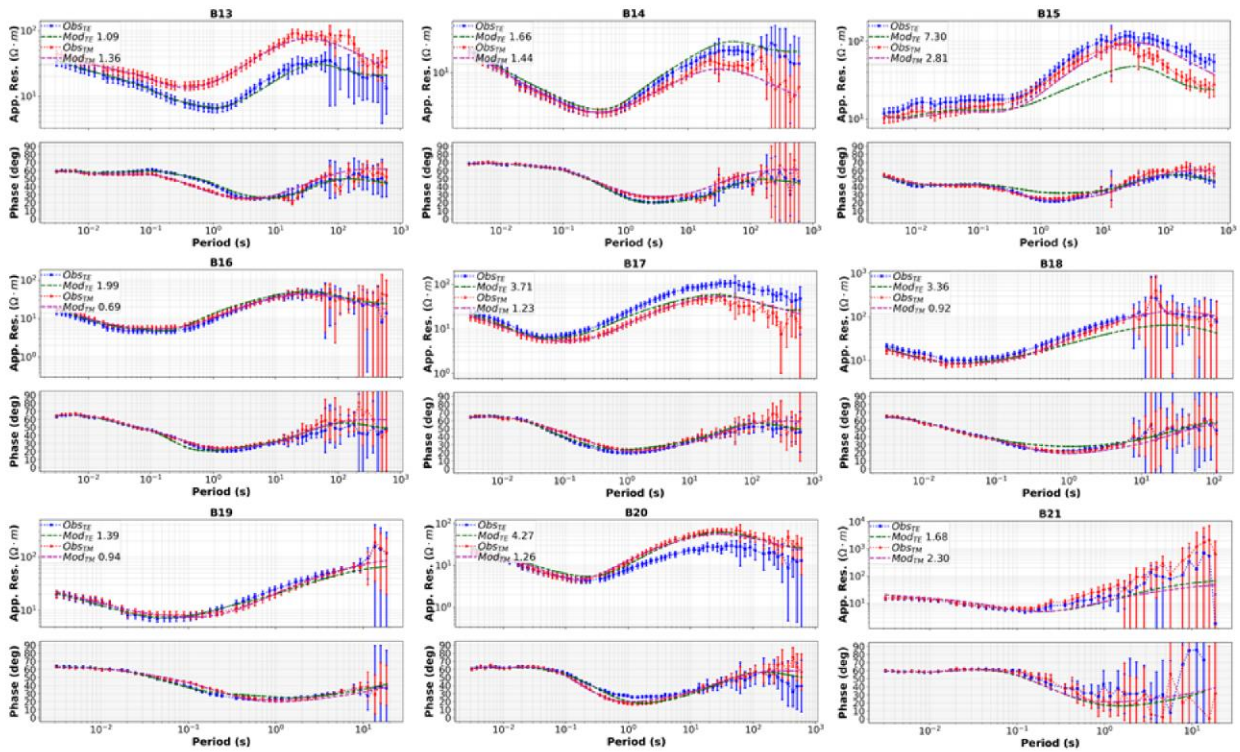

Figure 5.9 2D inversion data fits the observed data and calculated responses for nine stations from B13 to B21 of the study area. The blue squares represent the TE observed response, the red dot represents the TM observed response, the green dash line represents the TE modeled (calculated) response, and the pink dash line represents the TM modeled (calculated) response.

In this investigation, the preferable model obtained in the initial RMS of the 2D inversion model at the starting misfit was 8.35 and decreased to 1.11. The joint inversion of TE and TM modes has a larger misfit than the two modes, as shown in Figures 5.7 and 5.10. Compared with TE and TM modes, the TE-mode inversion has a large misfit, and the corresponding model is also different from the real one (Figures 5.7 and 5.10). The resulting model's data misfit is reasonable, with only a few under or over-fitted data portions. The fitness of observed data and calculated (model) response produced for the models are displayed in Figures 5.8 and 5.9, and site-by-site plots of the model response acquired for this model are provided in the supporting information for the final 2D resistivity model in Figure 5.7.

Therefore, in addition to solving an ill-posed mathematical issue, one needs to carefully evaluate the sensitivity of the data in order to obtain a physically and geologically acceptable model (Schwalenberg et al., 2002). The optimal model constraints can be constructed using a priori information about regions of lower seismic shear wave velocities beneath the Silti-Debre Zeit Fault Zone (SDFZ) on the western side of the CMER studied by Kim et al. (2012). For the 2D model of MT data, determining the stability and robustness of performing features and performing tests to check whether the anomaly found is necessary for the final model. This helps to determine the validity of the anomalies in the model. For this, we tried to adjust some necessary parameters when running the program in the 2D inversion model of TE, TM, and joint inversion of TE and TM modes.

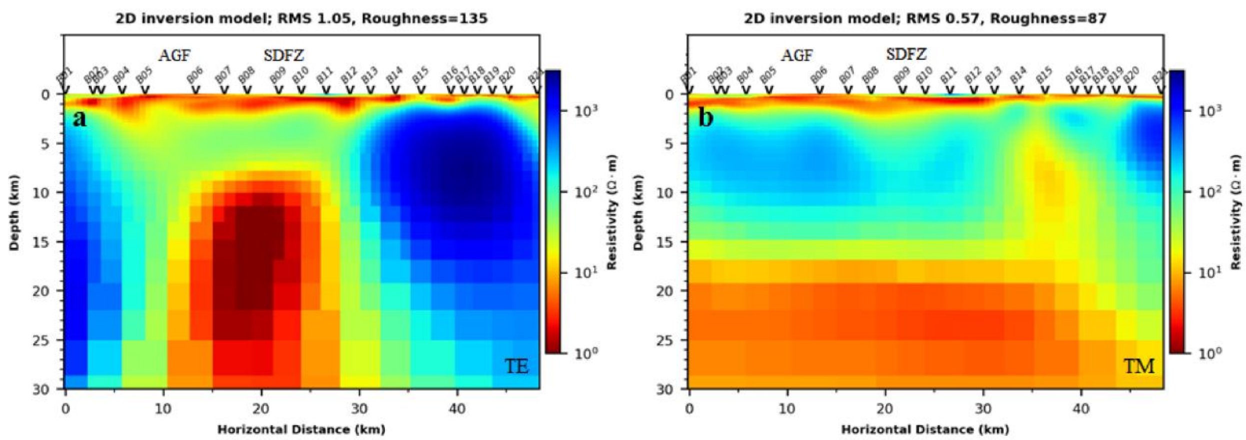

Figure 5.10 The 2D model of a) Transverse electric (TE) mode and b) Transverse magnetic (TM) mode obtained from the profile along the Butajira to Adami Tulu travers crossing the western flank of the CMER.

In the case of 2D inversion magnetotelluric data, the sensitivity is responsible for the transverse electric (TE) and transverse magnetic (TM) modes of inversion of magnetotelluric data to detect shallow and deep structures (Chao & Osella, 2003; Berdichevsky, 1998; Malleswari et al., 2019; Schwalenberg et al., 2002). Berdichevsky (1998) suggested that the TM mode is more sensitive to near-surface resistive structures and outlines the deep conductive faults than the TE impedance, while the TE mode helps to detect the conductive zones in deep layers of the lithosphere and the asthenosphere. In the 2D model of this study as shown in Figure 5.7 the deep conductivity zone in the mid-crustal depth is observed in the TE mode whereas the shallow resistive structure is more resolved in the TM mode as shown in Figure 5.10. Therefore, the information that can be obtained from the individual TE and TM modes complement one another. The joint inversion of TE and TM exhibits some features from each of the inversions of the individual modes of TE and TM (Malleswari et al., 2019). Moreover, cross-checks were made between the anomalous body and fitting curves of each station. Finally, the fitting curves were compared at each station, especially those above the anomaly body, with the inversion results in order to check the thickness of the mid-crustal anomaly, and they are consistent with the previously studied result of Kim et al. (2012) along the SDFZ.

It is known that the non-uniqueness of models is one of the major pitfalls of magnetotelluric data inversion. A large number of other possible models may explain the observations within a given range of misfits (error). In this study, a hypothesis testing approach (Unsworth & Bedrosian, 2004) was utilized to determine if prominent features in the model are required by the data.

The model for Adami Tulu to the western margin of the CMER was altered in the first step such that the Silti Debre Zeit Fault Zone conductor (SDFZC) ended at 1 km. Figure 5.11a depicts the expected TE mode phase at station 10 on the given traverse and shows the forward and predicted responses of the model. The MT data are incompatible with a shallow (1 km) conductor, and the SDFZC resistivity results in a lower phase than observed at the short and long periods.

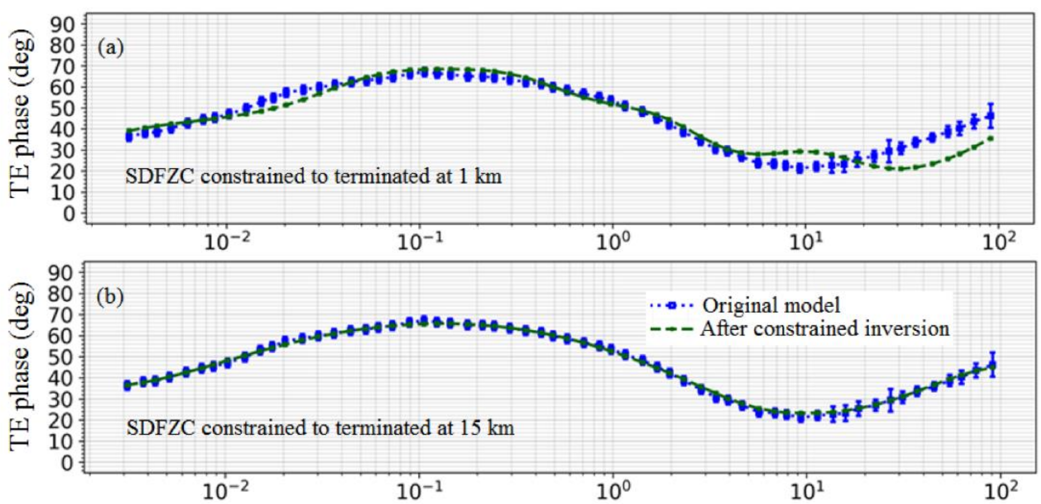

Figure 5.11 (a) TE mode phase response at station 10 on the profile along SDFZ, illustrating the constrained inversion. This is the 10th station in the continuous array. The SDFZC beneath the SDFZ was terminated at 1 km, producing a lower phase than observed. After restarting the inversion, the original fit was not regained. (b) Same responses when the SDFZC is extended to 15 km depth and the original fit is almost recovered.

However, this forward modeling approach is a necessary complement to other methods and a condition for proving that the SDFZC does not terminate at 1 km. Because MT data are inherently non-unique, altering other parts of the model might also produce a statistically acceptable data misfit (Unsworth & Bedrosian, 2004). The conductance of a buried layer is often calculated using MT data (the product of conductivity and thickness). Equivalence is the phenomenon whereby several models with the same conductivity but different thicknesses can all fit the same data (Unsworth and Bedrson, 2004). This can be seen in the constrained inversion, where the algorithm lowers the resistivity in the SDFZC between the surface and 1 km of depth in an attempt to fit the MT data. However, the MT data directly constrains the layer's resistivity, which makes this approach only partially successful for surface layers. The new response of this SDFZC that terminated at 1 km is depicted in Figure 5.11a for station 10 after the constrained inversion converged, and its misfit is 2.1. The fact that the original fit is unable to be recovered shows that the surface resistivity is too low. From the surface to 1 km depth, a similar test was carried out with the entire model fixed except for the SDFZC, and the same results were obtained. As a result, we conclude that the data is incompatible with a model of SDFZC at 1 km deep.

The comparable tests were carried out on a model with a 15 km SDFZC at station 10, as seen in Figure 5.11b. The constrained inversion almost completely recovers the original fit. The response misfit under station 10 of SDFZC, which terminates at 15 km, is 0.67. Therefore, the responses achieved by the tests (sensitivity) are coherent with the original responses at a deeper depth than the shallow in the same conductor.

5.6 Result and Discussion

Phase tensor analysis has been used to get dimensionality information on the regional structure and determine the regional strike direction across the CMER along the profile from the western margin of the rift (near Butajira) to Adami Tulu. The dimensionality analysis result indicates 1D and 2D structures at shallow depths, and deeper depths show 3D. The regional geoelectric structure obtained from phase tensor Azmuith, and Z strike are consistent and N15^{0}E striking.

Therefore, the 2D inversion model of MT data were executed after rotating the components of the impedance tensor at N15^{0}E.

Referring to Figure 5.7, the 2D inversion model of MT data along a profile on the western edge of CMER (from Adami Tulu to near Butajira) shows the subsurface electrical resistivity picture to a depth of 30 km. The best-fit model revealed four main resistivity structures: high-resistance layers (> 100 Ωm), mixed with the low resistivity body at the top layer, followed by a conductive layer below 10 Ωm which overlies of a moderately resistive layer with values of resistivity (10–100 Ωm), and at deeper depths and underlay by a conductive layer with a resistivity < 5 Ωm. Most of the uppermost layer has a resistivity of < 10 Ωm and starts from the surface with a variable thickness running from 50 m to 2 km. The conductive zone in the Ashute geothermal field (AGF) that appears beneath the station between B05 and B07 is the alteration zone (argillic zone), with smectite or illite as the dominant mineral and low resistivity (< 10 Ωm). The mud pools and hot springs are also manifest in this area. The remaining conductive zone in the uppermost layers exists in the east part of the profile with a thin layer of low resistivity exposed, which might represent lacustrine sediment. Two distinct resistive bodies of > 100 Ωm are located in the uppermost layer of the extinct Gademotta caldera, which is located to the west of Ziway (Figure 5.1), beginning at the surface and rising to approximately 200 m, whereas the other high resistive body found in the western part of the profile is closer to the Guraghe border fault with thin layers of Quaternary volcanic from station B01 to B05. The second zone, with a resistivity value of < 10 Ωm, is located beneath the upper thin layer and may be associated with the presence of smectite or illite as a result of mineral alteration. The third zone (illite/chloride) has an intermediate resistivity value of 10–100 Ωm. Whereas below this zone is characterized by the high conductivity layer of < 5 Ωm. It could be related to the source of heat for the Ashute and Aluto geothermal fields. The high conductive zone located at a depth of approximately 12–22 km beneath stations B07 to B11 in the middle of the profile is expected to melt. Directly above the high conductive zone, the intermediate resistivity zone (up-flow zone) that is connected to the low resistivity zone is likely an active fault zone. The WFB and the SDFZ are two linear belts in the CMER where recent magmatic and tectonic activities have been concentrated during the Quaternary (Bonini et al., 2005; Casey et al., 2006; Chiasera et al., 2018; Ebinger & Casey, 2001; Morton, 1979; T. O. Rooney et al., 2014; Woldegabriel et al., 1990). The seismic velocities of the upper crustal layers are 5–10% higher than those outside the rift beneath the rift axis as a result of mafic intrusions linked with magmatic centers found in the Main Ethiopian rift valley (Mackenzie et al., 2005). Forward modeling of the tipper results of Samrock et al. (2015) and 2D magnetotelluric data results of Hübert et al. (2018) is consistent with the presence of a magmatic source obtained beneath stations B07 to B11 along the SDFZ. In their ambient seismic noise investigations, Kim et al. (2012) found low-seismic velocity zones at mid-crustal depth beneath the WFB, in the transition between the NMER and the Central Main Ethiopian Rift (CMER), and beneath the SDFZ on the western side of the CMER. The low magnetic anomaly map begins at Aluto and extends towards the Western plateau border in the NW direction of Aluto at a depth extending down to 3 km (H. Kebede et al., 2021). This could be related to the pre-existing striking subsurface, which is revealed by a negative gravimetric anomaly caused by NW-SE striking subsurface graben filled with the effect of low sediment density between 7^0N and 8^0N latitudes, a 15 km wide zone along the CMER floor (Korme et al., 2004). This traverse indicates the existence of heat conduction structural elements expected as a heat flow path. This could be related to a pre-existing subsurface, which is revealed by a negative gravimetric anomaly caused by NW-SE striking subsurface graben filled with the low-density sediment in a 15 km wide zone along the CMER floor between 7^0N and 8^0 latitudes (Korme et al., 2004). This traverse indicates the existence of heat conducting structural elements expected as a heat flow path.Therefore, the magma chamber that exists along the SDFZ could be used as the heat source of the Ashute geothermal field.

5.7 Conclusion

The 2D inversion model of the magnetotelluric method, which determines the subsurface regional resistivity structure, is a frequently used technique in tectono- magmatic studies. The dimensionality analysis of the profile along Adami Tulu- western margin of CMER at shallow depths indicates 1D and 2D structures, and deeper depths show 3D structures. The dominant geoelectrical strike obtained by Z-invariant and phase tensor azimuth were consistent and estimated as N15^0E. Hence, a 2D inversion model of MT data was executed after rotating the components of the impedance tensor at N15^0E. Based on DeGroot-Hedlin and Constable (1990), the Scripps Institution of Oceanography developed the 2D inversion modeling code for Occam's inversion, which was employed in this study. For the 2D inversion, 21 sites of MT data covering a total of 67 frequencies over a frequency range of 0.0014–320 Hz were utilized for the inversion process. The preferred model revealed four main resistivity structures very high resistivity (>

100 Ωm) mixed with the low resistivity body at the top layer, followed by a conductive layer < 10 Ωm overlays the moderately resistive layer with values of resistivity (10–100 Ωm), at deeper depths. The high conductive anomalies below the intermediate resistivity layer in the upper crust from 12 to 22 km are expected to be associated with partial melt and/or fluids in dike intrusion between stations B07 and B11 in the middle of the profile. The high conductivity zone of < 5 Ωm obtained from this study is expected to be a partial melt zone observed along the SDFZ. This result is in good agreement with the previous study of Hübert et al. (2018) using 2D magnetotelluric data and Samrock et al. (2015) suggested an area where the existence of a conductive body by his forward modeling results of tipper approximately 40 km NW of Aluto. The presence of pre-existing structures in the CMER that were identified by Korme et al. (2004) is expected as a heat flow path. Kebede et al. (2021) also obtained the low magnetic anomaly that begins at Aluto and extends towards the Western plateau border in the NW direction of Aluto at a depth extending down to 3 km. This may be expected to be a heat flow path. Therefore, the magma chamber obtained from this study could be related to the source of heat for the Ashute geothermal fields.

Chapter 6 Joint 1D inversion of TEM and MT data and Comparison of 3D Inversion Results with and without Static Shifted Magnetotelluric Data in the Ashute Geothermal Field, Central Main Ethiopian Rift (CMER)

6.1 Introduction

The Ashute geothermal field is one of the geothermal sites discovered in the Central Main Ethiopian Rift (CMER) near the Silti Debre Zeit fault zone (SDFZ). To assess geothermal resources, the magnetotelluric (MT) approach has been widely employed (Chave & Jones, 2012). However, because of near-surface inhomogeneity, magnetotelluric data in the geothermal area suffers from a static shift effect for inaccurate estimation of apparent resistivity curves. The static shift corrected MT data gives better and more accurate estimates of subsurface structure of resistivities and thicknesses, whereas uncorrected magnetotelluric data displayed by the vertical shift curves of apparent resistivity can lead to erroneous and unreliable estimates (Sharma & Biswas, 2011; Tournerie et al., 2007). To correct static shifts, several solutions have been presented. Some of these techniques include spatial filtering (Berdichevskiy, 1976; V. I. D. and E. E. P. M. N. Berdichevsky, 1998; Simpson & Bahr, 2005), curve shift estimation (Árnason et al., 2010; Pellerin, 1990; Simpson & Bahr, 2005; Sternberg et al., 1988), geostatistical model to estimate static shift by cokriging method (Tournerie et al., 2007), spatial curve averaging (Singer, 1992; SINGER, 1990; Sternberg et al., 1988), electromagnetic field modeling using thin sheet modeling programs (Grandis & Menvielle, 2015; Robertson, 1988; Vasseur & Weidelt, 1977), and the Gauss-Newton inversion scheme (Sasaki, 2004; Uchida & Sasaki, 2006). The Transient Electromagnetic (TEM) method, in combination with the MT method, has been widely used to examine the subsurface properties of geothermal reservoirs, such as porosity, rock–water reactions, temperature, salinity, and permeability, and their direct relationships (Hersir & Bjornsson, 1991; Marwan et al., 2019).

In this work, the static correction was achieved by joint 1D inversion of TEM and MT data from the same site to mitigate the limitation of a 1D subsurface and comparison of 3D inversion results with and without Static Shifted full impedance tensor MT data of 30 MT stations from the Ashute geothermal area, CMER. In the inversion, 76 frequencies with periods of 0.001 to 1000 s were used. This leads to better knowledge of subsurface resistivity structures as well as the amount and scope of geothermal activity. The main focus of the study is to apply a static shift correction scheme to MT data and compare models obtained from 3D MT inversion with and without static shift correction, specifically focusing on the Ashute geothermal field. In comparison to earlier research to confirm their validity, it also showed agreement with the complex geology of the Ashute geothermal field.

6.2 Location of Ashute geothermal area

The Ashute geothermal field is situated in the CMER near the western escarpment, near the SDFZ with a latitude of $7.94^0\mathrm{N} - 8.05^0\mathrm{N}$ and a longitude of $38.31^0\mathrm{E} - 38.47^0\mathrm{E}$.. This area is swampy, with geothermal manifestations and concentrated tectonic and volcanic activity. In such geothermal areas, static shift can be a major issue due to high resistivity fluctuations. By reducing the static shift effect owing to subsurface inhomogeneity from MT data, geophysical surveys such as TEM and MT were conducted to delineate the anomaly and examine the source of heat in the geothermal area. The emphasis of this study is to examine the distribution of resistivity in the Ashute geothermal field in order to determine the geothermal system and structural properties of the area.

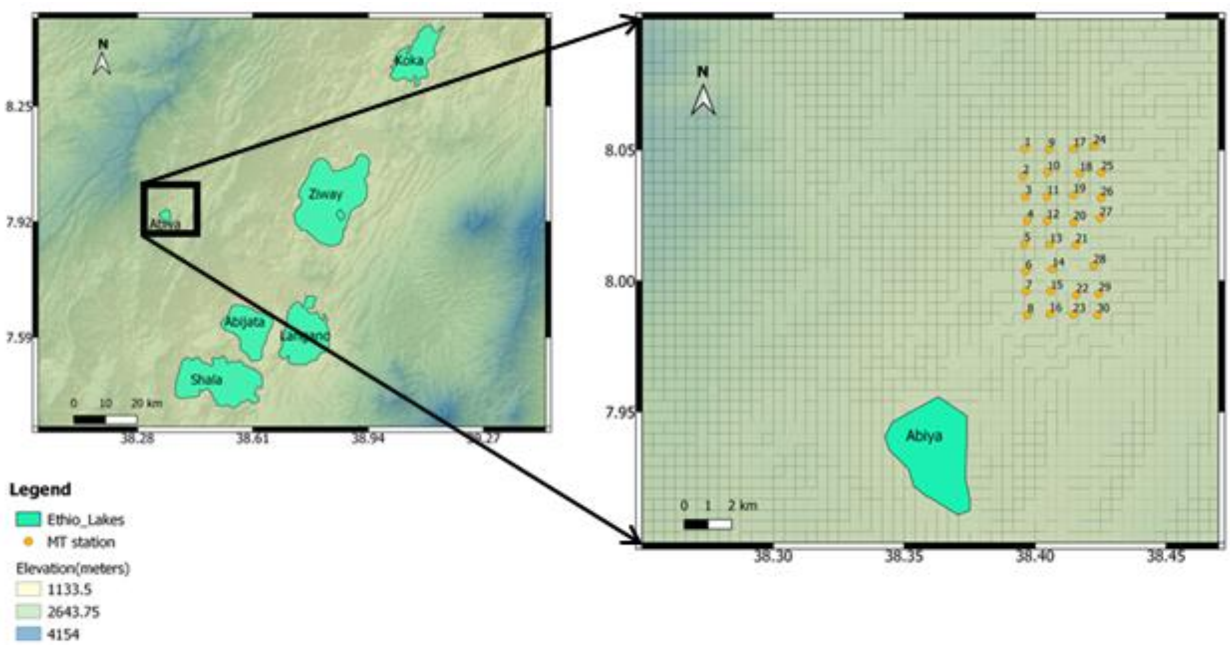

Figure 6.1 shows the Ashute geothermal field with MT station in the CMER

6.3 Geological setting

Several traces of manifestations, such as hot springs, Crater Lake, Fumarole, and a mud pool, can be found in the Ashute area. Most of the hot springs appear in the west and southwest directions of the study area (see Figure 6.2). Hot springs, which have a high flow rate and a high discharge temperature, were points of consideration. The thermal manifestation around the area shows a good permeable zone and high CO_2 flux near the western rift escarpment (Abossie et al., 2023a; Hunt et al., 2017; Sinetebeb et al., 2020).

The Butajira and Debre Zeit/Bishoftu volcanic chains are part of the SDFZ and have experienced volcanic activity during the Quaternary period on the western side of the CMER. The majority of the SDFZ on the western side of CMER is characterized by Quaternary central volcanoes and basaltic lava flow, along with phreatomagmatic deposits and scoria cones CMER (T. Abebe et al., 2010). Woldegabriel et al.(1990) observed welded tuff with nested scoria cones that run parallel to the Guraghe escarpment in the Ashute area. The study area contains highly vesicular basalt, scoria, rhyolite, pyroclastic flow deposits, layered pumice, and crystalline ignimbrite, with the Ashute geothermal field covered by lacustrine sediment deposits. Rooney (2010) suggested that Plio-Quaternary volcanism along the eastern rift margin is attributed to the WFB, while activity along the western rift border is attributed to the SDFZ within the CMER, with the SDFZ extending from 6.5 to 9 degrees north.

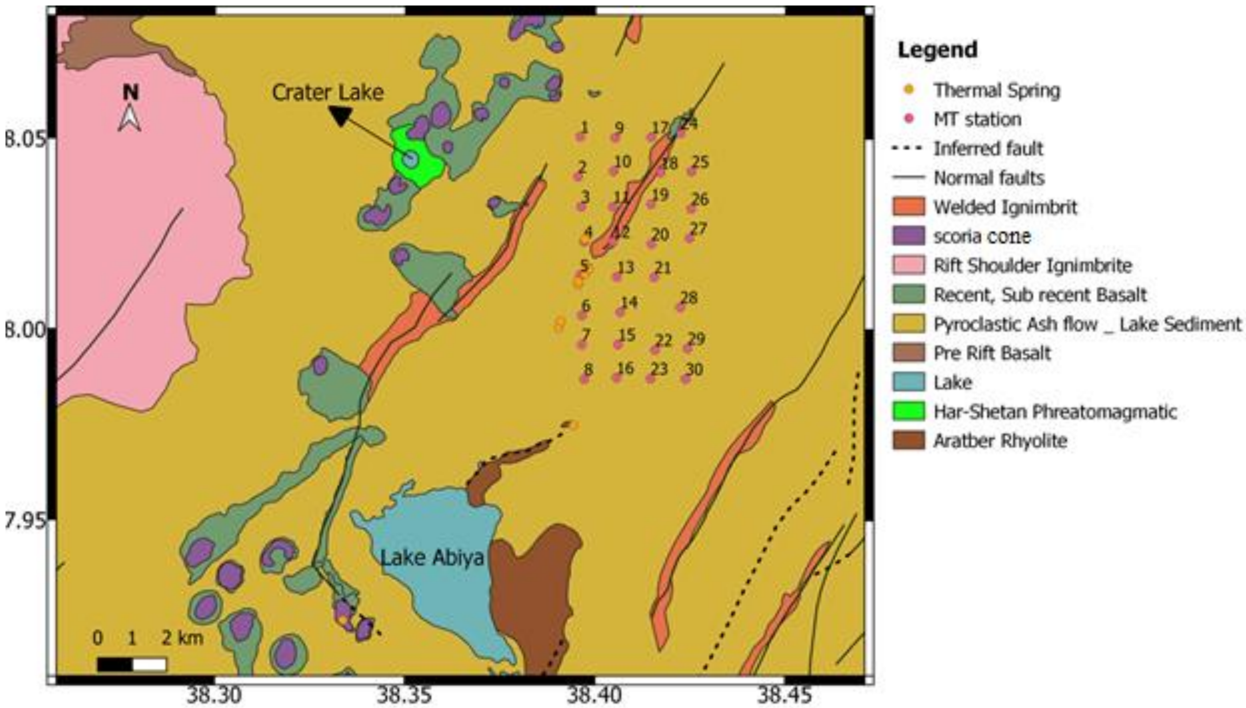

Figure 6.2 Geological map of the Ashute area, which explains the existence of the normal fault structure. The geological strata area was composed of the Ashute volcanic rocks. The map also shows the manifestation area on the western sides of the MT station (yellow dot).

6.4 Electromagnetic methods for the study of the geothermal field

The electric conductivity distribution of the subsurface can be determined via electromagnetic (EM) induction studies, which are based on time-varying electric and magnetic field measurements at an observation site on the Earth's surface. Applying electric conductivity measurements EM is the best geophysical method used in geothermal sites to characterize the geothermal setting as a system of faults and/or fractures filled with conducting geothermal fluids and altered rocks (Abossie et al., 2023a; Muñoz, 2014). The measurement of electric conductivity is an important characteristic for defining the geothermal setting. The method provides useful information by relating the geothermal system's resistivity structure to parameters such as salinity, temperature, porosity, permeability, and the degree of hydrothermal alteration of the host rock, all of which are commonly used to describe geothermal systems (Hersir & Bjornsson, 1991). Controlled sources of electromagnetic, such as TEM, and natural source electromagnetic methods, such as MT, are the most extensively utilized sources of electromagnetic methods for geothermal areas.

6.4.1 Magnetotelluric method

The MT method is a natural EM approach for determining the subsurface electrical resistivity distribution by measuring orthogonal EM fields at the ground surface. The depth of penetration of EM waves is a function of frequency and subsurface resistivity, magnetotelluric measurements at various frequencies provide information on the variation of resistivity with depth. Lighting discharge in the equatorial area of the planet with frequencies greater than 1Hz and interaction between Earth's magnetosphere and solar winds with frequencies less than 1Hz are the two sources of MT signal generation. The instrumental challenges associated with magnetotelluric (MT) data acquisition include difficulties in accurately capturing rapid fluctuations in the magnetic field, which poses a limitation to the method. Additionally, at shallow subsurface, MT data may be affected by the issue of static shift induced by near-surface variations in resistivity structure. It is important to note that a significant limitation of this approach is the assumption of a 1D subsurface, which is not strictly valid in 3D geological settings. The method's instrumental difficulties were in sensing a rapid fluctuation in the magnetic field, which is a restriction. At high frequencies, it suffers from the problem of static shift induced by the near-surface inhomogeneity of the resistivity structure. The telluric or static shift problem plagues the MT method, as it does entire resistivity methods that rely on the electric field measurement at the surface (Hersir & Flovenz, 2015).

The penetration depth (skin depth), is the depth at which the amplitude of a plane EM wave is reduced to 1/e 0.37 (Vozoff, 1991) of its surface amplitude and the wave's inverse Amplitude Factor (1/v).

$$\delta = \frac{1}{v} = \sqrt{\frac{2}{\sigma\omega\mu}} \qquad (6.1)$$

Since the magnetic permeability μ does not vary substantially on the Earth. Therefore the skin depth in (m) can be approximated as:

$$\delta(T,\rho) \approx 500\sqrt{T\rho} \qquad (6.2)$$

where ρ_a is the apparent resistivity of the uniform half-space in (Ωm) and $T = \frac{2\pi}{\omega}$ is the period in (s).

$$E(r,\omega) = Z(r,\omega)\, H(r,\omega),\;\; Z = \begin{pmatrix} Z_{xx} & Z_{xy} \\ Z_{yx} & Z_{yy} \end{pmatrix}, \qquad (6.3)$$

The impedance Z is complex and can be restated in both real and imaginary parts. As a result, each component of Z has both magnitude and phase (Simpson & Bahr, 2005; Vozoff, 1991).

$$\rho_{aij}(r,\omega) = \frac{1}{\mu_0 \omega} \left| Z_{ij}(r,\omega) \right|^2 \qquad (6.4)$$

$$\varphi_{ij}(r,\omega) = tan^{-1}\left(\frac{I\{Z_{ij}(r,\omega)\}}{R\{Z_{ij}(r,\omega)\}}\right) \qquad (6.5)$$

"Static shift" refers to the multiplicative frequency-independent vertical offsets of the apparent resistivity of MT data in the 1D or 2D situations when data are presented as apparent resistivities on a log-log scale. The electric field is one type of galvanic distortion in MT measurements.

Jones (2011, 2012) points out that real multipliers only modify the magnitudes of impedances when they are applied to an impedance tensor with a 1D or 2D form. This is not true for impedance tensors with 3D forms that contain non-zero diagonal members. Instead, practical distortions result in the mixing of diagonal and off-diagonal components, which has an impact on the impedance's magnitudes and phases. In interpretation techniques, observed data is typically compared to theoretical curves.

6.4.2 Transient Electromagnetic Method (TEM)

The TEM method is an active geophysical method that uses a transmitter to deliver electric currents. The primary field is supposed to be electricity, which oscillates with time. It's also known as time-domain electromagnetic (TDEM) or pulse electromagnetic (PEM), and it's been around since the 1980s. Instruments and interpretation methods for TEM soundings have grown to a high level of development, and they are extensively used and understood (Frischknecht et al., 1991) The technique is based on two of Maxwell's electromagnetic equations. It's an active method in which a wire loop is placed on the ground and a current is generated to run through it before it's abruptly stopped. According to Ampere's law, a changing electric field or current causes a magnetic field to form around it. Faraday's Law asserts that in a closed circuit, the induced electromotive force or voltage is caused by the time-changing magnetic flux going through the circuit. The transient electromagnetic method measures both the electric and magnetic fields, and it also calculates the electric field running through the electrodes connected to the ground. This data is not significantly influenced by subsurface inhomogeneity (Chouteau & Bouchard, 1988; Marwan et al., 2019; Yanis et al., 2017). In rugged terrain conditions, the static shifting of MT data is likely to introduce substantial errors in the subsequent inversion and interpretation processes using TEM (Watts et al., 2013). The Transient Electromagnetic (TEM) method, in combination with the MT method, has been widely used to examine the subsurface properties of geothermal reservoirs, such as porosity, rock–water reactions, temperature, salinity, and permeability, and their direct relationships (Hersir & Bjornsson, 1991; Marwan et al., 2019). Because of its ease of use and capacity to yield diagnostic data, the TEM method is commonly used in environmental, hydrogeological, geothermal energy, and mineral resource research.

The electrical current induced within conductors by a changing magnetic field inside the conductor causes the EM eddy currents to fade due to Ohmic dissipation on Earth in the TEM method. The depth at which eddy currents can travel on Earth is determined by the time it takes for the current to cut off and the conductivity of the Earth as follows:

$$\delta_{TEM}(t) = 1.28\sqrt{\frac{t}{\sigma\mu}}\ (m) \qquad (6.6)$$

where $\delta_{TEM}(t)$ is the depth, μ, and σ are the magnetic permeability and the conductivity, respectively and t is the time from the current turn-off.

Based on the quantity of power transmitted, and ambient noise the investigation depth changes from tens of meters to over 1000 meters chiefly reliant on the size of the transmitter loop in use.

Árnason, (1989) describes the induced voltage in the receiving coil at so-called late times (described later) on a homogeneous half-space of conductivity, σ is:

$$V_{(t,r)} \approx I_0 \frac{C(\mu_0 \sigma r^2)^{\frac{3}{2}}}{10\pi^{\frac{1}{2}} t^{\frac{5}{2}}} \qquad (6.7)$$

where I_0 is represents current in the transmitting loop (A); $C = A_r n_r A_s n_s \frac{\mu_0}{2\pi r^3}$, and A_r is represents area of the receiver coil (m^2); μ_0 is represents Magnetic permeability [Henry/m]; n_r is represents the number of the receiver coil turns; A_s is represents the transmitting area of the loop (m^2); n_s represents the number of turns in the transmitting loop; t represents the time elapsed after the transmitter current is turned off (s); $V(r,t)$ is represents transient voltage (V); R represents the radius of the transmitter loop (m); This demonstrates that the transient voltage is proportional to $\sigma^{\frac{3}{2}}$ and decreases over time as $t^{\frac{-5}{2}}$ for late times after the transmitter current is abruptly switched off.

Árnason, (1989) describes in terms of the receiver-induced voltage after the source current is turned off the late-time apparent resistivity,ρ_a, is given by:

$$\rho_a(r,t) = \frac{\mu_0}{4\pi}\left(\frac{2\mu_0 A_r n_r n_s I_0}{5t^{\frac{5}{2}}V(t,r)}\right)^{\frac{2}{3}} \tag{6.8}$$

6.5 Data acquisition and processing

In the Ashute geothermal field, data collection involved the use of Broadband MT (BBMT) and TEM methods at 30 MT sites. The MT data was gathered using a 5-channel MTU unit from Phoenix Geophysics Company Canada Geophysics, while the Zonge GDP-32 system was utilized for acquiring TEM data. To address static shift issues in the MT method, 1D joint MT and TEM methods were conducted at the same stations. The spacing between these sites averaged about 1 km, with 30 MT stations installed in 2017 by GSE. The TEM survey was carried out in 2019 within the Ashute area near SDFZ, covering an area of 8 km by 4 km with a 1 km interval distance. Most MT stations' electrode dipole lengths were 100 m, and recording hours exceeded 24 hours to ensure a continuous time series. The remote reference method was employed to avoid local correlations. A central loop of 100 by 100 m with a square transmitter was used to measure the TEM instrument. A strong magnetic field was generated around the loop by using a 10 A electric current. The magnetic field generated from current induction into the material, which oscillates against the passage of time, will be recorded by the coil loop in the middle. Synchronized precision crystal clocks manage the timing of the digital receiver and the current transmitter. Every time the transmitted current changes, the receiver measures the voltage produced in the receiver coil. The voltage induced in the receiver coil is always measured by the receiver each time the transmitted current is turned off. The TEM instrument made measurements at frequencies of 1, 8, and 16 Hz, with the raw data processed using the Temx tool created by Árnason (2006) to average the data and calculate late-time apparent resistivity as a function of time after the turn-off. Before inversion and interpretation, the MT data underwent processing to eliminate outliers and treacherous data points using the SSMT2000 software. This involved Fourier transformation of the time series data into the frequency domain, calculating averaged cross-powers and auto-powers, and removing noisy data points. The resulting auto and cross-powers were recorded in Electronic Data Interchange (EDI) files, which were then fed into the Linux program TEMTD for joint inversion with the TEM data.

6.6 Static shift correction

A static shift problem emerges as a result of near-surface inhomogeneity disregarding the MT data. A constant value movement of the apparent resistivity curve is produced by a static shift of the MT log-log apparent resistivity vs. the period curve (Lichoro, 2009). The static shift can be a major issue in volcanic geothermal locations with high resistivity fluctuations (Árnason et al., 2010). The issue is that because of resistivity heterogeneity close to the measuring dipole, the electric field on the surface. Correcting the static shift in magnetotelluric (MT) data can lead to improved and more precise estimations of subsurface resistivity and thickness structures. On the other hand, uncorrected MT data, as shown by the vertical shift curves of apparent resistivity, can produce inaccurate and unreliable estimates (Sharma & Biswas, 2011; Tournerie et al., 2007). To address this, the apparent resistivity is scaled by an unknown dimensionless factor (shifted on the log scale), which can range from 0.1 to 3 (Árnason et al., 2010; Marwan et al., 2019). This shift persists at all frequencies and is independent of frequency (Árnason et al., 2010; Delhaye et al., 2017; A. G. Jones, 1988). If S = 0.1 is reduced, the resistivity values will be 10 times lower and the depths of resistivity boundaries be three times smaller (Árnason, 2008; Árnason et al., 2010). A clear indication of the presence of a static shift in the data is a parallel shift between the two polarizations of the apparent resistivity curves. However, the absence of a parallel shift between two apparent resistivity curves that can be moved by the same amount does not always imply the absence of a static shift (Simpson & Bahr, 2005).Galvanic distortion and current channeling cause the static shift problem (Árnason et al., 2010).

Galvanic distortions of magnetotelluric (MT) data can result in inaccurate resistivity estimation and improper geometry modeling, leading to a misinterpretation of subsurface electrical resistivity structures (Delhaye et al., 2017). Current channeling or repelling is also thought to be caused by topographic effects. The rugged topography is observed to cause static distortion, with currents concentrating beneath depressions and dispersing behind peaks. But here in the study area, there are no topographic differences. Galvanic effects cause an increase in the electric field in valleys and a decrease in the electric field in hills. Accordingly, in a valley, MT fields and current density are higher than on a hill. The curve of apparent resistivity is shifted by the same multiplicative factor at all frequencies as a result, maintaining the shape of the curve when plotted on a log-ordinate scale, without causing a consistent change in the phase curve, and this is how the static shift is described (A. G. Jones, 1988).

For a frequency-independent 2×2 real tensor, the static shift tensor C distorts the genuine MT tensor $Z(\omega)$ to produce the observed tensor $Z_0(\omega)$, via

$$Z_o(\omega) = CZ(\omega) = \begin{pmatrix} C_{xx}Z_{xx} + C_{xy}Z_{yx} & C_{xx}Z_{xy} + C_{xy}Z_{yy} \\ C_{yx}Z_{xx} + C_{yy}Z_{yx} & C_{yx}Z_{xy} + C_{yy}Z_{yy} \end{pmatrix} \tag{6.9}$$

Several ways have been presented to rectify the static shift. In this study, the static shift problem was resolved by integrating TEM data with MT data from the same site to adjust for static shifts in MT data (Árnason, 2008; Louise Pellerin, 1990; Simpson & Bahr, 2005; Sternberg et al., 1988).

The static shift correction is assumed to be primarily caused by electric field distortion. Scaled apparent resistivity curves obtained from MT data that have an upward or downward shift agree with TEM curves or are inverted together with TEM data (Sternberg et al., 1988). The TEM does not suffer from the static shift problem because the decreasing magnetic field at the surface is less affected by local inhomogeneity than the electric field associated with MT. As a result, the Telluric shift correction in the MT is accomplished in this work by inverting both the MT and TEM sounding data gathered at the same location. Hence, the transient electromagnetic technique (TEM) is the most consistent and extensively used solution for static shift.

6.7 Joint inversion of TEM and MT data

To correct the static shifts in the MT data, a joint inversion of the electromagnetic (EM) data were used, which can be rather severe due to the significant inhomogeneity of near-surface resistivity. In order to mitigate the static shift issue, the 1D joint inversion model was simultaneously applied to both TEM and MT data by fitting both datasets together. The TEM and MT data were inverted together and individually in 1D using the TEMTD program. The TEM and MT data were jointly and separately inverted in 1D using the TEMTD program, developed by Kntur Árnason of ÍSOR (Árnason, 2006), with successful results. This is accomplished by applying an algorithm that chooses the right shift factor to limit the MT data such that it fits the TEM response. Inversions of minimum structure (Occam) can also be performed with the program (e.g., Constable et al., 1987).

A joint 1D Occam inversion was performed over all of the MT soundings and TEM soundings at the same sites, for the rotationally invariant determinant apparent resistivity and phase of the Ashute area. It is one-of-a-kind, and it's unaffected by strike direction (Árnason, 2015). Due to its rotational invariance and ability to average out all of the "dimensionality" of the data, determinant data is preferred.

Figure 6.3 depicts a 1D combined inversion of MT and TEM data, with red (dark) diamonds representing TEM apparent resistivities and blue (grey) squares indicating MT apparent resistivities and phase. The apparent resistivity panel's upper right-hand corner shows the shift multiplier. The best estimate of the shift parameter for this MT sounding is located in the apparent resistivity panel's top right corner, therefore in order to make the MT apparent resistivity consistent with the TEM sounding; it must be divided by 0.706.

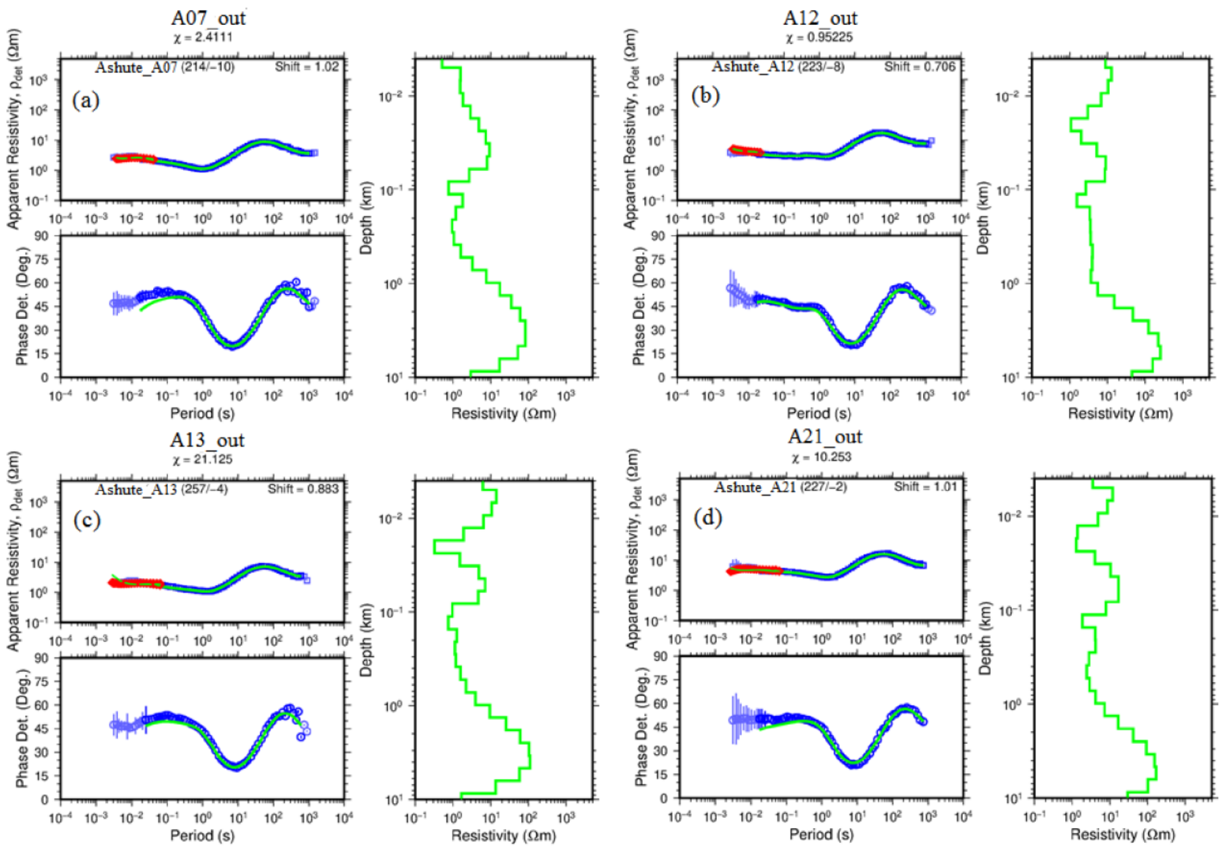

Figure 6.3 illustrates the results of a 1D joint inversion of TEM and MT stations at four selected locations. In the figure, red diamonds represent apparent TEM resistivities, which are converted into a pseudo-MT curve. Blue circles depict the apparent resistivity and phase of MT, while blue squares represent the measured apparent resistivities. Light blue symbols on both sides of the green curves indicate data that was not used for the inversion, and bluish vertical lines represent error bars. The shift multiplier is shown in the upper right corner of apparent resistivity in Figure 6.3a. The resistivity inversion results of the 1D model are shown in the right panel by vertical blue lines on each side of the image. The numbers on top of the figure represent the MT station, while the name "Ashute" with a number in the resistivity panels represents the TEM station.

The application performed on both inversion of resistivity and layer thicknesses (standard layered inversion) and Occam's inversion which increases layer thickness exponentially. The users can damper the first and second-order derivatives of model parameters (logarithm of resistivity and layer thickness) (Árnason, 2006).

When utilizing this process, the 1D assumptions of the near-surface and measurement correction for TEM and MT procedures must hold. In the immense majority of cases, a model with an acceptable misfit between the data of TEM and MT measured and estimated may be found. Acceptable misfit in 1D joint inversion can be difficult to accomplish in some situations, frequently due to inadequate data or multidimensional effects, which can lead to misleading predictions. Commonly used approaches to enhance the misfit are widely utilized, although they are very dependent on the option selected.

The shift multipliers of MT stations of the Ashute geothermal site of 30 MT soundings as illustrated in the histogram is shown in Figure 6.4. They are found in the range of 0.3–1.7, with shift multipliers <1 being more common than those >1. The geometric mean of the Ashute shift multipliers is approximately 0.86, while the mean of the shift multipliers is around 0.9.

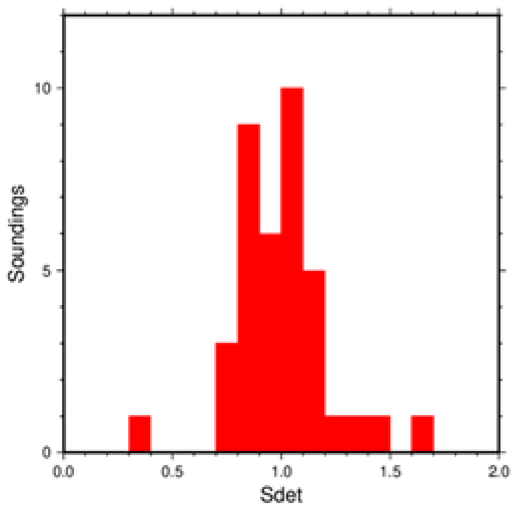

Figure 6.4 the static shift parameters histogram for determinant apparent resistivity in the Ashute area.

6.8 3D inversion of MT inversion model

The Earth is a three-dimensional entity with varying conductivity along all axes (x, y, and z). When assessing this, a comprehensive impedance tensor was derived through 3D Magnetotelluric (MT) inversion, providing more reliable and detailed insights compared to 1D and 2D models. Although 2D and 3D inversion models are generally similar, the depth of the 3D model presents a more realistic depiction than its 2D counterpart (Oryński et al., 2022). Deeper resistivity models often pose challenges, and as a result, 3D MT inversion techniques have been routinely employed to address such complexities. These 3D models align more closely with geological models of geothermal reservoirs, offering enhanced interpretation for geothermal exploration and other applications within intricate geological settings (Uchida & Sasaki, 2006). Consequently, a 3D inversion model of magnetotelluric data was employed to investigate the subsurface electric conductivity distribution of the Ashute geothermal field, situated in the CMER.

The apparent resistivity and phase data impedance elements were computed and then inverted to align with the electric field perpendicular to the strike (known as the TM-mode), parallel to the strike (known as the TE-mode), or both simultaneously. The impedance tensor's dimensional indicators suggested a 3D resistivity structure during periods exceeding 50 s. To solve the Maxwell equations, the forward technique used a staggered grid finite-difference method. Notably, the 3D algorithm in this case assumed a flat surface, as simulating current distortion due to topography would be unfeasible if a level surface were used. The initial model for 3D inversion comprised 54 x 34 x 45 cells in the x, y, and z dimensions, with the full impedance components assigned error margins of 5%. Incorporating full impedance tensor data, as recommended by Tietze et al. (2015), improved the recovery of the actual resistivity structure and reduced reliance on previous models. The 3D inversion of full impedance tensor elements from 30 MT resistivity soundings was conducted with and without static shift correction in the Ashute geothermal area, CMER. The inversion process involved 76 frequencies with periods ranging from 0.001 to 1000 seconds, and the full impedance tensors were inverted using the 3D inversion software ModEM, which is available for the research community of EM induction study (Egbert & Kelbert, 2012; Kelbert et al., 2014; Meqbel, 2009). The ModEM inversion program utilized the non-linear Conjugate gradient (NLCG) algorithm for the inversion of the data.

The objective function of the linearized inversion penalized departures from the initial model by minimizing both data misfit and model roughness. Additionally, two inversion tests were conducted for resistivities of 50 and 100 Ωm for corrected and uncorrected full impedance tensor components of Z. Various initial models, including half-spaces of 50 and 100 Ωm and those derived from smooth 1D models, were employed to validate the results. The preferred model, with and without static shift correction, utilized a background resistivity of 100 Ωm.

6.9 Comparison between with and without static shifted corrected 3D inversion result.

The MT data was subjected to 3D inversions with and without static shift correction, and two inversion tests were conducted using data from 30 stations. These are compared by closely examined depth slice and vertical cross-section as shown in Figures 6.5-6.11. The models that come from all of the inversions are compared, and the findings are analyzed in terms of the methods' effectiveness. For comparison, we prefer to use the model which has the best-fit data. The findings show that 3D resistivity models interpolated from 1D joint inversion of MT and TEM data reproduce the resistivity structure of near-surface rather well, but become erroneous at depth (Lichoro, 2015). Overall, 3D inversion models perform better, reconstructing resistivity structures with high precision at the entire depths.

6.9.1 Depth slice resistivity maps with and without static shifted data

The 3D model of magnetotelluric data inverted with and without static shift correction was used in the Ashute geothermal field. This study examined and compared the horizontal slice of both 3D models and employed the components of the MT impedance data that were jointly inverted with TEM data for the static shift-corrected 3D inversion. According to the 3D inversion techniques, the Ashute field is characterized by a layer with low resistivity near the surface, underlain by higher resistivity in general (Figures. 6.5 and 6.6). Both the 3D inversion model with and without static shift correction techniques identified a deep, NE-SW oriented conductor at a depth ranging from 0.368 to 0.539 km beneath Ashute. Additionally, both techniques revealed low resistivity on the surface, extending to a depth down to 50 m in the central and southwestern parts of the study area. The 3D models with and without static shift correction exhibited slight differences at this depth.

Figures 6.5 and 6.6 display horizontal slices of resistivity from the 3D model. These figures depict the horizontal plane resistivity distribution at six different depths (0.015–0.032 km; 0.368–0.420 km; 0.477–0.539 km; 0.684–0.767 km; 2.729–3.017 km, and 4.487–4.951 km), revealing clear resistivity contrasts within the imaged model. The shallow structures started from the surface showed a distinct conductive region (<5 Ωm), and a resistivity greater than 10 Ωm found elsewhere, indicating a low resistive zone covering most of the southern part of the survey area. This low resistivity is likely due to lacustrine sediments, followed by low resistive altered zones, with a smectite zone of thickness 750 Ωm exhibiting low resistivity (<5 Ωm) approximately started from 368 m to 539 m and roughly oriented NE-SW direction and being surrounded by a resistive value of 10 Ωm, with a thickness of 250 m (Abossie et al., 2023a).

This underlay it by a body of a resistivity value < 10 Ωm oriented in the same direction at a depth of (684-767 m).

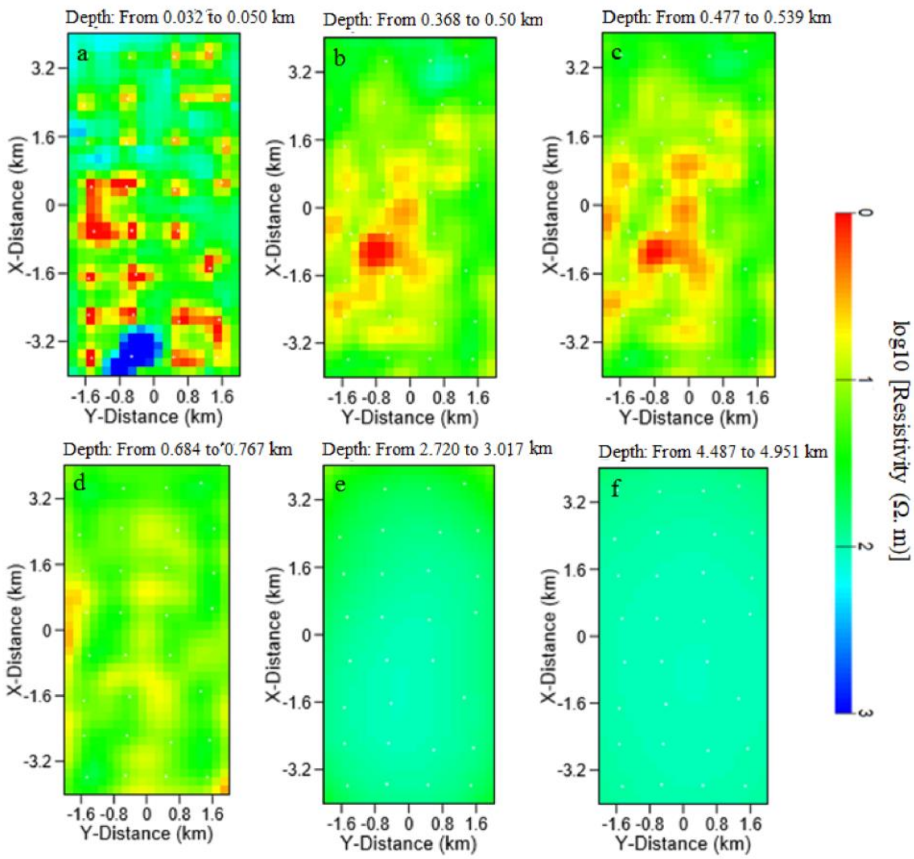

Figure 6.5 The 3D MT data inversion of resistivity model with static shift correction prior to inversion for six different depth slices from ie., (a) 0.015-0.032 km; (b) 0.368-0.420 km; (c) 0.477-0.539 km; (d) 0.684-0.767 km; (e) 2.729-3.017 km; (f) 4.487-4.951 km. White dots represent MT stations

Figures 6.5 to 6.6 depict the comparison of the depth slice of the 3D resistivity model with and without static shift corrected of the Ashute geothermal field. From the Ashute geothermal field comparison between with and without static-shift corrected data revealed that little difference at the shallow depth. However, at deeper depths, the two models approximately agree on resistivity below at 2.7 km depth.

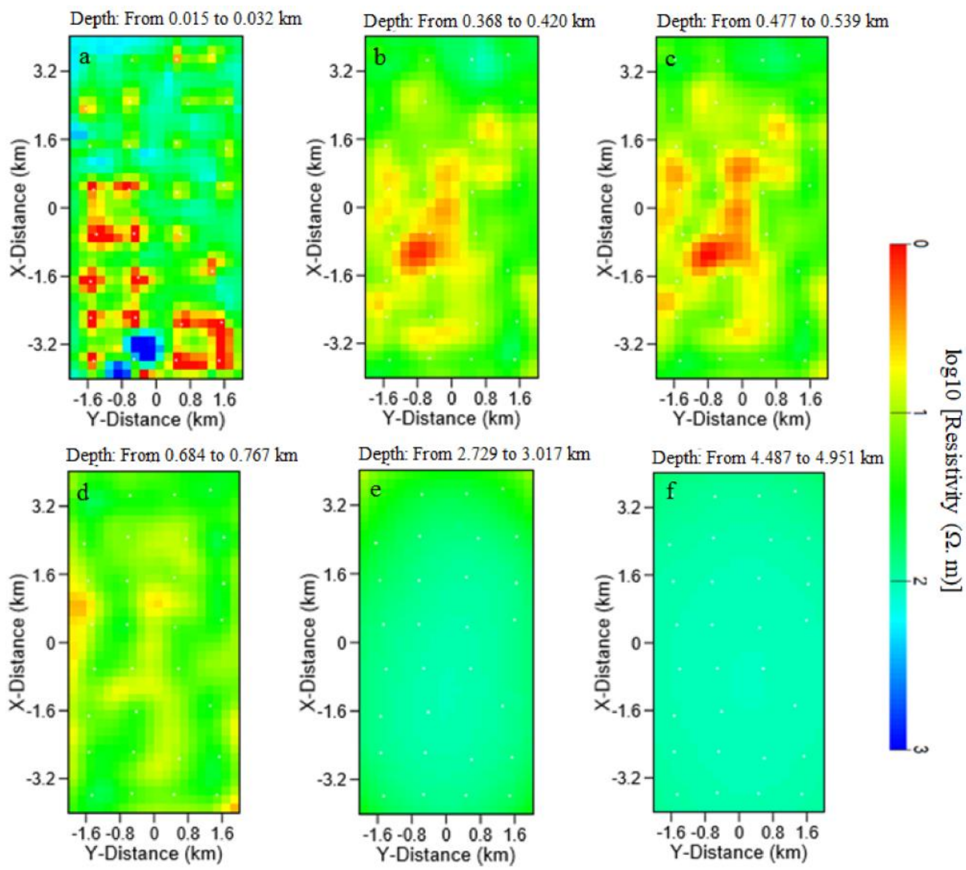

Figure 6.6 The resistivity model of MT data underwent 3D inversion without static shift correction across six different depth ranges: (a) 0.015-0.032 km; (b) 0.368-0.420 km; (c) 0.477-0.539 km; (d) 0.684-0.767 km; (e) 2.729-3.017 km; (f) 4.487-4.951 km. Block dots represent MT stations.

6.9.2 The vertical cross-sections of resistivity

Figures 6.8 to 6.11 depict the comparison of two profiles, one in the North-South direction and the other in the East-West direction, showing vertical resistivity cross-sections of the Ashute geothermal field resulting from 3D resistivity models, with and without static shift correction. These vertical cross-sections are obtained from a 3D inversion model along the line indicated in the horizontal slice in Figure 6.7, and they are presented up to a maximum depth of 5 kilometers for simplicity. The significant features in the 3D resistivity distribution of cross-sections of the Ashute geothermal field, with and without static-shift correction, include a juxtaposition of very high resistivity (> 100 Ωm) with a low resistivity body, followed by a conductive layer of 10 Ωm overlaying a moderately resistive layer with resistivity values ranging from 10 to 46 Ωm at greater depths (Abossie et al., 2023a).

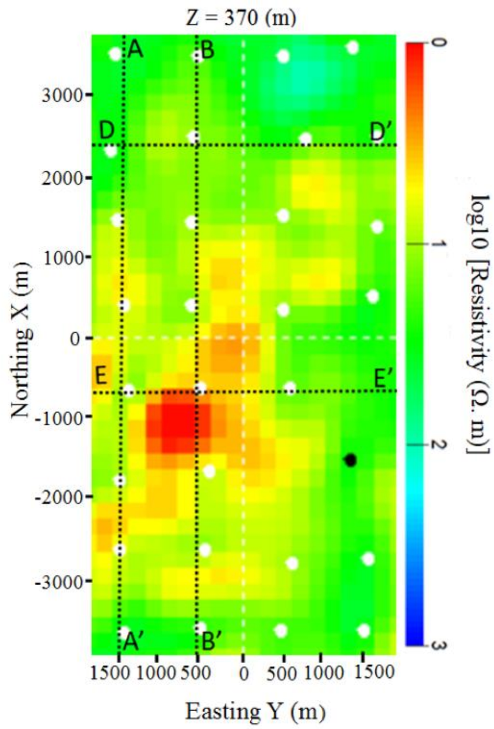

Figure 6.7 A 3D inversion model with static correction was used to produce a horizontal slice at a depth of Z = 370 m. An MT station is represented as a white dot. Figures 6.8, 6.9, 6.10, and 6.11 depict resistivity cross-sections obtained in the N-S and E-W directions along with the lines AA', BB', DD', and EE'.

These structures reveal a complex geoelectric structure at a shallow depth in the Ashute site, with a horizontal non-uniform resistivity distribution of unconsolidated sediments covering most of the study area and unaltered volcanic products exposed in the central south part of the study area (Abossie et al., 2023a). The low resistivity zone ($\rho < 5$ Ωm) and ($\rho < 10$ Ωm) were observed on the top layer at a depth down to 50 m. From the observation of four profiles beneath the first layer in most of the study area, a low resistivity body ($\rho < 5$ Ωm) appears at 300 m. Some dissimilarities were observed when comparing the model with and without static shift-corrected data, particularly in the conductive layer thickness. Resistivity gradually rises below the conductive zone for both models, with the presence of conductive clay minerals in the middle ($1.6 < x < 6.4$ km) of the profile at depths between 30 and 1500 m, and high resistivity (> 100 Ωm) in the top few hundred meters of the shallow strata, extending down to 200 m. At increasing depths, resistivity gradually rises, reaching maximum values of > 100 Ωm from resistivity levels of 10-46 Ωm. As a result, in this study region, there are no significant conductive structures at further depths (Abossie et al., 2023a).

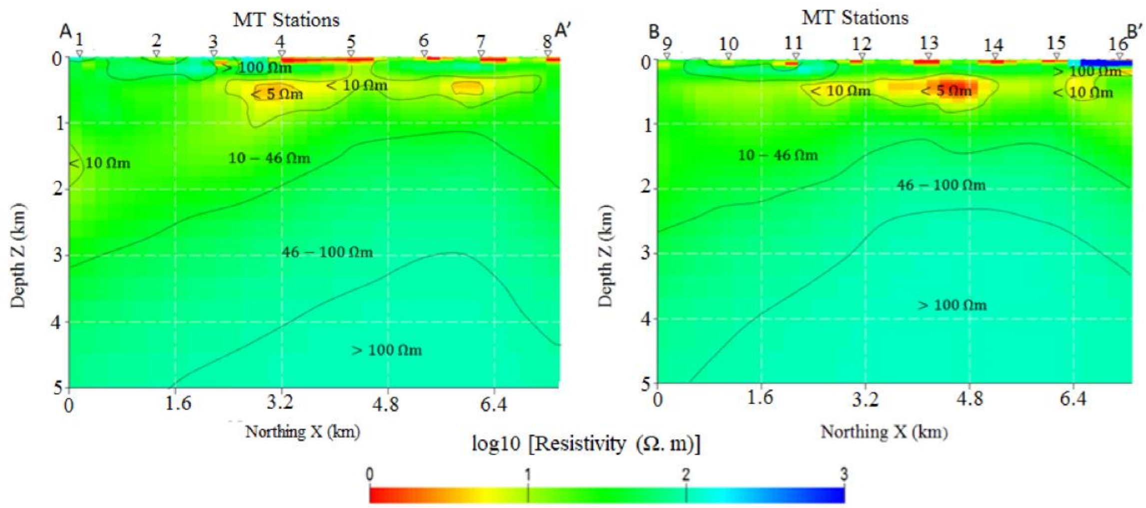

Figure 6.8 The vertical resistivity cross-sections with static shifted correction of the Ashute geothermal field resulting from 3D models of resistivity along a North-south orientated cross-section.

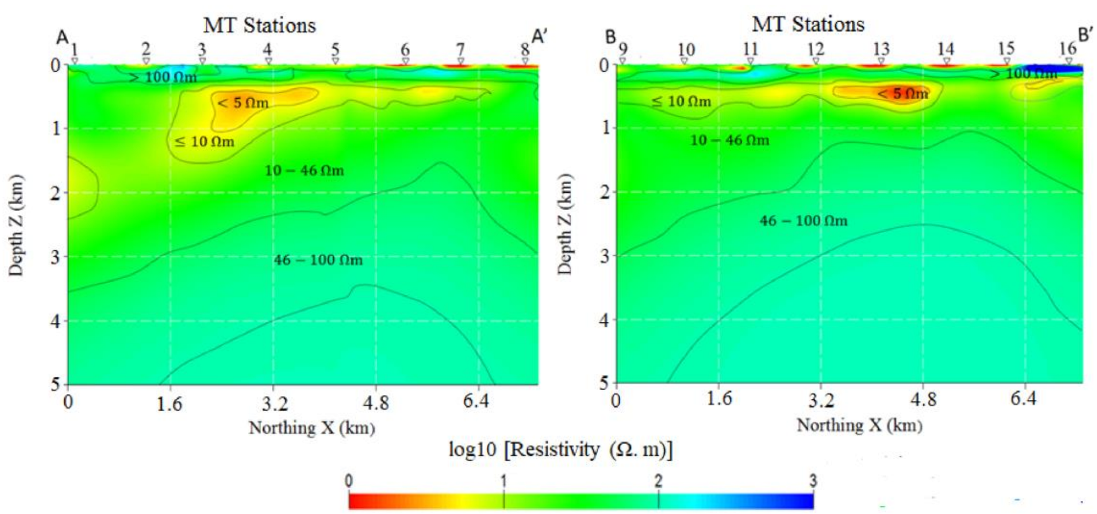

Figure 6.9 presents the vertical resistivity cross-sections without static shifted correction of the Ashute geothermal field resulting from 3D models of resistivity along North-south orientated.

.

Figures. 6.8-6.11 depicts the comparison of a vertical cross-section of resistivity of the 3D resistivity model with and without static shift correction of the Ashute geothermal field. The Ashute geothermal field comparison between with and without static-shift corrected data revealed that the static-shift corrected data have a good correlation with the nearby borehole data. Comparing the observed resistivity structure in a nearby borehole to a model created from observed data, it was discovered that the model created from the inversion of static-shift corrected data performed better estimation. It should be noted that the method described here is only applicable in places where the distribution of near-surface resistivity is about one-dimensional (Delhaye et al. 2017). Models in Figures 6.8 and 6.9 are incredibly dissimilar, especially on the conductive layer thickness. Due to its extreme underdetermination, 3D inversion is a problem that requires significant regularisation to get useful findings. Imposing some sort of model smoothness is the conventional method for accomplishing it. However, the models must be allowed to be rough at shallow depths in order to accommodate the near-surface anomalies that result in the shifts. For the models to be rough near the surface (not resolved by the MT data) but smooth at depth, complex regularisation schemes will be required.

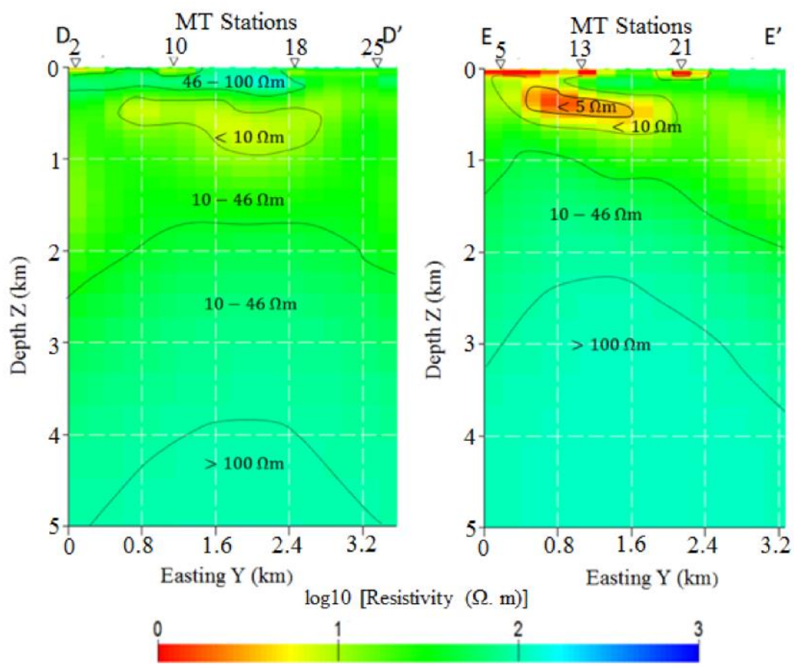

Figure 6.10 The vertical resistivity cross-sections with static shifted correction of the Ashute geothermal field resulting from 3D models of resistivity along East-West orientated.

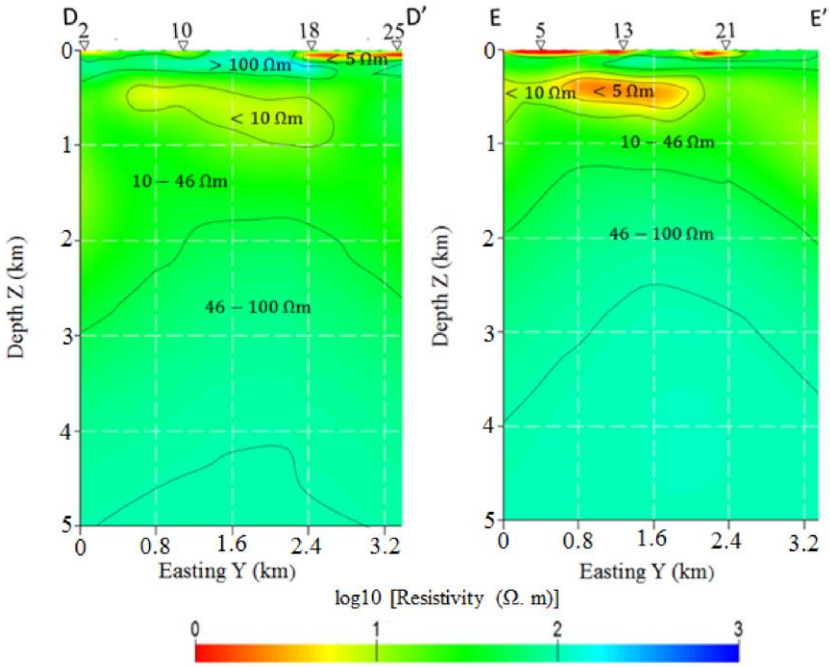

Figure 6.11 The vertical resistivity cross-sections without static shifted correction of the Ashute geothermal field resulting from 3D models of resistivity along East-West orientated.

The subject of 3D inversion of MT data is critically underdetermined, and the model needs to be regularized. The regularization usually includes some type of smoothness condition. The 3D model with one static shift correction recovers a resistive subsurface structure. However, the size or shapes of the high resistivity structures in both 3D models are partially recovered at deeper depth. With regards to the margins of the geothermal system and the dominance of the low resistivity layer at shallow depth, there are some variations between the reconstructed models from the 3D inversion of MT data without and with the inclusion of a statistical shift correction (see Figures 6.10 and 6.11).

Two contrasting inversion models have been developed, one incorporating static-shift corrections and the other without, and the outcomes provide valuable insights. The vertical adjustment of resistivity-thickness in the model results from addressing static-shift effects, leading to an enhanced alignment with the pre-existing borehole wireline resistivity data. Consequently, lateral distributions of resistivity are also influenced, resulting in estimates of up to a five-fold difference in resistivity between the models at depths as shallow as 2000 m. This discrepancy arises because these vertical adjustments are largely unaffected by nearby locations.

Therefore, The main difference between the two 3D resistivity models with and without static shifted correction at shallow depth lies in the accuracy and reliability of the resistivity values. The static shifted correction helps to account for near-surface effects and improves the accuracy of resistivity measurements at shallow depths. This can impact the interpretation of subsurface structures and geological features. The resistivity values themselves may not change, but the corrected model provides a more accurate representation of subsurface resistivity distribution.

6.10 Conclusion

The Ashute geothermal field is one of the geothermal sites discovered in the CMER near the SDFZ. The inhomogeneity of near-surface in geothermal field magnetotelluric data suffers from a static shift effect in the high-frequency band. The static shift can be a major issue in volcanic geothermal locations with high resistivity fluctuations (Árnason et al., 2010). To address this issue, a combined approach using transient electromagnetic (TEM) and MT methods was employed to study the Ashute geothermal field from the surface to great depths. TEM, unaffected by the static-shift problem, provided more accurate estimates of subsurface resistivity and thickness compared to uncorrected MT data. This gives better and more accurate estimates of subsurface structure of resistivities and thicknesses, whereas uncorrected magnetotelluric data displayed by the vertical shift curves of apparent resistivity can lead to erroneous and unreliable estimates (Sharma & Biswas, 2011; Tournerie et al., 2007). The main focus of this study is on the application of correction of static shift scheme for MT data and comparing models found by 3D MT inversion with and without static shifted data. To resolve this problem the static shift correction was achieved by using 1D joint inversion of TEM and MT data from the same site.

In the inversion, 76 frequencies with periods of 0.001 to 1000 s were used. A model was created by the 1D joint inversion of the TEM and MT of 30 soundings, and the 3D inversion of the observed and the static-shift-corrected full impedance tensor were compared. Different initial models were utilized for the inversion, including half-spaces of 50 and 100 Ωm. The preferable model with and without static shift corrected model is 100 Ωm used for background resistivity. The ModEM inversion program was used to perform 3D inverse modeling of magnetotelluric data (Abossie et al., 2023a; Egbert & Kelbert, 2012; Kelbert et al., 2014; Meqbel, 2009). Hence 3D inversion model recovers the surface resistivity reasonably well if borders between resistivity structures are visible, however, the recovered and the original model differ in the resistivity of the structures (Lichoro, 2015).

The resulting 3D inversion models of the MT data, with and without static shift correction, displayed a strong correlation and demonstrated improved agreement with the original model when static shift correction was applied before inversion. When the static shift correction is applied before the inversion, models that agree better with the original model appear to be recovered, especially when the static shift is enormous (Lichoro, 2015).

The comparison of observed resistivity structure in a nearby borehole with models created from static-shift corrected data demonstrated improved estimation. The 3D model with one static shift correction recovers the subsurface resistivity structure. However, the size or shapes of the high resistivity structures in both 3D models are partially recovered at deeper depth. With regards to the margins of the geothermal system and the dominance of the low resistivity layer at shallow depth, there are some variations between the reconstructed models from the 3D inversion of MT data without and with the inclusion of a statistical shift correction (see Figures 6.10 and 6.11). Therefore, the Ashute geothermal field between with and without static-shift corrected data revealed little difference at the shallow depth. However, at deeper depths, the two models approximately agree on resistivity below 2.7 km depth.

Chapter 7 General Conclusion and Recommendations

7.1 General Conclusion

This dissertation focuses on analyzing 2D/3D crustal geoelectric models derived from magnetotelluric (MT) data inversion in the Central Main Ethiopian Rift (CMER). The study includes the 2D joint inversion of transverse electric (TE) and transverse magnetic (TM) modes and a 3D inversion model in the Ashute geothermal field, which is found close to the western escarpment. These aimed at investigating heat sources, heat flow paths, and geothermal resources to delineate and characterize the geothermal structures and comprehend the tectono-magmatic setting of the crust beneath the study area. Additionally, the static shift correction MT data of the Ashute geothermal field were utilized to improve the accurate estimates of subsurface resistivities structure and thicknesses by using 1D joint inversion of TEM and MT data.

In this study, the 3D grided along with four profiles of 30 MT stations in an area of 32 km^2 provided by the Geological Survey of Ethiopian (GSE) and 21 MT stations along the profile across the rift from the western margin to Adami Tulu, spanning 52 km, were collected during fieldwork. The approach could provide information on the subsurface geoelectrical structures, detect hydrothermal alteration zones, delineate and explore geothermal resources for further implementation, and determine the 3D resistivity distribution of the Ashte geothermal field. The research also employed a 2D inversion model to examine deep resistivity patterns and magma storage beneath the CMER from Adamitulu to western Mergin.

Similarly, TEM data from 30 stations closer to MT stations in the Ashute geothermal field acquired in the fieldwork were used for processing, analyzing, modeling, and interpretation in order to have better and more accurate estimates of shallow subsurface resistivities structure and thicknesses because TEM data is not significantly influenced by distortion. To overcome the static shift problem, the 1D joint inversion model was applied simultaneously to both TEM and MT data to correct for static shifts in the MT data.

The 2D inversion model of magnetotelluric data were implemented using Occam inversion software. The phase tensor analysis was used to determine the dimensionality and geoelectrical strike direction, as well as the estimation of geoelectric strike parameters. The results of dimensionality analysis across the rift (western margin to Adami Tulu) the majority of our MT data show a small beta value at low periods (nearly below 10 s), which indicates 1D or 2D structures, while at long periods (almost above 10 s), the data show 3D structures with a large value of |β| >3^0. However, from the results of the dimensionality analysis of MT data, the 2D inversion model is suitable for imaging the resistivity of subsurface structures. The dominant geo-electrical strike is estimated to be N15^0E using a Z-invariant and phase tensor azimuth. The results of a 2D joint inversion of TE (transverse electric) and TM (transverse magnetic) mode revealed partial melt and an upper crustal fracture zone (fault) as a result of dike intrusion, with a resistivity of less than 5 Ωm, at a depth of 12–22 km**.** The partial melt extends beneath along SDFZ with about a horizontal width of 10 km. It could be related to the source of heat for the Ashute geothermal field. This obtained by optimal model constraints could be constructed using a priori information about regions of lower seismic shear wave velocities beneath the Silti-Debre Zeit Fault Zone (SDFZ) on the western side of the CMER studied by Kim et al.(2012). It is known that the non-uniqueness of models is one of the major pitfalls of magnetotelluric data inversion. In this study, a hypothesis testing approach (Unsworth & Bedrosian, 2004) was utilized to determine if prominent features in the model are required by the data.

The Ashute (around Butajira) geothermal field is found closer to the western rift escarpment in the CMER, where thermal manifestations like mud pools and hot springs are aligned NNE-SSW (Sinetebeb et al., 2020). The full impedance magnetotelluric data were used for the 3D resistivity inversion model using the ModEM inversion program. According to the 3D inversion resistivity model, the subsurface directly beneath the Ashute geothermal site can be represented by three major geoelectric horizons. On top, a relatively thin resistive layer (> 100 Ωm) represents the unaltered volcanic rocks at shallow depths. This is underlain by a conductive body (< 10 Ωm), possibly associated with the presence of clay horizon (smectite and illite/chlorite zones), resulting from the alteration of volcanic rocks within the shallow subsurface. In the third bottom geoelectric layer, the subsurface electrical resistivity gradually increases to an intermediate range (10–46 Ωm). This could be related to the formation of high-temperature alteration minerals such as chlorite and epidote at depth, suggesting the presence of a heat source. As in a typical geothermal system, the rise in electrical resistivity under the conductive clay bed (products of hydrothermal alteration) may indicate the presence of a geothermal reservoir. Otherwise, no exceptional low resistivity (high conductivity) anomaly is detected at depth. The TEM and MT data were inverted together and individually in 1D using the TEMTD program. The program was written by Kntur Árnason of ÍSOR (Árnason, 2006), and it works. This is accomplished by applying an algorithm that chooses the right shift factor to limit the MT data such that it fits the TEM response. Inversions of minimum structure (Occam) can also be performed with the program (e.g., Constable et al., 1987). The inhomogeneity of near-surface in Ashute geothermal field magnetotelluric data suffers from a static shift effect in the high-frequency band. The static-shifted corrected data were found to recover the resistivity more effectively as a consequence of the 3D inversion resistivity results. This gives better and more accurate estimates of subsurface structure resistivities and thicknesses, whereas uncorrected magnetotelluric data displayed by the apparent resistivity vertical shift curves can lead to erroneous and unreliable estimates. In comparison to earlier research to confirm their validity, it also showed agreement with the complex geology of the Ashute geothermal field. The correlation between 3D inversions of MT data without and with a stochastic shift correction is good. When the static shift correction is applied before the inversion, models that agree better with the original model appear to be recovered, especially when the static shift is enormous (Lichoro, 2015). The 3D model with one static shift correction recovers the subsurface resistivity structure. However, the size or shapes of the high resistivity structures in both 3D models are partially recovered at deeper depth. With regards to the margins of the geothermal system and the dominance of the low resistivity layer at shallow depth, there are some variations between the reconstructed models from the 3D inversion of MT data without and with the inclusion of a statistical shift correction. Therefore, the Ashute geothermal field between with and without static-shift corrected data revealed little difference at the shallow depth. However, at deeper depths, the two models approximately agree on resistivity below 2.7 km depth.

Generally, the results obtained in this dissertation are in good agreement with the known geological structures and identified the Ashute geothermal field not known before. In addition, the source of heat for the Ashute and Aluto geothermal fields was identified by using a 2D inversion model along the SDFZ, and the Identification of major geoelectric horizons in the Ashute geothermal system using a 3D inversion model incorporated with the static shift correction is the new results and new information in the CMER can be considered a scientific contribution of this dissertation towards understanding the significant of static shift correction, the tectono-magmatic setting, and geoelectrical structures of the study area.

7.2 Recommendations

Based on the results obtained and the limitations of this research, the following points are recommended:

- Conduct resistive stratigraphic well data, seismic surveys, or other geophysical measurements to confirm the study's findings and gain additional information for future geothermal resource planning.
- Additional good-quality MT data in the profile parallel across the rift is recommended in CMER in order to obtain a clear picture or extension of magma storage, and a 3D analysis model is needed by adding more than two profile parallels to this study area.
- It needs to investigate in detail the study of subsurface geology in the region considered.
- Perform joint 2D seismic and magnetotelluric modeling across the rift axis to gain complementary information, and insights, and validate the interpretation of the models.

References

Abebe, B., Acocella, V., Korme, T., & Ayalew, D. (2007). Quaternary faulting and volcanism in the Main Ethiopian Rift. *Journal of African Earth Sciences*, *48*(2–3), 115–124. https://doi.org/10.1016/j.jafrearsci.2006.10.005

Abebe, T., Balestrieri, M. L., & Bigazzi, G. (2010). The Central Main Ethiopian Rift is younger than 8 Ma: Confirmation through apatite fission-track thermochronology. *Terra Nova*, *22*(6), 470–476. https://doi.org/10.1111/j.1365-3121.2010.00968.x

Abossie, A., Fisseha, S., & Abebe, B. (2023a). 3D analysis of the MT data for resistivity structure beneath the Ashute geothermal site , Central Main Ethiopian Rift (CMER). *Heliyon*, *9*(2), e13202. https://doi.org/10.1016/j.heliyon.2023.e13202

Abossie, A., Fisseha, S., & Abebe, B. (2023b). Crustal resistivity structures beneath the western flank across the Central Main Ethiopian Rift : Its implications for partial melt and pathways. *Journal of Volcanology and Geothermal Research*, *441*(June), 107888. https://doi.org/10.1016/j.jvolgeores.2023.107888

Acocella, V., Korme, T., Salvini, F., & Funiciello, R. (2003). Elliptic calderas in the Ethiopian Rift: Control of pre-existing structures. *Journal of Volcanology and Geothermal Research*, *119*(1–4), 189–203. https://doi.org/10.1016/S0377-0273(02)00342-6

Agostini, A., Bonini, M., Corti, G., Sani, F., & Manetti, P. (2011). Distribution of Quaternary deformation in the central Main Ethiopian Rift, East Africa. *Tectonics*, *30*(4), 1–21. https://doi.org/10.1029/2010TC002833

Agostini, A., Pira, V. G. La, Florence, I.-, Corti, G., Florence, I.-, & Zeoli, A. (2009). *Evolution, pattern, and partitioning of deformation during oblique continental rifting: Inferences from lithospheric-scale centrifuge models*. https://doi.org/10.1029/2009GC002676

Alan D. Chave and J. Torquil Smith. (1994). *On electric and magnetic galvanic distortion tensor decompositions*.

Ambunya, M. N. (2017). *Processing and Inverting Resistivity*.

Andersen, C., & Wei, and P. (2020). *Heat Transfer From Convecting Magma Reservoirs to Hydrothermal Fluid Flow Systems Constrained by Coupled Numerical Modeling*. 1–11. https://doi.org/10.1029/2020GL089463

Árnason, K. (1989). *Central loop transient electromagnetic sounding over a horizontally layered earth*. Orkustofnun, Reykjavík, report.

Árnason, K. (2006). TEMTD, a Program for 1D Inversion of Central-loop TEM and MT Data. In *Unpublished ÍSOR Internal Report* (p. 17).

Árnason, K. (2008). The Magneto-Telluric Static Shift Problem. Iceland GeoSurvey. In *Report ÍSOR/08088*.

Árnason, K. (2015). The Static Shift Problem in MT Soundings. *Proceedings World Geothermal Congress*

2015, *April*, 19–25.

Árnason, K., Eysteinsson, H., & Hersir, G. P. (2010). *Geothermics Joint 1D inversion of TEM and MT data and 3D inversion of MT data in the Hengill area , SW Iceland*. *39*, 13–34. https://doi.org/10.1016/j.geothermics.2010.01.002

Avdeev, D., & Avdeeva, A. (2009). 3D magnetotelluric inversion using a limited-memory quasi-Newton optimization. *Geophysics*, *74*(3). https://doi.org/10.1190/1.3114023

Avdeeva, A., Moorkamp, M., Avdeev, D., Jegen, M., & Miensopust, M. (2015). Three-dimensional inversion of magnetotelluric impedance tensor data and full distortion matrix. *Geophysical Journal International*, *202*(1), 464–481. https://doi.org/10.1093/gji/ggv144

Bahr, K. (1988). Interpretation of the magnetotelluric impedance tensor: regional induction and local telluric distortion. *Journal of Geophysics - Zeitschrift Fur Geophysik*, *62*(2), 119–127.

Bahr, K. (1991). Geological noise in magnetotelluric data: a classification of distortion types. *Physics of the Earth and Planetary Interiors*, *66*(1–2), 24–38. https://doi.org/10.1016/0031-9201(91)90101-M

Becken, M., Ritter, O., & Burkhardt, H. (2008). Mode separation of magnetotelluric responses in three-dimensional environments. *Geophys. J. Int*, *172*, 67–86. https://doi.org/10.1111/j.1365-246X.2007.03612.x

Beka, T. I. (2016). *Geoelectrical structures beneath Spitsbergen- Svalbard derived from magnetotelluric imaging*. *April*.

Beka, T. I., 1, Smirnov, M., 2, Bergh, S. G., 3, Birkelund, & Y., & 1. (2015). The first magnetotelluric image of the lithospheric-scale geological architecture in central Svalbard, Arctic Norway. *Polar Research*, *34*(1), 26766. https://doi.org/10.3402/polar.v34.26766

Berdichevskiy, and D. (1976). *DISTORTION OF MAGNETIC AND ELECTRICAL FIELDS BY NEAR-SURFACE LATERAL INHOMOGENEITIES*. *11*(1976a), 447–483.

Bertani, R. (2010). *Geothermal Power Generation in the World 2005 – 2010 Update Report*. *2015*(April 2010), 25–29.

Beutel, E., Wijk, J. Van, Ebinger, C., Keir, D., & Agostini, A. (2010). Formation and stability of magmatic segments in the Main Ethiopian and Afar rifts. *Earth and Planetary Science Letters*, *293*(3–4), 225–235. https://doi.org/10.1016/j.epsl.2010.02.006

Bibby, H. M., Caldwell, T. G., & Brown, C. (2005). Determinable and non-determinable parameters of galvanic distortion in magnetotellurics. *Geophysical Journal International*, *163*(3), 915–930. https://doi.org/10.1111/j.1365-246X.2005.02779.x

Biggs, J., I. D. Bastow, D. Keir, and E. L. (2011). *Pulses of deformation reveal frequently recurring shallow magmatic activity beneath the Main Ethiopian Rift*. *12*(9), 1–11. https://doi.org/10.1029/2011GC003662

Boccaletti, M., Bonini, M., Mazzuoli, R., Abebe, B., Piccardi, L., & Tortorici, L. (1998). Quaternary oblique extensional tectonics in the Ethiopian Rift (Horn of Africa). *Tectonophysics*, *287*(1), 97–116. https://doi.org/https://doi.org/10.1016/S0040-1951(98)80063-2

Bonini, M., Corti, G., Innocenti, F., Manetti, P., Mazzarini, F., Abebe, T., & Pecskay, Z. (2005). Evolution of the Main Ethiopian Rift in the frame of Afar and Kenya rifts propagation. *Tectonics*, *24*(1), 1–21. https://doi.org/10.1029/2004TC001680

Booker, J. R. (2014). The Magnetotelluric Phase Tensor: A Critical Review. *Surveys in Geophysics*, *35*(1), 7–40. https://doi.org/10.1007/s10712-013-9234-2

Bretzler, A., Osenbrück, K., Gloaguen, R., Ruprecht, J. S., Kebede, S., & Stadler, S. (2011). Groundwater origin and flow dynamics in active rift systems - A multi-isotope approach in the Main Ethiopian Rift. *Journal of Hydrology*, *402*(3–4), 274–289. https://doi.org/10.1016/j.jhydrol.2011.03.022

Brian R. Spies and Frank C. Frischknecht. (1991). *ELECTROMAGNETIC SOUNDING*.

Brigham, E. O. (1988). *THE FAST FOURIER TRANSFORM AND ITS APPLICATIONS*.

Burnside, N., Montcoudiol, N., Becker, K., & Lewi, E. (2021). *Geothermal energy resources in Ethiopia : Status review and insights from hydrochemistry of surface and groundwaters*. *June*, 1–27. https://doi.org/10.1002/wat2.1554

Cagniard. (1953). Basic theory of the magnetotelluric method of geophysical prospecting. *Geophysics*, *18*, 605–635.

Caldwell, T. G., Bibby, H. M., & Brown, C. (2004). The magnetotelluric phase tensor. *Geophysical Journal International*, *158*(2), 457–469. https://doi.org/10.1111/j.1365-246X.2004.02281.x

Casey, M., Ebinger, C. J., Keir, D., Gloaguen, R., & Mohamed, F. (2006). Strain accommodation in transitional rifts: extension by magma intrusion and faulting in Ethiopian rift magmatic segments. *Geological Society Special Publication*, *259*(2003), 143–163. https://doi.org/10.1144/GSL.SP.2006.259.01.13

Chao, G., & Osella, A. (2003). Numerical simulations of the current channeling effect on MT responses due to shallow conductive structures. *Journal of Applied Geophysics*, *52*(2–3), 123–137. https://doi.org/10.1016/S0926-9851(02)00244-6

Chave, A. D., & Jones, A. G. (2012). *The magnetotelluric method: Theory and practice*. Cambridge University Press. https://doi.org/10.1017/CBO9781139020138

Cherevatova, M., Smirnov, M., Korja, T., Kaikkonen, P., Pedersen, L. B., Hübert, J., Kamm, J., & Kalscheuer, T. (2014). Crustal structure beneath southern Norway imaged by magnetotellurics. *Tectonophysics*, 1–16. https://doi.org/10.1016/j.tecto.2014.04.036

Cherkose, B. A., & Mizunaga, H. (2018). Resistivity imaging of Aluto-Langano geothermalfield using 3-D magnetotelluric inversion. *Journal of African Earth Sciences*, *139*, 307–318. https://doi.org/10.1016/j.jafrearsci.2017.12.017

Cherkose, B. A., & Saibi, H. (2021). Geothermics Investigation of the Ayrobera geothermal field using 3D magnetotelluric data inversion , Afar depression , NE Ethiopia. *Geothermics*, *94*(April), 102114. https://doi.org/10.1016/j.geothermics.2021.102114

Chiasera, B., Rooney, T. O., Girard, G., Yirgu, G., Grosfils, E., Ayalew, D., Mohr, P., Zimbelman, J. R., & Ramsey, M. S. (2018). Magmatically assisted off-rift extension — The case for broadly distributed strain accommodation. *Geosphere*, *14*(4), 1544–1563. https://doi.org/10.1130/GES01615.1

Chorowicz, J. (2005). The East African rift system. *Journal of African Earth Sciences*, *43*(1–3), 379–410. https://doi.org/10.1016/j.jafrearsci.2005.07.019

Chouteau, M., & Bouchard, K. (1988). Two-dimensional terrain correction in magnetotelluric surveys. *Geophysics*, *53*(6), 854–862. https://doi.org/10.1190/1.1442520

Christiansen, A. V., Auken, E., & Sørensen, K. (2006). *The transient electromagnetic method BT - Groundwater Geophysics: A Tool for Hydrogeology* (R. Kirsch (ed.); pp. 179–225). Springer Berlin Heidelberg. https://doi.org/10.1007/3-540-29387-6_6

Christopherson, K. R. (1998). *EXPLORER MT Gauges Earth's Electric Fields*.

Clarke, J., Gamble, T. D., Goubau, W. M., & Miracky, R. F. (1983). Remote-Reference Magnetotellurics : Equipment and Procedures *. *Geophysical Prospecting*, *31*(1), 149–170. doi:10.1111/j.1365-2478.1983.tb01047.x

Conde, L. (2018). Plasmas in space and in the laboratory. *An Introduction to Plasma Physics and Its Space Applications, Volume 1: Fundamentals and Elementary Processes*, *July*, 15–19. https://doi.org/10.1088/2053-2571/aae132ch1

Constable, S. C., Parker, R. L., & Constable, C. G. (1987). *models from electromagnetic sounding data*. *52*(3), 289–300.

Corti, G. (2009). Continental rift evolution: From rift initiation to incipient break-up in the Main Ethiopian Rift, East Africa. *Earth-Science Reviews*, *96*(1–2), 1–53. https://doi.org/10.1016/j.earscirev.2009.06.005

Corti, G., Sani, F., Florio, A. A., Greenfield, T., Keir, D., Muluneh, A. A., & Ayele, A. (2020). Tectonics of the Asela-Langano margin , Main Ethiopian Rift (East Africa). *American Geophysical Union*, 0–2. https://doi.org/10.1029/2020TC006075

Cumming, W., & Mackie, R. (2007). 3D MT resistivity imaging for geothermal resource assessment and environmental mitigation at the Glass Mountain KGRA, California. *Transactions - Geothermal Resources Council*, *31*, 331–334.

Dambly, M. L. T., Samrock, F., Grayver, A. V., & Saar, M. O. (2023). Insights on the Interplay of Rifting, Transcrustal Magmatism and Formation of Geothermal Resources in the Central Segment of the Ethiopian Rift Revealed by 3-D Magnetotelluric Imaging. *Journal of Geophysical Research: Solid Earth*, *128*(7). https://doi.org/10.1029/2022JB025849

DeGroot-Hedlin, C.,and Constable, S. (1990). Occam's inversion to generate smooth, two-dimensional models from magnetotelluric data. *Society of Exploration Geophysicists*, *55*(12), 1613–1624.

Delhaye, R., Rath, V., Jones, A. G., Muller, M. R., & Reay, D. (2017). *Correcting for static shift of magnetotelluric data with airborne electromagnetic measurements : a case study from Rathlin Basin , Northern Ireland*. 637–660. https://doi.org/10.5194/se-8-637-2017

Demissie, G. (2010). Mantle Influence , Rifting and Magmatism in the East African Rift System (EARS): A Regional View of the Controls on Hydrothermal Activity . *Proceedings World Geothermal Congress 2010 Bali, Indonesia, 25-29 April 2010*, *April*, 25–29.

Desissa, M., Johnson, N. E., Whaler, K. A., Hautot, S., Fisseha, S., & Dawes, G. J. K. (2013). A mantle magma reservoir beneath an incipient mid-ocean ridge in Afar, Ethiopia. *Nature Geoscience*, *6*(10), 861–865. https://doi.org/10.1038/ngeo1925

Di Paola, G. M. (1972). The Ethiopian Rift Valley (between 7° 00′ and 8° 40′ lat. north). *Bulletin Volcanologique*, *36*(4), 517–560. https://doi.org/10.1007/BF02599823

Didana, Y. L., Thiel, S., & Heinson, G. (2014). Magnetotelluric imaging of upper crustal partial melt at Tendaho graben in Afar, Ethiopia. *Geophysical Research Letters*, *41*(9), 3089–3095. https://doi.org/10.1002/2014GL060000

DiPippo, R. (2015). *Geothermal Power Plants: Principles, Applications, Case Studies and Environmental Impact: Fourth Edition*.

Dugda, M. T., Nyblade, A. A., Julia, J., Langston, C. A., Ammon, C. J., & Simiyu, S. (2005). Crustal structure in Ethiopia and Kenya from receiver function analysis: Implications for rift development in eastern Africa. *Journal of Geophysical Research: Solid Earth*, *110*(1), 1–15. https://doi.org/10.1029/2004JB003065

Ebinger, C. J., & Casey, M. (2001). Continental breakup in magmatic provinces : An Ethiopian example. *Geology*, *29*, 527–530. https://doi.org/10.1130/0091-7613(2001)029<0527

Egbert, G. D., & Kelbert, A. (2012). Computational recipes for electromagnetic inverse problems. *Geophysical Journal International*, *189*(1), 251–267. https://doi.org/10.1111/j.1365-246X.2011.05347.x

Fischer, G., & Le Quang, B. V. (1982). Parameter trade-off in one-dimensonal magnetotelluric modelling. *Journal of Geophysics - Zeitschrift Fur Geophysik*, *51*(3), 206–215.

Flóvenz, G., Hersir, G. P., Sæmundsson, K., Ármannsson, H., & Friðriksson. (2012). Geothermal Energy Exploration Techniques. In *Comprehensive Renewable Energy* (Vol. 7). Elsevier Ltd. https://doi.org/10.1016/B978-0-08-087872-0.00705-8

Frischknecht, F. C., Labson, V. F., Spies, B. R., & Anderson, W. L. (1991). 3. Profiling Methods Using Small Sources. In *Electromagnetic Methods in Applied Geophysics* (pp. 105–270). https://doi.org/10.1190/1.9781560802686.ch3

Furman, T., Bryce, J. G., Karson, J., & Iotti, A. (2004). East African Rift System (EARS) plume structure:

Insights from Quaternary mafic lavas of Turkana, Kenya. *Journal of Petrology*, *45*(5), 1069–1088. https://doi.org/10.1093/petrology/egh004

Gamble, T. D., Goubau, W. M., & Clarke, J. (1979). Magnetotellurics with a remote magnetic reference. *Geophysics*, *44*(1), 53–68. https://doi.org/10.1190/1.1440923

Garcia, X., & Jones, A. G. (2002). *Atmospheric sources for audio-magnetotelluric (AMT) sounding Atmospheric sources for audio-magnetotelluric (AMT) sounding*. *May 2014*, 447–458. https://doi.org/10.1190/1.1468604

Gashawbeza, E. M., Klemperer, S. L., Nyblade, A. A., Walker, K. T., & Keranen, K. M. (2004). *-wave splitting in Ethiopia : Precambrian mantle anisotropy locally modified by Neogene rifting*. *31*, 2–5. https://doi.org/10.1029/2004GL020471

Gasparon, M., Innocenti, F., Manetti, P., Peccerillo, A., & Tsegaye, A. (1993). Genesis of the pliocene to recent bimodal mafic-felsic volcanism in the Debre Zeyt area, central Ethiopia: volcanological and geochemical constraints. *Journal of African Earth Sciences*, *17*, 145–165.

Gebregzabher, Z. (1986). Hydrothermal alteration minerals in Aluto Langano geothermal wells, Ethiopia. *Geothermics*, *15*(5–6), 735–740. https://doi.org/10.1016/0375-6505(86)90086-6

Gebrewold, Y. (2017). *Geothermal Geochemistry of Butajira prospect area, Central Main Ethiopian: Implication for potential areas to Geothermal Energy in Ethiopia*.

GIDAY WOLDEGABRIEL, JAMES L. ARONSON, and R. C. W. (1990). Geology, geochronology, and rift basin development in the central sector of the Main Ethiopian Rift. *Geological Society Of America Bulletin*, *102*, 439–458. https://doi.org/10.1130/0016-7606(1990)102<0439

Glassley. (2010). *Geothermal Energy: Renewable Energy and the Environment*. CRC Press. https://doi.org/10.1201/EBK1420075700

Godio, A., & Santilano, A. (2017). PT. *Journal of Applied Geophysics*. https://doi.org/10.1016/j.jappgeo.2017.11.016

Goubau, W. M., Gamble, T. D., & Clarke, J. (1978). Magnetotelluric Data Analysis: Removal of Bias. *Geophysics*, *43*(6), 1157–1166. https://doi.org/10.1190/1.1440885

Grandis, H., & Menvielle, M. (2015). Thin-sheet electromagnetic modeling of magnetovariational data for a regional-scale study Geomagnetism. *Earth, Planets and Space*, *67*(1). https://doi.org/10.1186/s40623-015-0290-3

Grandis, H., Nurhasan, N., Widarto, D. S., & Mogi, T. (2006). Importance of Geophysical Investigations of Active Faults and Crustal Structures in Earthquake Hazard Mitigation. *International Workshop on Integration of Geophysical Parameter as a Set of Large Earthquake Precursors*, *April 2016*, 7pp.

Grayver, A. V. (2015). Parallel three-dimensional magnetotelluric inversion using adaptive finite-element method. Part I: Theory and synthetic study. *Geophysical Journal International*, *202*(1), 584–603.

https://doi.org/10.1093/gji/ggv165

Gribenko, A., & Zhdanov, M. (2007). Rigorous 3D inversion of marine CSEM data based on the integral equation method. *Geophysics*, *72*(2). https://doi.org/10.1190/1.2435712

Groom, R. W., & Bailey, R. C. (1989). *Decomposition of Magnetotelluric Impedance Tensors in the Presence of Local Three-Dimensional Galvanic Distortion*. *94*, 1913–1925.

Groom, R. W., Kurtz, R. D., Jones, A. G., & Boerner, D. E. (1993). A quantitative methodology to extract regional magnetotelluric impedances and determine the dimension of the conductivity structure. *Geophysical Journal International*, *115*(3), 1095–1118. https://doi.org/10.1111/j.1365-246X.1993.tb01512.x

Guillen, A., Calcagno, P., Courrioux, G., Joly, A., Ledru, P., Guillen, A., Calcagno, P., Courrioux, G., Joly, A., & Ledru, P. (2010). *Geological modelling from field data and geological knowledge , Part II - Modelling validation using gravity and magnetic data inversion To cite this version : HAL Id : hal-00532156*. https://doi.org/10.1016/j.pepi.2008.06.014

Gupta, H. (2007). *Geothermal Energy An Alternative Resource for the 21st Century*.

Habteweld, F. (2014). *GRAVITY STUDIES OF THE CRUSTAL STRUCTURES BENEATH THE NORTHERN MAIN ETHIOPIAN RIFT AND THE ADJOINING EASTERN PLATEAU*.

Heise, W., Caldwell, T. G., Bibby, H. M., & Brown, C. (2006). Anisotropy and phase splits in magnetotellurics. *Physics of the Earth and Planetary Interiors*, *158*, 107–121. https://doi.org/10.1016/j.pepi.2006.03.021

Hersir, G. P., & Bjornsson, A. (1991). *Geophysical exploration for geothermal resources: principles and application*. 94. http://scholar.google.com/scholar?hl=en&btnG=Search&q=intitle:Geophysical+exploration+for+geothermal+resources+Principles+and+application#0

Hersir, G. P., & Flovenz, O. G. (2015). Resistivity surveying and electromagnetic methods. In *IGA Academy Report*.

Hill, G. J., Caldwell, T. G., Heise, W., Chertkoff, D. G., Bibby, H. M., Burgess, M. K., Cull, J. P., & Cas, R. A. F. (2009). Distribution of melt beneath Mount St Helens and Mount Adams inferred from magnetotelluric data. *Nature Geoscience*, *2*(11), 785–789. https://doi.org/10.1038/ngeo661

Hochstein, M. P. (2005). Heat Transfer by Hydrothermal Systems in the East African Rifts. *Proceedings World Geothermal Congress*, *April*, 24–29.

Hübert, J., Whaler, K., & Fisseha, S. (2018). The Electrical Structure of the Central Main Ethiopian Rift as Imaged by Magnetotellurics: Implications for Magma Storage and Pathways. *Journal of Geophysical Research: Solid Earth*, *123*(7), 6019–6032. https://doi.org/https://doi.org/10.1029/2017JB015160

Hunt, J. A., Zafu, A., Mather, T. A., Pyle, D. M., & Barry, P. H. (2017). Spatially Variable CO2 Degassing in the Main Ethiopian Rift: Implications for Magma Storage, Volatile Transport, and Rift-Related Emissions. *Geochemistry, Geophysics, Geosystems*, *18*(10), 3714–3737. https://doi.org/10.1002/2017GC006975

Hutchison, W., 1, 2, Mather, T. A., 1, Pyle, D. M., 1, Boyce, A. J., 3, 3, M. L., Gleeson, M., 4, Yirgu, G., 5, Blundy, J. D., 6, Ferguson, D. J., 7, Vye-Brown, C., 8, … Rose, W. (2018). *The evolution of magma during continental rifting : new constraints from the isotopic and trace element signatures of silicic magmas from Ethiopian volcanoes*.

Inman, J. R. (1975). Resistivity inversion with ridge regression. *Geophysics*, *40*(5), 798–817. https://doi.org/https://doi.org/10.1190/1.1440569

JICA & GSE. (2015). The Project for Formulating Master Plan on Development of Geothermal Energy in Ethiopia. Final Report. *Nippon Koei Co., Ltd. Jmc Geothermal Engineering Co., Ltd. Sumiko Resources Engineering and Development Co., Ltd.*

Jiracek, G. R. (1990). *NEAR-SURFACE AND TOPOGRAPHIC DISTORTIONS IN ELECTROMAGNETIC INDUCTION*. *1970*, 163–203.

Johnson, N. E., Whaler, K. A., Hautot, S., Fisseha, S., Desissa, M., & Dawes, G. J. K. (2016). Magma imaged magnetotellurically beneath an active and an inactive magmatic segment in Afar, Ethiopia. *Geological Society Special Publication*, *420*(1), 105–125. https://doi.org/10.1144/SP420.11

Johnston, J. M., Pellerin, L., & Hohmann, G. W. (1992). Evaluation of electromagnetic methods for geothermal reservoir detection. *Transactions - Geothermal Resources Council*, *16*, 241–245.

Jones, A. G. (1988). *Sfafic shift of magnetotelluric in a sedimentary data and its removal basin environment*. *53*(7), 967–978.

Jones, A. G., & Foster, J. H. (1986). An objective real-time data adaptive technique for efficient in-field model resolution improvement in magnetotelluric studies. *SEG Annual Meeting*, *51*(I), 145–148. https://doi.org/10.1190/1.1893798

Jones, A. G., & Groom, R. W. (1993). Strike-angle determination from the magnetotelluric impedance tensor in the presence of noise and local distortion: rotate at your peril! *Geophysical Journal International*, *113*(2), 524–534. https://doi.org/10.1111/j.1365-246X.1993.tb00905.x

Jones, C. and. (1997). *Electric and Magnetic Field Galvanic Distortion Decomposition of B087 Data*. *1989*, 767–789.

Jones, F. W., & Price, A. T. (1970). The Perturbations of Alternating Geomagnetic Fields by Conductivity Anomalies. *Geophysical Journal of the Royal Astronomical Society*, *20*(3), 317–334. https://doi.org/10.1111/j.1365-246X.1970.tb06073.x

Jupp, D. L. B., & Vozoff, K. (1977). Two-dimensional magnetotelluric inversion. *Geophysical Journal of the Royal Astronomical Society*, *50*(2), 333–352. https://doi.org/10.1111/j.1365-246X.1977.tb04177.x

Kaufman, A. A. (1988). *Reduction of the Geological Noise in Magnetotelluric Soundings*. *25*, 145–161.

Kebede, B., Alemu, A., Kebede, H., Melaku, E., Feyissa, D., & Legesse, G. (2023). *Unraveling the Geothermal Potential of Corbetti Caldera Using Integrated Geophysical Methods , Central Main Ethiopian Rift*. *6*(1), 333–351.

Kebede, H., Alemu, A., Nedaw, D., & Fisseha, S. (2021). Depth estimates of anomalous subsurface sources using 2D/3D modeling of potential field data: implications for groundwater dynamics in the Ziway-Shala Lakes Basin, Central Main Ethiopian Rift. *Heliyon*, *7*(4), e06843. https://doi.org/10.1016/j.heliyon.2021.e06843

Kebede, S. (2010). Status of Geothermal Exploration and Development in Ethiopia. *Unu-Gtp*, 1–10.

Keeva Vozoff. (1972). The magnetotelluric method in the exploration of sedimentary basins. *GEOPHYSICS, 37*(1), 98–141. doi:10.1190/1.1440255

Keir, D., Bastow, I. D., Corti, G., Mazzarini, F., & Rooney, T. O. (2015). The origin of along-rift variations in faulting and magmatism in the Ethiopian Rift. *Tectonics*, *34*(3), 464–477. https://doi.org/10.1002/2014TC003698

Keir, D., Stuart, G. W., Jackson, A., & Ayele, A. (2006). Local earthquake magnitude scale and seismicity rate for the Ethiopian rift. *Bulletin of the Seismological Society of America*, *96*(6), 2221–2230. https://doi.org/10.1785/0120060051

Kelbert, A., Meqbel, N., Egbert, G. D., & Tandon, K. (2014). ModEM: A modular system for inversion of electromagnetic geophysical data. *Computers and Geosciences*, *66*(May), 40–53. https://doi.org/10.1016/j.cageo.2014.01.010

Keller, G. V. (1988). *and Mineral Properties*.

Keranen, K., & Klemperer, S. L. (2008). Discontinuous and diachronous evolution of the Main Ethiopian Rift: Implications for development of continental rifts. *Earth and Planetary Science Letters*, *265*(1–2), 96–111. https://doi.org/10.1016/j.epsl.2007.09.038

Keranen, K., Klemperer, S. L., Gloaguen, R., Asfaw, L., Ayele, A., Ebinger, C., Furman, T., Harder, S., Keler, G. R., Mackenzie, G. D., Maguire, P. K. H., & Stuart, G. W. (2004). Three-dimensional seismic imaging of a protoridge axis in the Main Ethiopian rift. *Geological Society of America*, *32*(11), 949–952. https://doi.org/10.1130/G20737.1

Keto, Y. K., & Saibi, H. (2016). 2-D Inversion of magnetotelluric data from Tendaho Geothermal Field (NE Ethiopia). *International Symposium on Earth Science and Technology*. https://www.researchgate.net/publication/305688060

Key, K. (2009). 1D inversion of multicomponent , multifrequency marine CSEM data : Methodology and synthetic studies for resolving thin resistive layers. *Geophysics*, *74*(2), F9–F20. https://doi.org/doi:10.1190/1.3058434

Kim, S., Nyblade, A. A., Rhie, J., Baag, C. E., & Kang, T. S. (2012). Crustal S-wave velocity structure of the Main Ethiopian Rift from ambient noise tomography. *Geophysical Journal International*, *191*(2), 865–878. https://doi.org/10.1111/j.1365-246X.2012.05664.x

Kirkby, A., & Duan, J. (2019). Crustal Structure of the Eastern Arunta Region, Central Australia, From Magnetotelluric, Seismic, and Magnetic Data. *Journal of Geophysical Research: Solid Earth*, *124*(8), 9395–9414. https://doi.org/10.1029/2018JB016223

Korme, T., Acocella, V., & Abebe, B. (2004). The role of pre-existing structures in the origin, propagation and architecture of faults in the Main Ethiopian Rift. *Gondwana Research*, *7*(2), 467–479. https://doi.org/10.1016/S1342-937X(05)70798-X

Korme, T., Chorowicz, J., Collet, B., & Bonavia, F. (1997). Volcanic vents rooted on extension fractures and their geodynamic implications in the Ethiopian Rift. *Journal of Volcanology and Geothermal Research*, *79*(3–4), 205–222. https://doi.org/10.1016/S0377-0273(97)00034-6

Krieger, L., & Peacock, J. R. (2014). MTpy: A Python toolbox for magnetotellurics. *Computers and Geosciences*, *72*, 167–175. https://doi.org/10.1016/j.cageo.2014.07.013

Le Turdu, C., Tiercelin, J. J., Gibert, E., Travi, Y., Lezzar, K. E., Richert, J. P., Massault, M., Gasse, F., Bonnefille, R., Decobert, M., Gensous, B., Jeudy, V., Tamrat, E., Mohammed, M. U., Martens, K., Atnafu, B., Chernet, T., Williamson, D., & Taieb, M. (1999). The Ziway-Shala lake basin system, Main Ethiopian Rift: Influence of volcanism, tectonics, and climatic forcing on basin formation and sedimentation. *Palaeogeography, Palaeoclimatology, Palaeoecology*, *150*(3–4), 135–177. https://doi.org/10.1016/S0031-0182(98)00220-X

Leeuwen, W. A. Van. (2016). *Geothermal exploration using the magnetotelluric method*.

Lei, Q., Latham, J., & Tsang, C. (2017). Computers and Geotechnics The use of discrete fracture networks for modelling coupled geomechanical and hydrological behaviour of fractured rocks. *Computers and Geotechnics*, *85*, 151–176. https://doi.org/10.1016/j.compgeo.2016.12.024

LEVENBERG, K. (1944). A method for the solution of certain non-linear problems in least squares. *Quarterly of Applied Mathematics*, *2*(2), 164–168. https://doi.org/doi:10.1090/qam/10666

Lichoro, C. M. (2009). *JOINT 1-D INVERSION OF TEM AND MT DATA FROM OLKARIA DOMES GEOTHERMAL AREA , KENYA* (Issue 16).

Lichoro, C. M. (2015). A comparison of 1-D, 2-D and 3-D approaches of interpreting electromagnetic data of Silali geothermal area. *Transactions - Geothermal Resources Council*, *37*(PART 1), 501–507.

Lines, L. R., & Treitel, S. (1984). *TUTORIAL A REVIEW O F LEAST-SQUARES INVERSION A N D ITS APPLICATION TO GEOPHYSICAL PROBLEMS *. December 1982*, 159–186.

Louise Pellerin, and G. W. H. (1990). *Transient electromagnetic inversion: A remedy for magnetotelluric static shifts*.

Lund, J. W. (2010). Direct utilization of geothermal energy. *Energies, 3*(8), 1443–1471. https://doi.org/10.3390/en3081443

M. N. Berdichevsky, and V. I. D. (1976). *Basic principles of interpretation of magnetotelluric sounding curves*. *1976b*, 1976.

M. N. Berdichevsky, V. I. D. and E. E. P. (1998). On two-dimensional interpretation of magnetotelluric soundings. *Geophysical Journal International*, *133*, 585–606.

Maccaferri, F., Rivalta, E., Keir, D., & Acocella, V. (2014). Off-rift volcanism in rift zones determined by crustal unloading. *Nature Geoscience*, *7*(4), 297–300. https://doi.org/10.1038/ngeo2110

Mackenzie, G. D., Thybo, H., & Maguire, P. K. H. (2005). Crustal velocity structure across the Main Ethiopian Rift : results from two-dimensional wide-angle seismic modelling. *Geophys. J. Int*, *162*, 994–1006. https://doi.org/10.1111/j.1365-246X.2005.02710.x

Mahatsente, R., Jentzsch, G., & Jahr, T. (1999). Crustal structure of the Main Ethiopian Rift from gravity data : 3-dimensional modeling. *Tectonophysics 3*, *313*(4), 363–382. https://doi.org/doi:10.1016/s0040-1951(99)00213-9

Malleswari, D., Veeraswamy, K., Abdul Azeez, K. K., Gupta, A. K., Babu, N., Patro, P. K., & Harinarayana, T. (2019). Magnetotelluric investigation of lithospheric electrical structure beneath the Dharwar Craton in south India: Evidence for mantle suture and plume-continental interaction. *Geoscience Frontiers*, *10*(5), 1915–1930. https://doi.org/10.1016/j.gsf.2018.10.011

Marquardt, D. W. (1963). An algorithm for least-squares estimation of nonlinear parameters. *Journal of the Society for Industrial and Applied Mathematics*, *11*(2), 431-441. https://doi.org/https://doi.org/10.1137/011103

Martí, A., Queralt, P., Ledo, J., & Farquharson, C. (2010). Dimensionality imprint of electrical anisotropy in magnetotelluric responses. *Physics of the Earth and Planetary Interiors*, *182*(3–4), 139–151. https://doi.org/10.1016/j.pepi.2010.07.007

Martí, A., Queralt, P., & Roca, E. (2004). Geoelectric dimensionality in complex geological areas: Application to the Spanish Betic Chain. *Geophysical Journal International*, *157*(3), 961–974. https://doi.org/10.1111/j.1365-246X.2004.02273.x

Marwan, M. Yanis, Rinaldi Idroes, Nazli Ismail. (2019). 2D INVERSION AND STATIC SHIFT OF MT AND TEM DATA FOR IMAGING THE GEOTHERMAL RESOURCES OF SEULAWAH AGAM VOLCANO , INDONESIA. *International Journal of GEOMATE*, *17*(62), 173–180.

Marwan, Yanis, M., Idroes, R., & Ismail, N. (2019). 2D inversion and static shift of MT and TEM data for imaging the geothermal resources of Seulawah Agam Volcano, Indonesia. *International Journal of GEOMATE*, *17*(62), 173–180. https://doi.org/10.21660/2019.62.11724

McNeice, G. W., & Jones, A. G. (2001). Multisite, multifrequency tensor decomposition of magnetotelluric data. *Geophysics*, *66*(1), 158–173. https://doi.org/10.1190/1.1444891

Menke, W. (1984). *GEOPHYSICAL DATA ANALYSIS : William M e n k e*.

Menke, W. (1989). *GEOPHYSICAL DATA ANALYSIS: DISCRETE INVERSE THEORY* (R. Edition (ed.)).

Menke, W. (2018). *GEOPHYSICAL DATA ANALYSIS Discrete Inverse Theory* (FOURTH EDI).

Meqbel, N. (2009). *The electrical conductivity structure of the Dead Sea Basin derived from 2D and 3D inversion of magnetotelluric data Dipl . Geophys . Naser Mohammad Meqbel Meqbel*.

Miensopust, marion petra. (2010). *Multi-dimensional magnetotellurics a 2d case study and a 3d approach to simultaneously invert for resistivity structure and distortion parameters*.

Mohamed, A. K. (2002). *APPLICATIONS OF MAGNETOTELLURIC AND TRANSIENT ELECTROMAGNETIC METHODS IN*.

Mohamed Abdelzaher, Jun Nishijima, Hakim Saibi, Gad El-Qady, Usama Massoud, Mamdouh Soliman, Abdellatif Younis, and S. (2012). *A Coastal Aquifer Study Using Magnetotelluric and Gravity Methods in Abo Zenema , Egypt*. *169*, 1679–1692. https://doi.org/10.1007/s00024-011-0407-y

Mohr, P. (1987). Patterns of faulting in the Ethiopian rift valley. *Tectonophysics*, *143*(1–3), 169–179. https://doi.org/10.1016/0040-1951(87)90086-2

Mohr P. A. (1962). Surface Cauldron Subsidence with Associated Faulting and Fissure Basalt Eruptions at 6ariboldi Pass, Shoa, Ethiopia. *Bulletin Volcanologique*, *Bulletin V*(1), 421–428. https://doi.org/10.1007/BF02599358

Molin, P., & Corti, G. (2015). Topography, river network and recent fault activity at the margins of the Central Main Ethiopian Rift (East Africa). *Tectonophysics*, *664*, 67–82. https://doi.org/10.1016/j.tecto.2015.08.045

Morley, C.K., Ngenoh, D.K., Ego, J. . (1999). Introduction to the East African Rift System. *Geoscience of Rift Systems - Evolution of East Africa*, *44*, 1–18.

Morton, W. . (1979). Riftward younging of volcanic unit in the Addis Ababa region Ethiopia rift valley. *Nature*, *280*(5720), 284–288. https://doi.org/doi:10.1038/280284a0

Muñoz, G. (2014). Exploring for Geothermal Resources with Electromagnetic Methods. *Surv Geophys*. https://doi.org/10.1007/s10712-013-9236-0

Muñoz, G., Weckmann, U., Pek, J., Kováčiková, S., & Klanica, R. (2018). Regional two-dimensional magnetotelluric profile in West Bohemia/Vogtland reveals deep conductive channel into the earthquake swarm region. *Tectonophysics*, *727*, 1–11. https://doi.org/10.1016/j.tecto.2018.01.012

N., Tikhonov, A. (1950). On Determining Electrical Characteristics of the Deep Layers of the Earth's Crust. *Doklady*, *73*(2), 295–297.

Newman, G. A., & Alumbaugh, D. L. (2000). Three-dimensional magnetotelluric inversion using non-linear conjugate gradients. *Geophysical Journal International*, *140*(2), 410–424. https://doi.org/10.1046/j.1365-

246X.2000.00007.x

Nowacki, A., Wilks, M., Kendall, J. M., Biggs, J., & Ayele, A. (2018). Characterising hydrothermal fluid pathways beneath Aluto volcano, Main Ethiopian Rift, using shear wave splitting. *Journal of Volcanology and Geothermal Research*, *356*, 331–341. https://doi.org/10.1016/j.jvolgeores.2018.03.023

Ogawa, Y. (2002). On two-dimensional modeling of magnetotelluric field data. *Surveys in Geophysics*, *23*(2/3), 251–273. https://doi.org/10.1023/a:1015021006018

Ogawa, Y., & Uchida, T. (1996a). A two-dimensional magnetotelluric inversion assuming Gaussian static shift. *Geophysical Journal International*, *126*(1), 69–76. https://doi.org/10.1111/j.1365-246X.1996.tb05267.x

Ogawa, Y., & Uchida, T. (1996b). A two - dimensional magnetotelluric inversion assuming Gaussian static shift A two-dimensional magnetotelluric inversion assuming Gaussian static shift. *Geophysical Journal International*, *126*, 69–76. https://doi.org/10.1111/j.1365-246X.1996.tb05267.x

Oldenburg, D. W. (2005). *INVERSION FOR APPLIED GEOPHYSICS : A TUTORIAL* (Issue January 2005). https://doi.org/10.1190/1.9781560801719.ch5

Oryński, S., Jó, W., & Nowo, K. (2022). *Comparison of 3D , 2D , and 1D Magnetotelluric Inversion Results on the Example of Data from Fore-Sudetic Monocline*. *2022*.

Palacky, G. J. (1987). *Resistivity Characteristics of Geologic Targets*.

Pandeli, E., Gabbani, G., Valentini, S., Margottini, C., & Naso, V. (2013). Medium-enthalpy geothermal energy systems: New opportunities of renewable energy in China. *International Conference on Power Engineering 2013, ICOPE 2013*.

Parker, R. L. (1980). The Inverse Problem of Electromagnetic Induction: Existence and Construction of Solutions Based On Incomplete Data. *GEOPHYSICAL RESEARCH*, *85*, 4421–4428.

Parker, R. L. (1994). *Geophysical Inverse Theory*. Princeton University Press.

Parkinson, W. D. (1959). Directions of Rapid Geomagnetic Fluctuations. *Geophysical Journal of the Royal Astronomical Society*, *2*(1), 1–14. https://doi.org/10.1111/j.1365-246X.1959.tb05776.x

Parkinson, W. D., Miguel, S., Kuyper, K., & Darwin, D. (1962). The Infiuence of Continents and Oceans on Geomagnetic Variation & ssw s sw wsw. *Geophysical Journal of the Royal Astronomical Society*, *6*, 441–449.

Patro, B. P. K., & Sarma, S. V. S. (2007). Trap thickness and the subtrappean structures related to mode of eruption in the Deccan Plateau of India : results from magnetotellurics. *Earth Planets Space*, *59*, 75–81. https://doi.org/doi:10.1186/bf03352679

Paulson, Y. Z. and K. V. (1997). *Enhancement of Signal-to-noise Ratio in Natural-source Transient Magnetotelluric Data with Wavelet Transform*. *149*, 405–419.

Peccerillo, A., Barberio, M. R., Yirgu, G., Ayalew, D., Barbieri, M., & Wu, T. W. (2003). Relationships between mafic and peralkaline silicic magmatism in continental rift settings: A petrological, geochemical and isotopic study of the Gedemsa volcano, Central Ethiopian rift. *Journal of Petrology*, *44*(11), 2003–2032. https://doi.org/10.1093/petrology/egg068

Petrick, W. R., Pelton, W. H., and Ward, S. H. (1977). *RIDGE REGRESSION INVERSION APPLIED TO CRUSTAL RESISTIVITY SOUNDING DATA FROM SOUTH AFRICA*. *42*(5).

Philip E. Wannamaker *, Gerald W. Hohmannl, A., & San Filipo S, W. A. (1984). *Electromagnetic modeling using integral equations of bodies in layered earths*. *49*(I), 60–74.

Pizzi, A., Colotrti, M., Abebe, B., Disperati, L., Sacchi, G., & Salvini, & R. (2006). structural and geomorphological constraints lp Ik. *Geological Society, London, Special Publications*, 191–207. https://doi.org/10.1144/GSL.SP.2006.259.01.16

Pürschel, M., Gloaguen, R., & Stadler, S. (2013). Geothermics Geothermal activities in the Main Ethiopian Rift : Hydrogeochemical characterization of geothermal waters and geothermometry applications. *Geothermics*, *47*, 1–12. https://doi.org/10.1016/j.geothermics.2013.01.001

Radhakrishnamurty, C. and, & Likhite, S. D. (1970). Hopkinson effect, blocking temperature and Curie point in basalts. *Earth and Planetary Science Letters*, *7*(5), 389–396. https://doi.org/https://doi.org/10.1016/0012-821X(70)90080-4

Ranganayaki, R. P. (1984). An interpretive analysis of magnetotelluric data. *Geophysics*, *49*(10), 173G1748. https://doi.org/https://doi.org/10.1190/1.1441580

Ring, U. (2014). The East African rift system. *Austrian Journal of Earth Sciences*, *107*(1), 132–146. https://doi.org/10.1007/978-3-319-73785-0_3

Robertson, R. C. (1988). The electromagnetic response of a heterogeneous layer modeled by two thin sheets in a uniformly conducting half-space. *IEEE Transactions on Geoscience and Remote Sensing*, *26*(1), 2–10. https://doi.org/10.1109/36.2993

Rodi, W., & Mackie, R. L. (2001). Nonlinear conjugate gradients algorithm for 2-D magnetotelluric inversion. *Geophysics*, *66*(1), 174–187. https://doi.org/10.1190/1.1444893

Rooney, T., Furman, T., Bastow, I., Ayalew, D., & Yirgu, G. (2007). Lithospheric modification during crustal extension in the Main Ethiopian Rift. *Journal of Geophysical Research*, *112*(B10201). https://doi.org/10.1029/2006JB004916

Rooney, T. O., Bastow, I. D., & Keir, D. (2011). Insights into extensional processes during magma assisted rifting: Evidence from aligned scoria cones. *Journal of Volcanology and Geothermal Research*, *201*(1–4), 83–96. https://doi.org/10.1016/j.jvolgeores.2010.07.019

Rooney, T. O., Bastow, I. D., Keir, D., Mazzarini, F., Movsesian, E., Grosfils, E. B., Zimbelman, J. R., Ramsey, M. S., Ayalew, D., & Yirgu, G. (2014). The protracted development of focused magmatic intrusion during continental rifting. *Tectonics*, *33*(6), 875–897. https://doi.org/10.1002/2013TC003514

Rooney, T. O., Furman, T., Yirgu, G., & Ayalew, D. (2005). Structure of the Ethiopian lithosphere: Xenolith evidence in the Main Ethiopian Rift. *Geochimica et Cosmochimica Acta*, *69*(15), 3889–3910. https://doi.org/10.1016/j.gca.2005.03.043

Rosenkjaera, G. K., Gasperikova, E., Newman, G. ., Arnason, K., & Lindsey, N. J. (2015). *Geothermics Comparison of 3D MT inversions for geothermal exploration : Case studies for Krafla and Hengill geothermal systems in Iceland*. *57*, 258–274.

Rybach, L. (2010). The Future of Geothermal Energy" and Its Challenges. *World Geothermal Congress, April*, 1–4. http://www.geothermal-energy.org/pdf/IGAstandard/WGC/2010/3109.pdf

S.H. Yungul. (1996). Electrical Methods in Geophysical Exploration of Deep Sedimentary Basins. *Geophysical Journal International*, *128*(2), 501–501. https://doi.org/10.1111/j.1365-246x.1997.tb01574.x

Saibi, H., Khosravi, S., Abera, B., Smirnov, M., Kebede, Y., & Fowler, A. (2021). Magnetotelluric data analysis using 2D inversion : A case study from Al-Mubazzarah Geothermal Area (AMGA), Al-Ain , United Arab Emirates. *Heliyon*, *7*(June 2020), e07440. https://doi.org/10.1016/j.heliyon.2021.e07440

Samrock, F., Grayver, A. V., Eysteinsson, H., & Saar, and M. O. (2018). *Magnetotelluric Image of Transcrustal Magmatic System Beneath the Tulu Moye Geothermal Prospect in the Ethiopian Rift*. *45*(23).

Samrock, F., Grayver, A. V, Bachmann, O., Karakas, Ö., & Saar, M. O. (2021). Integrated magnetotelluric and petrological analysis of felsic magma reservoirs: Insights from Ethiopian rift volcanoes. *Earth and Planetary Science Letters*, *559*, 118785. https://doi.org/doi:10.1016/j.epsl.2021.116765

Samrock, F., Kuvshinov, A., Bakker, J., Jackson, A., & Fisseha, S. (2015). 3-D analysis and interpretation of magnetotelluric data from the Aluto-Langano geothermal field, Ethiopia. *Geophysical Journal International*, *202*(3), 1923–1948. https://doi.org/10.1093/gji/ggv270

Sasaki, Y. (2004). Three-dimensional inversion of static-shifted magnetotelluric data. *Earth, Planets and Space*, *56*(2), 239–248. https://doi.org/10.1186/BF03353406

Sasaki, Y., & Meju, M. A. (2006). *Three-dimensional joint inversion for magnetotelluric resistivity and static shift distributions in complex media*. *111*(May), 1–11. https://doi.org/10.1029/2005JB004009

Schmucker, U. (1970). *ANOMALIES OF GEOMAGNETIC VARIATIONS IN THE SOUTHWESTERN UNITED STATES BY* (First Edit). University of California Press.

Schmucker, U. (1973). Regional induction studies: A review of methods and results. *Physics of the Earth and Planetary Interiors*, *7*(3), 365–378. https://doi.org/10.1016/0031-9201(73)90061-7

Schwalenberg, K., Rath, V., & Haak, V. (2002). Sensitivity studies applied to a two-dimensional resistivity model from the Central Andes. *Geophysical Journal International*, *150*(3), 673–686. https://doi.org/10.1046/j.1365-246X.2002.01734.x

Segovia, M. J., Diaz, D., Slezak, K., & Zuñiga, F. (2021). Magnetotelluric study in the Los Lagos Region (Chile) to investigate volcano - tectonic processes in the Southern Andes. *Earth, Planets and Space*.

https://doi.org/10.1186/s40623-020-01332-w

Sharma, S. P., & Biswas, A. (2011). Global nonlinear optimization for the estimation of static shift and interpretation of 1-D magnetotelluric sounding data. *ANNALS OF GEOPHYSICS*, *54*(3). https://doi.org/10.4401/ag-4766

Shinjo, R., Chekol, T., Meshesha, D., Itaya, T., & Tatsumi, Y. (2011). Geochemistry and geochronology of the mafic lavas from the southeastern Ethiopian rift (the East African Rift System): Assessment of models on magma sources, plume-lithosphere interaction and plume evolution. *Contributions to Mineralogy and Petrology*, *162*(1), 209–230. https://doi.org/10.1007/s00410-010-0591-2

Simpson, F., & Bahr, K. (2005). *Practical Magnetotellurics*. Cambridge University Press.

Sims, W. E., Bostick, F. X., & Smith, H. W. (1971). the Estimation of Magnetotelluric Impedance Tensor Elements From Measured Data. *Geophysics*, *36*(5), 938–942. https://doi.org/10.1190/1.1440225

Sinetebeb, Y., Yirgu, G., & Barry, P. (2020). *Helium Isotopes As Heat Source Indicator of Butajira Geothermal Prospect , Ethiopia*. *November*, 2–8.

Singer, B. S. (1992). Correction for distortions of magnetotelluric fields: Limits of validity of the static approach. *Surveys in Geophysics*, *13*(4–5), 309–340. https://doi.org/10.1007/BF01903482

SINGER, B. S. (1990). *CORRECTION FOR DISTORTIONS OF MAGNETOTELLURIC FIELDS: LIMITS OF VALIDITY OF THE STATIC APPROACH*. 309–340.

Siripunvaraporn, W., & Egbert, G. (2000). An efficient data-subspace inversion method for 2-D magnetotelluric data. *GEOPHYSICS*, *65*(3), 791–803. https://doi.org/10.1190/1.1444778

Siripunvaraporn, W., & Egbert, G. (2009). WSINV3DMT: Vertical magnetic field transfer function inversion and parallel implementation. *Physics of the Earth and Planetary Interiors*, *173*(3–4), 317–329. https://doi.org/10.1016/j.pepi.2009.01.013

Siripunvaraporn, W., & Sarakorn, W. (2011). An efficient data space conjugate gradient Occam's method for three-dimensional magnetotelluric inversion. *Geophysical Journal International*, *186*(2), 567–579. https://doi.org/10.1111/j.1365-246X.2011.05079.x

Smith, J. T. (1997). *Estimating galvanic-distortion magnetic fields in magnetotellurics*. 65–72.

Smith, J. T., & Booker, J. R. (1991). Rapid inversion of two- and three-dimensional magnetotelluric data. *Journal of Geophysical Research*, *96*(B3), 3905–3922. https://doi.org/10.1029/90JB02416

Solutions of ill-posed problems. (1977). In *Scripta series in mathematics TA - TT* -. V.H. Winston ; J. Wiley. https://doi.org/LK - https://worldcat.org/title/716917748

Spichak. (2020). *Electromagnetic study of geothermal areas 6.1*. https://doi.org/10.1016/B978-0-12-819631-1.00006-7

Spichak, V., & Manzella, A. (2009). Electromagnetic sounding of geothermal zones. *Journal of Applied Geophysics*, *68*(4), 459–478. https://doi.org/10.1016/j.jappgeo.2008.05.007

Spichak, V. V., Zakharova, O. K., & Goidina, A. G. (2013). A new conceptual model of the Icelandic crust in the Hengill geothermal area based on the indirect electromagnetic geothermometry. *Journal of Volcanology and Geothermal Research*, *257*, 99–112. https://doi.org/10.1016/j.jvolgeores.2013.03.013

Sternberg, B. K., Washburne, J. C., & Pellerint, L. (1988). *transient electromagnetic soundings*. *53*(11), 1459–1468.

Stratton, J. A. (1941). *Electromagnetic Theory*. McGRAW-HILL BOOK CAMPANY.

Swift, C. M. (1967). A Magnetotelluric Investigation of an Electrical Conductivity Anomaly in the Southwestern united States. *Cambridge, Massachusetts Institute of Technology*, *Ph.D. dissertation*.

Szarka, L., & Menvielle, M. (1997). *Analysis of rotational invariants of the magnetotelluric impedance tensor*. 133–142.

Tadesse, A. Z., Ayalew, D., Pik, R., Yirgu, G., & Fontijn, K. (2018). Magmatic evolution of the Boku Volcanic Complex, Main Ethiopian Rift. *Journal of African Earth Sciences*. https://doi.org/10.1016/j.jafrearsci.2018.08.003

Tester, J. W., Anderson, B. J., Batchelor, A. S., Blackwell, D. D., & DiPippo, R. (2006). The Future of Geothermal Energy - Impact of Enhanced Geothermal Systems (EGS) on the United States in the 21st Century. *MIT - Massachusetts Institute of Technology*, 358. www1.eere.energy.gov/geothermal/pdfs/future_geo_energy.pdf

Tietze, K., Ritter, O., & Egbert, G. D. (2015). 3-D joint inversion of the magnetotelluric phase tensor and vertical magnetic transfer functions. *Geophysical Journal International*, *203*(2), 1128–1148. https://doi.org/10.1093/gji/ggv347

Tournerie, B., Chouteau, M., & Marcotte, D. (2007). Magnetotelluric static shift : Estimation and removal using the cokriging method. *Geophysics*, *72*(1), F25–F34. https://doi.org/10.1190/1.2400625 Downloaded

Trad, D. O., & Travassos, J. M. (2000). *Wavelet filtering of magnetotelluric data*. *65*(2), 482–491.

Tuyen, D. Van, Vu, T. A., Thi, N., & Thuong, K. (2014). *Geochemical Characteristics of Geothermal Hot Water Sources on the Territory of Vietnam*. 1–8.

Uchida, T., & Sasaki, Y. (2006). Stable 3D inversion of MT data and its application to geothermal exploration. *Exploration Geophysics*, *37*(3), 223–230. https://doi.org/10.1071/EG06223

Unsworth, M., & Bedrosian, P. A. (2004). Electrical resistivity structure at the SAFOD site from magnetotelluric exploration. *Geophysical Research Letters*, *31*, 10–13. https://doi.org/10.1029/2003GL019405

Ussher, G., Harvey, C., Johnstone, R., Anderson, E., & Zealand, N. (2000). Understanding the resistivities observed in geothermal systems. *Proceedings World Geothermal Congress*, 1915–1920.

Vasseur, G., & Weidelt, P. (1977). Bimodal electromagnetic induction in non-uniform thin sheets with an application to the northern Pyrenean induction anomaly. *Geophysical Journal International*, *51*(3), 669–

690. https://doi.org/10.1111/j.1365-246X.1977.tb04213.x

Vozoff, K. (1972). THE MAGNETOTELLURIC METHOD IN THE EXPLORATION OF SEDIMENTARY BASlNSt. *GEOPHYSICS*, *37*(1), 98–141. https://doi.org/doi:10.1190/1.1440255

Vozoff, K. (1991). The Magnetotelluric Method. In *Electromagnetic Methods in Applied Geophysics* (Vol. 2, Ap, pp. 641–712). Soc. Explor. Geophys. https://doi.org/10.1190/1.9781560802686.ch8

Wagner, V. R., Díaz, D., Cordell, D., & Unsworth, M. (2017). Regional electrical structure of the Andean subduction zone in central Chile (35 ° – 36 ° S) using magnetotellurics. *Earth, Planets and Space*, *69*(1), 142. https://doi.org/10.1186/s40623-017-0726-z

Wannamaker, P., Hill, G., Stodt, J., Maris, V., Ogawa, Y., Selway, K., Boren, G., Bertrand, E., Uhlmann, D., Ayling, B., Green, A. M., & Feucht, D. (2017). Uplift of the central transantarctic mountains. *Nature Communications*, 1–11. https://doi.org/10.1038/s41467-017-01577-2

Watts, M. D., Mackie, R., Scholl, C., & Hallinan, S. (2013). Limitations of MT static shift corrections using time-domain EM data. *Society of Exploration Geophysicists International Exposition and 83rd Annual Meeting, SEG 2013: Expanding Geophysical Frontiers*, 681–684. https://doi.org/10.1190/segam2013-1078.1

Weaver, J. T., Agarwal, A. K., & Lilley, F. E. M. (2000). Characterization of the magnetotelluric tensor in terms of its invariants. *Geophysical Journal International*, *141*(2), 321–336. https://doi.org/10.1046/j.1365-246X.2000.00089.x

Weidelt, P. (1972). The Inverse Problem of Geomagnetic Induction. *Journal of Geophysics*, *38*, 257-289.

Whaler, K. A., & Hautot, S. (2006). The electrical resistivity structure of the crust beneath the northern Main Ethiopian Rift Elevation (m). *Main*, 293–305.

Whaler K.A. and Hautut S. (2006). The electrical resistivity structure of the crust beneath the northern Main Ethiopian Rift. *Geological Society*, *259*(1), 293–305. https://doi.org/doi:10.1144/gsl.sp.2006.259.01.22

Wiese, H. (1962). Geomagnetische Tiefentellurik Teil II: Die Streichrichtung der untergrundstrukturen des elektrischen Widerstandes, erschlossen aus geomagnetischen Variationen. *Geofisica Pura e Applicata*, *52*(1), 83–103. https://doi.org/10.1007/BF01996002

Wight, D. E., & Bostick, F. X. (1980). Cascade decimation-A technique for real time estimation of power spectra. *IEEE International Conference on Acoustics, Speech, and Signal Processing*.

Woldegabriel, G., Aronson, J. L., & Walter, R. C. (1990). Geology, geochronology, and rift basin development in the central sector of the Main Ethiopia Rift. *Bulletin of the Geological Society of America*, *102*(4), 439–458. https://doi.org/10.1130/0016-7606(1990)102<0439:GGARBD>2.3.CO;2

Word, D. R., Smith, H. W., & Bostick, F. X. (1970). *Crustal Investigations by the Magnetotelluric Tensor Impedance Method*. *14*, 145–167. https://doi.org/10.1029/gm014p0145

Wu, N., Booker, J. R., & Smith, J. T. (1993). Rapid Two-Dimensional Inversion of COPROD2 Data. *J.*

Geomag. Geoelec, *45*, 10.73-1087. https://doi.org/doi:10.5636/jgg.45.1073

Xiang, Y., Yu, P., Zhang, L., Feng, S., & Utada, H. (2017). Regularized magnetotelluric inversion based on a minimum support gradient stabilizing functional. *Earth, Planets and Space*, *69*, 158. https://doi.org/10.1186/s40623-017-0743-y

Yanis, M., Bakar, M., & Ismail, N. (2017). *The Use of VLF-EM and Electromagnetic Induction Methods for Mapping the Ancient Fort of Kuta Lubok as Tsunami Heritage i*. https://doi.org/10.3997/2214-4609.201701996

Yemane, T., Woldegabriel, G., Tesfaye, S., Berhe, S. M., Durary, S., Ebinger, C., & Kelley, S. (1999). Temporal and geochemical characteristics of Tertiary volcanic rocks and tectonic history in the southern Main Ethiopian Rift and adjacent volcanic fields. *Acta Vulcanologica*, *11*, 99–119.

Yoshin, T. (2011). *ELECTRICAL PROPERTIES OF ROCKS*. https://doi.org/10.1007/978-90-481-8702-7

Yungul, S. H. (1996). *Electrical Methods in Geophysical Exploration of Deep Sedimentary Basins*.

Zhdanov, M. S. (2002). GEOPHYSICAL INVERSE TH EORY AND RECULARIZATION PROBLEMS. In *Elsevier Science B.V* (1st editio). Elsevier Science; 1st edition (May 8, 2002).

Zhdanov, M. S., & Keller, G. V. (1994). The geoelectrical methods in geophysical exploration : M.S. Zhdanov & G.V. Keller, (Elsevier; Methods in Geochemistry and Geophysics, 31), ISBN (hardback) 0 444 89678 3, price Dfl 375.00 (US$214.25), 1994, 873 pp, index. *International Journal of Rock Mechanics and Mining Sciences & Geomechanics Abstracts*, *31*(4), 195. https://doi.org/10.1016/0148-9062(94)91092-8

Appendices

Appendices 1 Title and Abstract of published and submitted manuscripts to different journals

Appendix 1.1 **3D analysis of the MT data for resistivity structure beneath the Ashute geothermal site, Central Main Ethiopian Rift (CMER).**

Abstract

Heliyon 9 (2023) e13202

Contents lists available at ScienceDirect

Heliyon

journal homepage: www.cell.com/heliyon

Research article

3D analysis of the MT data for resistivity structure beneath the Ashute geothermal site, Central Main Ethiopian Rift (CMER)

Aklilu Abossie [a,c,*], Shimeles Fisseha [b], Bekele Abebe [a]

[a] School of Earth Science, Addis Ababa University, P. O. Box 1176, Addis Ababa, Ethiopia
[b] Institute of Geophysics, Space Science and Astronomy, Addis Ababa University, P. O. Box 1176, Addis Ababa, Ethiopia
[c] Department of Earth Science, Wollega University, P. O. Box 395, Nekemt, Ethiopia

ARTICLE INFO

Keywords:
Ashute
Magnetotelluric
3D inversion
Resistivity
Ethiopia

ABSTRACT

The Ashute geothermal field (around Butajira) is located near the western rift escarpment of the Central Main Ethiopian Rift (CMER), about 5–10 km west of the axial part of the Silti Debre Zeit fault zone (SDFZ). Several active volcanoes and caldera edifices are hosted in the CMER. Most of the geothermal occurrences in the region are often associated with these active volcanoes. The magnetotelluric (MT) method has become the most widely used geophysical technique for the characterization of geothermal systems. It enables the determination of the subsurface electrical resistivity distribution at depth. The high resistivity under the conductive clay products of hydrothermal alteration related to the geothermal reservoir is the main target in the geothermal system. The subsurface electrical structure of the Ashute geothermal site was analyzed using the 3D inversion model of MT data, and the results are endorsed in this work. The ModEM inversion code was used to recover the 3D model of subsurface electrical resistivity distribution. According to the 3D inversion resistivity model, the subsurface directly beneath the Ashute geothermal site can be represented by three major geoelectric horizons. On top, a relatively thin resistive layer (>100 Ωm) represents the unaltered volcanic rocks at shallow depths. This is underlain by a conductive body (< 10 Ωm), possibly associated with the presence of clay horizon (smectite and illite/chlorite zones), resulting from the alteration of volcanic rocks within the shallow subsurface. In the third bottom geoelectric layer, the subsurface electrical resistivity gradually increases to an intermediate range (10–46 Ωm). This could be related to the formation of high-temperature alteration minerals such as chlorite and epidote at depth, suggesting the presence of a heat source. As in a typical geothermal system, the rise in electrical resistivity under the conductive clay bed (products of hydrothermal alteration) may indicate the presence of a geothermal reservoir. Otherwise, no exceptional low resistivity (high conductivity) anomaly is detected at depth.

Appendix 1.2 **Crustal resistivity structures beneath the western flank across the Central Main Ethiopian Rift: Its implications for partial melt and pathways**

Abstract

Contents lists available at ScienceDirect

Journal of Volcanology and Geothermal Research

journal homepage: www.journals.elsevier.com/journal-of-volcanology-and-geothermal-research

ELSEVIER

Crustal resistivity structures beneath the western flank across the Central Main Ethiopian Rift: Its implications for partial melt and pathways

Aklilu Abossie [a,c,*], Shimeles Fisseha [b], Bekele Abebe [a]

[a] *School of Earth Science, Addis Ababa University, P.O. Box 1176, Addis Ababa, Ethiopia*
[b] *Institute of Geophysics, Space Science and Astronomy, Addis Ababa University, P.O. Box 1176, Addis Ababa, Ethiopia*
[c] *Department of Earth Science, Wollega University, P.O. Box 395, Nekemet, Ethiopia*

ARTICLE INFO

Keywords:
Magnetotelluric
Dimensional analysis
Strike analysis
2D inversion
CMER
SDFZ

ABSTRACT

The Wonji Fault Belt (WFB) and the Silti Debre Zeit Fault Zone (SDFZ) are two linear belts in the Central Main Ethiopian Rift (CMER) where recent magmatic and tectonic activities have been concentrated. To examine deep resistivity patterns, magma storage, and its path beneath the Earth's crust across the CMER, the researchers used a two-dimensional (2D) inversion model of magnetotelluric data. The time series magnetotelluric data ranging from 0.003125 to 1450.0 s were collected during >24 h of installations at 21 sites, with an average station separation of 2.5 km along a profile perpendicular to the rift from the western margin of the rift (near Butajira) to AdamiTulu (near the rift axis). This work describes the use of phase tensor analysis to determine the dimensionality and geoelectrical strike direction, as well as the estimation of geoelectric strike parameters and the 2D inversion model of MT data. The results of dimensionality analysis of the majority of our MT data show a small beta value ($|\beta|<3^0$) at low periods (nearly below 10 s), which indicates 1D or 2D structures, while at long periods (almost above 10 s), the data show 3D structures with a large value of $|\beta| >3^0$. However, from the results of the dimensionality analysis of MT data, the 2D inversion model is suitable to image the resistivity of subsurface structures. The dominant geo-electrical strike is estimated to be N15^{0}E using a *Z*-invariant and phase tensor azimuth. The 2D inversion model was performed after the MT data were rotated to the proper geoelectric strike direction of N15^{0}E. The desired 2D inversion of the resistivity model was obtained for the MT profile using joint inversion of TE (transverse electric) and TM (transverse magnetic) mode data with an RMS misfit of 1.11. The results of the 2D inversion model reveal partial melt and upper crustal fracture zone (fault). They are attributed to a large mass of batholithic or magmatic intrusion found at a depth of 12–22 km that is characterised by a resistivity of <5 Ωm. The partial melt extends beneath stations B07 to B11 along SDFZ with a horizontal width of approximately 10 km. It could be related to the source of heat for the Ashute and Aluto geothermal fields.

Appendix 1.3 **Joint 1D inversion of TEM and MT data and Comparison of 3D Inversion Results with and without Static Shifted Magnetotelluric Data in the Ashute Geothermal Field, Central Main Ethiopian Rift.**

Abstract

Heliyon

Joint 1D inversion of TEM and MT data and Comparison of 3D Inversion Results with and without Static Shifted Magnetotelluric Data in the Ashute Geothermal Field, Central Main Ethiopian Rift (CMER)

--Manuscript Draft--

Manuscript Number:	
Article Type:	Original Research Article
Section/Category:	Physical and Applied Sciences
Keywords:	Joint inversion, TEM, Static shift, 3D inversion, Geothermal field
Manuscript Classifications:	100.150: Geology; 100.150.130: Geophysics
Corresponding Author:	AKLILU ABOSSIE ANSHEBO, MSC Addis Ababa University ADDIS ABABA, ETHIOPIA, ADDIS ABABA ETHIOPIA
First Author:	AKLILU ABOSSIE ANSHEBO, MSC
Order of Authors:	AKLILU ABOSSIE ANSHEBO, MSC
	Shimeles Fisseha, PhD (Assocate professor)
	Bekele Abebe, PhD (Professor)
Abstract:	The inhomogeneity of near-surface in the Ashute geothermal field magnetotelluric data suffers from a static shift effect in the high-frequency band due to a high fluctuation of resistivity. To correct static shifts, several solutions have been presented. In this study, we carried out the joint 1D inversion of transient electromagnetic (TEM), and magnetotelluric (MT) data from 30 stations to correct static-shift effects. The primary focus of the study is to apply a static shift correction scheme to MT data and compare the relationship between the 3D inversion model of the MT data with and without static shift correction, specifically focusing on the Ashute geothermal field. Through the joint inversion of TEM and MT soundings, as well as the 3D inversion of the full impedance tensor, we developed a model for a homogeneous earth with resistivity values of 50 and 100 Ωm, respectively. The preferable model with and without static shift corrected model is 100 Ωm used for background resistivity. In contrast to uncorrected magnetotelluric data, which exhibited vertical shifts in apparent resistivity curves, leading to potentially inaccurate and unreliable estimations. Whereas the static-shift-corrected data provided improved and more accurate estimates of subsurface resistivity structures and thicknesses. Comparing the observed data to the model, it was found that the model derived from the inversion of static-shift-corrected data more accurately captured the resistivity structure compared to the uncorrected data, particularly in geologically constrained areas. The static-shifted corrected data were found to recover the resistivity more effectively as a consequence of the 3D inversion resistivity results. Therefore, the Ashute geothermal field between with and without static-shift corrected data revealed little difference at the shallow depth. However, at deeper depths, the two models approximately agree with resistivity below at 2.7 km depth.

Appendix 2.1 Joint Inversion of TEM and MT Sounding Curves

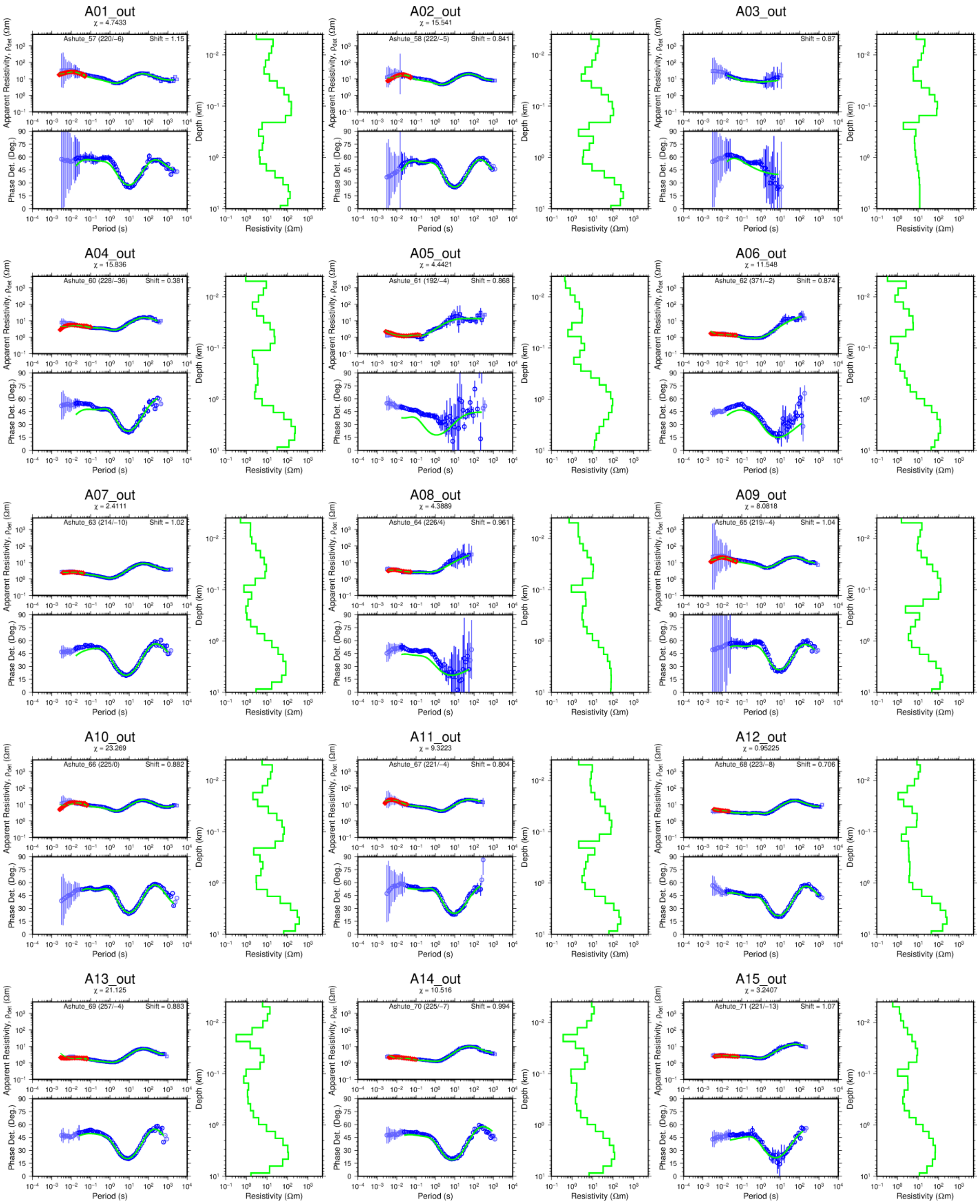

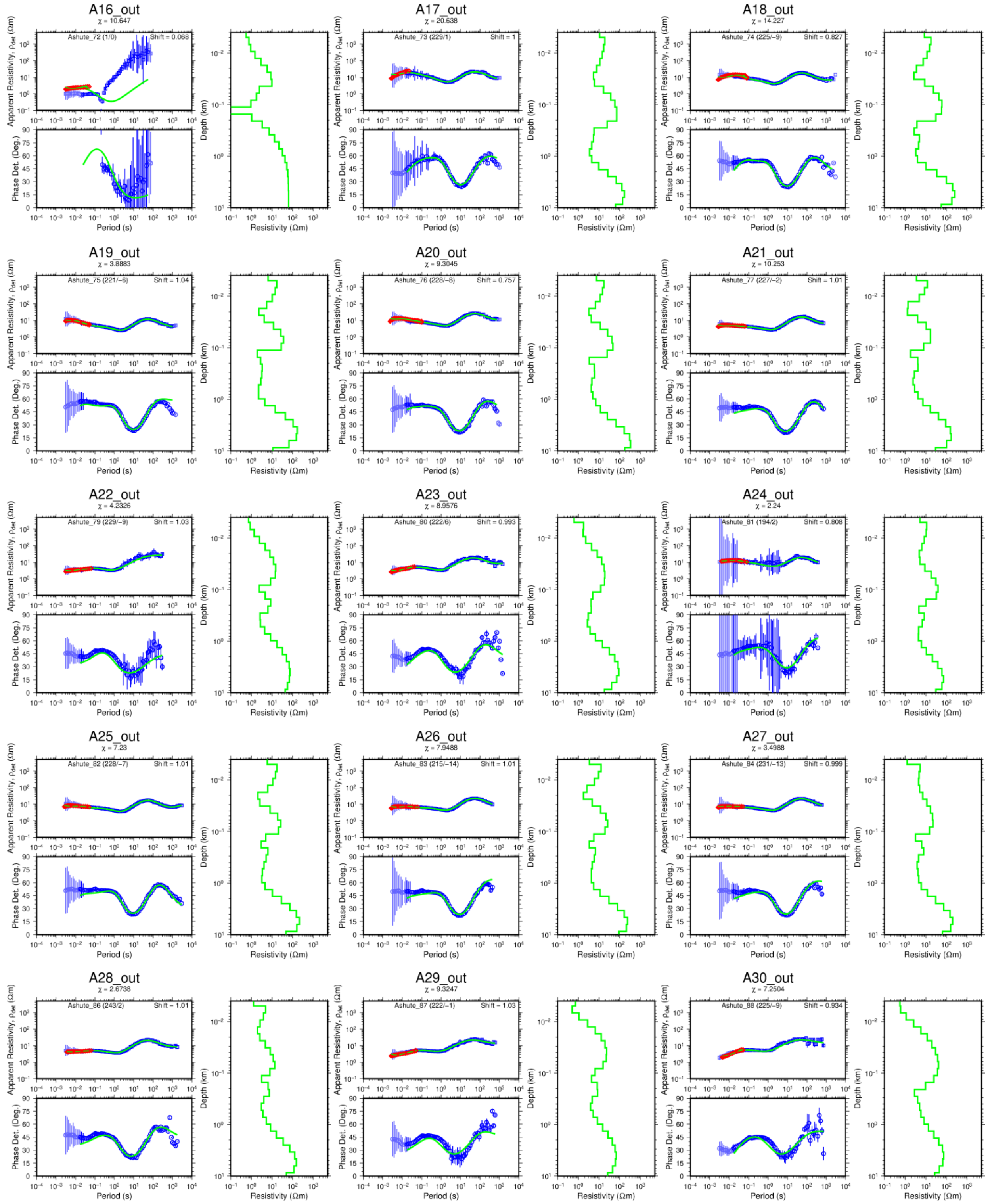

A16_out
χ = 10.647
Ashute_72 (1/0)
Shift = 0.068
A17_out
χ = 20.638
Ashute_73 (229/1)
Shift = 1
A18_out
χ = 14.227
Ashute_74 (225/−9)
Shift = 0.827
A19_out
χ = 3.8883
Ashute_75 (221/−6)
Shift = 1.04
A20_out
χ = 9.3045
Ashute_76 (228/−8)
Shift = 0.757
A21_out
χ = 10.253
Ashute_77 (227/−2)
Shift = 1.01
A22_out
χ = 4.2326
Ashute_79 (229/−9)
Shift = 1.03
A23_out
χ = 8.9576
Ashute_80 (222/6)
Shift = 0.993
A24_out
χ = 2.24
Ashute_81 (194/2)
Shift = 0.808
A25_out
χ = 7.23
Ashute_82 (228/−7)
Shift = 1.01
A26_out
χ = 7.9488
Ashute_83 (215/−14)
Shift = 1.01
A27_out
χ = 3.4988
Ashute_84 (231/−13)
Shift = 0.999
A28_out
χ = 2.6738
Ashute_86 (243/2)
Shift = 1.01
A29_out
χ = 9.3247
Ashute_87 (222/−1)
Shift = 1.03
A30_out
χ = 7.2504
Ashute_88 (225/−9)
Shift = 0.934
Apparent Resistivity, ρdet (Ωm)
Phase Det. (Deg.)
Period (s)
Depth (km)
Resistivity (Ωm)

Appendix 3.1 The tables shown below illustrates coordinates of MT stations for A) 3D analysis area and B) 2D analysis area of the study.

A

MT Stations	Latitude	Longitude
A01	8.050528	38.39603
A02	8.040028	38.39544
A03	8.032167	38.39628
A04	8.022972	38.39706
A05	8.013611	38.39764
A06	8.003611	38.39644
A07	7.996	38.39647
A08	7.986972	38.39711
A09	8.050222	38.40519
A10	8.041389	38.40478
A11	8.032222	38.40461
A12	8.022972	38.40458
A13	8.013889	38.40564
A14	8.004556	38.40656
A15	7.996056	38.40597
A16	7.987333	38.40561
A17	8.050389	38.41467
A18	8.041056	38.41714
A19	8.032833	38.41464
A20	8.022389	38.41475
A21	8.013694	38.41553
A22	7.994611	38.41572
A23	7.987139	38.41456
A24	8.051389	38.42236
A25	8.041389	38.42525
A26	8.031639	38.42519
A27	8.023917	38.42478
A28	8.005806	38.42231
A29	7.995056	38.42428
A30	7.987056	38.42375

B

MT Stations	Latitude	Longitude
B01	8.050167	38.32978
B02	8.035639	38.35103
B03	8.026722	38.35481
B04	8.013639	38.36992
B05	7.994417	38.38364
B06	7.981028	38.42939
B07	7.963028	38.45006
B08	7.950111	38.46714
B09	7.93425	38.49147
B10	7.924722	38.51028
B11	7.916556	38.53164
B12	7.903806	38.54994
B13	7.897139	38.56839
B14	7.885694	38.588
B15	7.877111	38.61056
B16	7.868528	38.63703
B17	7.862472	38.64806
B18	7.857833	38.65964
B19	7.853306	38.67261
B20	7.852028	38.68839
B21	7.838889	38.71225